THE FUNDAMENTALS OF TWO-PHASE FLOW IN WET DOMESTIC CENTRAL HEATING SYSTEMS

A thesis submitted for the degree of Doctor of Philosophy

By

Andrew M. Fsadni

School of Engineering and Design

Brunel University

April 2012

Abstract

An emerging trend in the building services industry is the installation of passive deaerators on the flow line of domestic wet central heating systems. To date, no data and theoretical models predicting the two-phase flow characteristics in domestic wet central heating systems are available in the open literature. This gap in literature has prevented essential design improvements to passive deaerators thus impeding the efficiency enhancement of such devices.

Hence, the current study is aimed at assisting designers of deaeration devices by providing fundamental data and model correlations with respect to the two-phase flow characteristics typical in a wet domestic central heating system.

For this purpose an experimental research project was adopted and several studies were carried out, including; (1) a comprehensive review to understand the background of the phenomena, (2) the design and construction of an experimental test rig to conduct the necessary investigations into the phenomenon of two-phase flow in domestic wet central heating systems, (3) the development of a reliable image capture and analysis technique, (4) the completion of a number of experiments to investigate typical bubble sizes, volumetric void fractions, bubble distributions and nucleation and dissolution rates and (5) the correlation of the data gathered as part of the present study with existing bubble size, nucleation and dissolution prediction models.

This research has, for the first time, provided an in depth analysis into two-phase flow characteristics in wet domestic central heating systems through the use of a high speed camera and image analysis techniques. The two-phase phenomenon finds its origins in high dissolved gas concentrations present in the water flowing through the closed loop system, thus resulting in super saturation conditions at the primary heat exchange wall conditions. Bubble sizes at the boiler flow line were found to be dependent on the bulk fluid velocity, heat flux and pressure, with a measured mean diameter in the range of 0.13 mm to 0.39 mm. The Winterton (1972a) force balance model for bubble size prediction was in reasonable agreement with the experimental results. This model was further improved through the correlation of our data with the inclusion of dimensionless

groups. Bubble nucleation rates have been calculated in the range of 0.3 to 4 bubbles / cm^2 s with total system bubble production rates measured in the range of 784 to 6920 bubbles per second. Bubble nucleation rates have been calculated through the consideration of the heat exchanger surface under super saturation conditions. A correlation for the model by Hepworth et al. (2003) for non-classical heterogeneous nucleation is proposed based on the experimental data gathered during the present study.

Experimental results have shown dissolution rates for the bubble size ratio in the range of 0.4 to 12 % per second with system conditions. A modification of the model developed by Epstein and Plesset (1950) for stationary bubble dissolution is proposed with the inclusion of the Sherwood number to capture the effects of turbulent diffusion. The volumetric void fraction distribution in vertical pipes was found to be quasi-homogenous across the pipe section while being strongly dependent on gravitational and turbulence effects in horizontal pipe bubbly flow. A CFD simulation predicted the volumetric void fraction distribution with reasonable accuracy.

Author's Declaration

The research presented in this thesis is the original work of the author except where otherwise specified, or where acknowledgments are made by references. This project was carried out at the School of Engineering and Design, Brunel University, under the supervision of Dr. Yunting Ge.

The work has not been submitted for another degree or award to any other institution.

Andrew Fsadni

Date: 20th April, 2012

I further authorise Brunel University to reproduce this thesis by photocopying or by other means, in total or in part, at the request of other institutions or individuals for the purpose of scholarly research.

Andrew Fsadni

Date: 20th April, 2012

Acknowledgements

Table of Contents

Table of Figures

List of Tables

Nomenclature

Latin

a	Acceleration of fluid	(m/s^2)
A	Tube (pipe) cross sectional area	(m^2)
A_{ss}	Tube area under super saturation conditions	(m^2)
A_t	Tube surface area	(m^2)
A_{ts}	Heating tube cross sectional area	(m^2)
AR_{ss}	Ratio of tube area under super saturation conditions	(-)
B	Dimensionless group as given in Eq. (2.22)	(-)
B_c	Bubble count per sample image	(-)
B_{ss}	Dimensionless group as given in Eq. (2.30)	(-)
B_w	Constant as given in Eqs. (2.8) & (2.9)	(-)
C_{bg}	Dissolved gas concentration in system	(mol/m^3)
C_E	Gas concentration in bubble	(kg/m^3)
C_g	Dissolved gas concentration in system	(standard cm^3/L Water)
C_o	Dissolved gas concentration in system	(kg/m^3)
C_p	Specific heat capacity for water	(J/kg K)
C_s	Dissolved gas concentration at saturation conditions	(standard cm^3/L Water)
C_{sg}	Dissolved gas concentration at saturation conditions	(mol/m^3)
C_μ	Function of the mean strain and rotation rates, the angular velocity of the system and the turbulence fields	(-)
$C_{1\varepsilon}$	Constant as in Eq. (5.10)	(-)
$C_{2\varepsilon}$	Constant as in Eq. (5.10)	(-)
$C_{3\varepsilon}$	Constant as in Eq. (5.10)	(-)
d_t	Tube dimensions as in Fig. 3.17	(m)
D	Diffusivity	(m^2/s)
D_b	Bubble diameter	(m)
D_{bc}	Diameter of helical coil structure	(m)
D_{bm}	Maximum bubble diameter	(m)

DF	Depth of field	(m)
D_h	Tube hydraulic diameter	(m)
D_n	Bubble width as defined in Fig. 4.16	(m)
D_p	Bubble width as defined in Fig. 4.16	(m)
E_o	Eotvos number	(-)
F	Empirical proportionality constant	(-)
F_b	Buoyancy force	(N)
F_d	Drag force	(N)
F_s	Surface tension force	(N)
F_w	Constant as given in Eq. (2.8)	(-)
g	Acceleration due to gravity	(m/s^2)
G_b	Generation of turbulent kinetic energy due to the buoyancy of the second phase	$(J/m^3 s)$
G_K	Generation of turbulent kinetic energy due to the mean velocity tensor	$(J/m^3 s)$
h	Heat transfer coefficient	$(W/m^2\,K)$
J	Bubble nucleation rate	$(bubbles/cm^2\,s)$
J_1	Bubble nucleation rate	$(bubbles/m^2\,s)$
k	Thermal conductivity of water	(W/mK)
k_b	Boltzmann constant	(erg/molecule K)
K	Turbulent kinetic energy	(m^2/s^2)
K''	A variation of the Henry's constant	(bar/mole fraction)
K_h	Henry's gas solubility constant at the stated temperature	(standard cm^3/L water/bar)
L_c	Heating tube coil length	(m)
L_{css}	Point on heating tube, measured from return side, under saturation conditions	(m)
L_{sg}	Length of sight glass section	(m)
L_{si}	Length of sample image	(m)
L_t	Tube dimensions as in Fig. 3.17	(m)
m	Constant as given in Eq. (2.8)	(-)
$\dot{m}$	Mass flow rate	(kg/s)
M_g	Molecular mass of gas	(g)

M_l	Molecular mass of the liquid.	(g)
n_g	Number of moles of gas	(-)
n_l	Number of moles of liquid	(-)
n_s	Active nucleation site density	(sites/m^2)
N	Molecular density	(molecules/cm^3)
N_a	Dimensionless group as given in Eq. (2.25)	(-)
N_b	Dimensionless group as given in Eq. (2.26)	(-)
N_c	Number of coils	(-)
N_{cb}	Bubble nucleation rate in a single cavity	(Bubbles/ s)
N_{ec}	Empirical constant as in Eq. (2.18)	(-)
N_f	Dimensionless group as in Eq. (2.3)	(-)
N_g	Mole fraction	(-)
Nu	Nusselt number	(-)
P_a	Gas partial pressure	(Pa)
P_{atm}	Atmospheric pressure	(Pa)
P_g	Dissolved nitrogen partial gas pressure	(Pa)
P_{l1}	Bulk fluid pressure	(dyn/cm^2)
P_l	Bulk fluid pressure	(Pa)
P_{sat}	Partial pressure of dissolved nitrogen gas at saturation conditions	(Pa)
P_{sys}	System pressure	(Pa)
P_{TGM}	Total dissolved gas pressure	(Pa)
P_{ts}	Tube wetted perimeter	(m)
Pr	Prandtl number	(-)
PR	Bubble production rate	(Bubbles/s)
P_v	Vapour pressure	(Pa)
q	Heat flux	(kW/m^2)
q_{max}	Maximum heat flux	(kW/m^2)
Q	Heating load	(W)
r	Bubble radius at detachment	(m)
r'	Nucleation cavity radius	(m)
r_c	Bubble critical radius	(m)
r_{c1}	Bubble critical radius	(cm)
r_p	Interval along pipework radius	(m)

r_t	Tube dimensions as in Fig. 3.17	(m)
R	Tube radius	(m)
Re	Reynolds number	(-)
R_g	Universal gas constant	(J/mol K)
R_o	Bubble radius measured at *HSG1*	(m)
R_p	Pipe work radius	(m)
R_t	Bubble radius after time interval	(m)
R_x	Bubble Radius measured at *HSG2*	(m)
S	Deformation tensor	(-)
S_w	Constant as given in Eq. (2.8)	(-)
Sc	Schmidt number	(-)
Sh	Sherwood number	(-)
t	Time for bubble to flow across sample image	(sec)
t_e	Bubble lifetime	(sec)
t^*	Dimensionless time as in Eq. (2.27)	(-)
T_b	Bulk fluid temperature	(K)
T_w	Fluid temperature at the primary heat exchanger wall conditions	(K)
T_{wo}	Wall temperature at exit	(K)
T_{wr}	Wall temperature at boiler return side	(K)
T_{wsat}	Wall temperature	(K)
u	Bulk fluid velocity	(m/s)
u_{rel}	Relative velocity between phases	(m/s)
v_*	Friction velocity	(m/s)
$\dot{V}$	Volumetric flow rate	(L/min)
V_b	Volume of bubble	(m^3)
V_{ba}	Mean bubble volume per sample image	(m^3)
v_{sg}	Bubble velocity in sight glass	(m/s)
V_{sv}	Sample image volume	(m^3)
V_T	Total bubble volume	(m^3)
W_g	Mass of the gas	(g)
W_l	Mass of the liquid	(g)
We	Weber number	(-)

W_{sg}	Width of sight glass section	(m)
W_{si}	Width of sample image	(m)
x	Dimensionless group as given in Eq. (2.23)	(-)
x_g	Mole ratio	(Moles gas/ Moles Liquid)
X_b	Saturation mole fraction at temperature T_A in Fig. 2.1	(-)
X_i	Saturation mole fraction at temperature T_B in Fig. 2.1	(-)
X_g^T	Bunsen solubility coefficient	(standard cm^3/L water/bar)
X_{sat}^T	Bunsen solubility coefficient at saturation conditions	(standard cm^3/L water/bar)

Greek

α	Saturation ratio	(-)
β	Conical half-angle	(^{o})
Υ	Surface tension	(N/m)
Υ_1	Surface tension	(erg/cm^2)
Υ_e	Dimensionless group as given in Eq. (2.23)	(-)
ΔP	Difference in pressure between the gas inside the bubble and the bulk liquid or system pressure.	(Pa)
ΔT	Change in temperature	(K)
ε	Turbulent dissipation	(m^2/s^3)
ε_m	Energy dissipation per unit mass	(J/s/kg)
ε_v	Volumetric void fraction	(-)
$\in_b$	Bubble size ratio	(-)
η	Dimensionless value used to describe the velocity profile	(-)
θ_a	Advancing contact angle	(^{o})
θ_o	Static contact angle	(^{o})
θ_r	Receding contact angle	(^{o})
μ	Dynamic viscosity	(Ns/m^2)
μ_t	The eddy viscosity	(Kg/m s)
ρ	Density of water	(Kg/m^3)
ρ_g	Density of gas	(Kg/m^3)

σ	Super saturation ratio	(-)
σ_K	Turbulent Prandtl numbers for K	(-)
σ_ε	Turbulent Prandtl numbers for ε	(-)
v	Kinematic Viscosity	(m^2/s)
τ	Viscous stress	(N/m^2)

Abbreviations

abs	Absolute pressure
CFD	Computational fluid dynamics
HSG1	Horizontal sight glass number one as in Fig. 3.1
HSG2	Horizontal sight glass number two as in Fig. 3.1
PPB	Parts per billion
SR	Saturation ratio
TGM	Total gas measurement transducer as in Figs. 3.1 & 3.7
VSG1	Vertical sight glass on flow line as in Fig. 3.1
VSG2	Vertical sight glass on return line as in Fig. 3.1

List of Appendices

Dimensionless Groups

Group	Definition	Expression
Bubble size ratio, $\in_b$	$\dfrac{Bubble\ radius\ after\ time\ t}{Original\ bubble\ radius}$	$\dfrac{R_t}{R_o}$
Eotvos number, E_o	$\dfrac{Buoyancy\ force}{Surface\ tension}$	$E_o = \dfrac{g\Delta\rho D_b^2}{\gamma}$
Prandtl number, Pr	$\dfrac{Viscous\ diffusion\ rate}{Thermal\ diffusion\ rate}$	$\dfrac{C_p\mu}{k}$
Reynolds number, Re	$\dfrac{Inertia\ forces}{Viscous\ forces}$	$\dfrac{uD_h}{\nu}$
Saturation ratio, α	$\dfrac{Actual\ gas\ concentration}{Gas\ concentration\ at\ saturation\ conditions}$	$\dfrac{C_g}{C_s}$
Schmidt number, Sc	$\dfrac{Momentum\ diffusivity}{Mass\ diffusivity}$	$\dfrac{\nu}{D}$
Sherwood number, Sh	$\dfrac{Convective\ mass\ transfer\ coefficient}{Diffusive\ mass\ transfer\ coefficient}$	$Sh = F\dfrac{D_b}{2R}Re^{0.75}Sc^{0.5}$
Super saturation ratio, σ	*Excess gas concentration above the maximum concentration that the solvent can dissolve*	$\alpha - 1$
Weber number, We	$\dfrac{Inertia\ of\ fluid}{Surface\ tension}$	$\dfrac{\rho u^2 D_h}{\gamma}$

CHAPTER 1

Introduction

1.1 Background

The space heating of domestic buildings results in a substantial use of energy, thus contributing towards a large share of the carbon footprint emitted by the domestic sector. A survey commissioned by the European Commission (2002), reported that the total space heating energy consumption in nine European Union countries lies in a range of 1.5 to 1.7E+15 kWh/year. The latter energy usage, results in circa 365 million tons of carbon dioxide emissions on a yearly basis.

Domestic wet central heating systems are widely used in households across the world. This is particularly true in Europe where, in the UK, domestic wet central heating systems amount to circa 16% of the carbon dioxide emissions (The Building Regulations Part L1A, 2006). In Germany, almost all residential buildings make use of a wet central heating system, that consequently amount to circa 40% of the primary energy consumed on a national level (Spreitzer et al., 2002). Furthermore, in Germany, wet central heating systems are responsible for 70% of all domestic emissions (Sauer et al., 2007).

The installation of efficient condensing boilers in new and refurbished dwellings has been widespread in the recent years (Weiss et al., 2009). Condensing boilers are characterized by typical efficiencies in excess of 90%. However, the comprehensive system efficiency, hence incorporating potential issues with the system pipework and radiators is relatively unknown. One of the principal factors affecting the system efficiency, is the presence of air bubbles in the water flowing through the closed loop system. Such bubbles are known to originate from the dissolved gasses present in the water flowing through the system pipework. Hence, the dissolved gasses are degassed at the boiler wall due to the elevated temperatures, thus resulting in super saturation conditions. Such bubbles

1

could reduce the overall system efficiency, and hence should be exhausted from the sealed system. The latter could be achieved through the installation of a passive deaerator.

When considering the widespread use of domestic wet central heating systems, and the carbon reduction targets for the domestic sector as set by the European Union of 20% by the year 2020 and 80 – 95 % by the year 2050 (European Commission, 2010), the emphasis on the importance of an efficient system deaerator design and positioning within the system setup, is more valid. However, experimental data and numerical models that could predict the behavior of bubbles in such systems are necessary as a precursor to a redesigned efficient deaerator component. Such data is not available in the open literature.

This chapter is organized as follows; Section 1.2 discusses the motivations for the current study. Section 1.3 presents the aims and objectives of the current study, while Section 1.4 lists the contributions of the current study. The outline of the thesis is presented in Section 1.5.

1.2 Motivation

The nucleation and subsequent detachment and flow of bubbles in a system, is a process that affects a wide spectrum of industries, often with undesirable results. Hence in the power, food, chemical and other processing industries, large quantities of deaerated water are required to achieve an optimum system performance or product purity (Battaglia, 1995). As reported by Dean (1944), the formation of bubbles in water finds its origins in the presence of either a supersaturated or a superheated liquid.

As highlighted in the aforementioned discussion, in a domestic central heating system, micro bubble formation finds its origins in gas super saturation levels present in the water flowing through the closed loop system, thus resulting in bubbles nucleating on the boiler wall primary heat exchanger (Lamers, 2005). The use of the latter term for a standard domestic central heating unit, may suggest that some form of boiling takes place in the system's primary heat exchanger, consequently leading to the formation of bubbles through superheat. However, under no operating conditions does the phenomenon of flow boiling or

sub-cooled flow boiling take place in a modern domestic central heating condensing boiler. Therefore, micro bubble nucleation is solely attributed to the presence of gas super saturation levels in the water flowing in the system's closed loop circuit. Air is absorbed in the system through the radiators, expansion vessels and pipe connections during the system's heating cycle. The filling procedure, also introduces dissolved air in the water. At low temperatures, water can absorb the highest quantity of dissolved gasses (Gerrard, 1976; Young et al., 1982). In most systems, this occurs during night time when the system's boiler shuts off. The subsequent morning restart would consequently result in high saturation ratios. The detachment of bubbles into the system, results in a bubbly two-phase flow in the circuit's flow line, characterized by the presence of bubbles of maximum size much less than the containing vessel or duct (Roffelsen, 1984).

The principal motivation leading to the present study, is the need for a comprehensive understanding of the general behaviour of two-phase flow in domestic central heating systems. The formation of air bubbles in a central heating system is currently not well understood (Lamers, 2005). As a matter of fact, most studies available in the open literature on bubble formation due to high dissolved gas concentrations in water, are based on laboratory tests that are mostly theoretical in nature (Winterton, 1972a; Wilt, 1986; Jones et al., 1999a&b). Similar trends are also evident with the dissolution of bubbles in water (Epstein and Plesset, 1950).

It is a known fact that bubbles present in heating systems, will accumulate in the system radiators consequently resulting in the reduction in the heat transfer rates due to a head of gas being formed at the top end of the radiator with prolonged usage of the system. This would result in a reduction in the overall efficiency of the central heating system, mostly due to the operation of the boiler for longer intervals (Karapantsios et al., 2008). Furthermore, gas bubbles could also result in blockages in the system pipework and in corrosion issues (Davis, 1987). Air bubbles could also produce a knocking effect in the system pipework and thus cause a certain level of unwanted noise in dwellings. Hence, these undesirable effects all call for more research in this area, with the aim of developing a comprehensive understanding of the two-phase phenomenon in wet domestic

central heating systems. This research, should therefore lead to enhanced passive deaerator designs by Spirotech bv. The contribution of the present study, will also lead to an optimized deaerator positioning with respect to the boiler unit for enhanced deaeration efficiencies.

Water deaerators installed in domestic central heating systems are of the passive type, while in larger industrial systems vacuum deaerators could be used. The latter make use of a vacuum pump for an enhanced deaeration technique. A typical passive deaerator (Spirotech, AA100 model), installed on the flow line of a boiler is illustrated in Fig. 1.1. Similar designs are produced by other leading suppliers. Such devices consist of a vertical column and a float valve at the upper end of the column. Hence, air bubbles float up the column and accumulate at the top end. The excess air is then exhausted through the action of a float valve.

Figure1.1: Typical passive bubble deaerator design (Spirotech AA100 design)

1.3 Aims and Objectives

It is clear from the aforementioned issues that, bubble formation and the general characteristics of two-phase flow in domestic central heating systems, are still unclear and hence require more research. Lamers (2005) presented a comprehensive analysis of the expected gas concentration in a closed loop central heating system due to long term usage. However, reliable experimental

techniques and data on bubble characteristics are still not available. As a result, the objectives of the current study include:

- The research and development of an experimental test rig for a long term experimental project for the investigation of the general characteristics of two-phase flow in wet domestic central heating systems.

- The general development of experimental techniques for the investigation of two-phase flow, together with an investigation into the relevant uncertainties.

- The development of an image processing macro capable of automatically analysing the stored images.

- The investigation of the dissolved gas composition in a closed loop central heating system.

- The experimental investigation of bubble distribution in vertical downflow two-phase bubbly flow.

- The experimental investigation of bubble characteristics at the boiler exit, as a function of the system pressure, heating load, saturation ratio and flow rate.

- The development of a mathematical model, for the prediction of the bubble diameter at the boiler exit, as a function of the relevant system parameters.

- The development of a mathematical model, for the prediction of bubble nucleation at the boiler wall, as a function of the relevant system parameters, these being the; system pressure, bulk fluid velocity, dissolved gas concentration and the heat flux at the primary heat exchanger wall.

- The experimental investigation of bubble dissolution in under saturated bulk fluid, in straight horizontal pipes.

- The development of a mathematical model for the prediction of bubble size due to dissolution in under saturated bulk fluid conditions, as a function of the relevant system parameters.

- The experimental investigation of bubble behaviour in super saturated bulk fluid in straight horizontal pipes.

- The experimental investigation of bubble distribution in horizontal two-phase bubbly flow.

- The development of a two-phase simulation for bubble distribution through the use of a CFD code as developed by FLUENT and based on the Finite Volume Method, with a comparison of the predicted results to the experimental results.

1.4 Contributions

The main contributions of the current research work can be split in two sectors, one being the contribution towards the sponsoring company and the contribution to the open literature and academic circles. Hence, as discussed in the previous sections, the research work presented in this thesis will be used by the sponsoring company Spirotech bv. for an optimized deaerator design and positioning in the system, hence leading to more efficient domestic central heating systems. In addition, the work presented in this thesis has been submitted for publication in peer reviewed journal papers, an edited book and international conferences. The feedback received from the peer reviews, has been instrumental for an enhanced interpretation of the experimental results obtained as part of the current study.

1.4.1 Journal papers

Three papers were presented for publication in peer reviewed journals, with two papers accepted for publication by the Applied Thermal Engineering Journal. The third paper will be submitted to the International Heat and Mass Transfer journal. The papers were written to cover the three main research areas, these being; the bubble size prediction and nucleation on the boiler wall, and bubble size prediction due to dissolution in straight horizontal pipe work. The relevant details are as follows;

1. Fsadni A.M., Ge Y.T., Lamers A.G., 2011, Measurement of bubble detachment diameters from the surface of the boiler heat exchanger in a domestic central heating system, *Applied Thermal Engineering*, 31, (14-15), pp. 2808-2818.

2. Fsadni A.M., Ge Y.T., Lamers A.G., 2012, Bubble nucleation on the surface of the primary heat exchanger in a domestic central heating system, *Applied Thermal Engineering,* 45, pp. 24-32.

3. Fsadni A.M., Ge Y.T., Bubble dissolution in turbulent bubbly flow in domestic central heating horizontal pipe work, *Paper to be submitted to the International Journal of Heat and Mass Transfer.* Target submission date: April 2012.

1.4.2 Book section

A paper presenting general results with respect to the current research work, was presented for publication in an annual publication produced by the Wessex Institute Press. The relevant details are as follows;

1. Fsadni A.M., Ge Y.T., Lamers A.G., 2011, Experimental analysis of two-phase flow in domestic central heating systems – micro bubble characteristics, In: Mammoli A.A., Brebbia C.A., ed. 2011, *Multiphase Flow VI*, WIT Press, Southampton, pp. 165-176.

1.4.3 Conference papers

Two conference papers were presented for publication. The first paper presented the results following the research done on bubble dissolution in horizontal pipes, while the second paper presented the experimental and simulation (CFD) results for bubble distribution, interpreted through the volumetric void fraction, in horizontal pipes.   The first conference paper, has also been accepted for publication in the peer reviewed European Physical Journal Web of Conference Proceedings. The relevant paper details are as follows;

1. Fsadni A.M., Ge Y.T., Micro bubble formation and bubble dissolution in domestic wet central heating systems, *Experimental Fluid Mechanics Conference (EFM),* Liberec, Czech Republic, 22nd-25th November 2011.

2. Fsadni A.M., Ge Y.T., Experimental analysis of two-phase distribution in horizontal pipes for enhanced system deaeration, *International Conference on Applied Energy, ICAE 2012*, Suzhou China, 5th-8th July 2012.

1.5 Layout of the Thesis

The current thesis is organized as follows. Chapter 2 presents an overview of the previous research into the phenomenon of two-phase flow in supersaturated water solutions. Hence, the review in this Chapter covers several topics such as the general theory and existing research results for the; solubility of gasses in liquids, the fundamentals of bubble nucleation in supersaturated solutions, bubble size prediction theory, bubble behaviour in two-phase bubbly flow and wet central heating systems. Chapter 3 gives a detailed description for the experimental facility, measurement system, the validation of the single-phase heat transfer model used to predict the boiler wall temperature and uncertainty analysis.

Chapter 4 presents and discusses the results obtained from the experimental tests and is divided into five principal sections, these being the results and discussion for the; dissolved gas composition in the closed loop system, the bubble characteristics in vertical downward flow at the boiler exit, the bubble production and nucleation rates on the boiler wall, the bubble behaviour in straight horizontal pipes and the repeatability of results. Chapter 5 presents the evaluation of the bubble size, nucleation and dissolution prediction models, as well as proposed correlations. Chapter 5 also presents the results for bubble distribution in horizontal pipes extracted from two-phase simulations through the use of a CFD commercial code as developed by FLUENT. Chapter 6 outlines the principal conclusions and recommendations for future work.

CHAPTER 2

Literature Review

2.1 Introduction

The two-phase phenomenon in central heating systems is currently not well understood. In fact, most published studies on bubble formation in water due to gas super saturation conditions are based on laboratory tests that are unrealistic in nature. Therefore, considering the principal aim of the present study; i.e. to generate a thorough understanding of bubble formation, growth characteristics and general behaviour in wet domestic central heating systems, a review of existing literature will be presented in this chapter. Therefore, the relevant background material as published in the open literature is reviewed in the following section, Section 2.2, while Section 2.3 summarizes this chapter.

2.2 Background material and literature survey

This section reviews the background material relevant to the present investigation. The phenomenon of dissolved gasses in water is discussed in Section 2.2.1, while Section 2.2.2 analyses existing literature sources with respect to bubble nucleation. Section 2.2.3 analyses and presents the existing literature with respect to bubble size prediction at detachment from the nucleation cavity. Section 2.2.4 presents the existing literature on bubble behaviour in under and super saturated bubbly flows while Section 2.2.5 discusses wet domestic central systems together with associated problems and concerns. It is worth noting that Section 2.2.2 outlines the three sources of possible bubble nucleation in a solution. However, subsequent sub-sections are focused on the bubble behaviour in terms of nucleation and growth in super saturated solutions. This was done after considering the fact that in contemporary domestic boilers, it is unlikely that the boiler wall temperature exceeds the saturation temperature at the typical system pressure (Naslund, 1997). Therefore, the phenomenon of boiling should not be a source of bubble formation at the

9

primary heat exchanger wall in a standard contemporary wet central heating system.

2.2.1 The solubility of gasses in liquids

Fogg (2003) reported that the solubility of gases in a liquid is a property of a gas which is a function of its partial pressure, temperature as well as the nature of the liquid phase. In fact, for most gas-liquid systems there tends to be a linear variation of solubility with partial pressure as the partial pressure approaches zero. When defining the solubility of gases, Young et al. (1982) highlighted the point that the distinction between vapour-liquid equilibria and the solubility of gases in liquids is arbitrary, and often the distinction between the two is not clear. This issue arises from the general inability to rigorously distinguish between a gas, a vapour and a liquid. Gerrad (1976), defined gases as all the elements and compounds having a boiling point at 1 atm less than 286K.

When defining the solubility of gasses in liquids Gerrad (1976), made reference to the graphical presentation of the way in which solubility of gases varies with the pressure. He reported that these methods have been used in a limited sense and they find their origins in Henry's experimental work (1803). In their study of the solubility of nitrogen in water, Rettich et al. (1984) also reported that the solubility of nitrogen in liquids has received a lesser amount of attention when compared to other dissolved gases.

2.2.1.1 Henry's law

Henry's law is one of the gas laws formulated following extensive experimental research by William Henry in 1803. Henry's work could be described as the first systematic study that led to the publication of a series of results on the solubilities of some gases. Gerrard (1976) and Fogg (2003) defined the general form of Henry's law as a constant multiplied by pressure, the latter being equal to the partial pressure of the gas being considered. Hence, Henry's law states that;

At a constant temperature, the amount of a gas that dissolves in a type and volume of liquid is directly proportional to the partial pressure of the gas in equilibrium with the liquid.

Reid et al. (1987) reported that for dilute solutions, Henry's law provides a good approximation for the actual dissolved gas concentration in a fluid. In contrast, the related gas law, Raoult's law, formulated by Francois-Marie Raoult in 1882, is a theoretical law which is valid for an ideal gas and could be applied to highly concentrated solutions. Hence, both laws are limit laws and apply at the opposite ends of the composition range (Gerrard, 1976). Therefore, as realistic solutions are characterised with typically dilute solutions, Henry's law is more relevant for such applications. This is also the case with the present study.

Frolich et al. (1931) reported that if a gas does not form a chemical compound with the solvent, it would follow Henry's law over a wide pressure range within the limits of error allowed in engineering calculations. Hence, the actual concentration of a gas in a solution can be calculated through the use of Eq. (2.1).

$$C_g = K_h P_a \tag{2.1}$$

where; C_g is the actual concentration of a gas expressed as a volume ratio, K_h is the Henry's law constant at a measured or stated temperature and P_a is the partial pressure of the gas.

Gerrard (1976) reported that the mathematical formula as stated in Eq. (2.1) was originally applied for water as a solvent for five gases these being, carbon dioxide, hydrogen sulphide, nitrous oxide, oxygen and hydrogen. However, this equation has subsequently been adopted for the behaviour of any gas and any liquid and consequently adopted the name Henry's law.

Gerrard (1976) reported that the original Henry's law constant is in the form of the ratio of the volume of gas to the volume of the original liquid considered. However, this constant could also be presented as a mass or mole ratio. Gerrard reported that the mole ratio is the most fundamental form of expressing the mass of a gas absorbed by a given mass of liquid at a specified temperature and gas pressure. Hence, after converting the volume ratio to a mass ratio, Eq. (2.2) yields the equivalent mole ratio, x_g.

$$x_g = \frac{n_g}{n_l} = \frac{\dfrac{W_g}{M_g}}{\dfrac{W_l}{M_l}} \qquad (2.2)$$

where; n_g is the number of moles of gas, n_l is the number of moles of liquid; W_g is the mass of the gas; M_g is the molecular mass of gas; W_l is the mass of the liquid and M_l is the molecular mass of the liquid.

More recent data presented the Henry's law constant in the form of a mole ratio and a volume ratio (Battino, 1982). A widely used Henry's law constant expressed as a volume ratio is known as the Bunsen solubility coefficient. A number of studies, Schäfer and Lax (1962) and Battino (1982) presented the Bunsen solubility coefficients as a function of temperature. As stated by Sander (1999), Henry's constants have been presented for a number of gases and are often classified under two main sections, these being the Henry's constant for inorganic and organic gases.
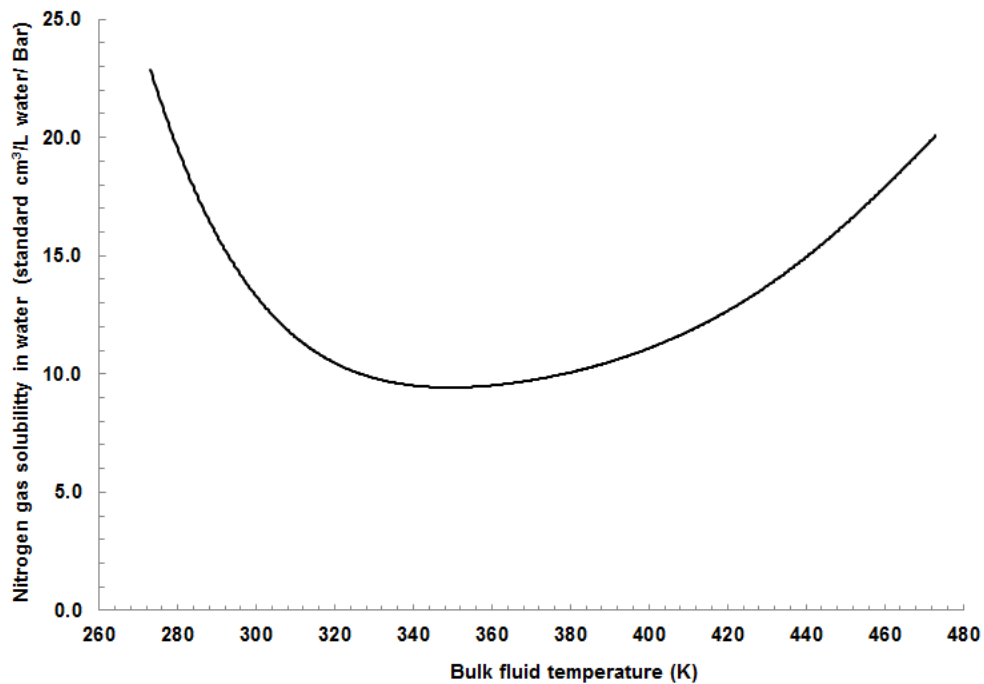
Figure 2.1: Solubility of nitrogen gas with the bulk fluid temperature (Schäfer and Lax, 1962).

Fogg (2003) reported that the solubility gas constants in water at a constant partial pressure pass through a minima with an increase in temperature. In fact, as illustrated in Fig. 2.1, the minimum solubility of nitrogen in water occurs at

about 355 K at a partial pressure of nitrogen of 1.013 bar. Battino (1982) also reported that the solubility of one gas is not affected by the presence of another gas, at the solubility levels considered in his data series. Furthermore, he reported that the solubility of a gas is usually more sensitive to impurities in the gaseous component than to liquid impurities in the liquid component.

Gerrard (1976) argued that the limitation of Henry's laws, are inherent to the fact that they do not provide a comprehensive mathematical form. In fact, while Eq. (2.1) is essentially a mole ratio relationship, many writers also make use of its so called mole fraction relationship variant. The latter is mostly written in the form expressed in Eq. (2.3).

$$P_a = K^{"} N_f \tag{2.3}$$

where; P_a is the partial pressure of the gas, K'' is a variation of the Henry's constant and considered as a pressure per mole fraction and $N_f = \frac{x_g}{(1+x_g)}$. Sander (1999) referred to K'' as the reciprocal to the original Henry's Law constant, thus representing the volatility instead of the solubility of the gas.

Eq.	Source	Mathematical model	Model classification	Units of Henry's constant	Temperature range for Henry's law constants (K)
(2.1)	Gerrard (1976) Sander (1999)	$C_g = K_h P_a$	Original form of Henry's law also referred to as the volume or mole ratio form (Gerrard, 1986)	(cm^3/Litre /Bar) (Volume ratio) (moles gas/moles solvent/Bar) (Mole ratio)	273-353 (Battino, 1982) 273-473 (Schäfer and Lax, 1962)
(2.3)	Gerrard (1976) Sander (1999)	$P_a = K^{"} N_f$	Variant of the original Henry's law also referred to as the mole fraction form (Gerrard, 1986)	(Bar/mole fraction)	273-353 (Battino, 1982)

Table 2.1: Henry's law equation variants.

Throughout the years, different Henry's constants were derived through experimentation for several known gases in a number of solvents. However, as highlighted by Rettich et al. (1984), the variation between the experimentally derived Henry's constants could be significant. Table 2.1 summarizes the two variants for Henry's law as discussed in this Section. The present study has adopted Eq. (2.1) for the calculation of the actual gas concentration due to its widespread use (Gerrard, 1976) and the availably of Henry's constants expressed as a volume or mole ratio (Schäfer and Lax, 1962; Battino, 1982).

In a compilation of the Henry's law constants for nitrogen in water, Battino (1982) presented the data obtained by a number of researchers. The Bunsen coefficient data as originally compiled by Winkler (Battino, 1982) is considered to be the most suitable for the present study. This is due to the experimental conditions used in the compilation of this data and the reasonably low experimental error of 0.03%. However, the temperature range of this compilation, this being between 273K and 353K, did not allow this data to be adopted for the calculation of the actual gas concentrations at the elevated temperatures of the primary heat exchanger in the central heating boiler unit.

Water temperature (K)	Bunsen gas solubility coefficients (standard cm^3/L water/bar)
273	23.0
283	18.0
293	15.0
303	13.0
313	11.0
323	10.0
333	10.0
343	9.5
353	9.5
363	9.5
373	9.5
383	10.0

Table 2.2: Solubility of nitrogen gas in water as a volume ratio for a temperature range of 273 K to 382K (Schäfer and Lax, 1962).

Therefore, the Bunsen gas solubility coefficients as presented by Schäfer and Lax (1962), as tabulated in Table 2.2, were adopted for the present study. The latter constants with temperature are quasi-identical to the Bunsen coefficients presented by Battino as originally measured by Winkler (Battino, 1982). However, the temperature range for the Bunsen coefficients presented by Schäfer and Lax (1962) is between 273K and 473K, hence more adaptable for the experimental conditions of the present study. Furthermore, this data has been used in related studies by Lamers (2005) and Verschaeren (2010).

2.2.1.2 Supersaturated solutions

Jones et al. (1999a) defined a supersaturated solution in relation to quantifying the tendency of a system to produce bubbles. They referred to the gas solubility as a function of the system temperature and pressure. Jones at al. (1999a) reported that a solution could go into the supersaturated state through the increase of its temperature. In fact, as a case in point, Point A in Fig. 2.2 represents a saturated solution at a temperature T_A with a saturation mole fraction amounting to X_b. When the temperature of this solution is increased to T_B, the solution would be in its supersaturated state while still retaining the previous mole fraction of the dissolved content. The desorption of gas from the solvent then causes the state of the system to move gradually from point B to point B' with a new saturation mole fraction equal to X_i. In view of this solution, the resultant saturation ratio is defined by Jones et al. (1999a) through the relationship in Eq. (2.4).

$$\alpha = \frac{X_b}{X_i} \tag{2.4}$$

where; α is the saturation ratio, X_b is the saturation mole fraction at temperature T_A and X_i is the saturation mole fraction at temperature T_B.

Furthermore, the super saturation ratio is defined as

$$\sigma = \alpha - 1 \tag{2.5}$$

where; σ is the super saturation ratio and α is the saturation ratio.
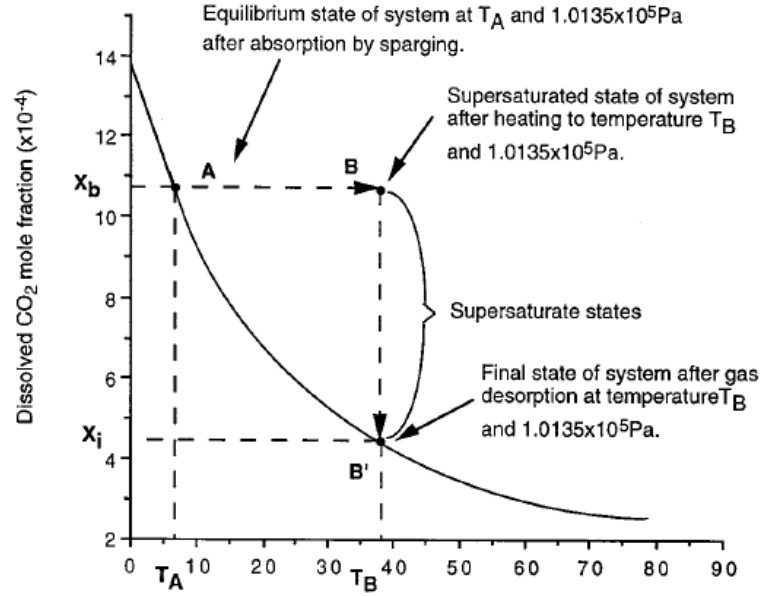
Figure 2.2: Solubility of carbon dioxide as a function of the temperature at a pressure of 1.013E+5 Pa (Jones et al., 1999a, Page 30).

Jones et al. (1999a) also referred to the use of incorporating the Henry's law constant in the relationships given through Eqs. (2.4) and (2.5). This enables the super saturation state to be viewed from the perspective of a pressure difference. Therefore, they make use of the mole fraction relationship as stated in Eq. (2.3) and set up the relationship in Eq. (2.6) for the difference in carbon dioxide equilibrium pressure in the two states *B* and *B'*.

$$\Delta P = P_b - P_i = K''(X_b - X_i) = P_i\left(\frac{X_b}{X_i} - 1\right) = P_i\sigma \tag{2.6}$$

where; P_b is the equilibrium carbon dioxide pressure at *B* and P_i is the atmospheric pressure of 1.013E+5 Pa.

2.2.1.3 Dissolved gasses – Applications and importance

Kostoglou and Karapantsios (2007), stated that the understanding of the dynamics of bubble growth during the desorption of gases (degassing) in liquids is significant for the effective design of many industrial applications. In fact, in many applications, degassing is caused by a reduction of the system pressure. Knapp et al. (1970) reported that this could happen in cavitating turbines, pumps, general fluid circuitry and other fluid systems, where micro bubbles could lead to cavitation corrosion. Bisperink and Prins (1994) also stated that the study of

16

dissolved gasses is also important in carbonated drinks. In fact CO_2 bubbles are formed in carbonated drinks when a release of pressure takes place. Therefore, a thorough understanding of the gas phase is important as this could have a considerable effect on the mouth feel and flavour release together with the fact that the size distribution and the number of bubbles formed per unit of time determine the appearance and the stability of the beverage foam.

Fluid degassing and thus micro bubble formation and growth could also result through the increase in the fluid temperature. Heide et al. (1996) stated that this application was used so as to study the crystallization of cordierite glass, done through the analyses of the evolved gas during constant heating. This technique is also used in the degassing of metal-carbon selective surfaces and alloy powders.

Winterton (1972b), reported that dissolved gases could cause reactivity changes in a sodium cooled fast nuclear reactor. This is due to the fact that the argon cover gas that is used above the sodium surface is more soluble at high temperatures and consequently dissolves in the hot sodium leaving the reactor core and subsequently forms bubbles in the cool parts of the circuit. The formation of such bubbles could in turn lead to cavitation and the possible burn out of fuel pins. Edzwald (1995) discussed the application of Dissolved Air Flotation, *DAF*, in mineral separation, clarification of paper mill wastewaters, refinery wastewaters, combined sewer and storm waters, municipal waste waters in tertiary treatment , municipal and industrial waste sludge thickening, recycled paper de-inking and waste water reclamation. Furthermore, *DAF* is used for drinking water clarification as widely used in countries such as Belgium, The Netherlands and the United Kingdom. The principle of this process involves the formation of small air bubbles with an average size of 100 µm or less through the injection of pressurized recycle water into a flotation tank using specially designed nozzles or needle valves. This process relies on bubble particle interactions mostly bubble attachment or adhesion to particles present in the solution being treated. Therefore, such a process would subsequently result in a reduction on the load of the filters.

Cable and Frade (1988) discussed the importance for the removal of small bubbles of gases such as oxygen, nitrogen, carbon dioxide, helium and water vapour during the glass making process. They reported that, the removal of gas bubbles from molten glass requires long processing times, as the rise of such bubbles to the surface is often too slow to be effective. This is due to the high viscosity of molten glass. In fact, refining agents that enable bubbles to grow or dissolve are usually added so as to speed up this process.

The presence of dissolved gasses and the subsequent degassing, could affect thermal processes such as heat exchangers, boilers and distillation columns. Kostoglou and Karapantsios (2007) reported that degassing in such systems is a detrimental side effect that reduces the liquid heat transfer coefficients and evaporation rates. This occurs as a result of the formation of layers of air over hot surfaces. This fact is of particular interest to the present study, as the understanding of bubble behaviour in central heating systems should result in an enhanced deaeration of the gas bubbles and consequently should lead to improved system efficiencies due to the performance optimisation of deaerators installed in domestic central heating systems.

2.2.2 The fundamentals of bubble formation

This section presents a critical review of the existing literature on the bubble formation due to gas super saturation conditions. Section 2.2.2.1 provides an overview as to the possible mechanisms leading to bubble formation in water, whilst Section 2.2.2.2 provides a review of the bubble nucleation studies.

2.2.2.1 Sources of bubble formation – An overview

Hailemariam et al. (2007), defined a bubble as a small body of gas enclosed in a surrounding fluid. Also, they describe the fluid outside a bubble as that containing a dissolved gas whereas the inside of the bubble consists of a mixture of gas and vapour.

Jones et al. (1999) explained that gas bubble formation or nucleation in liquids could take place through three distinct processes. The first process is commonly referred to as boiling and this takes place when a pure homogeneous liquid undergoes a phase change. In this case, the tendency to produce a phase change

is quantified by the degree of superheat. Therefore, this process is principally governed by the diffusion of heat. Desloge (1968) defined the boiling point of a pure liquid, as the temperature at which the vapour pressure is equal to the applied pressure. This implies that the vapour pressure of the liquid would be equal to the pressure exerted on the liquid by the surrounding environmental pressure.

The second bubble production process is caused by a chemical process such as electrolysis. As this mechanism is an induced chemical mechanism, it will not be further investigated. The third process is that involving gas desorption. Knapp et al. (1970), refer to this process as degassing. In this case, the generation of bubbles is quantified in terms of the degree of super saturation. Hence, through the assumption that the heat of desorption is negligible, the rate of bubble growth is governed principally by the concentration gradient of the dissolved gas.

2.2.2.2 Bubble nucleation in supersaturated solutions

Bubble nucleation due to supersaturated solutions, is a phenomenon present in a number of industrial processes such as the chemical, pharmaceutical, food and power generation industries. However, most of the research in this area has been purely theoretical in its nature. Hepworth et al. (2003), attributed this lack of research to the difficulties in obtaining reliable experimental nucleation data and to the complex physical parameters that characterize systems where the nucleation phenomenon is observed. This is also due to the inherent difficulties in analysing two-phase mechanisms as outlined by Winterton and Munaweera (2001).

Studies on bubble nucleation in supersaturated solutions done by Wilt (1986), Lubetkin and Blackwell (1988), Carr et al. (1995), Jones et al. (1999a,b), Slezov et al. (2003) and Kwak and Oh (2004), all reported that the nucleation rate was a very sensitive function of the degree of super saturation. Therefore, the nucleation rate, defined as the bubble production rate per unit surface area, changes from essentially zero to large values in a small range of super saturation levels. Lubetkin and Blackwell's experimental results for the number of bubbles released as a function of time at various super saturation ratios is illustrated in Fig. 2.3. The classical theory of nucleation is based on the theories for

homogenous and heterogeneous nucleation in supersaturated solutions. Delale et al. (2003), reported that homogeneous nucleation is characterized by nucleation in the bulk of a homogenous solution and heterogeneous nucleation is characterized by nucleation in a pit in the surface of a container, on a molecularly smooth surface or on a particle in the bulk fluid.
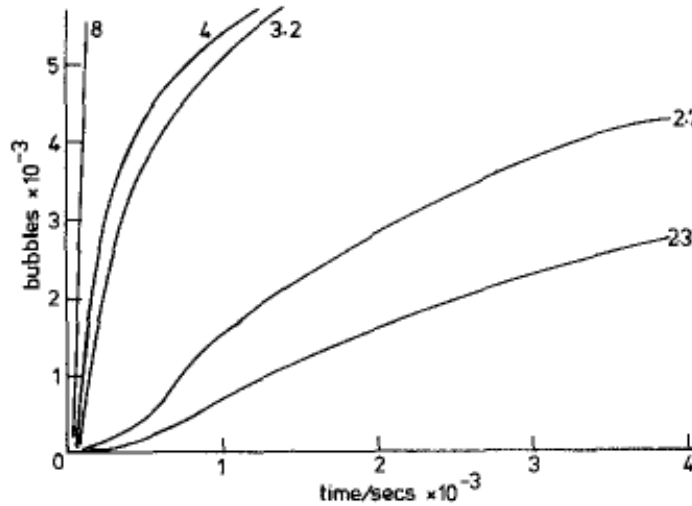
Figure 2.3: Number of bubbles released as a function of time at various super saturation ratios at 295K. The super saturation ratios are shown as index numbers associated with each curve (Lubetkin and Blackwell, 1988, Page 612).

Jones et al. (1999a), reported that super saturation levels in excess of 100 are required for both classical forms of nucleation. However, studies done by Wilt (1986) for carbon dioxide and water solutions reported that super saturation levels between 1100 and 1700 are required for homogenous nucleation at room temperature whereas Lubetkin and Blackwell (1988), reported that heterogeneous nucleation was observed in H_2O and CO_2 solutions with much lower super saturation levels between 2 and 8. Dean (1943), stated that the fundamental prediction of bubble formation is based on the law relating pressure, surface tension and bubble diameter. This relationship is given through the Laplace Equation as given in Eq. (2.7).

$$\Delta P = \frac{2\gamma}{r_c} \qquad\qquad (2.7)$$

where; ΔP is the difference in pressure between the gas inside the bubble (calculated as a sum of the gas partial pressures and the vapour pressure), and the

bulk liquid or system pressure, γ is the surface tension of the liquid and r_c is the critical radius of the bubble.

Hence, as illustrated in Fig. 2.4, the total gas pressure inside the bubble should be larger than the pressure in the fluid surrounding the liquid for bubble growth. Jones et al. (1999a) defined the critical radius of curvature as that radius when the bubble is in thermodynamic equilibrium with the solution. Hence, when the system is super saturated, the bulk free energy per unit of liquid volume associated with transferring molecules to the new phase is negative and consequently thermodynamically favourable.
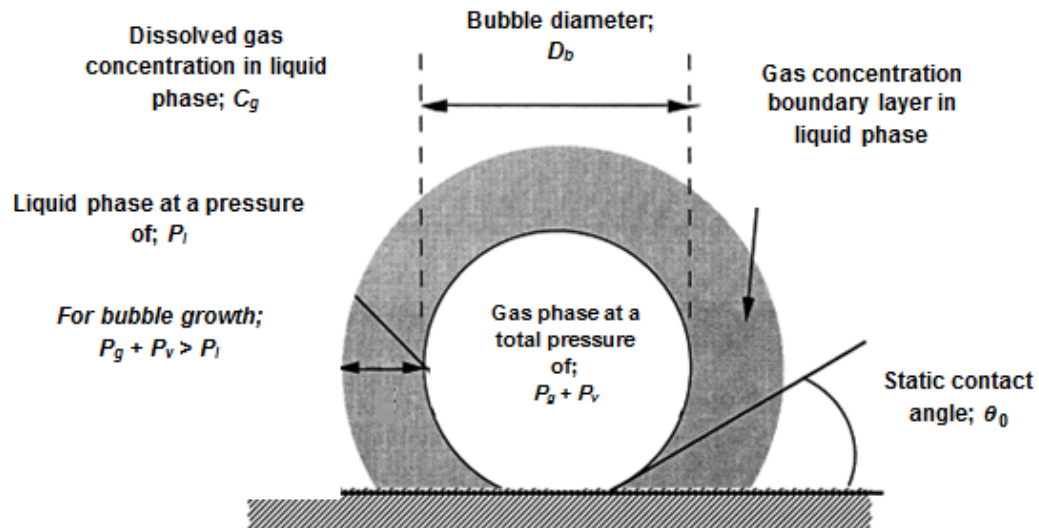
Figure 2.4: Schematic representation of a bubble with a static contact angle θ_o growing on a surface in a super saturated bulk fluid (Jones et al., 1999b, Page 56).

Jones et al. (1999a) reported that the classical nucleation models as initially developed by Blander and Katz (1975), do not represent the nucleation phenomenon in many practical systems. This is due to the relatively low super saturation levels observed in more practical systems, typically being less than 5, where the nucleation energy for each gas cavity is much lower than for the classical case. In their study, Jones et al. (1999a) attributed nucleation in low super saturation solutions to the presence of pre-existing gas cavities. This concept was shared by many, including Dean (1944) and in more recent studies by Hepworth et al. (2003). Dean (1944) supported the fact that water supersaturated with a gas will not produce bubbles, unless there are gas particles available below the surface on dust particles or other contamination, or the water

is subjected to mechanical shock. In fact, Dean (1944) focused his studies on the formation of bubbles due to mechanical shock through the elimination of bubbles formed through gas particles below the surface, present on dust particles or other forms of contamination.

Jones et al. (1999a), also reported that most nucleation events observed in research are due to this phenomenon. They referred to this type of nucleation as non-classical nucleation having two distinct types, these being Type III and Type IV non-classical nucleation where as illustrated in Fig. 2.5, bubble nucleation takes place as long as the minimum radius of curvature of the meniscus in the cavity, r, is greater than the critical nucleation radius, r_c, defined through the classical theory of nucleation as given in Eq. (2.7). Jones et al. (1999a) reported that this theory is backed through experimentation. In fact, experiments done where care was taken to eliminate gas cavities from the liquid environment required high levels of super saturation that were not required for similar experiments where no preparation was done to eliminate the gas cavities.
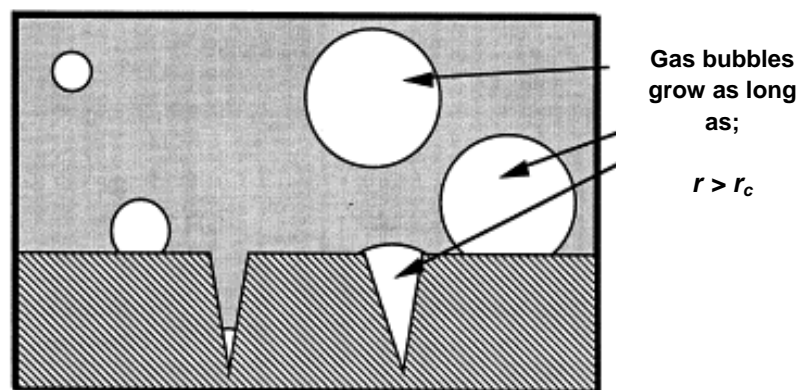
Figure 2.5: Type III and IV non-classical nucleation (Jones et al., 1999a, Page 33).

In Type III non-classical nucleation, the radius of curvature of each meniscus is less than the critical radius when the system is made supersaturated. In Type IV non-classical nucleation all pre-existing gas cavities house menisci with radii of curvature greater than the critical radius of nucleation (Jones et al., 1999a). Therefore, in Type III non-classical nucleation, each cavity has a finite nucleation barrier that must be overcome for nucleation to proceed whereas in a Type IV non-classical event, no nucleation energy barrier should be overcome and therefore, a stable source of nucleation is available.

Hepworth et al. (2003), attributed the origin of the pre-existing gas cavities to three main causes these being, a classical nucleation event which is considered as unlikely in low supersaturated solutions, gas entrainment from a liquid jet and gas entrapment under an advancing liquid front. Jones et al. (1999a), argued that it is inappropriate to use the equations developed by Wilt (1986) for classical homogenous nucleation when the nucleation observed is non-classical. This view is also supported by Hepworth et al. (2003), who reported that the classical nucleation models do not take into account the effects of liquid motion and therefore are not adaptable to the case of a flowing liquid. The reason for this, being the fact that liquid motion will alter the rate of bubble growth and alter the radius of bubble detachment from their nucleation sites as originally predicted by Winterton (1972a). Such views contrast with the predictions made by Lubetkin and Blackwell (1988) and more recently by Verschaeren (2010) who fitted the classical heterogeneous models to low super saturation solutions. Jones et al. (1999a), developed a model for the calculation of the nucleation time in a Type IV non-classical event but do not provide a model for the calculation of the overall nucleation rates.

There have been very few studies on the theoretical prediction of active nucleation site densities. Yang and Kim (1988), predicted the active nucleation site density in pool boiling through the use of two probability density functions based on the cavity radius and half angles assumed to fit a Poisson and normal distribution respectively. Hepworth et al. (2003) calculated the active nucleation site densities in supersaturated solutions through the use of the expected molecule densities in nucleation sites and the area of a single nucleation site.

The open literature does not present nucleation models that can accurately predict the nucleation rates in solutions with low superstations that may be adapted to more practical systems. However, Hepworth et al. (2003), developed a model with good experimental predictions to predict nucleation rates in dispensed beer where relatively low super saturation levels dominate. This was done through the use of the Scriven (1959) bubble growth rate model as adapted by Jones et al. (1999b) and the force balance model developed by Winterton (1972a), to predict the bubble detachment radius.

2.2.2.2.1 Classical models of nucleation

Hepworth et al. (2003), analyzed classical nucleation models, namely those developed by Lubetkin and Blackwell (1988) based on previous studies by Blander and Katz (1975) and Wilt (1986). As predicted by Wilt (1986), homogenous nucleation would require substantially high saturation ratios. Such gas concentration levels would not be found in a closed circuit wet central heating system and therefore another form of nucleation should be considered in the present study (Verschaeren, 2010). Hepworth et al. (2003), Lubetkin and Blackwell (1988) and Wilt (1986) reported that classical heterogeneous nucleation would be possible at saturation ratios below 10. However, as predicted by Wilt (1986), unreasonably high contact angles would render the nucleation phenomenon unlikely. Contact angles required for heterogeneous nucleation on a smooth planar interface in water and carbon dioxide solutions are unusually high (circa 175°) for low super saturation levels. Wilt's formula for heterogeneous nucleation on a smooth planar interface is given by Eq. (2.8).

$$J = N^{\frac{2}{3}} S_w \left[\frac{2\gamma_1 B_w}{\pi m F_w} \right]^{\frac{1}{2}} exp^{\frac{-4\pi r_{c1}^2 \gamma_1 F_w}{3 k_b T_b}} \tag{2.8}$$

where; $m = -cos\theta_o$; $S_w = \frac{(1-m)}{2}$; $F_w = \frac{(2-3m+m^3)}{4}$; $B_w = 1$

where J is the bubble nucleation rate, N is the molecular density, θ_o is the static contact angle, γ_1 is the surface tension, r_{c1} is the critical radius, k_b is the Boltzmann constant, T_b is the bulk fluid temperature.

Wilt (1986), reported that heterogeneous nucleation in low supersaturated solutions is likely on conical cavities whose solid walls are in contact with the liquid and dissolved-gas solution. Wilt (1986) derived Eq. (2.9) for nucleation on a conical cavity with a static contact angle of θ_o and a conical half angle of β.

$$J = N^{\frac{2}{3}} f_{3c}(\theta_o, \beta) \left[\frac{2\gamma_1 B_w}{\pi m f_{1c}} \right]^{\frac{1}{2}} exp^{\frac{-4\pi r_{c1}^2 \gamma_1 f_{1c}}{3 k_b T_b}} \tag{2.9}$$

Where: $f_{1c}(\theta_o, \beta) = \left[\frac{2 - 2\sin(\theta_o - \beta) + \frac{cos\theta_o cos^2(\theta_o - \beta)}{sin\beta}}{4} \right]$; $f_{3c}(\theta_o, \beta) =$

$\left[\frac{1 - \sin(\theta_o - \beta)}{2} \right]$; $B_w = 1$

where β is the conical cavity half-angle.

In both cases, the work done for a bubble nucleation event has a maximum when the bubble detachment radius is equal to the radius of the critical nucleus. Wilt (1986), reported that nucleation on a conical cavity could result through conical cavities of various geometries, thus making the model more adaptable to various nucleation situations. The other forms of heterogeneous nucleation, these being the conical projection, the spherical cavity and the spherical projection do not result in observable nucleation rates at low saturation ratios.

Therefore, Wilt's (1986) Eq. (2.9) model for nucleation is more relevant to the present study. This model was also used in a recent study done by Verschaeren (2010) for bubble nucleation on a heating plate in contact with water. Eq. (2.9) is dependent on the geometry of the heat exchanger wall and the resultant contact angles of the liquid and the gas. Lubetkin and Blackwell (1988) simplified Wilt's Eq. (2.9) to eliminate the dependence on the geometry and contact angles through the elimination of all the pre-exponential terms. Hence, the use of a single empirical constant, *F,* replaced all the pre-exponential terms. This was necessary due to the lack of knowledge with respect to the contact angles and the nucleation surface properties. The result is their simplified model as in Eqs. (2.10) and (2.11).

$$J = F exp^{\frac{-4\pi\gamma_1 r_{c1}^2}{3k_b T_b}} \tag{2.10}$$

That is further simplified into Eq. (2.11):

$$J = F exp^{\frac{-16\pi\gamma_1^3}{3k_b T_b P_{l1}(\alpha-1)}} \tag{2.11}$$

where *F* is the empirical constant.

A close analysis of Eq. (2.11) suggests that the exponent part is identical to Wilt's model for homogeneous nucleation. Therefore, while the simplification of the pre-exponential terms is necessary when no details are known with respect to the contact angles and the nucleation surface, the elimination of the surface geometry term f_{1c} in the exponent, renders the nucleation model in Eq. (2.11) essentially a homogenous nucleation model. Therefore, as discussed in Section 5.3, Eq. (2.11) requires high saturation ratios, in excess of 1000. Consequently,

the present study suggests that Lubetkin and Blackwell (1988) may be incorrect in stating that their simplified model as given in Eq. (2.11) yields reasonable nucleation predictions at saturation ratios less than 10.

When discussing the possibility of the coalescence of the bubble nuclei while still resident on the experimental vessel's stainless-steel surface, Lubetkin and Blackwell (1988) reported that such a possibility is unlikely as the sites of nucleation are well separated and at the initial stages of nucleation, bubbles are not considered to be mobile. Furthermore, they consider the possibility of the coalescence of bubbles during their rise through the solution to be low as the concentration of these bubbles is low and consequently bubble collisions are unlikely.

Talanquer and Oxtoby (1995) also made use of Wilt's equation in their studies on the nucleation of bubbles in binary solutions. However, through their experiments, Talanquer and Oxtoby (1995) suggested that contrary to the normal expectation of an increase in the nucleation rates with an increase in temperature and mole fraction of the more volatile component, a decrease in the nucleation rates was actually observed with an increase of the latter parameters. They attributed this observation to the fact that although the bubbles that eventually reach macroscopic size are gaseous, the critical nucleus may involve more of a change in composition than a change in density of the fluid. Therefore, in such a case, nucleation can be considered as a two-dimensional process, where the growth of a critical nucleus may involve first a liquid-liquid phase separation and only later a change in density. Hence, through the observations of Talanquer and Oxtoby (1995), the classical theory of nucleation would fail completely.

2.2.2.2.2 Non-classical nucleation model based on the penetration theory

Hepworth et al.'s (2003) presented a bubble nucleation model based on the gas penetration theory. The nucleation rate at a single cavity is expressed through Eq. (2.12), where one gas is assumed to be responsible for nucleation. The bubble radius at detachment was calculated through the force balance equations as predicted by Winterton (1972a).

$$N_{cb} = \frac{K_g(C_{bg} - C_{sg})}{r^{\frac{3}{2}}} \qquad\qquad (2.12)$$

where; $K_g = \frac{3R_gT_b(1+cos\theta_o)(Du)^{\frac{1}{2}}}{\sqrt{2}P_l(2+3cos\theta_o-cos^3\theta_o)}$ and C_{bg} is the actual gas concentration; C_{sg} is the gas concentration at saturation conditions; r is the bubble detachment radius; R_g is the Universal gas constant; T_b is the temperature; θ_o is the static contact angle; D is the gas diffusivity; u is the bulk fluid velocity and P_l is the bulk fluid pressure.

Eq. (2.12) is based on the Jones et al. (1999a) findings that the molecular diffusion through the gas-liquid interface governs most of the bubble growth processes. Jones et al. (1999a), then derived a relationship between the growth time and the bubble radius. Hepworth et al. (2003), reported that liquid motion can also affect the bubble growth rate by changing the mass transfer coefficient for gas diffusing into a nucleating bubble from the liquid bulk. Therefore, their model incorporates the adaptation done by Al-Hayes and Winterton (1981a,b), whereby the penetration theory was used to calculate the mass transfer coefficient in the bubble growth model.

The calculation of the overall bubble nucleation rate per unit area requires the knowledge of the number of active nucleation sites per unit area. Hepworth et al. (2003), calculated the expected active nucleation site densities through the application of Eq. (2.13), this being a function of the cavity critical radius and an estimation of the number of nitrogen molecules per unit surface area. Hence, Hepworth et al. (2003), extrapolated the cavity bubble production rate calculated through Eq. (2.12) to a bubble production rate per unit surface area through the application of Eq. (2.13).

$$n_s = \frac{10^{-7}}{\pi r_c^2} \qquad\qquad (2.13)$$

Hepworth et al. (2003) reported a nucleation prediction accuracy of 20% through the use of this model. However, there are no other adaptations of this model available in the open literature.

Table 2.3 summarizes the classical and non-classical heterogeneous nucleation models reviewed in the present study. As discussed in Section 5.3, the Hepworth

et al. (2003) non-classical model as given in Eq. (2.12), was adopted to correlate the nucleation results obtained in the present study. The latter non-classical model is considered to be the most adapted for predicting bubble nucleation in more practical solutions, characterized with a relatively low degree of super saturation. Furthermore, it does not require a comprehensive knowledge of the surface conditions at the nucleation surface.

Eq.	Source	Mathematical model	Model type	Surface	Degree of satur-ation
(2.8)	Wilt (1986)	$J = N^{\frac{2}{3}} S_w \left[\frac{2\gamma_1 B_w}{\pi m F_w} \right]^{\frac{1}{2}} exp^{\frac{-4\pi r_{c1}^2 \gamma_1 F_w}{3 k_b T_b}}$	Classical – Heterog-eneous	Flat – Planar with contact angles >175^0	<10
(2.9)	Wilt (1986)	$J = N^{\frac{2}{3}} f_{3c}(\theta, \beta) \left[\frac{2\gamma_1 B_w}{\pi m f_{1c}} \right]^{\frac{1}{2}} exp^{\frac{-4\pi r_{c1}^2 \gamma_1 f_{1c}}{3 k_b T_b}}$	Classical – Heterog-eneous	Conical Cavities	<10
(2.11)	Lubetkin and Blackwell (1988)	$J = F exp^{\frac{-16\pi \gamma_1^3}{3 k_b T_b P_{l1}(\alpha-1)}}$	Classical – Heterog-eneous	Unspecif-ied cavity geometry	>1000
(2.12)	Hepworth et al. (2003)	$N_{cb} = \frac{K_g (C_{bg} - C_{sg})}{r^{\frac{3}{2}}}$	Non-classical model for single cavity	Unspecif-ied cavity geometry	>1

Table 2.3: Classical and non-classical theoretical bubble nucleation models.

2.2.3 Bubble size prediction at nucleation point

The theoretical approach that exists for predicting the detachment size of bubbles originating in a supersaturated solution with no knowledge of the nucleating time is based on the resolution of the forces acting on the surface of the nucleating bubble on the boiler heat exchanger wall, parallel to the wall surface. Winterton's

(1972a) approach, as given in Eqs. (2.14) and (2.15) in Table 2.4, for the prediction of bubble detachment diameters is based on this theory. More models have been developed for predicting the bubble detachment diameters under stagnant conditions, such as the approach originally suggested by Scriven (1959) and later adapted by Jones et al. (1999a,b) for supersaturated solutions that are based on the symmetric phase growth controlled by heat and mass transfer. Other models such as that by Akiyama and Tachibana (1974) were developed for predicting vapour bubble diameters in flow boiling conditions. Such models were developed for modelling bubble nucleation and require a comprehensive knowledge of the surface conditions and the bubble nucleating time.

In his analysis of bubble growth, Scriven (1959) considered a spherical vapour bubble growing in a superheated liquid of infinite extent. Therefore Scriven's predictions are mostly based on a nucleate boiling mechanism. He reported that the growth rate is determined by the difference between the pressure within the bubble and the ambient pressure, liquid inertia and viscosity, surface tension and transport of heat and volatile material through the liquid to the bubble surface. This draws a similarity to the predictions done by Dean (1944) for bubble nucleation due to a reduction in pressure in a super saturated solution. Furthermore, Scriven stated that his predictions could disregard compressibility effects, vapour inertia and viscosity, pressure, temperature and concentration gradients within the vapour. Scriven developed a mathematical model for the growth of a vapour bubble where the growth was governed by heat and mass momentum transfer and where viscosity, surface tension and inertia were neglected for most of the growth. Therefore through his model, Scriven (1959), established the influence of radial convection on spherically symmetric phase growth controlled by diffusion. Scriven's Solution can be expressed through Eq. (2.16) in Table 2.4.

The term D in Eq. (2.16) could assume the value of thermal diffusivity for growth by heat conduction whilst the gas diffusivity is used for growth governed by molecular diffusion. β, being a dimensionless growth parameter is dependent on the superheat or super saturation of the bulk fluid, referred to as the concentration driving force for bubble growth. Jones et al. (1999a) reported that

29

for a negligible Laplace pressure, Scriven's Eq. (2.16) suggests that the radius is proportional to the square root of the growth time. Therefore, the bubble radius in a uniform temperature field at a certain time could be approximated through the use of Eq. (2.17) as given in Table 2.4.

Kostoglou and Karapantsios (2007) reported that Eq. (2.17) proved useful in describing the quasi-isothermal mass-diffusion induced bubble growth from supersaturated solutions during their decompression. Furthermore, they reported that experimental evidence in boiling literature suggested that the exponent n can vary over a broad range of values. Hence, they added that the diversity in the reported values of n for nucleation boiling reflects the difficulties in performing well-controlled experiments and the possible contributions from several rate-controlling mechanisms such as surface tension, viscosity and inertia.

In their study of vapour bubble growth and condensation rates in terms of maximum bubble radius and bubble lifetime for sub-cooled flow boiling, Akiyama and Tachibana (1974) developed a correlation for the equivalent bubble diameter with time as in Eq. (2.18) in Table 2.4. Through their studies, Akiyama and Tachibana concluded that the bubble lifetime and maximum equivalent diameter change monotonously with the fluid flow velocity and sub-cooling. The latter parameters also decrease linearly with the log of the flow velocity for velocities ranging between 0.3 m/s and 0.5 m/s. Furthermore, these parameters decrease linearly with the magnitude of the sub cooling temperature. They also reported that the maximum equivalent diameter is proportional to the thermal boundary layer thickness for velocities in the range of 1–5 m/s. In a similar study, Prodanovic et al. (2002) reported that the bubble lifetime and size decrease with increasing heat flux and bulk liquid velocity. Furthermore, they stated that the effect of the heat flux and flow rate on bubble diameters and life span is greater at lower heat transfer rates. They also reported that bubble size and life span decrease with increasing sub-cooling and pressure. This is in agreement with the predictions of Akiyama and Tachibana. In contrast to the above findings, Abdelmessih et al. (1972) observed larger bubbles and longer lifetimes with an increase in heat flux.

An analogy could be made between the present study and theories developed for the prediction of bubble diameters in two-phase fully developed turbulent bubbly flow in ducts. Hence, the present study could be extended through a consideration of the two known models for predicting bubble sizes, these being the Hinze model as defined by Winterton and Munaweera (2001) and the Winterton and Orby (1992) approach. The maximum bubble diameter, expected in bubbly flow in a tube, for isotropic homogenous turbulence distribution is predicted by Hinze as in the Winterton and Munaweera's (2001) adaptation through Eq. (2.19) in Table 2.4. This model considers the breakup of the bubbles by turbulent forces in the flow. Winterton and Munaweera's (2001) adaptation of the Hinze model for two-phase duct flow was achieved through the use of the mixture energy dissipation factor, velocity, density, friction factor, Reynolds number and dynamic viscosity.

The Winterton and Orby (1992) approach, as in Eq. (2.20), is a simplistic model based on the structure of single-phase flows. They made use of the fact that in turbulent single-phase duct flows, eddies exist and the structure of the flow is stable with eddies present in the flow. The adaptation of this theory to two-phase flow was done by assuming that gas bubbles are present in the eddies considered. Such bubbles could replace these eddies with the flow structure remaining stable. Winterton and Orby (1992) made use of the Nikuradse formula for the mixing length to calculate the bubble diameter which is assumed to be equal to the mixing length average value. The mixing length is defined as the distance through which a volume of fluid in single-phase flow retains its identity and velocity. However, these studies are based on experimental data obtained through the artificial insertion of air bubbles in the flow and hence their application to the present study is limited.

Table 2.4 summarizes the models highlighted in this section. The Winterton (1972a) approach is considered the most relevant to the present study as it is based on the detachment of bubbles under super saturated flow conditions. Furthermore, it does not require the knowledge of the bubble nucleation time.

Eq.	Source	Mathematical model	Duct	Fluid conditions	Fluid	Contact angle
(2.14)	Winterton (1972a)	$$\frac{r}{R} = 1.2\,\mathrm{Re}^{0.12}\left[\frac{\frac{r'}{R}}{We}\right]^{0.5}$$	Circular	Flow	Water - Supersaturated	Zero
(2.15)	Winterton (1972a)	$$\frac{r}{R} = 1.4\left[\frac{F(\theta)}{We}\right]\mathrm{Re}^{0.24}$$ $F(\theta) = sin\theta_0(cos\,\theta_r - cos\,\theta_a).$	Circular	Flow	Water – Supersaturated	Finite
(2.16)	Jones et al. (1999a,b)	$$r = 2\beta\sqrt{Dt}$$	N/A	Stagnant	Water - Superheated / Supersatured	Finite
(2.17)	Jones et al. (1999a,b)	$$r \cong t^{n=0.5}$$	N/A	Stagnant	Water – Superheeated / Supersatured	Finite
(2.18)	Akiyama and Tachibana (1974)	$$\frac{D_b}{D_{bm}} = 1 - 2^F\left[\frac{1}{2} - \left[\frac{t}{t_e}\right]^{N_{ec}}\right]^F$$ $where; \left[\dfrac{t}{t_e}\right]^{N_{ec}}_{\max} = \dfrac{1}{2}$	Annular	Flow	Water – Superheeated	N/A
(2.19)	Hinze as in Winterton and Munaweera (2001)	$$D_{bm} = 0.725\left[\frac{\rho}{\gamma}\right]^{-0.6}\varepsilon_m^{-0.4}$$	Circular	Flow	Water - Supersaturated	N/A
(2.20)	Winterton and Orby (1992)	$$D_b = 0.04D_h$$	Circular	Flow	Water – Supersaturated	N/A

Table 2.4: Bubble diameter prediction models in two-phase solutions.

Therefore, this model was adopted for a comparison to the present study results as discussed in Section 5.2. As illustrated in Fig. 2.6, there are three forces acting

on a bubble nucleating in a flow system, these being; the drag F_d, surface tension F_s, that is split into the horizontal and vertical components (F_{sx}, F_{sy}) and the buoyancy forces F_b. Hence, the drag force tends to pull the bubble off the surface into the flow whereas the surface tension force keeps the bubble attached to its surface nucleation point. Winterton (1972a) reported that the pressure gradient along the channel results in another force acting on the bubble. However, at low flow rates, most of the pressure gradient will be due to the gravitational force. Hence, the pressure gradient force is assumed to be equal to the normal buoyancy force. In vertical pipe flow, the buoyancy force could assist or oppose the surface tension force depending on the direction of flow whereas in horizontal flow it does not result in a force component in the flow direction. Winterton (1972a) does not take into consideration the buoyancy force in his bubble detachment model as this is proportional to the bubble volume and hence is considered to be negligible for small bubbles in high liquid velocities.
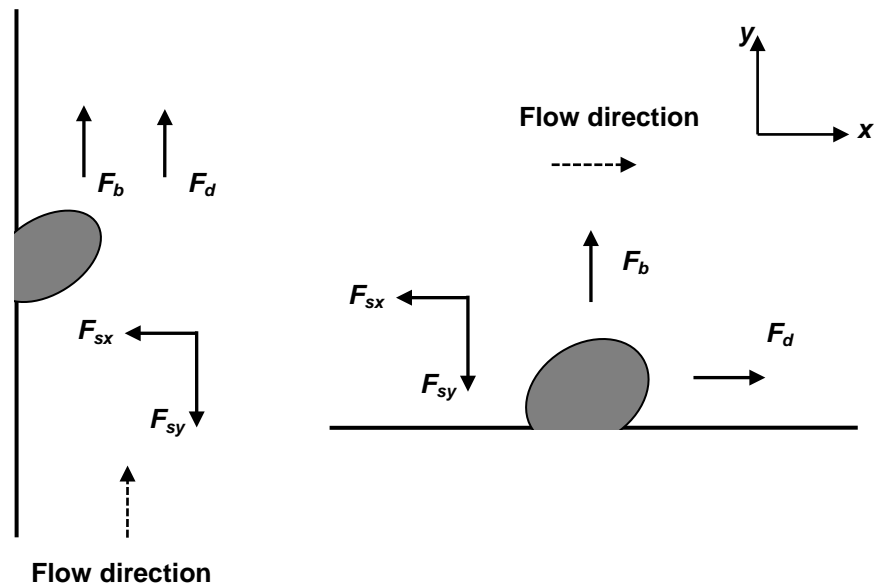
Figure 2.6: Forces acting on a nucleating bubble in vertical and horizontal fluid flow.

Hence, Winterton's (1972a) bubble detachment model is based on the knowledge that bubbles break away from the surface into the flow when the drag force F_d equals the surface tension force parallel to the tube surface (F_{sx} or F_{sy}). For zero and finite contact angles, a balance of the forces acting parallel to the tube surface results in equations for the prediction of the bubble detachment

33

diameters. For the experimental conditions where the bubbles are projected into the transition region of the flow, Winterton (1972a) derived Eq. (2.14) for predicting the bubble detachment diameters at a zero contact angle. The transition region was identified through the use of Eq. (2.21) to calculate the velocity profile in the channel at one bubble radius from the boiler wall, through the dimensionless value η. Hence, after substituting the calculated bubble radius using Eq. (2.14) and using the experimental bulk fluid velocity, η values between 5 and 30, suggest a bubble projection into the transition flow region.

$$\eta = \frac{r v_*}{\upsilon} \tag{2.21}$$

where; v_* is the friction velocity. Winterton (1972a) calculated the friction velocity v_* through the equation $v_*^2 = 0.0396 u^2 Re^{-0.25}$ where the Reynolds number is based on the tube diameter.

The nucleation cavity radius, r', was calculated through the use of Eq. (2.7) which represents the excess pressure required for the growth of a bubble in its nucleating cavity. The difference in pressure between the bubble and the bulk fluid, ΔP in Eq. (2.7), was calculated by subtracting the system pressure, P_l, from the sum of the gas partial pressure, P_g, and the fluid vapour pressure, P_v. For a finite contact angle, Winterton (1972a) derived Eq. (2.15) for the experimental conditions resulting in a transitional flow. To calculate the net surface tension force holding the bubble to the wall, Winterton assumed that the contact angle is different on each side of the bubble thus introducing the concept of the dynamic and static contact angles as illustrated in Fig. 2.7. Hence, the dynamic contact angles are the advancing, θ_a, and receding, θ_r, contact angles and result due to the distortion of a nucleating bubble under fluid flow conditions. Similarly the transition flow region was identified through the application of Eq. (2.21).
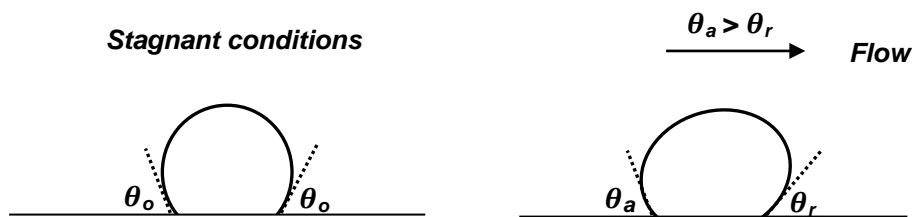
Figure 2.7: Dynamic contact angles on a nucleating bubble.

Limited consideration has been given in literature to the expected dynamic contact angles with surface and fluid flow conditions. Most literature sources provide details as to the expected static contact angle with the surface material. Static contact angles are calculated through the ratio of the measured contact area and bubble diameter for bubbles whose spherical shape has not been distorted by the flow. As reported by Ponter and Yekta-Fard (1985) static contact angles are dependent on the bubble diameter and surface conditions.

A number of recent studies have adapted the use of the Winterton (1972a) model with good results. Amongst these are studies done by Al-Hayes and Winterton (1981a,b) and Hepworth et al. (2003). Al-Hayes and Winterton adapted the original Winterton (1972a) model to include the effect of liquid motion on the bubble growth rate due to the change in the mass transfer coefficient for the gas entering the bubble from the bulk liquid. Their final approach, is similar to the original Scriven (1958) and Jones et al. (1999a,b) models and thus requires a comprehensive knowledge of the bubble nucleating time.

2.2.4 Bubble behaviour in bubbly flow

This section analyses literature concerning bubble dissolution in under saturated bubbly flows and bubble enlargement in supersaturated flows. Bubbly flow is characterized by the presence of bubbles of maximum size much less than the containing vessel or duct (Winterton and Munaweera, 2001). Hence, bubbly flow is relevant to the present study as the nucleation of bubbles and subsequent detachment at the primary heat exchanger wall is expected to develop into a bubbly flow in the system flow line.

2.2.4.1 Bubble dissolution in an under saturated bulk fluid

A number of authors have developed numerical models based on the gas diffusion model whereby the time for an initial sphere radius R_o, to dissolve to a radius R_t is predicted for isolated bubbles (Epstein and Plesset 1950, Cable 1967, Duda and Vrentas 1971, Cable and Frade 1988). Other studies have developed dissolution models to predict the time for complete dissolution (Ljunggren and Eriksson 1997, Honda et al. 2004). Two principal mechanisms are known to govern the bubble dissolution process, these being the solution of the gas into the

liquid at the bubble fluid interface and the diffusion of dissolved gas away from the interface into the outer phase of infinite extent. The former mechanism is much faster when compared to the latter and consequently, the dissolution process is assumed to be diffusion controlled. Kentish et al. (2006) summarized the principle assumptions used in these models as follows:

(i)   A uniform and constant gas density is present in the bubble.

(ii)   The transfer of gas from the bubble is controlled by Fickian diffusion and the concentration of dissolved gas at the interface is constant at the equilibrium concentration.

(iii)   The diffusivity, temperature and pressure of the system are constant.

(iv)   The partial specific volumes of solute and solvent are constant.

(v)   The velocity field in the liquid is purely radial. Hence the bubble is considered as a perfect isolated sphere so that the concentration field is spherically symmetrical.

(vi)   All gravitational effects are neglected.

The advection and diffusion equations of solute in the host liquid are the principal equations used in these analytical models. These models also include, the kinematic condition at the moving bubble surface which models the shift in the bubble radius in terms of the diffusion flux.

Epstein and Plesset (1950) reported that the effect of the bubble boundary motion as a result of shrinkage introduces a transport term in the diffusion equation which makes it difficult to obtain an analytical solution. Hence, as advection results in a minimal effect on the dissolution time, they neglected this effect. They reported that this estimation is accurate, as the concentration of the dissolved gas in the liquid surrounding the bubble is much smaller than the gas density in the bubble. Also, the region in the solution around the bubble is considered to be much larger than the bubble itself. They expressed their model through the differential equation for the dissolution time of a stationary bubble as in Eq. (2.22).

$$\frac{dR}{dt} = -B\left[\frac{1}{R_t} + \frac{1}{(\pi Dt)^{1/2}}\right] \tag{2.22}$$

where; $B = \frac{D(C_E - C_0)}{\rho_g}$ and R_t is the bubble radius after a time interval t, D is the gas diffusivity, C_E and C_o are the gas concentrations in the bubble and the bulk liquid respectively and ρ_g is the gas density.

Epstein and Plesset (1950), used three constants; $\in_b$, x^2 and γ_e to express Eq. (2.22) in a dimensionless form as given in the differential Eq. (2.23).

$$\frac{d\in_b}{dx} = -\frac{x}{\in_b} - 2\gamma_e \tag{2.23}$$

where; $\in_b = \frac{R_t}{R_o}$; $x^2 = \left[\frac{2B}{R_o^2}\right] t$; $\gamma_e = \left[\frac{C_E - C_O}{2\pi\rho_g}\right]^{\frac{1}{2}}$ and R_o is the original bubble radius.

Epstein and Plesset (1950), simplified their model through the knowledge that the second term γ_e in Eq. (2.23) is small for long dissolution times, thus allowing significant diffusion to take place. Hence, they ignored this term with the result of a simplified analytical dissolution model as in Eq. (2.24).

$$\in_b^2 = 1 - x^2 \tag{2.24}$$

Duda and Vrentas (1971) developed a comprehensive set of finite-difference solutions describing heat and mass transfer controlled dissolution of stationary spherical particles through the use of two dimensionless parameters N_a and N_b. The former is an indication of the solubility of the solute in the fluid, while the subtraction of N_b from N_a highlights the importance, relative to diffusion, of the advection of solute due to the liquid velocity field which results from the volume change as the bubble dissolves. Their Class I-A solution for particle dissolution controlled by diffusion in an infinite binary bulk phase whose components have constant partial specific volumes is of particular interest to present study. In their analysis, Duda and Vrentas (1971) also assumed that the dissolution process proceeds isothermally and hence the effect of heat released or absorbed during phase change is considered as negligible. The relevant dimensionless equations are given in Eqs. (2.25) and (2.26).

$$N_a = \frac{C_E - C_O}{\rho_g (1 - \nu C_E)} ; \tag{2.25}$$

$$N_b = \frac{\nu(C_E - C_O)}{1 - \nu C_E} \tag{2.26}$$

where; v is the kinematic viscosity of the fluid.

Kirkaldy (1956) and Bankoff (1964), discussed a quasi-steady state solution to the dissolution problem. Their analytical solution, given in Eq. (2.27), is valid for small values of N_a and N_b. Such steady state solutions model the spherical dissolution phenomena under conditions where the interface velocity is small and consequently the temperature or concentration field eventually reaches what is effectively a steady-state distribution.

$$\epsilon_b^2 = 1 - \frac{2N_a t^* ln(1+N_b)}{N_b} \tag{2.27}$$

where; $t^* = \frac{Dt}{R_o^2}$, referred to as the dimensionless time.

Most bubble dissolution studies have assumed independence with the surface tension (Kirkaldy 1956, Bankoff 1964, Shedd 2005). However, Epstein and Plesset (1950) had originally also presented the bubble dissolution theory with the inclusion of the surface tension. Liebermann (1957) reported that the inclusion of surface tension in a numerical model increases the density of the gas in the bubble hence increasing the gas concentration gradient between bubble and the bulk fluid. Therefore, due to the surface tension effects, the dissolution time can be reduced even during the initial stages of dissolution. The resultant model is complex and more recent studies by Cable and Frade (1988) have suggested that when the surface tension is considered, the resultant behaviour is highly complex and hence, useful analytical approximations are more difficult to establish. This is due to the effect that the surface tension has on the density of the gas in the bubble, which introduces a variable interfacial concentration into the solution of the diffusion problem. They presented a quasi-steady state solution to the bubble dissolution problem that is valid for values of $N_a < 0.01$. Cable and Frade reported an increase in the bubble dissolution rate with an increase in the surface tension. In their study, Kentish et al. (2006), reported that the surface tension effects can be considered to be minimal when considering the dissolution of small bubbles.

Cable (1967) stated that as most experimental results are not based on the consideration of an isolated sphere in spherically symmetrical conditions, a

comparison of such experimental data with the diffusion model often requires the adoption of a specific correlation. Hence, should a bubble move in relation to the surrounding fluid, or be subjected to a velocity gradient as is the case of stationary bubbles on a wall over which fluid flows, then the interaction between the flow of liquid around the bubble and the non-symmetrical concentration field in the liquid in the vicinity of the bubble must be taken into consideration. Cable (1967), reported that in mobile liquids, even when the bubble is held stationary, density differences caused by differences in temperature or composition could induce convective flow and hence disturb the symmetry of the diffusion field and thus accelerate the bubble dissolution process.

Yang et al. (1971) and Shedd (2005) reported that the speed at which bubbles dissolve in a liquid whereby relative motion is present between the bubble and the liquid is accelerated as the velocity of the flowing liquid is increased. This is due to the effect of the translatory motion on the mass transfer coefficient. Shedd (2005), reported that for a relative velocity of 1 m/s the dissolution time is expected to decrease by 1 to 2 orders of magnitude. A number of recent studies such as those done by Semmens and Ahmed (2003) and Elperin and Fominykh (2003) presented detailed numerical models for the dissolution of bubbles moving in a liquid. However, as these studies are focused on the general behaviour of dissolving bubbles, no correlations are included for the expected dissolution time.

A number of authors have considered the dissolution of a stationary bubble held on a flat plane through the modification of the Epstein and Plesset model. (Liebermann, 1957; Cable, 1967; Kentish et al., 2006). Hence, a correlation of this model was necessary to compensate for the non-symmetrical concentration field around the bubble. Liebermann (1957), adopted the theory of electrostatics whereby the capacitance of a conducting sphere is reduced by a factor of ln (2) when it placed next to an ungrounded infinite plane, to correlate the Epstein and Plesset diffusion model for stationary bubbles on a plane. Hence, the apparent diffusivity obtained using a spherical bubble tangentially in contact with a plane will be ln2 (0.693) times the true diffusivity and thus Eq. (2.24) was correlated as Eq. (2.28) for bubble dissolution on a flat plane.

$$\epsilon_b^2 = 1 - \ln(2)x^2 \tag{2.28}$$

Cable (1967), suggested that the correlation in Eq. (2.28) is valid only for a low solubility, when the concentration boundary layer is infinite in size. Similarly Kentish et al. (2006), reported that the correction factor should increase to a value between 0.695 and 0.773 with an increase in the gas solubility and time lag. This is inherent to the fact that as the solubility increases, the shell of liquid around the bubble in which diffusion takes place would get thinner and thus the presence of the plate would interfere with a smaller part of this shell, hence increasing the physical similarity to the case of an isolated spherical bubble.

Shedd (2005) reported that when considering a turbulent diffusion regime, it is reasonably correct to consider the use of the pure diffusion models for cases where no or minimal slip is present between the bubble and the flowing liquid. Hence, in contrast to the situation whereby a stationary bubble is subject to fluid impinging on it or a bubble rising through a fluid, the relative velocity for the bubble moving with a fluid is considered as negligible for bubbles with radii less than 0.001 m (Shedd, 2005). However, studies done by Kress and Keyes (1973) and Lezhnin et al. (2003) have described the bubble dissolution in turbulent flow through the application of the Sherwood number, thus capturing the ratio of the convective to the diffusive mass transport through the inclusion of the dimensionless Reynolds and Schmidt numbers. Lezhnin et al. (2003) reported that four principal correlations are available for the calculation of bubble dissolution in agitated waters and pipe flow. Such correlations are based on a proportionality constant and the power for the Reynolds number, whilst the Schmidt number is calculated at a power of 0.5 for all correlations. Furthermore, they identify the correlation given in Eq. (2.29) as the most widely used by researchers investigating bubble dissolution in similar conditions as the present study. Hence, the Sherwood number captures the enhanced bubble dissolution due to the turbulent diffusion characteristics present in turbulent bubbly pipe flow.

$$Sh = F \frac{D_b}{2R} Re^{0.75} Sc^{0.5} \tag{2.29}$$

where; Sh is the dimensionless Sherwood number, F is the proportionality empirical constant, D_b is the bubble diameter, R is the pipe radius, Re is the Reynolds number and Sc is the dimensionless Schmidt number.

Table 2.5 summarizes the models highlighted in this section. As discussed in Section 5.4, the isolated bubble dissolution models as originally developed by Epstein and Plesset (1950) was adapted for the present study, through the inclusion of the Sherwood number as given in Eq. (2.29) to quantify the effects of the turbulent diffusion.

Eq.	Source	Mathematical model	Model classification	Surface tension effects on dissolution mechanism	Fluid
(2.22) & (2.24)	Epstein and Plesset (1950)	$$\frac{dR}{dt} = -B\left[\frac{1}{R_t} + \frac{1}{(\pi D t)^{1/2}}\right]$$ simplified as; $$\epsilon_b^2 = 1 - x^2$$	Predicts bubble size ratio for isolated bubbles under no flow conditions	Assumed to be negligible	Water
(2.27)	Bankoff (1964)	$$\epsilon_b^2 = 1 - \frac{2N_a t^* ln(1+N_b)}{N_b}$$	Predicts bubble size ratio for isolated bubbles under no flow conditions	Assumed to be negligible	Water
(2.28)	Liebermann (1957)	$$\epsilon_b^2 = 1 - \ln(2)x^2$$	Predicts bubble size ratio for bubbles attached to a wall under no flow conditions	Assumed to be negligible	Water
(2.29)	Lezhnin et al. (2003)	$$Sh = F\frac{D_b}{2R}Re^{0.75}Sc^{0.5}$$	Predicts the magnitude of turbulent diffusion for bubbly two-phase flow as a dimensionless quantity	Assumed to be negligible	Water

Table 2.5: Summary of the theoretical bubble dissolution models.

2.2.4.2 Bubble growth in a supersaturated bulk fluid

Most studies on bubble growth in super saturated solutions have been done through the consideration of isolated bubbles in stagnant water conditions. Hence, minimal consideration has been given in the open literature to the growth of bubbles in supersaturated bulk fluid turbulent flow. The fundamental models for bubble growth have already been discussed in Section 2.2.3. However, these models consider the bubble growth at its nucleation point rather than as a free bubble expanding in a supersaturated solution.

Research into isolated bubble growth in supersaturated solutions, finds its origins in the works of Rayleigh in 1917 (cited in Hailemarian et al., 2007) who considered the equality of the work done by the liquid attempting to fill a suddenly liquid-free, gas filled spherical cavity and the kinetic energy of the incoming liquid shell to determine a relation for the change of radius of the cavity as a function of time.

As discussed in Section 2.2.2.2, Dean (1944) reported that if the total gas pressure in the bubble is sufficiently large, then the bubble will expand spontaneously at a rate controlled principally by the rate of diffusion of gas or vapor into the bubble. Furthermore, Dean (1944) reported that due to the fact that the diffusion coefficients of most gases are very similar the rate at which a gas enters a bubble will be controlled principally by the amount of gas close to the bubble, thus depending on the absolute solubility of the gas. In fact, experiments have shown that solutions of carbon dioxide in water form bubbles with much less mechanical agitation than solutions of air. This is inherent to the fact that carbon dioxide in water is about 50 times as soluble as nitrogen and consequently, more gas will be available near a newly formed cavity following a nucleation phenomenon.

Epstein and Plesset (1950) reported that an isolated gas bubble in a liquid solution will grow through diffusion with a direct relation to the degree of over saturation of the solution. Using the same assumptions as listed in Section 2.2.4.1, Epstein and Plesset's mathematical formula for bubble growth in a super saturated solution is given through the differential Eq. (2.30).

$$\frac{dR}{dt} = B_{ss} \left\{ \frac{1}{R_t} + \frac{1}{(\pi D t)^{\frac{1}{2}}} \right\}$$

(2.30)

where; B_{ss} the positive constant given as $B_{ss} = \dfrac{D(C_o - C_E)}{\rho_g}$. Therefore, using the same methodology as used for bubble dissolution, as described Section 2.2.4.1, Epstein and Plesset (1950) simplified Eq. (2.30) as in Eq. (2.31), where $\in_b$, is the resultant bubble size ratio and x is outlined in Eq. (2.23).

$$\in_b^2 = 1 + x^2$$

(2.31)

where; $\in_b = \dfrac{R_t}{R_o}$; $x^2 = \left[\dfrac{2B_{ss}}{R_o^2} \right] t$; $B_{ss} = \dfrac{D(C_o - C_E)}{\rho_g}$;

In view of the latter mathematical relationships, Epstein and Plesset (1950) presented a tabulation of the times for bubble growth from R_o to $10\,R_o$ for air bubbles in water at 22°C. Studies in the numerical analysis of bubble growth in super saturated two-phase flows were done by Payvar (1987) and Shafi and Flumerfelt (1997). The latter reported that bubble growth numerical solutions are arbitrary as bubble growth dynamics could be dependent on a combination of complex physical conditions, particularly in turbulent flow conditions as is the case with the present study.

2.2.4.3 Bubble shape characteristics in bubbly flows

Studies done by Thang and Davis (1979), Van der Welle (1985), Michiyoshi and Serizawa (1986), Winterton and Orby (1994) and Winterton and Munaweera (2001) in vertical two-phase bubbly flow have assumed a perfectly spherical bubble shape. However, Liu (1993) reported that bubble elongation along the flow is observed with the presence of larger bubbles, with minimal elongation observed with smaller sized bubbles. Similar conclusions were made by Thorncroft et al. (1998) in their studies in vertical up flow and down flow boiling. When discussing the bubble shape in horizontal bubbly flow, Kocamustafaogullari et al. (1994) reported that due to the negligible relative velocity between the two phases, the average pressure fluctuations generated by

the turbulent liquid fluctuations acting across a bubble diameter are the only means which could cause a distortion to the bubble shape.

Hesketh et al. (1991) linked the bubble shape to bubble breakage events. They reported that prior to breakage, bubbles were observed to stretch up to four times their original diameter in turbulent vertical pipe bubbly flow. Furthermore, Iskandrani and Kojasoy (2001) reported that bubble coalescence is expected at a void fraction above 65% in bubbly flows. Winterton (1972a) discussed the shape of bubbles detaching from a wall in supersaturated solutions. They reported that as bubbles get larger they would vibrate in the flow. However, the contact area would remain fixed in position.

Winterton (1972a) reported that just before breaking off from its point of nucleation, the typical bubble shape would be considerably distorted. Very often, the bubble would move jerkily along the surface before finally being carried into the mainstream flow. Similar trends were reported by Prodanovic et al. (2002) in sub-cooled flow boiling. They reported that upon inception at their nucleation point, bubbles are flattened due to strong inertial forces. However, as they grow, possibly sliding on the wall surface prior to detachment, they become more rounded thus developing a spherical shape near the maximum diameter. Prodanovic et al. (2002), reported typical aspect ratios in the range of 0.8 to 0.85 at detachment while similar studies done by Akiyama and Tachibana (1974) and Faraji et al. (1994) reported typical ratios of 0.8. Furthermore, Hepworth et al. (2003) stated that the assumption that bubbles must be almost a complete sphere at their nucleation point is only valid for low contact angles. Through the application of direct numerical simulations for bubbly air water two-phase downward flow, Lu and Tryggvason (2007) reported quasi spherical bubbles with diameters of 1.53 mm and slightly ellipsoidal bubbles with diameters of 1.84 mm.

Mishima et al. (1999) and Singh and Shyy (2007) classified the shape of a single isolated bubble rising in a stagnant pool in terms of the dimensionless Eotvos number, E_o given in Eq. (2.32) and the bubble Reynolds number, Re given in Eq. (2.32), through the use of the bubble shape regime diagram as illustrated in Fig. 2.8.

$$E_o = \frac{g\Delta\rho D_b^2}{\gamma} \qquad\qquad (2.32)$$

where g is the gravity, $\Delta\rho$ the density difference between the two phases, D_b is the mean bubble diameter and γ is the surface tension.

$$Re = \frac{u_{rel}D_b}{\nu} \qquad\qquad (2.33)$$

where u_{rel} is the relative velocity between the two phases and ν is the kinematic viscosity.
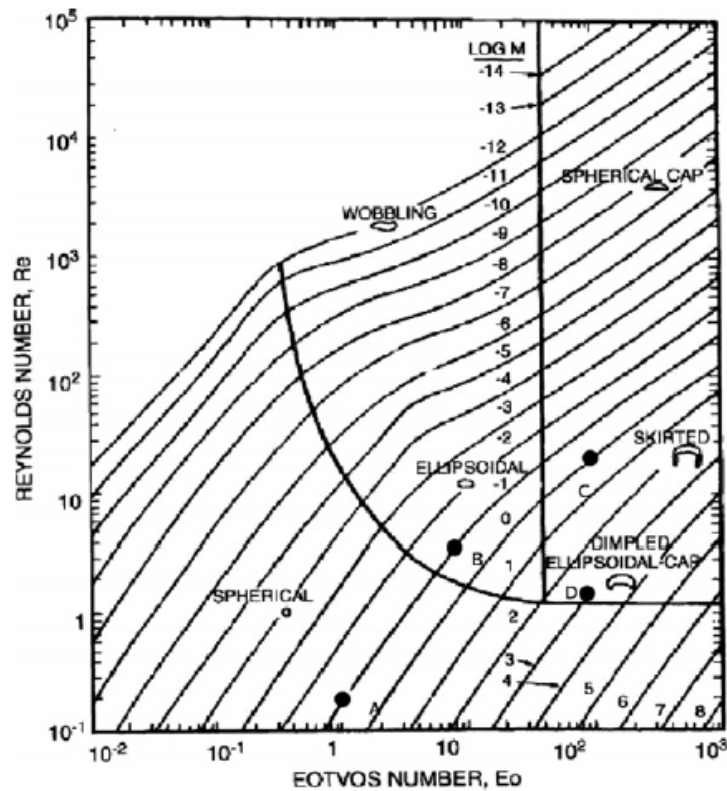
Figure 2.8: Bubble shape regime diagram (Mishima et al., 1999, Page 231).

2.2.5 Wet domestic central heating systems

This section provides an overview of the existing literature sources with respect to domestic central heating systems, relevant legislation, corrosion issues and system water deaeration.

2.2.5.1 Overview

The importance of central heating systems is highlighted by Dwyer (2008), who reported that since 1971, the use of central heating systems in United Kingdom

households increased from 34% of the dwellings to 90%. Furthermore, The Building Regulations Part L1A (2006) reported that circa 16% of the carbon dioxide that the UK produces originates from boilers used to heat domestic houses. Dwyer (2008) reported that most of these systems are fuelled by natural gas and that most of the older installed boilers are of the non-condensing type and therefore do not capture the latent heat in the flue gas. However Dwyer (2008) also reported that this trend is shifting due to the mandatory installation of condensing boilers since 2006 in most European states. In fact, 99% of the boilers currently being installed in the UK are of the condensing type (The Heating and Hot Water Industry Council, 2010). Spreitzer et al. (2002) reported that almost all residential buildings in Germany make use of a wet central heating system that consequently results in circa 40% of the primary energy consumed in Germany. In addition, Sauer et al. (2007) reported that central heating systems are responsible for 70% of all domestic emissions in Germany.

2.2.5.2 Legislation

The installation of condensing boilers has become standard in most European Union states through the introduction of the Energy Performance in Buildings Directive in 2003. This requires European member states to take appropriate measures to significantly improve the energy efficiency of both new and existing buildings. As a case in point, the United Kingdom has introduced The Building Regulations (2006), recently updated through The Building Regulations (2010), where Part *L* of this document specifies the maximum energy requirements for new buildings and for existing buildings. The latter document caters for both new and existing buildings and is further sub-divided into domestic and non-domestic buildings. Hence, Part *L1A* and *L2B* are particularly relevant to the present study as these sections cater for new domestic and non-domestic buildings respectively.

Dwyer (2008) reported that apart from considering the quality of the building fabric, these regulations require the certification of the completed systems to confirm that the completed works include energy efficient fixed building services. The latter should have effective controls which are normally commissioned by a competent person. Hence, these regulations ensure that the

resultant carbon performance of the building is an improvement on the target emission rate *TER*, this being calculated in terms of the mass of carbon dioxide in kilograms per square meter of floor area per year emitted as the result of heating, cooling, hot water, ventilation and internal fixed lighting. Therefore, The Building Regulations Part *L1A* (2006) specify that apart from exceptional cases (where the installation of a condensing boiler could be impractical or too costly) all new buildings should be equipped with a condensing boiler having a SEDBUK efficiency in bands A or B. Therefore, considering the SEDBUK (2009) database's specification of a minimum band *B* boiler efficiency of 86%, all new domestic buildings should be equipped with a condensing boiler performing at an efficiency of 86% or better. The building regulations are particularly relevant when considered in view of Bakos et al. (1999) statement that, the use of energy efficient buildings could appease the future need for capital investment in power plants that would otherwise be required to offset the expected annual increase in power demands.

2.2.5.3 The condensing boiler

The Building Regulations Part L1A (2006), define the condensing boiler as an efficient boiler that reduces the amount of heat released through the flue. This is achieved through the condensing of the flue vapor leading to the recovery of the latent heat in the flue gas. As illustrated in Fig. 2.9, this heat is transferred to the return water through additional heat transfer surfaces. Natural gas boilers are particularly suitable for latent heat recovery due to the high latent heat content (i.e. water vapour) present in the products of combustion. This is evident through the combustion equation for natural gas as shown in Eq. (2.34).

$$CH_4 + 2O_2 \Rightarrow 2H_2O + CO_2 + Heat \qquad \textbf{(2.34)}$$

Where by mass;

4kg methane + 16kg oxygen $\Rightarrow$ 9kg water vapor + 11kg carbon dioxide
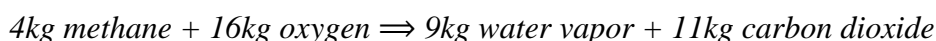
Dwyer (2008) reported that the recovery of the latent heat in the flue gas through condensation could potentially release 3.5MJ per cubic meter volume of natural gas burnt in the boiler. Furthermore, at a stoichiometric air to gas volume ratio

the condensing temperature of the flue gas from a natural gas boiler is 57°C. Therefore, Dwyer reported that the efficiency of a condensing boiler can only be higher than 90% if the return water temperature is below 57°C. Consequently, manufacturers of condensing boilers typically recommend boiler return water temperatures between 30°C and 45°C.   However, at higher return water temperatures, condensing boilers still result in higher efficiencies when compared to non-condensing boilers. This is due to the extended heat transfer surfaces. In fact, Yildiz and Güngör (2009) reported that the maximum design flow temperature of their test condensing boiler was of 90°C with a return temperature of 70°C.

1. Gas valve
2. Mixing Chamber
3. Fan
4. Burner
5. Heat Exchanger
6. User Control and Display
7. Return Sensor
8. Water Pump
9. Flow Sensor
10. Condensate Trap
11. Water Pressure Switch
12. Flow Overheat Thermostat
13. Flue Overheat Thermostat
14. Automatic Air Vent
15. Ignition Electrode
16. Flue Pipe
17. Combustion Test Point
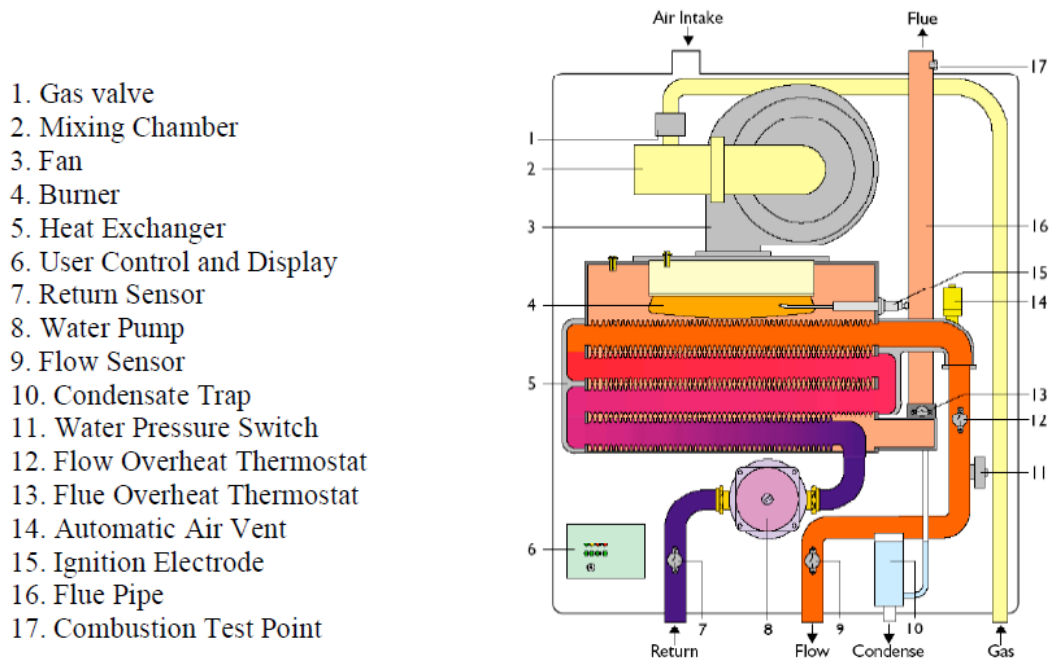
Figure 2.9: Sectional Schematic Diagram through a typical domestic condensing boiler (Dwyer, 2008, Page 4).

The condensing boiler has dominated the market in the recent years, mainly due to the new building regulations, requiring the mandatory installation of efficient boiler units. However, some 66% of the 22 million boilers currently in operation in UK domestic households are of the non-condensing type (The Heating and Hot Water Industry Council, 2010), which if replaced by the year 2020 could result in a reduction of 2 MtCO$_2$ (Committee on Climate Change, 2008). Weiss et al. (2009) reported that the levelling of the price difference between the condensing and non-condensing boilers has also contributed to the increase in the

48

sales of condensing boilers. In fact they state, that the condensing *combi* boilers result in an additional price of 16 ± 8% when compared to the non-condensing type. Furthermore, Che et al. (2004) reported that through the installation of a condensing boiler, a payback period between 3 and 4.5 years should be expected as a result of the energy savings done in relation to the expected consumption of a non-condensing boiler. This study is based on the usage of the two systems where a flow and return temperature of 60/40 and 80/60 ^{o}C were used for the condensing and non-condensing boilers respectively.

Che et al. (2004) argued that apart from the energy saving benefits, condensing boilers also result in the prevention of the emission of water vapor containing toxic constituents such as SO_x and NO_x, dust and soot. Therefore, these emissions are partially or totally dissolved in the condensed water of a condensing boiler and consequently the pollutants released to the environment are reduced significantly.

2.2.5.4 Oxidation in wet central heating systems

Davis (1987) discussed the corrosion issues in central heating systems and stated that the first sign that corrosion is affecting a central heating system is the requirement for regular system venting required to maintain the system flow. Hence, venting would be required due to the build-up of gas originating from the oxidation reaction of the untreated steel surfaces. Such surfaces are normally to be found in the radiator's inner surface and in expansion vessels. Hydrogen is the gas that is formed as a by-product of the final oxidation process. In fact, as outlined by Hill and Holman (1995) through Eq. (2.35), the rusting process requires the presence of both oxygen and water in order to take place. In the initial stages of rusting, iron (II) ions pass into solution at the anodic area while at the same time, a reduction of atmospheric oxygen to hydroxide ions takes place at the cathodic area, where the concentration of dissolved oxygen is higher. The Fe^{2+} and OH^- ions then diffuse away from the metal surface and precipitate as iron hydroxide. This is then oxidized by dissolved oxygen to form rust. Hill and Holman (1995) stated that rusting could thus be considered to be a secondary process, taking place in the solution as the iron and hydroxide ions move away from the metal surface. However, if the solution contains a relatively high

concentration of dissolved oxygen, the iron ions are converted into rust more rapidly and in this case a protective layer of iron oxide may be formed on the metal surface that could retard further rusting.

$$Fe + H_2O + \frac{1}{2}O_2 \Rightarrow Fe(OH)_2$$
$$3Fe(OH)_2 \Rightarrow Fe_3O_4 + 2H_2O + H_2$$

(2.35)

Furthermore, Hill and Holman (1995) stated that other factors such as impurities in the iron and the availability of dissolved oxygen and electrolytes in the solution in contact with the iron could influence the rate of steel oxidation considerably. Davis (1987) reported that the corrosion process in a central heating system starts at the time of first filling with fully aerated water. This is due to the dissolved oxygen present in the water that could come out of solution as the water temperature is increased and thus the system's water moves into the super saturated state. Davis (1987) reported that the resultant air bubbles adhere to the metal surfaces of the radiator and could stay there for a significant amount of time. Furthermore, pockets of air could form on the upper parts of the radiator and the oxygen in these pockets could re-dissolve in the water as the radiator and system temperature falls. This could happen during night time when the system boiler is inactive for a relatively long period of time, thus resulting in a significant reduction in the overall system's temperature. This fact implies the need for a venting mechanism at the top most end of the radiator component.

The rate of the oxidation corrosion process increases with the rise in temperature and peaks at a temperature of circa 78°C. Therefore, this process will take place until all the dissolved oxygen is consumed. However, Davis (1987) argued that oxidation corrosion could still take place at very low levels of oxygen. In fact, corrosion could take place at dissolved oxygen concentrations as low as 0.1 ppm. Davis (1987) listed the conditions promoting oxidation corrosion as follows;

- Water losses from the system resulting in the addition of fresh oxygenated water
- Diffusion of oxygen during the thermal cycling of the system through pipe joints and other system joints

- The presence of porous jointing compounds on flanges on the negative side of the circulator that could result in air sucked into the system through micro leaks.
- Negative pressure developing in a sealed system equipped with an undersized expansion vessel.

Davis (1987) reported that the corrosion debris within a central heating system is the most common cause for premature circulator failure. This is due to the fine debris that drifts into the inner water-lubricated parts of the circulator, consequently increasing the frictional forces and resulting in the eventual overheating and seizure. Furthermore, Davis (1987) explained that the build-up of corrosion debris in areas of low flow rates leads to inefficient circulation of hot water and thus a reduced level of heat transfer. The latter, results in an extension to the time required for space heating thus resulting in an increase in the use of fuel together with the associated carbon footprint.

Other causes of corrosion could occur due to factors such as electrolytic corrosion and the presence of chemicals in the circulating water such as chlorides and sulphates. Electrolytic corrosion takes place between the differing metals in a system or even between the differing alloying constituents and impurities in the metals. Electrolytic corrosion takes place even in the near absence of oxygen and the rate of attack increases rapidly with the increase in water temperature. In fact, Davis (1987) reported that this rate doubles with every ten degree increase in the water temperature and unlike oxidation corrosion, it does not reach a maximum rate at 78°C.

2.2.5.5 Water deaeration in central heating systems

Minimal consideration has been given by literature to the technique of passive deaeration in wet heating. Some studies were published in Soviet Journals during the 1960s, 1970s and 1980s but could not be accessed in full text due to the fact that most of these studies are written in Russian.

Balaban-Irmenin and Fokina (2007) referred to the use of deaerated water in heating grids in Russia. They reported that deaeration is one of the mechanisms for the protection of such pipelines against internal corrosion, which accounts for

one fourth of all damages sustained by the pipelines in heating systems. Bulloch (2003) referred to the deaeration of boiler feedwater systems in steam production plants for the prevention of corrosion due to the presence of high levels of dissolved oxygen in the system's water. In fact, Bulloch (2003) stated that the deaerators in such systems consist of relatively simple devices that reduce the oxygen to typically less than 10 PPB.

Roffelsen (1984), referred to the role of deaeration in central heating systems in preventing corrosion due to the dissolved oxygen and other gasses present in the water. When referring to the actual process of water deaeration, Roffelsen (1984) stated that it is relatively simple to remove the larger bubbles of *picked-up* foreign air from the circulating water. Such bubbles are removed through the use of gas separators consisting of a pipe branch that extends upwardly from the line system and leads to a collecting chamber for the gas that rises from the liquid. However, the micro bubbles released due to the dissolved gasses are more difficult to capture and thus deaerate by time. Roeffelsen (1984), reported that such bubbles are deaerated through the use of an air separator, whereby the circulating liquid is conducted with a temporarily reduced flow velocity underneath a column of liquid. The latter is at rest in the upwardly extending pipe branch, formed by the separator housing. Therefore, in the boundary region between the circulating liquid and the liquid that is at rest in the air separator, the liquid that contains the released gas, mixes with the gas free liquid from where the micro bubbles would rise into the liquid column and subsequently collect in the air chamber. Roffelsen (1984) further stated that, due to the properties governing dissolved gasses in water, such an air separator operates most efficiently the closer it is installed to the point of the circulation system, where the fluid temperature is at its highest and the pressure is at its lowest.

Karapantsios et al. (2008), referred to the fact that the degassing of wet heating systems is necessary as the formation of the second phase results in the accumulation of a layer of air on hot surfaces that consequently reduces the liquid heat transfer coefficients. Hence, the necessity to the release such air pockets from the wet heating system for an improved system performance. Recent studies by Francis and Pashley (2006), Karagianni and Avranas (2009) and Eastoe and Ellis (2007), highlighted the fact that the degassing of water

causes the enhanced dispersion of a wide range of hydrophobic water-insoluble oils in water. This fact is attributed to a minimal lowering of the surface tension through degassing. Karagianni and Avranas (2009), argued that the lowering of the surface tension could be attributed to the fact that degassing results in the removal of impurities from the solvents. Furthermore, the removal of gas nucleation solutes or dissolved gas molecules eliminates the possibility of the formation of cavities between the two hydrophobic surfaces. Francis and Pashley (2006), reported that the degassing of water was achieved through the cycle of freezing and thawing of water. Francis and Pashley also reported that good levels of deaeration were achieved through a freeze and thaw cycle that was followed by vacuum pumping to a pressure of 0.01 mbar. Furthermore, Yanagida (2008), referred to the process of degassing through vacuum pumping followed by the use of ultrasound irradiation.

2.3 Summary

In this chapter, a range of topics were explored in relation to the aim of the present study. There are no known studies available in the open literature discussing the phenomenon of two-phase flow in domestic wet central heating systems. This fact emphasises the relevance of the present study in providing essential data and relevant theoretical interpretations in relation to this phenomenon.

The literature review has provided essential background information to the research objective. The fundamentals governing dissolved gases in liquids were researched. Literature confirms that the gas concentration, described through the saturation ratio, is a function of the temperature and pressure of the bulk liquid. The open literature discussing the theoretical knowledge on bubble formation in super saturated solutions was also researched. There exist two principal theories for bubble nucleation these being; the classical and non-classical models. The former are associated with higher bulk fluid saturation ratios, and are generally considered to be less adaptable for more practical applications. The latter are associated with more practical solutions characterised with low super saturation ratios. Hence, the non-classical models are considered to be more applicable to

realistic solutions and hence are considered to be more relevant to the present study.

The theory concerning the prediction of bubble detachment sizes under fluid flow conditions was also researched. The open literature suggests that the force balance method is the most relevant model for the prediction of the bubble detachment radii under super saturated fluid flow conditions. The theory of bubble dissolution in a two-phase bubbly flow was also researched. The open literature suggests that this is mostly a diffusion controlled process. In fact, most studies on the dissolution of bubbles in under saturated bulk fluid conditions have been done for isolated bubbles under non-flow conditions, hence emphasising the importance of the diffusion process on the dissolution regime. The open literature suggests that in two-phase bubbly flow, the dissolution process can be classified as a turbulent diffusion process, thus dependent on the diffusion and the degree of turbulence in the bulk fluid. The turbulent diffusion is quantified through the dimensionless Sherwood number. Finally, the open literature was consulted to research the general issues concerning wet domestic central heating systems. The relevant legislation, corrosion issues and system deaeration techniques were researched and summarized in this Chapter.

The next chapter will discuss the research methodology and the methods used in the current PhD research project.

CHAPTER 3

Experimental Facility and Methodology

3.1 Introduction

As highlighted in the preceding chapter, hitherto, the two-phase characteristics in a central heating system are not well understood. These include the fundamental concepts governing the expected bubble size, nucleation and system bubble production rates. An investigation leading to a comprehensive understanding of these characteristics was possible through the design and construction of an experimental test rig. Therefore, this chapter presents a detailed description of the experimental facility, the image analysis technique made use of, and the resultant measurements and uncertainty analysis. The chapter is organized as follows; Section 3.2 provides a detailed description of the experimental facility whereas Section 3.3 provides details with respect to the image analysis techniques used while Section 3.4 provides the details of the experimental runs conducted as part of this study. Section 3.5 provides the details for the calculations used in the present study while Section 3.6 outlines the experimental uncertainty analysis. Finally, Section 3.7 summarizes this chapter.

3.2 Experimental facility

The experimental facility was designed and constructed after assessing the requirements and objectives of the present study. The latter were set by Brunel University and Spirotech bv, the Netherlands. Such requirements were set in view of the project's principal aim at understanding the fundamentals governing the two-phase phenomenon in wet domestic central heating systems. Such requirements necessitated the construction of a central heating test rig making use of a standard condensing boiler as required by the Building Regulations Part L1A&B (2010), for all new building and renovation projects. Fig. 3.1 illustrates a schematic diagram of the designed test rig while Fig. 3.2 illustrates images of the actual test rig constructed at Laboratory TC006, Brunel University.
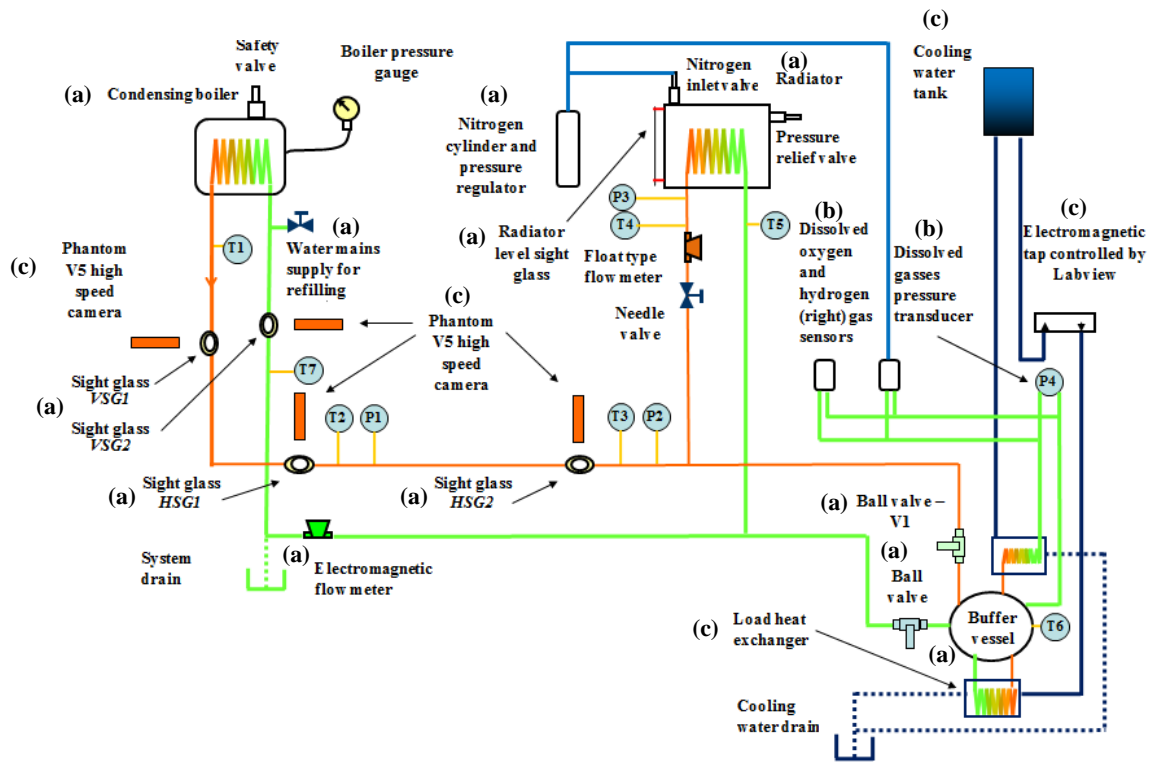
Figure 3.1: Test rig schematic diagram
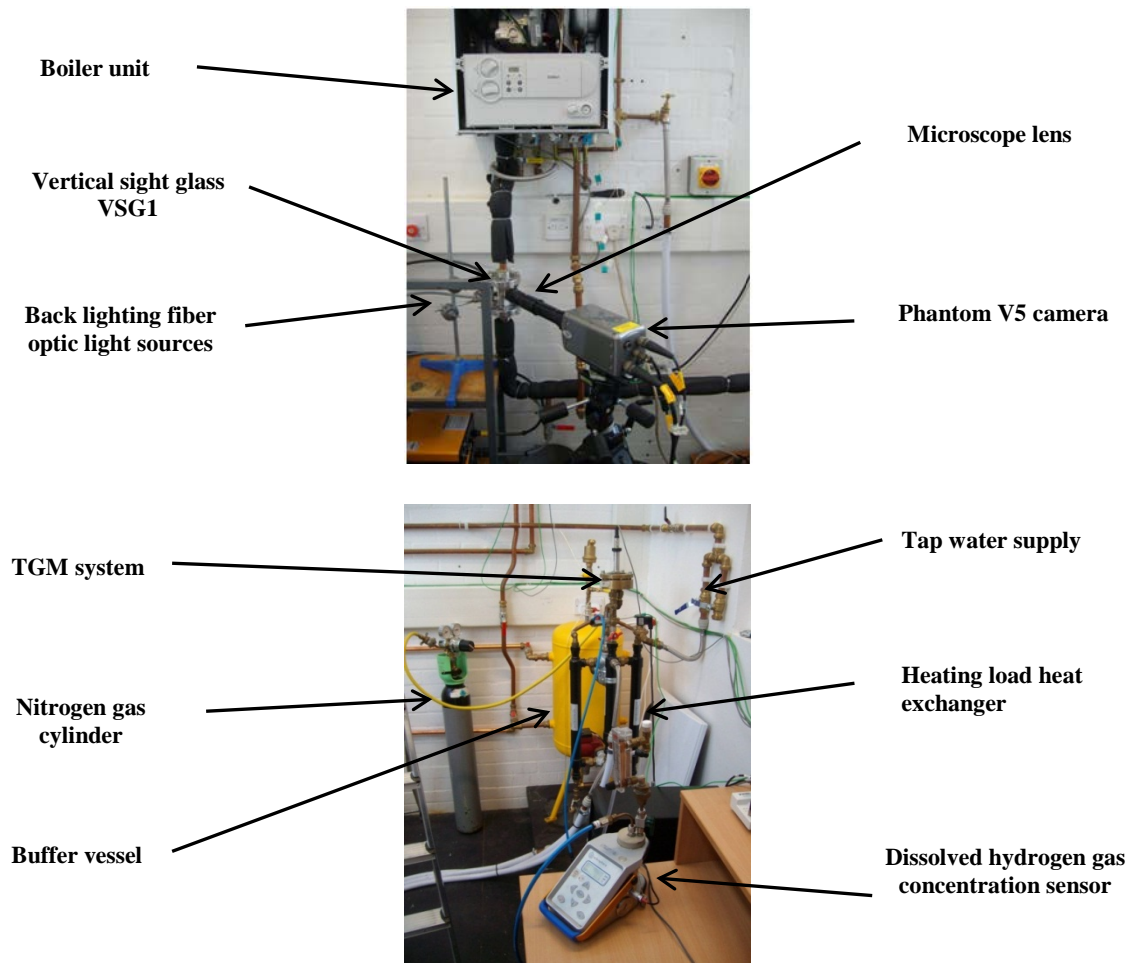
Figure 3.2: Test rig images; Top: Boiler and high speed camera focused on the boiler exit sight glass; Bottom: Radiator, buffer vessel and *TGM* system.

As illustrated in Fig. 3.1, the experimental test rig consists of three main systems these being the;

(a) Boiler unit, pipe work, buffer vessel, radiator and sight glass sections;
(b) Dissolved gas analysis sensors;
(c) Automated data collection systems and system heating load control.

3.2.1 Boiler, pipe work, buffer vessel, radiator and sight glass components

This section presents the details for the system gas boiler, pipe work, radiator and sight glass components installed in the experimental test rig.

3.2.1.1 Boiler

A Vaillaint ecoTEC pro 24 (Vaillant, 2010) combination boiler was selected for the present study. The combination function, enabling the supply of hot tap water is not used is the present study. The boiler was selected after considering the new building legal directives and due to the helical rectangular tube structure used for the primary heat exchanger as commonly found in most modern systems due to the improved space efficiency and the possibility of incorporating the condenser with the primary heat exchanger (Shah, 2003). The manufacturer's maximum flow temperature was set at 75°C. However, this was increased to an absolute maximum of 85°C through the application of supplier codes available in the boiler installer's manual.

As illustrated in Fig 3.3, the primary heat exchanger manufactured by Giannoni (Vaillant, 2010), consists of 12 rectangular tubes coiled around a gas burner in a helical structure. Four of these coils are located in the condenser section where the flue gases condense on the cold tubes at the water return side to the heat exchanger, thus ensuring that latent heat is recovered from the exhaust gases. The use of a commercial boiler did not permit a precise measurement of the inner wall temperature of the tubes in the primary heat exchanger. This is due to the physical system set up that only permitted the installation of thermocouples on the outer wall of the heat exchanger tubes.

Flue gas to atmosphere

Condenser heat exchanger

Flue gas duct from primary heat exchanger to condenser

Return flow

Primary heat exchanger with helical coil tubes

Gas burner located in the middle of the helical tube structure

System feed flow
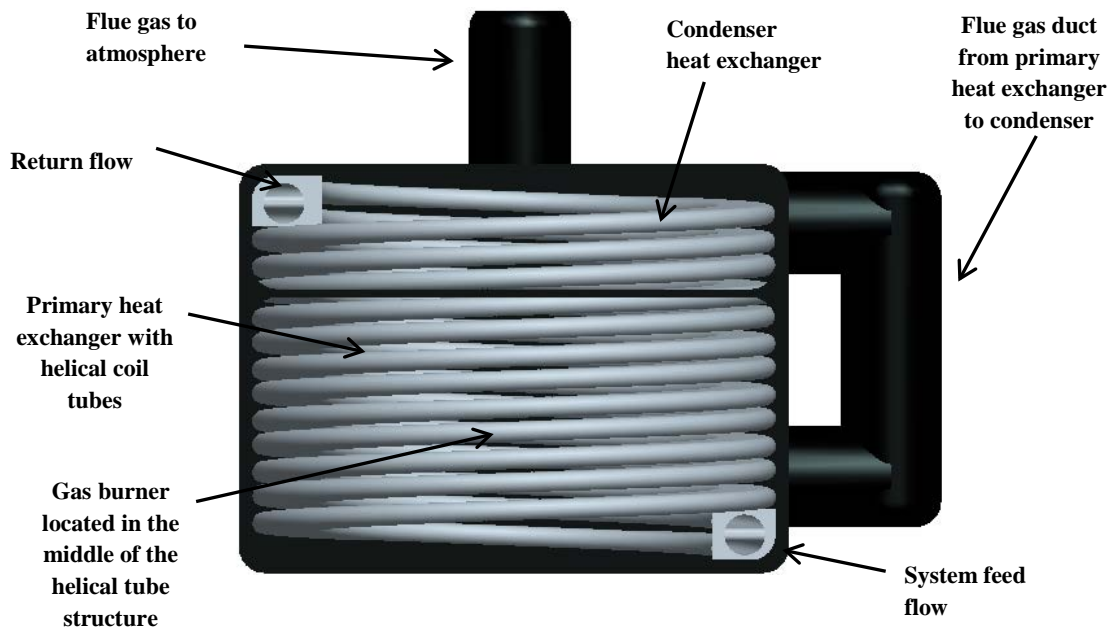
Figure 3.3: Pro Engineer Wildfire CAD model of the boiler primary heat exchanger unit combined with the condenser heating exchanger.

3.2.1.2 System pipe work, buffer vessel, and radiator

The boiler is linked to the system closed loop circuit through the use of 22 mm (outer diameter) standard copper piping. Standard 22 mm copper pipe fittings were used for the assembly of the closed loop circuitry. A T brass pipe section at the exit of the boiler enables the system to be filled up using the mains water supplied at a pressure of circa 3 bars (abs). A square section sight glass with internal dimensions of 20x20 mm is located at the exit end of the boiler. This section is lagged to ensure adiabatic conditions from the exit of the boiler primary circuit to sight glass *VSG1* (Fig. 3.1), thus minimizing bubble dissolution and ensuring that conditions are as close as possible to the conditions present at the exit of the primary heat exchanger.

K-type thermocouples were installed along the pipework due to their temperature monitoring range, typically ranging being between -40°C and 1000°C (Nicholas and White, 1994). K-type stainless steel 310 mineral insulated thermocouples with a 1.5 mm probe diameter were selected after considering the nature of the fluid used. The installation was done by drilling the copper pipe work and brazing female brass housings thus enabling the thermocouple probe to be

58

assembled as illustrated in the 3-D representation in Fig. 3.4. The probe was offset into the pipe by circa 8 mm. Three PTX 7500 (0 to 10 bar (abs)) series pressure transducers were used to monitor the system pressure through the pipework. The maximum operating temperature for these pressure transducers is 80°C. The fluid temperature in contact with the transducer was minimized through the assembly of the transducer on a stainless steel pipe measuring circa 150 mm that was subsequently brazed to the copper pipe. This is necessary so as to minimize the temperature effects on the pressure transducer.
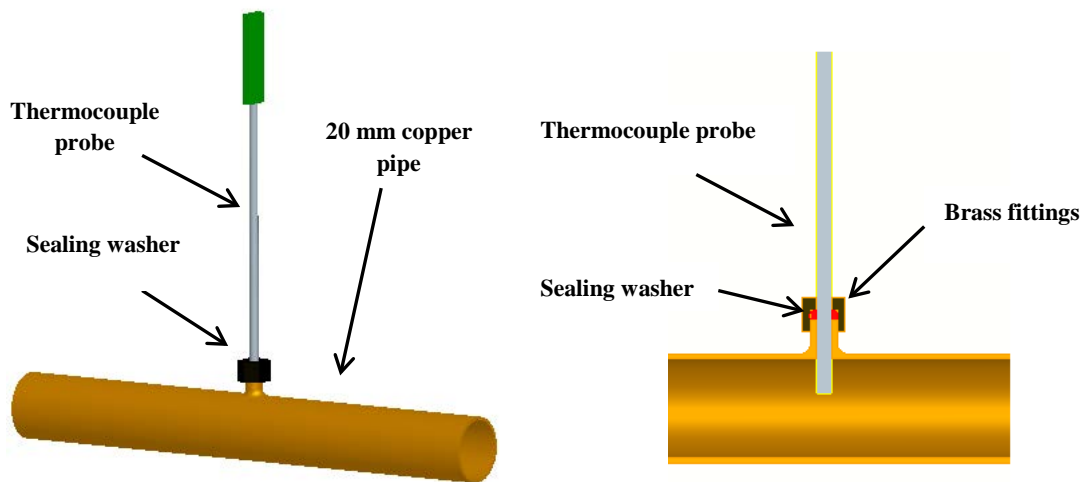
Figure 3.4: Pro Engineer Wildfire CAD model of the copper pipe mounted K-type thermocouple sub assembly (left) and cross section (right).

Thermocouple *T1*, as in Fig. 3.1, measures the boiler flow line temperature while pressure transducer *P1* measures the system pressure. As illustrated in Fig. 3.1, ball valve *V1* controls the system flow rate while the thermocouples *T2, T3* and pressure transducers *P1* and *P2* provide temperature and pressure readings for the straight line pipe run between sight glasses *HSG1* and *HSG2*. Sight glass *HSG1* is at a distance of 0.8 m from the first bend while *HSG2* is at a total distance of 3.1 m from the bend. Sight glass *VSG1*, as in Fig. 3.1, is located on the flow line of the boiler while sight glass *VSG2* is located on the return line to the boiler unit. The system radiator consists of a wall mounted seam-top radiator measuring circa 0.8x0.6 m with a maximum power output of circa 0.9 kW. The flow to the radiator is controlled through a needle valve while the localized flow rate is monitored through a manual float type flow meter on the side of the radiator. A manual pressure relief valve was installed at the top of the radiator to

facilitate the filling and pressurizing of the system. Another valve was installed so as to pressurize the system with nitrogen-oxygen free gas, supplied though the use of a size *X* nitrogen cylinder equipped with a pressure regulator. Thermocouples *T4* and *T5*, as in Fig. 3.1, provide the difference in temperature at the inlet and exit to the radiator while pressure transducer *P3* measures the pressure in the radiator. The system fluid flow rate is monitored through an Electromag 500 Series (LITREMETER, 2010) electromagnetic flow meter mounted on the return line to the boiler.

A buffer vessel (Fig. 3.5) with a capacity of circa 40 liters was installed so as to simulate the expected heating load from a typical house. As illustrated in the system schematic diagram in Fig. 3.1, the buffer vessel incorporates a heat exchanger, supplied by cold tap water, through which a range of system heating loads could be set. The flow of tap water into the heat exchanger is controlled through an electromagnetic tap wired to a control module as discussed in Section 3.2.3.

Tap water source

Total Gas Measurement (*TGM*) membrane unit and pressure transducer

System heating load heat exchanger

Buffer vessel

TGM heat exchanger

Circulation pump
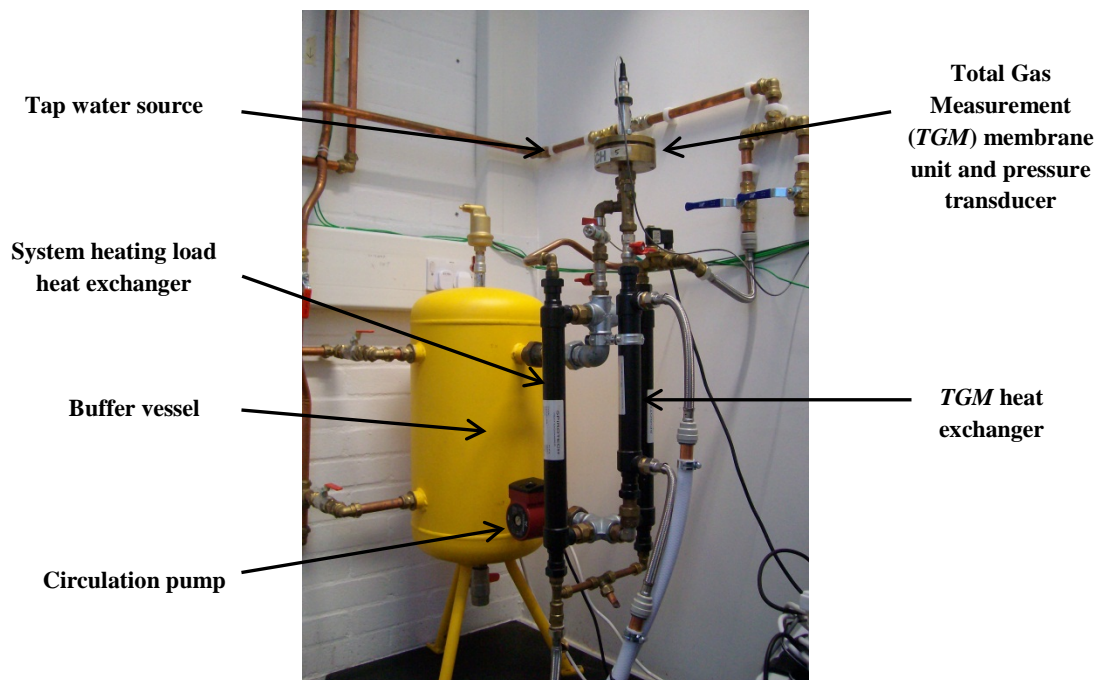
Figure 3.5: Buffer vessel unit.

3.2.1.3 Sight glass components

Three square section sight glass components were designed so as to minimize the errors due to light refraction as discussed by Prodanovic et al. (2002). The latter

components were not available '*off the shelf*' and consequently they were designed and modelled using the CAD Pro Engineer Wildfire software as part of the present study. The design was done to withstand the maximum system pressure of 3.75 bar (abs) and the maximum operating temperature of 85 $^{\circ}$C. Attention was taken to facilitate the use of the high speed camera and the application of side or back side illumination. As illustrated in Fig. 3.6, the assembly consists of two stainless steel flanges supporting a welded aluminium square section through the use of supporting bolts thus compressing the aluminium sub section between the flanges. Schott Borofloat 33 glass plates (3.3 mm thick) were assembled on the inner side of the aluminium section. Silicone was used to seal the sides and care was taken to ensure that no silicone protruded from the edges thus ensuring a smooth inner surface throughout the section. A short length of copper pipe was assembled to the outer side of the stainless steel flanges through the use of epoxy resin.
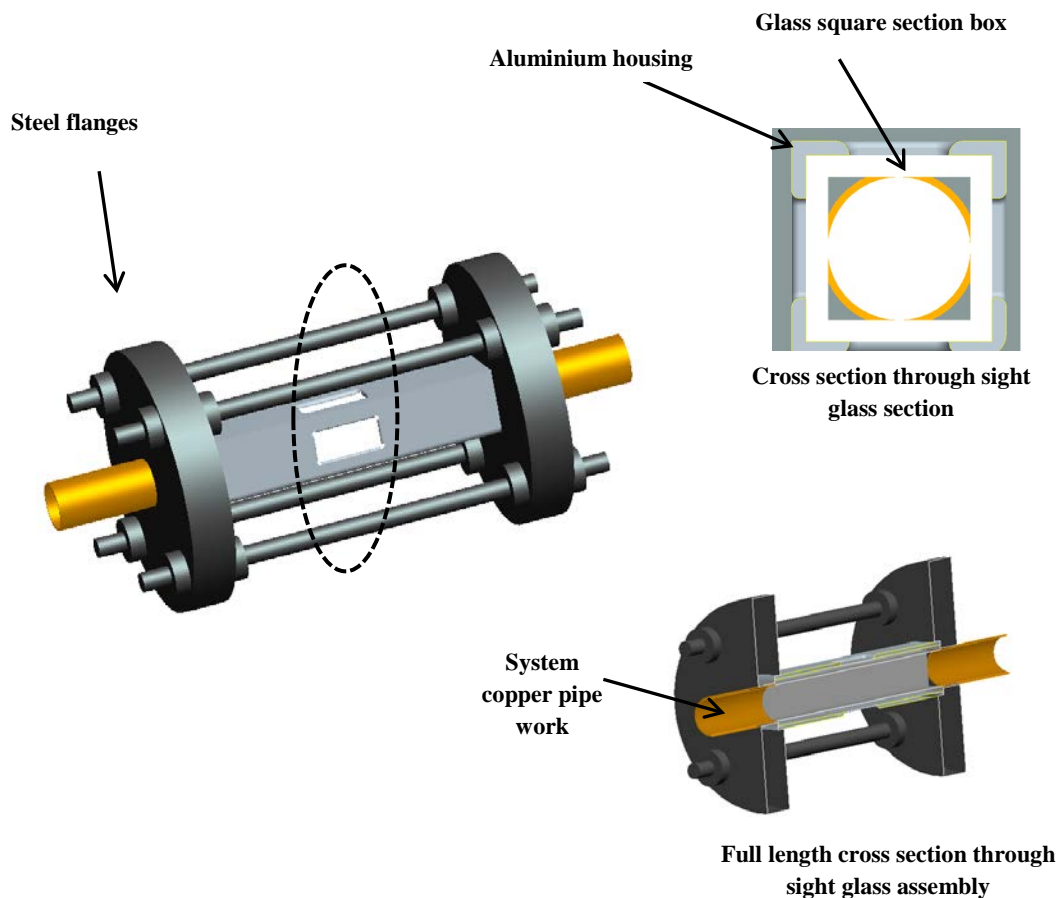
Figure 3.6: Pro Engineer Wildfire CAD model of the sight glass assembly and relevant cross sections.

3.2.2 Dissolved gas analysis

This section presents the details for the dissolved gas concentration monitoring equipment and techniques used in the present study.

3.2.2.1 Continuous gas partial pressure measurement

The total partial gas pressure of the dissolved gases is measured through the use of a Total Dissolved Gas Pressure Measurement (*TGM*) system supplied by Spirotech bv. The system works through the use of the direct sensing membrane diffusion method (Watten et al., 1997). As illustrated in Fig. 3.7, this system consists of a pressure transducer, mounted on top of an assembly consisting of porous steel gauze, topped by a gas permeable silicon membrane, as the primary mechanism for isolating dissolved gases and water vapour from liquid water. A nylon sheet and a Perspex unit, housing the pressure transducer are located on top of the silicone membrane. The Perspex housing includes a micro channel allowing the transducer to measure the total gas pressure in the system's water. As illustrated in Fig. 3.1, a heat exchanger supplied with cold tap water cools the water flowing to the system to a temperature of circa 30 $^{\circ}$C. This is necessary due to the limitations of the *TGM* system in handling higher temperatures. In fact, a maximum temperature of 45°C is specified for the *TGM* system. Care was taken to ensure that the cooling water supplying the *TGM* heat exchanger originated from a different channel to that supplying the heating load heat exchanger. This is necessary so as to ensure that the *TGM* heat exchanger does not receive fluctuating flows of cooling water thus preventing temperature spikes in the water supplied to the *TGM* system.

The *TGM* functions by allowing the dissolved gasses to diffuse through the silicone membrane, and move up to the gas chamber under the pressure transducer. This process is facilitated through the use of the nylon sheet. The latter's porous structure facilitates the diffusion of the dissolved gases and thus reduces the time required for the system to get to its steady state. A time allowance of circa 1 hour is required for the *TGM* to reach steady state. The *TGM* was cleaned regularly due to the negative effect of fouling on the gas permeable membrane. The latter was therefore cleaned or replaced on a regular basis (Watten et al., 1997).
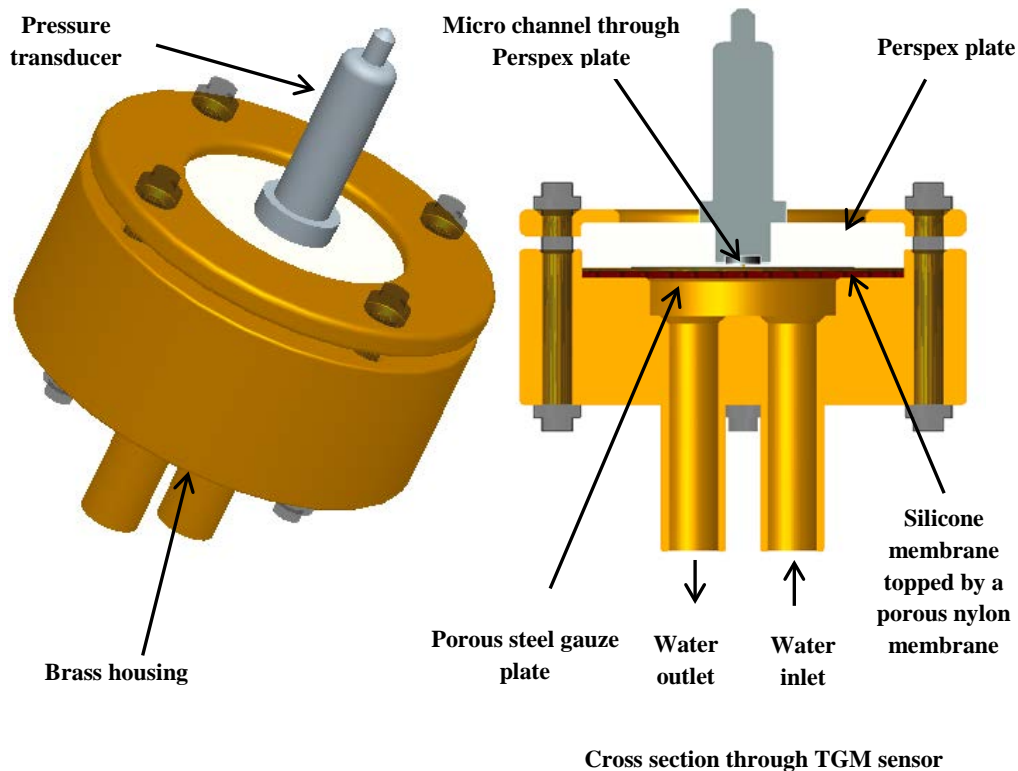
Figure 3.7: Pro Engineer Wildfire CAD model of the *TGM* system and relevant cross sectional diagram.

3.2.2.2 Dissolved gas composition

Tap water is known to contain oxygen and nitrogen (Fogg, 2003) as the principal dissolved gasses due to exposure to the atmosphere. Hydrogen is also known to be present in heating systems as a by-product to the oxidation reaction whereby oxygen reacts with exposed steel structures, such as radiators or storage vessels (Heat, 1998). As illustrated in the schematic diagram in Fig. 3.1, gas sensors for dissolved oxygen and hydrogen are used to analyse the concentrations of these two gases in the water flowing through the central heating system. Orbisphere dissolved gas sensors 3654 and 3655 are used for measuring the concentration of dissolved hydrogen and oxygen respectively. The former is fed with nitrogen required as a flushing gas and supplied from a nitrogen (oxygen free) size X cylinder. Both sensors required sample water supplied at a temperature below 35°C. (Orbisphere, 2009). Therefore, sample water to both sensors is fed through a *T* section from the channel feeding the *TGM* system.

63

3.2.3 Data logging and boiler return temperature control

Data logging is achieved through the use of a National Instruments cDAQ-9172 8-slot USB 2.0 chassis equipped with two NI 8211 4-Channel ±80 mV thermocouple differential analogue input modules, an NI 9203 8-Channel ±20 mA analogue input module and an NI 9481 4-Channel 250 V AC (2A) relay module. The K-type thermocouples are wired to the NI 8211 voltage module while the pressure transducers and the electromagnetic flow rate sensor are all wired to the NI 9203 current module. A block diagram was then developed in LabVIEW. The system was programmed to collect data points per second, hence, with a resultant speed of 1 Hz. The LabVIEW program is used so as to transfer all the data onto excel for the subsequent analysis. The resultant Lab View block diagram is illustrated in Fig. A1, in Appendix I.

The boiler return temperature is controlled through the use of logic gates in LabVIEW thus controlling the signal to the electromagnetic switch through the relay module. This logic is dependent on the temperature at the inlet to the boiler, monitored by thermocouple $T7$, as in Fig. 3.1. Therefore, the required inlet temperature can be adjusted through the use of a user adjustable parameter interface window on the user interface page in LabVIEW.

3.3 Imaging and analysis

This section presents the details for the photographic techniques and subsequent image analysis used in the present study.

3.3.1 Camera and illumination

A Vision Research Phantom V5 high speed camera connected to a PC is used to film and store the video clips as illustrated in Figs. 3.8 and 3.9. A monozoom (Navitar) microscope lens is used to develop the desired magnification. The high speed camera is mounted on a tripod incorporating an adjustable chassis enabling a precise vertical or horizontal camera movement. An image resolution of 1024 x 1024, a shutter speed of 30 µs and a frame speed of 100 frames per second were used for all experiments involving system parameters. Lighting is provided by

two high intensity EverestVIT ELSV 60 W light sources attached to semi-rigid fibre optic light guides.
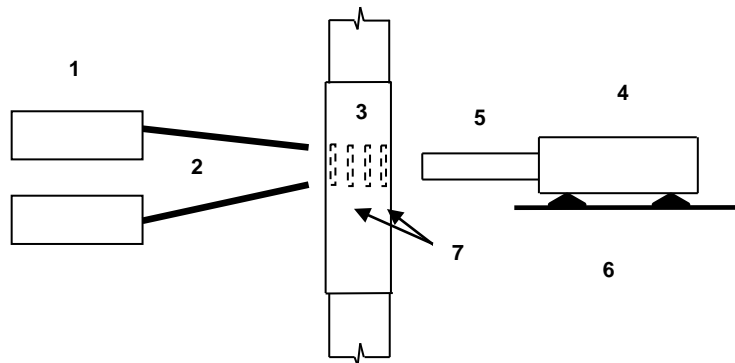
1. Light sources
2. Fibre optic light guide
3. Square sight glass section
4. High speed camera
5. Microscope lens
6. Adjustable camera chassis
7. Sample volumes across pipe section (1.5mm focal depth)

Figure 3.8: Imaging equipment and setup (Vertical sight glass).

Phantom V5 high speed camera

Microscope lens

Horizontal sight glass

System pipework

Tripod
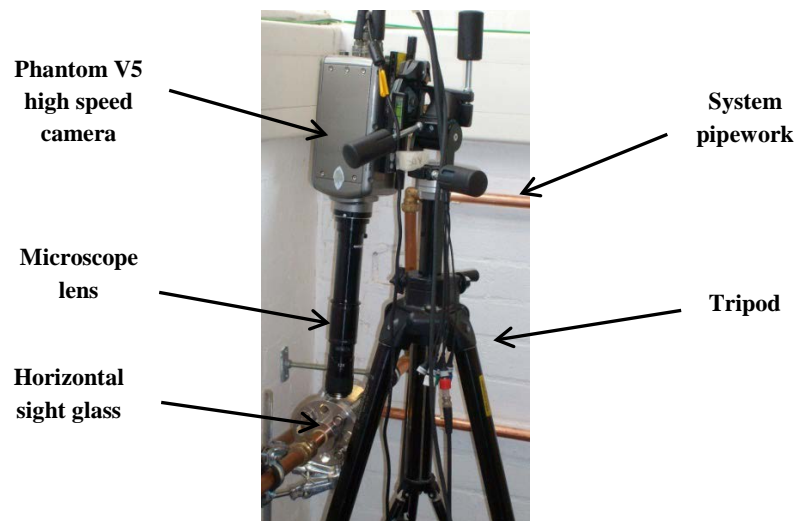
Figure 3.9: Actual camera and illumination set up (horizontal sight glass).

As illustrated in Fig. 3.8, back lighting is used. Therefore, the light sources and the camera are on the opposite ends of the vertical and horizontal sight glass units. An adjustable mounting was used to point the light sources on the sight glass. Care was taken to ensure that consistent mounting and light intensity settings were maintained throughout all experimental runs. The sight glasses were cleaned frequently to ensure that fouling of the glass is kept at a minimum.

This is necessary to ensure that homogenous lighting is always present in the picture frame, thus facilitating the subsequent image analysis.

3.3.2 Image processing

The video films were converted to image frames saved as 'tag image file format' or tiff files using the Phantom Version 606 camera software. A typical image is illustrated in Fig. 3.10. The manual analysis of bubbles at the exit side of the boiler was done through the use of the measurement function of the Phantom Camera Control Version 606 software. This task involved the scaling of the image followed by a measurement of the resultant bubble size using a coordinate system to ensure that consistent measurements are made. Two bubble diameters were recorded for each bubble and averaged for an improved result.
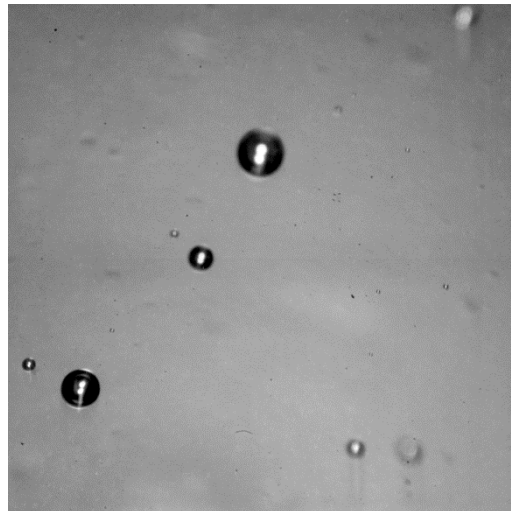
Figure 3.10: Typical camera image.

The analysis of the bubble production and nucleation rates necessitated the use of automated image analysis software for improved sample sizes and the consistent distinction between in focus and out of focus bubbles present on the same image frame. This was achieved through the use of the image analysis software, Image-Pro Plus developed by Media Cybernetics. Image-Pro Plus is a widely used image processing software that could be used for a variety of image processing tasks such as image filtering and enhancement, automated measurements, object tracking and macro recording. The use of Image-Pro Plus in the analysis of bubble characteristics in two-phase analysis was reported by Hepworth et al. (2003) and Wang et al. (2009). Image-Pro Plus functions through the conversion

of images into a numeric form for the subsequent analysis, a process referred to as image digitization. This process involved the division of an image into a horizontal array of very small regions referred to as picture elements or pixels. The latter are identified through their position in the grid referenced by its row and column number. (Image-Pro, 2010) A macro was written enabling a series of images to be analysed for in focus bubble counts and diameters (Appendix II). The main challenge in the development of this macro was the presence of both in focus and out of focus bubbles in the same image. This is due to the limited image depth of field of 1.5 mm and the total channel depth of 20 mm.

3.3.2.1 Macro setup

The macro incorporates five distinct steps where the input of the image processing settings required for the subsequent image analysis is done. Consistency in the results of such analysis was maintained through the use of the same settings for all the image analysis runs, coupled with background lighting consistency as highlighted in Section 3.3.1. Therefore, Table 3.1 tabulates the settings that were used for all the image processing runs. The first step necessitates the calibration of the image. This step was facilitated through a pre-saved calibration settings file and therefore, a recall of this file was done for most experimental runs.
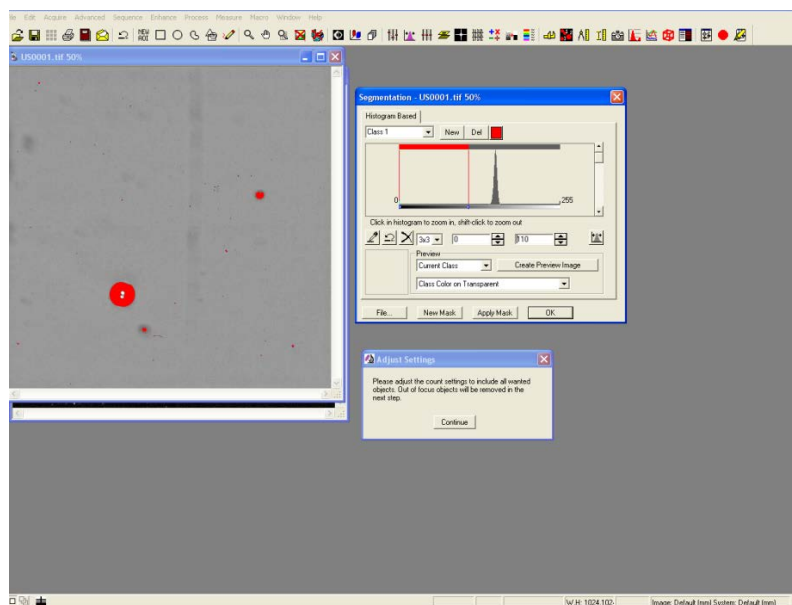
Figure 3.11: Macro grey scale thresholding – Macro step 2 Part I.

As illustrated in Fig. 3.11, the Step 2 in the macro necessitates the specification of the grey scale thresholding, on a scale between *0* and *255* for the target objects in the image. Other *Count/Size* functions were also specified. Due to the use of a filter in the following steps, at this stage, both in and out of focus objects are selected through the specification of the grey scale thresholding as specified in Table 3.1. As illustrated in Fig. 3.12, an *Outline* style was specified, thus activating the software's option of highlighting the object's perimeter during analysis for an improved display. Bubbles located on the edge of the frame were eliminated from the analysis through the use of the *Clean Borders* function. The *Fill Holes* function was activated thus ensuring that the image processing macro interprets all bubbles as whole single entities, with no gaps or voids. This step is necessary as bright spots are occasionally present in the centre of bubbles due to lighting effects. The smoothing function is activated with a specified smoothing factor of *5*. A factor of *0* specifies that no smoothing should be done, whereas a factor of 100 specifies the maximum smoothing level. This function ensures that uneven object perimeters would be smoothed for a more representative analysis. The flatten background function was activated with a bright background specified as the default background. The latter function ensured that any inconsistent lighting would be flattened to render an even background intensity.
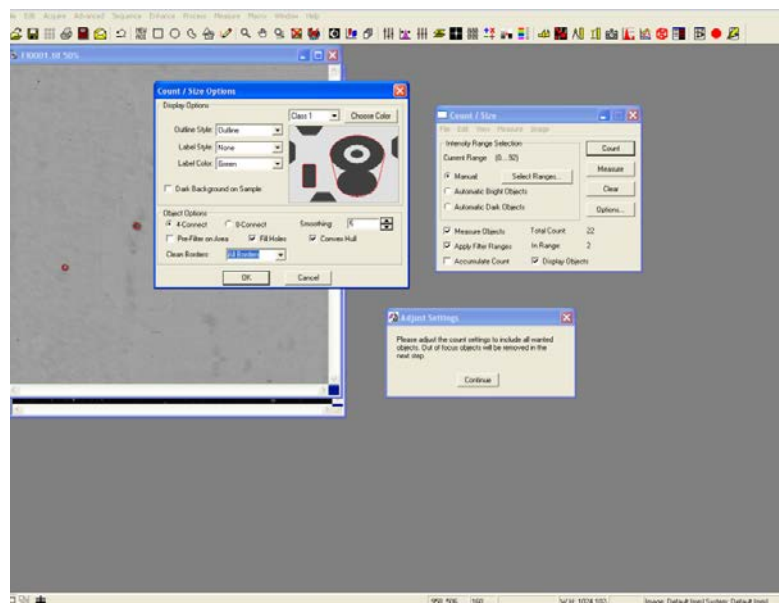
Figure 3.12: Macro count/size options – Step 2 Part II.

The desired measurements were specified and filter ranges (as in Table 3.1) were applied. The specification of filter ranges ensure that dark objects that may be present in the image such as dirt or other floating particles are not recognized as target objects or bubbles. The measurements selected are the *bubble count* and *bubble diameter.*

Step 3, incorporates the application of a Sobel filter. Therefore, as illustrated in Fig. 3.13, at this stage the grey scale thresholding range is fine tuned to exclude out of focus bubbles. The Sobel filter plots the gradient of intensity change between objects and their background through the extraction and enhancement of edges and contours. This is done by expressing intensity differences or gradients between neighbouring pixels as an intensity value. Therefore, objects that are in focus have sharp edges with a high gradient change and consequently result in a high intensity values, whereas out of focus objects do not display such a characteristic. The Sobel filter is used as it is less sensitive to image noise when compared to other filtering techniques (Image Pro, 2010).
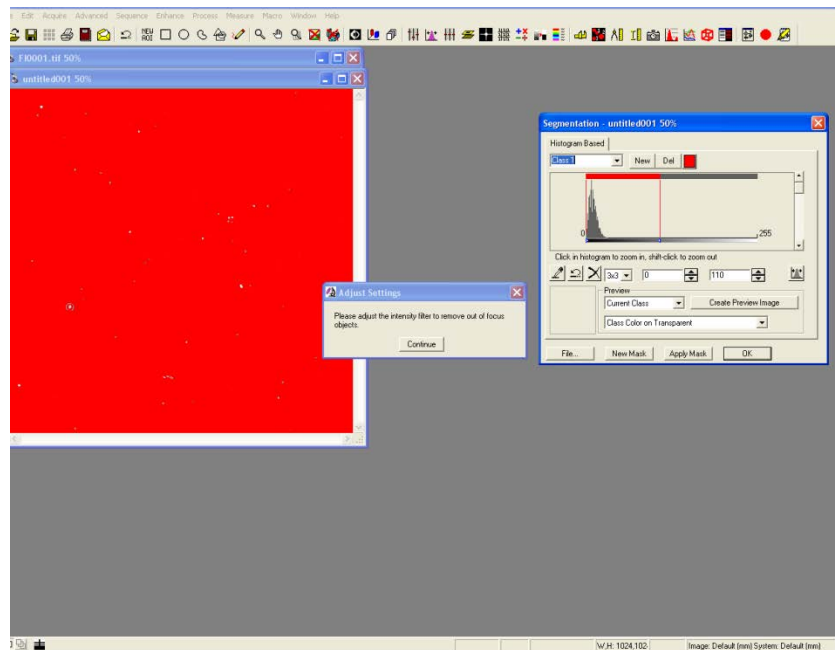
Figure 3.13: Macro Sobel filter grey scale range specification – Step 3.

Step 4, necessitates a specification of the data to be displayed in the data collector. The *image name*, *bubble count* and *diameter* were specified. Furthermore, the data is specified to be exported to an excel file in a tabulated format. The macro was programmed to save all the processed images for

subsequent analysis. Therefore, a typical processed image is illustrated in Fig. 3.14, where in focus bubbles are circled in red.
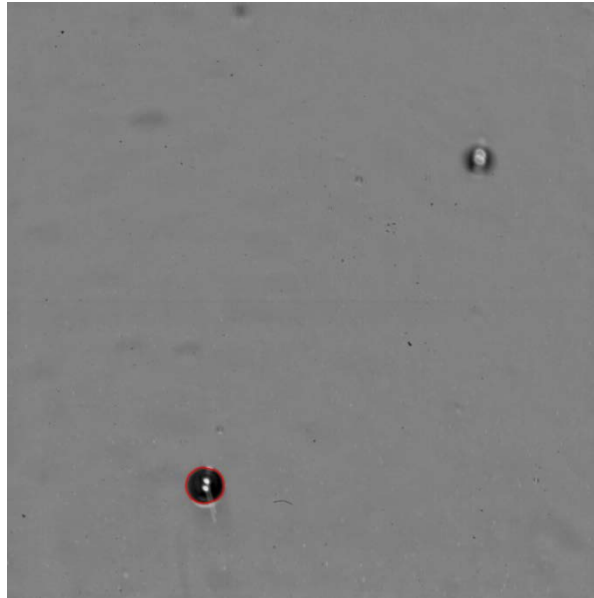
Figure 3.14: Typical camera images (post processing – in focus bubble circled in red).

Specified parameter	Parameter range
Grey scale threshold – Step 2	0 - 110
Filter range – Aspect ratio	0.8 - 1.2
Filter range – Diameter (Mean)	0.05 - 5.6 (mm)
Smoothing factor	5
Grey scale threshold – Sobel filter	0 - 88

Table 3.1: Main parameters used in the image processing macro routine.

3.4 Experimental methodology

All experiments discussed in the present study, were conducted after the experimental facility reaches steady state conditions. Circa 1.5 hours were required for the experimental test rig to reach the latter conditions, with all system signals yielding low fluctuations. The longest stabilization time is required by the Total Gas Measurement (*TGM*) system due to its direct sensing membrane diffusion method. The system parameters were adjusted prior to commencing this stabilization period. Fine-tuning of these parameters was done

after stabilization. Apart from the gas composition test discussed in Section 3.4.1, all tests were done using water that was allowed to circulate in the system for a minimum period of 5 days. As discussed in Section 3.2, the four variable system parameters were controlled as follows;

i   The system flow rate or velocity is varied through the use of the ball valve *V1* on the supply line. System flow volumetric rates in the range of 4.5 to 12.5 litres per minute were used. A constant heat flux with changing fluid velocities is achieved through the use of a range of return temperatures thus ensuring a constant heating load and heat flux at the primary heat exchanger wall.

ii   The system pressure is set through the use of the nitrogen gas cylinder connected to a standard cylinder regulator. As illustrated in Fig. 3.1, this was done through a one way valve at the top of the radiator. The system pressure was stepped between 2 and 3.75 Bars, the latter being the maximum pressure specification for a standard domestic heating system.

iii   The system heating load was varied between a minimum of 7.5 kW and a maximum of 21.5 kW through the step increase in the boiler flame settings. The return temperature was maintained constant through the use of the electromagnetic tap connected to the water mains supply line. The heating load is equal to a heat flux ranging between 17 to 50 kW/m^2 on the heat exchanger's wall.

iv   High dissolved gas saturation ratios were achieved through the filling of the upper part of the radiator with nitrogen gas. Lower saturation ratios were achieved through the sudden release in system pressure followed by a subsequent re-pressurization.   Maximum saturation ratios at the primary heat exchanger wall conditions ranging from 1 to 1.20, as defined by Jones et al. (1999a), were achieved. This range of saturation ratios was established following long term testing on a central heating test rig (Lamers, 2005).

3.4.1 Water gas composition after system filling

This test was done to analyse the actual dissolved gas composition of water after the system filling with tap water. As discussed in Section 3.2.2.2, the presence of

untreated steel surfaces in domestic central heating systems is expected to change the dissolved gas properties in water, due to the expected oxidation process. As a result of exposure to atmospheric air, tap water is known to contain dissolved gas concentrations identical to those found in atmospheric air. Therefore, the major dissolved gas is nitrogen accounting for 78.08% of the dissolved gas content. This is followed by oxygen, with a concentration of 20.94%. Argon and carbon dioxide collectively amount to circa 0.97%. Other gases, these being methane, neon, helium, krypton, hydrogen, nitrous oxide, carbon monoxide, xenon, ozone, nitrogen dioxide and iodine are present in very low concentrations. In fact, they collectively account to less than 1% of the dissolved gas content.

Prior to this experiment, the system was drained and flushed a number of times to ensure that no rust and other dirt residues are present. The system was then filled with fresh tap water and operated using the system parameters tabulated in Table 3.2 for a period of 8 hours per day. Dissolved gas concentrations using the Orbisphere 3654 Hydrogen and Orbisphere 3655 Oxygen gas sensors were collected twice daily. The dissolved gas concentration was monitored until the readings stabilized. The stabilization process was complete for both dissolved gases over a period of 4 days.

Test	Bulk fluid velocity in system pipe work (m/s)	System pressure (abs) (Bars)	Heat flux (kW/m^2)	System heating load (kW)	Maximum Saturation ratio at wall conditions (-)	System flow temp. (^{o}C)	System return temp. (^{o}C)
DGT	0.52	2.75	39	17	1.1	75	55

Table 3.2: Gas composition tests *(DGT: Dissolved gas test).*

3.4.2 Vertical pipe bubble distribution tests

Bubble distributions with changing system parameters in the vertical pipe at the exit of the boiler were investigated. As illustrated in Fig. 3.8, this was done through the use of the adjustable chassis thus enabling the focal plane to be shifted in pre-determined intervals of 4 mm across the sight glass sectional width of 20 mm. Hence, images were recorded with focal planes at a distance of

1,4,8,12,16,19 mm from the sight glass wall. Sight glass *VSG1* at the boiler flow line was used. Four experiments were done through the application of a range of bulk fluid velocities. This was done due to the knowledge that the bubble size and void fraction is mostly dependent on the bulk fluid velocity (Winterton, 1972a). The system parameters as tabulated in Table 3.3 were used and 1,000 images were recorded for each focal plane position across the sight glass section. Image analysis was done using the Image-pro routine as discussed in Section 3.3.2.

Test	Bulk fluid velocity in system pipe work (m/s)	System pressure (abs) (Bars)	Heat flux (kW/m^2)	System heating load (kW)	Maximum Saturation ratio at wall conditions (-)	System flow temp. (^{o}C)	System return temp. (^{o}C)
BDT	0.19-0.52	2.7	23	10	1.1	80	55-68

Table 3.3: Vertical pipe bubble distribution tests *(BDT: Bubble distribution test).*

3.4.3 Bubble size and shape characteristics at the boiler exit.

The experimental studies for the investigation of the bubble characteristics at the flow line of the boiler were done through the combination of the four principal system parameters, these being the system flow rate, pressure, the heat flux on the primary heat exchanger wall and the dissolved gas concentration. The system parameters used are tabulated in Table 3.4. Prior to conducting the experiments, the system was flushed and cleaned through the use of a SpiroPlus Lime system cleaner. This step was necessary to ensure that no lime scale deposits arising from dissolved calcium bicarbonate develop on the boiler's primary heat exchanger surface. The system was subsequently flushed a number of times with fresh tap water to ensure that no contamination takes place. The experimental tests were then done after 1 week of filling the system with tap water. As discussed in Section 3.3.2 the images recorded from these experiments were analysed manually for improved accuracy for bubble size and shape measurement.

The system parameters were controlled as highlighted in the first part of this section. As discussed in Section 4.3.1, a quasi-homogenous volumetric void fraction across the vertical pipe is expected with system parameters. Hence, the experiments done for bubble characteristics at the boiler exit were done through the recording of images on a single focal plane at a depth of circa 9 mm from the sight glass wall. Sight glass *VSG1* was used. As done by Prodanovic et al. (2002), approximately 100 bubbles per experimental run were analysed manually and used to calculate the mean bubble diameter. Two diameters were measured along the principal axis of the bubble and used to calculate the average bubble diameter. In recent studies done for the analysis of bubble growth on static surfaces, the ratio of such diameters was used as a calculation of the bubble elongation or aspect ratio with the flow. Hence, as discussed in Section 4.3.3, the ratio of the measured diameters for each bubble was used to calculate the bubble aspect ratio.

Test	Bulk fluid velocity in heat exchanger tubes (m/s)	System pressure (abs) (Bars)	Heat flux (kW/m^2)	System heating load (kW)	Maximum saturation ratio at wall conditions (-)	System flow temp. (^{o}C)	System return temp. (^{o}C)
BCT I	0.3-0.85	2.6	23	10.2	1.2	85	51-73
BCT II	0.8	2-3.75	39	17	0.9-1.2	75	55
BCT III	0.8	2.6	17-50	7.5- 21.5	1.05	77-59	50
BCT IV	0.8	2.6	39	17	0.9-1.20	75	55

Table 3.4: Bubble size and shape characteristics experiments at boiler exit *(BCT: Bubble Characteristics Tests).*

3.4.4 Bubble production and nucleation rates

The system bubble production and nucleation rates were investigated at the boiler exit through the use of the sight glass located at the boiler flow line. Hence, sight glass *VSG1*, as in Fig. 3.1, was used. Similar tests to those done for the bubble shape and size characteristics as discussed Section 3.4.3 were done for

this investigation. However, more data points were used as the images were analysed through the use of the image processing software. Furthermore, in contrast to the bubble characteristics test, a constant maximum saturation ratio at boiler wall conditions with system pressure was achieved through a variation in the nitrogen gas head in the radiator.

Hence, as tabulated in Table 3.5, four principal tests were conducted through the application of the system controlling parameters, these being the bulk fluid velocity, pressure, heating load and dissolved gas concentration. As done in the bubble characteristics test, images were recorded on a single focal plane, located at a distance of circa 9 mm from the sight glass wall for each experimental run. The subsequent image analysis was done using the Image-Pro routine as discussed in Section 3.3.2.

Test	Bulk fluid velocity in heat exchanger tubes (m/s)	System pressure (abs) (Bars)	Heat flux (kW/m^2)	System heating load (kW)	Maximum saturation ratio at wall conditions (-)	System flow temp. (^{o}C)	System return temp. (^{o}C)
BNT I	0.39-0.85	2.7	23	10.2	1.1	80	55-68
BNT II	0.8	2.7	17-50	7.5- 21.5	1.1	82-64	55
BNT III	0.8	2.7	39	17	1.01-1.20	75	55
BNT IV	0.8	2-3.75	39	17	1.1	75	55

Table 3.5: System bubble production and nucleation tests *(BNT: Bubble nucleation tests).*

3.4.5 Bubble characteristics and counts on return line to boiler

The investigation of the bubble nucleation rates as outlined in Section 3.4.4, necessitated an analysis of the possible presence of the second phase in the return water to the boiler's primary heat exchanger. Hence, through the use of sight glass *VSG2*, the bubble nucleation experiments tabulated in Table 3.5 in Section 3.4.4 were repeated for this investigation.

3.4.6 Bubble distribution and dissolution in horizontal pipes

Tests were done to investigate the bubble distribution and dissolution in the horizontal pipe work supplying the system with hot water and fed from the boiler flow line. Tests with supersaturated flow line conditions were also done to analyse the effect of the supersaturated bulk fluid on the resultant bubble size. The horizontal sight glasses *HSG1&2*, as in Fig. 3.1, were used for filming micro bubbles at two points on the horizontal straight line pipe. The sight glasses were spaced 2.3 m apart. As illustrated in Fig. 3.15, five focal planes were used, these being at 0, 4, 8, 12 and 16 mm from the top plane of the sight glass. Hence, the images recorded from these planes at each sight glass were used to analyse the two-phase characteristics in the horizontal pipe with the system conditions.
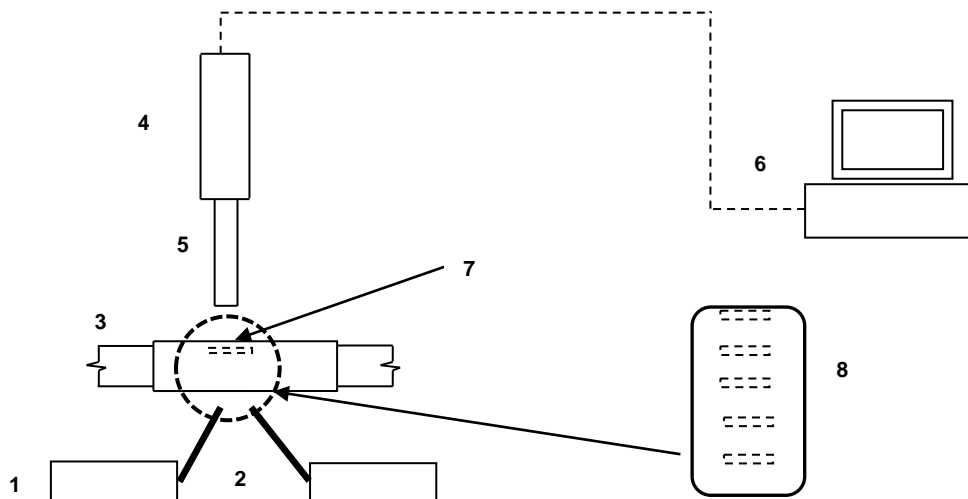
1. Light sources	4. High speed camera	7. Focal depth of 1.5 mm
2. Fibre optic light guide	5. Microscope lens	8. 5 focal planes at
3. Square sight glass section (20*20mm)	6. PC wired to camera	0,4,8,12,16mm from
		the top of sight glass

Fig. 3.15: Bubble size measurement equipment.

As a single high speed camera was available for the current study, recordings at both horizontal sight glasses could not be made simultaneously. Hence, recordings for each experimental run were initially made at *HSG1* followed by recordings at *HSG2*. Care was taken to ensure that the system was at steady state conditions during the recordings at both sight glasses. Hence, upon completion of the recordings at *HSG1*, the camera was moved and re-set at *HSG2* whereby another set of recordings was made. As tabulated in Table 3.6, the investigation conducted in this study involved seven principal tests.

All the experimental runs were used to analyse the bubble distribution in horizontal pipes with system parameters. Bubble dissolution at constant system conditions was investigated through the *HPT_US Tests* whereby four under saturated bulk fluid conditions were used. The investigation of bubble dissolution at under saturated conditions with a range of bulk fluid velocities and at a high flow line temperature was done through the *HPT_FR I Tests* while the investigation of the bubble dissolution with a range of bulk fluid velocities and at a low flow temperature was achieved through the *HPT_FR IV Tests*. Related experimental investigations, *HPT_FR II & V and HPT_FR III & VI,* were done to investigate the bubble behaviour at bulk fluid saturation and super saturation conditions respectively.

Test	Bulk fluid velocity in pipe work (m/s)	System pressu-re (abs) (Bars)	Bulk fluid Reynolds number (-)	Saturati-on ratio at bulk fluid condition-ns (-)	Boiler flow temper-ature (°C)	Boiler return temper-ature (°C)	Time for bubbles to flow bet. *HSG1&2* (s)
HPT_US	0.52	2.7	28.7E+3	0.89, 0.92, 0.95, 0.97	75	50	3.3
HPT_FR I	0.25, 0.33, 0.42, 0.52	2.7	13.8E+3, 18.4E+3, 23.0E+3, 28.7E+3	0.89	80	55-68.4	3.3-6.9
HPT_FR II	0.25, 0.42, 0.52	2.7	13.8E+3, 18.4E+3, 23.0E+3, 28.7E+3	1.0	80	55-68.4	3.3-6.9
HPT_FR III	0.25, 0.42, 0.52	2.7	13.8E+3, 18.4E+3, 23.0E+3, 28.7E+3	1.1	80	55-68.4	3.3-6.9
HPT_FR IV	0.25, 0.42, 0.52	2.7	11.1E+3, 18.5E+3, 23.1E3	0.89	65	40.5-53.4	3.3-6.9
HPT_FR V	0.25, 0.42, 0.52	2.7	11.1E+3, 18.5E+3, 23.1E3	1.0	65	40.5-53.4	3.3-6.9
HPT_FR VI	0.25, 0.42, 0.52	2.7	11.1E+3, 18.5E+3, 23.1E+3	1.1	65	40.5-53.4	3.3-6.9

Table 3.6: Horizontal pipe tests *(HPT_US: Horizontal pipe tests under saturated; HPT_FR –*
Horizontal pipe tests flow rate).

3.4.7 Effects of two-phase on the heat transfer coefficient in the boiler primary heat exchanger coil

Tests were done to analyse the effect of the presence of the second phase on the heat transfer coefficient in the primary heat exchanger. This was necessary due to the known effects that the presence of the second phase has on the heat transfer coefficient in boiling mechanisms (Naphon and Wongwises, 2006). The use of a commercial boiler did not permit the installation of a precision gas volume flow rate meter at the boiler unit gas supply side. This investigation was therefore done through the stabilization of the boiler return temperature, through the use of the electromagnetic heating load tap. The boiler power settings were then incremented from a minimum rating of 7 kW to the maximum of 19 kW through the use of the electronic control panel. The exit temperature setting on the boiler controller was set at its maximum for all the experiments conducted. Therefore, the actual system fluid flow bulk temperature fluctuated according to the power setting used, thus increasing with an incremental increase in the power setting. The resultant power output for different experimental conditions was calculated through the data collected for the bulk fluid exit temperature and the system mass flow rate. Two tests were conducted at different saturation ratios the lower being the minimum saturation level and the higher being the maximum saturation level observed in such systems. Table 3.7 tabulates the tests conducted in this experiment.

Test	Saturation ratio at flow line bulk fluid conditions (-)	Boiler power setting (kW)	Boiler return temperature (^{o}C)	System pressure (abs) (Bars)	System flow rate (L/min)	System flow temp. (^{o}C)
HET I	0.80-0.92	7-19	50	2.7	12.5	59-76
HET II	1.01-1.10	7-19	50	2.7	12.5	59-76

Table 3.7: Heat transfer tests *(HET: Heat exchanger tests).*

3.5 Data reduction

The objective of this work is to study the phenomenon of the presence of a second phase in domestic central heating systems. Hence as part of this research,

a number of parameters were calculated. The heat flux, boiler wall temperature, saturation ratio, bubble production and nucleation rates could not be measured directly. Therefore, a number of calculations were done to estimate these parameters through a data reduction method. This section presents the detailed equations used to calculate these parameters.

3.5.1 Heat flux

The heat flux, being the rate of heat transfer through the primary heat exchanger tube wall per unit area, is calculated through the use of Eq. (3.1). This is based on the first law of thermodynamics that provides the definition for heat flow. Rohsenow et al. (1988) refer to this method of calculating the heat flux as the temperature gradient method. Therefore, assuming a constant heat flux at the primary heat exchanger wall, Eq. (3.1) is a function of the measured system mass flow rate, temperature difference between the inlet and outlet to the primary heat exchanger, the fluid properties and the total surface area of the heating tubes in the primary heat exchanger.

$$q = \frac{\dot{m}\, C_p \Delta T}{A_t} \tag{3.1}$$

where $\dot{m}$ is the mass flow rate, C_p is the specific heat capacity for water at the bulk fluid temperature, ΔT is the difference between the flow and return fluid temperatures to the primary heat exchanger and A_t is the surface area of the heating tubes in the primary heat exchanger.

The mass flow rate in Eq. (3.1) is calculated from the measured system volume flow rate in litres per minute through the use of Eq. (3.2).

$$\dot{m} = \frac{\dot{V}\, \rho}{6x10^4} \tag{3.2}$$

where $\dot{V}$ is the system volumetric flow rate in L/min and ρ is the density of water in kg/m^3, at the measured bulk fluid temperature.

The primary heat exchanger heating tube surface area (water side) was calculated through Eq. (3.3):

$$A_t = P_{ts}\pi D_{bc} n_c \tag{3.3}$$

where P_{ts} is the perimeter of the rectangular tube section, D_{bc} is the mean diameter of the helical coil structure and n_c is the number of coils.

The tube wetted perimeter was calculated through Eq. (3.4).

$$P_{ts} = 2\pi r_t + d_t L_t \tag{3.4}$$

where r_t, d_t and L_t are illustrated in Fig. 3.16.
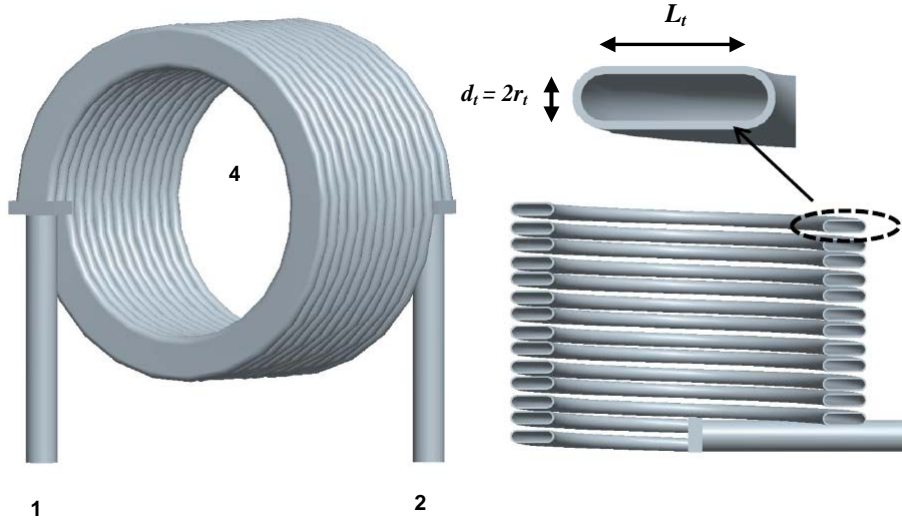
1. Water return
2. Water outlet
3. Sectional view of rectangular heating tubes
4. Location of gas fired burner

Figure 3.16: Primary heat exchanger assembly and rectangular tube sectional diagram.

3.5.2 Water side wall temperature in the boiler primary heat exchanger

The water side wall temperature of the heat exchanger was calculated through energy balance as given by Eq. (3.5). This is a function of the measured bulk fluid temperature and the calculated water side heat transfer coefficient.

$$q = h(T_w - T_b) \tag{3.5}$$

where h is the water side heat transfer coefficient, T_w is the wall temperature and T_b is the bulk fluid temperature. The water side heat transfer coefficient was calculated using Eq. (3.6), a correlation for predicting the Nusselt number in

heating tubes in a helical coil structure for single-phase flow, and Eq. (3.7) for predicting the heat transfer coefficient (Xin and Ebadian, 1997). The correlation for single-phase flow was assumed valid for the present study following the experimental tests as described in Section 3.4.7. Hence experiments were done to analyse any effects that the presence of micro bubbles on the primary heat exchanger water side wall could have on the overall heat transfer coefficient. Fig. 3.17 illustrates the results whereby no change in the power output is evident with under and super saturation flow line conditions for all system power settings. Naphon and Wongwises (2006), reported that two-phase heat transfer characteristics have been rarely reported for helical tube heat exchangers. Furthermore, the existing studies have been done on boiling conditions (Owhadi et al., 1968; Guo et al., 2001), resulting in a significantly different two-phase regime from the present study. Boiling is known to result in a general enhancement of the heat transfer coefficient due to three principal mechanisms, these being; the enhanced liquid agitation adjacent to the vapour bubbles on the heat exchanger wall; the vapour liquid exchange where bubbles break up the superheated layer on the boiler wall, enhancing the transfer of heat to the bulk fluid; and the vapour evaporation through bubbles on the heat exchanger wall (Dhir, 1998).

◇ Bulk fluid SR at flow line conditions 0.80-0.92   + Bulk fluid SR at flow line conditions 1.0-1.1
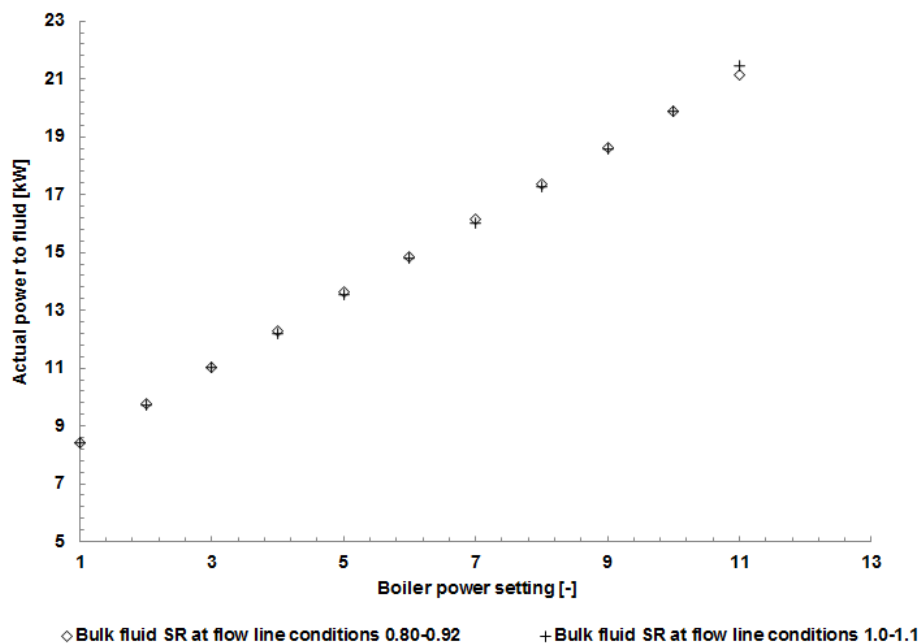
Figure 3.17: Power to fluid with boiler setting with system gas concentration levels at flow line conditions.

Hence, the presence of small gas bubbles rather than vapour bubbles and the low bubble counts and resultant void fractions on the heat exchanger wall could be attributed to the results illustrated in Figure 3.17, whereby single-phase characteristics are expected for under sand super saturation system conditions.

$$Nu = 0.00619 Re^{0.92} Pr^{0.4} (1 + 3.455 \frac{D_h}{D_{bc}}) \tag{3.6}$$

where; $5 \times 10^3 < Re < 10^5$; $0.7 < Pr < 5$; $0.0267 < \frac{D_h}{D_{bc}} < 0.0884$

where Re is the bulk fluid Reynolds number, Pr is the Prandtl number, D_h is the tube hydraulic diameter and D_{bc} is the mean helical coil diameter. The hydraulic diameter was calculated using Eq. (3.7)

$$D_h = \frac{4A_{ts}}{P_{ts}} \tag{3.7}$$

where P_{ts} is the tube wetted perimeter and A_{ts} is the heating tube cross sectional area. The tube cross sectional area was calculated through Eq. (3.8).

$$A_{ts} = \pi r_t^2 + d_t L_t \tag{3.8}$$

where the dimensions r_t, d_t and L_t are illustrated in Fig. 3.17. Hence, Eq. (3.9) was used to calculate the water side heat coefficient;

$$h = \frac{kNu}{D_h} \tag{3.9}$$

where k is conductivity of water at the bulk fluid temperature, Nu is the calculated Nusselt number and D_h is the tube hydraulic diameter.

3.5.3 Saturation ratio

The saturation ratio at the primary heat exchanger wall conditions and at the bulk fluid conditions was calculated through the method reported by Gerrard (1976) and Lubetkin and Blackwell (1988). This method requires the measurement of the total dissolved gas pressure through the use of the *TGM*. The gas partial pressure, P_g, was calculated through the subtraction of the vapour pressure of water at the relevant fluid temperature using Eq. (3.10).

$$P_g = P_{TGM} - P_v \tag{3.10}$$

where P_{TGM} is the total gas pressure and P_v is the vapour pressure of water at the measured water temperature.

The actual dissolved gas concentration, C_g (Eq. 3.11), was calculated using the Bunsen nitrogen gas solubility coefficients extrapolated for the relevant fluid temperature as reported by Schäfer and Lax (1962).

$$C_g = P_g X_g^T \tag{3.11}$$

where, X_g^T is the Bunsen nitrogen gas solubility coefficient calculated at the *TGM* fluid temperature.

As reported by Lubetkin and Blackwell (1988), at saturation conditions, the total gas pressure is assumed to be equal to the system pressure at bulk fluid conditions less the vapour pressure of water at the relevant fluid temperature. Therefore, the saturation gas concentration was calculated using Eqs. (3.12) and (3.13).

$$P_{sat} = P_{sys} - P_v \tag{3.12}$$

$$C_{sat} = P_{sat} X_{sat}^T \tag{3.13}$$

where P_{sys} is the system pressure and X_{sat}^T is the Bunsen dissolved gas coefficient at the system fluid temperature.

Eq. (3.14) was then used to calculate the resultant saturation ratio.

$$\alpha = \frac{C_g}{C_s} \tag{3.14}$$

The saturation ratio at the primary heat exchanger wall was calculated through the use of the relevant wall temperature for the calculation of the vapour pressure and Bunsen coefficients.

3.5.4 Bubble production rate

This calculation was necessary to calculate the system bubble production rate with system conditions. Therefore, assuming no slip conditions, and therefore assuming the two phases are at the same velocity, the experimental system bubble production rate was calculated through the use of Eq. (3.19) using the

results obtained in the experiments discussed in Sections 3.4.4 and 3.4.5. The bubble production rate equation (Eq. 3.19), is a function of the measured bubble count, as an output from the image processing software, the sight glass length and width, the image sample volume, width and the fluid velocity. Hence, Eq. (3.19) was derived through the extrapolation of the measured bubble concentration in the sample volume to a representative volume flowing through the sight glass over a period of time dependent on the bulk fluid velocity. This was then extrapolated to a standard period of one second. The representative volume after extrapolation is illustrated in the side view in Fig. 3.18. The derivation of Eq. (3.19) is given through Eqs. (3.15-3.18).

The image sample volume was calculated through Eq. (3.15):

$$V_{sv} = W_{si}^2 DF \tag{3.15}$$

where W_{si} is the width of the sample image thus representing the distance the fluid travelled during the time period under consideration and DF is the depth of field.

The bubble count recorded in the sample images was extrapolated for the representative volume, as illustrated in Fig. 3.18, through the application of Eq. (3.16). This equation is a simple proportion whereby the sample volume analysed is extrapolated to a representative section across the sight glass depth as illustrated in Fig. 3.18.

$$Bubble\ count\ extrapolation\ to\ rep\ volume = \left[\frac{B_c\ W_{sg} L_{sg} W_{si}}{V_{sv}}\right] \tag{3.16}$$

where B_c is the mean bubble count per sample image, W_{sg} and L_{sg} are the width and length of the sight glass section as illustrated in Fig. 3.18 (plan view).

The time for the volume of water and the second phase to flow through the sample volume was calculated through Eq. (3.17)

$$t = \frac{W_{si}}{v_{sg}} \tag{3.17}$$

where, v_{sg} is the velocity of the bulk fluid flowing through the sight glass.

The average bulk fluid velocity was calculated through the use of Eq. (3.18), which is a function of the pipe cross sectional area and measured volume flow rate.

$$v_{sg} = \frac{V}{60 L_{sg} W_{sg}} \qquad \text{(3.18)}$$

where V is the measured system volume flow rate. Therefore, the inverse of Eq. (3.17) was used to extrapolate the bubble count in the representative volume as calculated through Eq. (3.19) to a standard period of one second.

$$PR = \left[\frac{B_c\, W_{sg} L_{sg} W_{si}}{V_{sv}} \right] \left[\frac{v_{sg}}{W_{si}} \right] \qquad \text{(3.19)}$$

The final equation used to calculate the bubble production rate is given in Eq. (3.20).

$$PR = \left[\frac{B_c W_{sg} L_{sg} v_{sg}}{V_{sv}} \right] \qquad \text{(3.20)}$$
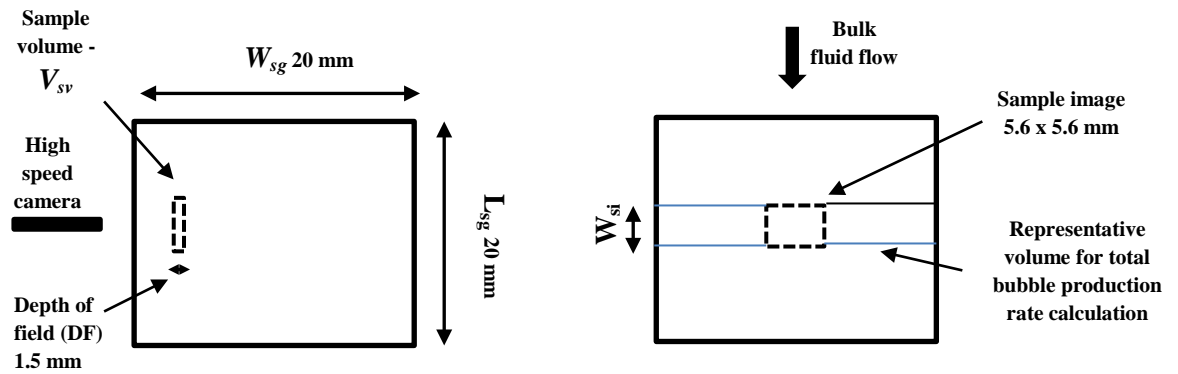
Figure 3.18: Sample volume and sight glass section plan (left) and side view (right).

3.5.5 Gas volume production rate

The total volume of gas produced was derived through the calculation of the average bubble volume in each sample image analysed. Therefore considering the bubble shape results discussed in Section 4.3.3, thus assuming spherical bubbles, the volume per bubble recorded was calculated using Eq. (3.21).

$$V_b = \left[\frac{\pi D_b^3}{6} \right] \qquad \text{(3.21)}$$

where, D_b is the measured bubble diameter. The equation derived for the bubble production rates in Section 3.5.4 was then used to calculate the overall volume of air produced by the system per unit time as in Eq. (3.22).

$$V_T = \left[\frac{V_{ba} W_{sg} L_{sg} v_{sg}}{V_{sv}} \right]$$
(3.22)

where V_{ba} is the average bubble volume per image.

3.5.6 Volumetric void fraction

This resultant fluid volumetric void fraction was calculated through the ratio between the mean volume of bubbles per image and the image sample volume. Hence, the resultant equation is given in Eq. (3.23).

$$\varepsilon_v = \left[\frac{V_{ba}}{V_{sv}} \right]$$
(3.23)

A cumulative void fraction was also calculated based on the total bubble diameters and sample images analysed.

3.5.7 Bubble nucleation rates

The bubble nucleation rate was calculated as a function of the bubble production rate as calculated in Eq. (3.20) and the primary heat exchanger surface area under super saturation conditions. As illustrated in Fig. 3.19, a linear relationship between the bulk fluid temperature in the heat exchanger tubes and the wall temperature was assumed (Prabhanjan et al., 2002). The point at which super saturation conditions occur was calculated through an iterative method thus calculating the primary heat exchanger wall temperature resulting in a saturation ratio of 1, using Eq. (3.14).

The ratio of the heat exchanger tube relative length calculated from the primary heat exchanger's flow side at which super saturation conditions occur in relation to the total tube relative length was calculated through Eq. (3.24).

$$AR_{ss} = \left[\frac{T_{wo} - T_{wsat}}{T_{wo} - T_{wr}} \right]$$
(3.24)

where, T_{wo} is the wall temperature at the exit, T_{wsat} is the wall temperature at which saturation conditions are present, T_{wr} is the wall temperature at the return side.
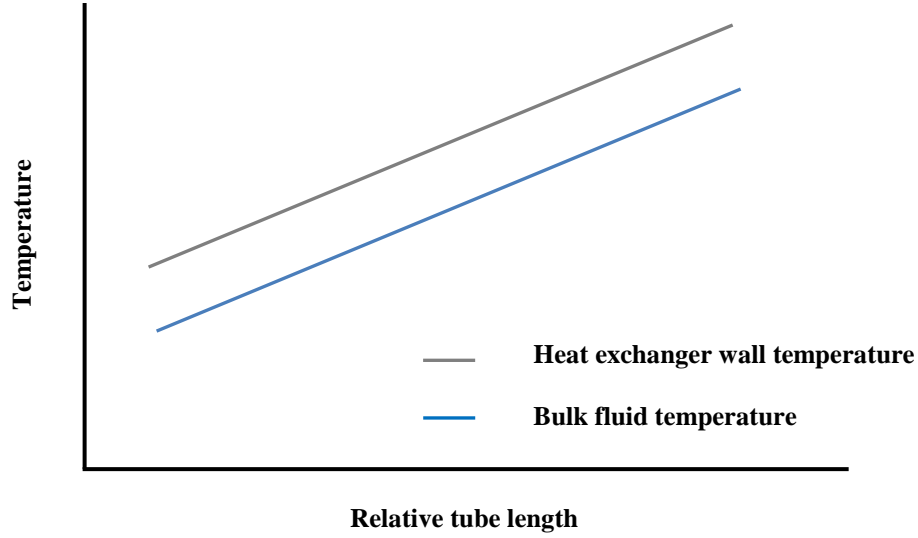
Figure 3.19: Bulk fluid temperature and primary heat exchanger wall temperature profile.

Therefore, through the knowledge of AR_{ss} the heat exchanger area under super saturation conditions was calculated as in Eq. (3.25).

$$A_{ss} = AR_{ss}A_t \tag{3.25}$$

where, A_t is the heat exchanger tube surface area. Hence, the bubble nucleation rate at the primary heat exchanger wall was calculated through the adaptation of Eq. (3.20) as in Eq. (3.26).

$$N = \left[\frac{B_c W_{sg} L_{sg} v_{sg}}{V_{sv} A_{ss}}\right] \tag{3.26}$$

3.6 Uncertainty of a measured or derived parameter

This research required the calculation of a number of results, in this text referred to as *y*, that are a function of a number of independent variables that in turn are a function of a number of measured parameters. A case in point is the heat flux that is a function of the measured return and flow temperatures to the boiler, the measured coil diameter and length and the mass flow rate. Therefore, the resultant uncertainty in the output *y* would be dependent on a number of independent variables X_n as summarized through Eq. (3.27).

$$y = f(X_1, X_2, \ldots \ldots \ldots X_n) \tag{3.27}$$

The resultant error in a measured quantity is dependent on the sum of the systematic errors, referred to as bias and the random errors referred to as precision. The former are repeatable and thus fixed. They usually originate from a fault in the measuring instruments. Such errors can be reduced by the calibration of the same instruments. Random errors are not repeatable and originate from uncontrolled influences while the experiment is in progress. Such errors can be reduced through an increase in the sample size. Coleman and Steele (1999) stated that for a variable *y* defined by Eq. (3.27), which is dependent on a number *n* of measured variables *X*, the relative uncertainty can be calculated using Eq. (3.28). The term U_{Xn} refers to the errors due to the measuring instruments originating through the process of data acquisition and calibration. Such errors can be derived from the specifications provided by the manufacturer or from calibration done in the laboratory.

$$\frac{U_r^2}{y^2} = \left[\frac{X_1}{y}\frac{\partial y}{\partial X_1}\right]^2 \left[\frac{U_{X_1}}{X_1}\right]^2 + \left[\frac{X_2}{y}\frac{\partial y}{\partial X_2}\right]^2 \left[\frac{U_{X_2}}{X_2}\right]^2 + \left[\frac{X_n}{y}\frac{\partial y}{\partial X_n}\right]^2 \left[\frac{U_{X_n}}{X_n}\right]^2 \tag{3.28}$$

Table 3.8 tabulates the ranges of the experimental parameters while the uncertainties for all the measured parameters are tabulated in Table 3.9.

Calculated parameter	Range
Heat flux, (kW / m^2)	18 – 52
Primary heat exchanger wall temperature (^{o}C)	52 - 95
Saturation ratio, (-)	0.80 – 1.20
Bubble production rate, (Bubbles/s)	784 - 6920
Gas volume production rate, (L / min)	0.03-0.47 L/hour
Volumetric void fraction, (-)	1E-6 - 2xE-3
Bubble nucleation rate (bubbles / cm^2 s)	0 – 4

Table 3.8: Range of experimental parameters.

The K-type thermocouples were calibrated through the use of standard calibrating equipment. A calibrating bath equipped with a refrigerator unit (RCTB 3050), supplied by Omega and working in the temperature range of -20 ^{o}C and 80 ^{o}C was used. A platinum (Pt 10) resistance probe, supplied by

Automatic Systems Laboratories (ASL – A division of Hartest Precision Instruments) was used as a standard thermometer. Thermocouple calibration charts are illustrated in Figs. A2 – A8 in Appendix III. The resultant calibration equations were inputted in the LabVIEW block diagram as illustrated in Fig. A1 in Appendix I. The maximum error of the K-Type thermometer amounts to 0.01K and is capable of measuring a maximum temperature of 250 ^{o}C. Therefore, the uncertainty analysis of each temperature sensor consists of the summation of errors due to the data logger, calibration system and curve fitting equations. The results are summarised in Table 3.9.

Measured parameter	Measuring instrument	Uncertainty (%)
Boiler tube inner dimensions – Width	Vernier caliper	± 1.72 % (Manufacturer)
Boiler tube inner dimensions – Length	Vernier caliper	± 0.57 % (Manufacturer)
Boiler helical structure diameter	Tape meter	± 0.55 % (Manufacturer)
T1 - Fluid temperature T2 - Fluid temperature T3 - Fluid temperature T4 - Fluid temperature T5 - Fluid temperature T6 - Fluid temperature T7 - Fluid temperature	K-type thermocouples	± 0.46 % ± 0.30 % ± 0.28 % ± 0.24 % ± 0.22 % ± 0.35 % ± 0.13 % (Calibration)
System pressure (P1/2/3)	DRUCK PTX 7500	± 1.5% (Manufacturer)
Gas partial pressure	Total Dissolved Gas Measuring Instrument (*TGM*)	±1.1% (Calibration)
Volumetric flow rate	Electromagnetic flow meter – Electromag 500 Series	± 0.066% (Manufacturer)
Bubble concentration per sample image	Image-Pro Analyser	± 10 % (Calibration)
Bubble size	Image-Pro Analyser	6% (Calibration)
Bubble diameter / Sample image dimensions	Manual analysis using the Vision Research Phantom V5 high speed camera software	± 3 % (Calibration)
Focal depth	Vernier caliper	± 15 % (Manufacturer)
Sight glass dimensions (internal)	Vernier caliper	± 0.5 % (Manufacturer)
Dissolved hydrogen sensor	Orbisphere 3654	± 1 % (Manufacturer)
Dissolved oxygen sensor	Orbisphere 3655	± 1% (Manufacturer)

Table 3.9: Uncertainty value in the measured parameters.

The *TGM* pressure sensor was calibrated through the use of a dead weight calibration jig (Fig. A9 in Appendix III). The camera images were scaled using a

number of standard sized gauges followed by the subsequent scaling. The scaled images were validated through the use of steel ball bearings which were measured using a micrometre gauge. The ball bearings were suspended in a water filled sight glass. A frame size of 5.62x5.62 mm was used and the depth of field was limited to approximately 1.5 mm. The depth of field was determined through the use of a precision vertical movement rack, coupled to a Vernier Calliper that was used to establish when a number of pre-defined objects were in and out of focus with the measured vertical movement of the camera.

3.6.1 Heat flux

The heat flux is calculated through the use of Eq. (3.1). This is a function of the resultant mass flow rate, temperature difference between the inlet and outlet to the primary heat exchanger, fluid properties and the area of the primary heat exchanger heating tubes. Hence the propagated uncertainty in the heat exchanger area calculation was initially calculated followed by the uncertainty in the heat flux. The primary heat exchanger's heating tubes surface area was calculated through Eq. (3.3) which is a function of the tube cross sectional perimeter, the helical coil diameter and the number of coils. Assuming that no error was done in the measurement of the number of coils, the percentage uncertainty in the heating tubes surface area calculation was calculated through Eq. (3.29) as simplified through Eq. (3.30). Hence, Table 3.10 represents the primary heat exchanger tube area used in the current study with the calculated uncertainty values.

$$U_{A_t} = \sqrt{\left[\frac{P_{ts}\pi D_{bc}n_c}{A_t}\right]^2 U_{P_{ts}}^2 + \left[\frac{D_{bc}P_{ts}\pi n_c}{A_t}\right]^2 U_{D_{bc}}^2} \qquad \textbf{(3.29)}$$

Simplified as:

$$U_{A_t} = \sqrt{U_{P_{ts}}^2 + U_{D_{bc}}^2} \qquad \textbf{(3.30)}$$

Measured parameters	Area	Uncertainty (%)
Tube section perimeter and number of coils and helical coil diameter (assembly)	4399 cm^2	± 1.89

Table 3.10: Uncertainty values in heating tube surface area calculation.

Assuming there is no uncertainty in the specific heat capacity for water C_p, the relative uncertainty of the heat flux was calculated through the application of Eq. (3.1), as in Eq. (3.31), simplified in Eq. (3.32). This was done for the two extreme values of the heat flux used in the present study.

$$U_q = \sqrt{\left[\frac{\dot{m}C_p\Delta T}{qA_t}\right]^2 U_{\dot{m}}^2 + \left[\frac{\Delta T\dot{m}C_p}{qA_t}\right]^2 U_{\Delta T}^2 + \left[-\frac{A_t\dot{m}C_p\Delta T}{qA_t^2}\right]^2 U_{A_t}^2}$$ (3.31)

$$U_q = \sqrt{U_{\dot{m}}^2 + U_{\Delta T}^2 + U_{A_t}^2}$$ (3.32)

Hence, Table 3.11 represents the heat flux range used in the current study with the uncertainty values.

Measured parameters	Heat flux range	Uncertainty (%)
Temperature at inlet and exit to the heat exchanger, mass flow rate, tube diameter and length	18 – 52 kW	± 1.93

Table 3.11: Uncertainty values in heat flux.

3.6.2 Primary heat exchanger wall temperature

The water side wall temperature of the heat exchanger was calculated through energy balance as given by Eq. (3.5). This is a function of the measured bulk fluid temperature at the inlet and exit to the primary heat exchanger and the calculated water side heat transfer coefficient (Bejan, 1993). The latter was calculated through Eq. (3.6), using a correlation for predicting the Nusselt number in helical coils and through Eq. (3.9) for predicting the heat transfer coefficient. Xin and Ebadian (1997), reported that their correlation for the prediction of the Nusselt number for helical coils predicted their experimental data with a mean absolute error of ± 6%. The calculation of the wall temperature uncertainties through the adaptation of Eq. (3.5) required the calculation of the uncertainties in the tube hydraulic diameter and the heat transfer coefficient.

The hydraulic diameter was calculated through the use of Eq. (3.7). This is a function of rectangular tube cross sectional area and the wetted perimeter. As illustrated in Fig. 3.17, the tube hydraulic diameter was calculated through the measurement of dimension L_t and d_t through the use of a Vernier Calliper.

Therefore, Eq. (3.7) requires a calculation of the relative uncertainty in the tube cross sectional area and the wetted perimeter calculations.

The tube cross sectional area was calculated through the application of Eq. (3.8) which is a function of the tube dimensions as illustrated in Fig. 3.17. Hence, the relative uncertainty of the tube cross sectional area was calculated through Eq. (3.33).

$$U_{A_{ts}} = \sqrt{\left[\frac{2\pi r_t^2}{A_{ts}}\right]^2 U_{r_t}^2 + \left[\frac{d_t L_t}{A_{ts}}\right]^2 U_{d_t}^2 + \left[\frac{L_t d_t}{A_{ts}}\right]^2 U_{L_t}^2} \tag{3.33}$$

The tube wetted perimeter was calculated through the application of Eq. (3.4) which is also a function of the dimensions of the tube section as illustrated in Fig. 3.17. Hence, the relative uncertainty of the tube wetted perimeter was calculated through Eq. (3.34).

$$U_{P_{ts}} = \sqrt{\left[\frac{r_t 2\pi}{P_{ts}}\right]^2 U_{r_t}^2 + \left[\frac{d_t L_t}{P_{ts}}\right]^2 U_{d_t}^2 + \left[\frac{L_t d_t}{P_{ts}}\right]^2 U_{L_t}^2} \tag{3.34}$$

Therefore, the relative uncertainty of the hydraulic diameter was calculated through the application of Eq. (3.7), as in Eq. (3.35), simplified through Eq. (3.36).

$$U_{D_h} = \sqrt{\left[\frac{A_{ts}4}{D_h P_{ts}}\right]^2 U_{A_{ts}}^2 + \left[-\frac{P_{ts}4A_{ts}}{D_h P_{ts}^2}\right]^2 U_{P_{ts}}^2} \tag{3.35}$$

Simplified as:

$$U_{D_h} = \sqrt{U_{A_{ts}}^2 + U_{P_{ts}}^2} \tag{3.36}$$

Hence, Table 3.12 represents the hydraulic diameter measured in the current study with the calculated uncertainty values.

Measured parameters	Hydraulic diameter	Uncertainty (%)
Tube width, length	7.9 mm	± 1.68

Table 3.12: Uncertainty values in the hydraulic diameter calculation.

Using the uncertainties as tabulated in Table 3.12, the uncertainty for the Nusselt number correlation (Xin and Ebadian, 1997) and assuming that there is no uncertainty in the thermal conductivity for water k, the relative uncertainty of the heat transfer coefficient was calculated through the Eq. (3.37), as simplified in Eq. (3.38).

$$U_h = \sqrt{\left[\frac{Nuk}{hD_h}\right]^2 U_{Nu}^2 + \left[-\frac{D_h Nuk}{hD_h^2}\right]^2 U_{D_h}^2} \tag{3.37}$$

Simplified as:

$$U_h = \sqrt{U_{Nu}^2 + U_{D_h}^2} \tag{3.38}$$

Therefore, rearranging Eq. (3.5) to calculate the wall temperature, the relative uncertainty of the primary heat exchanger water side wall temperature was calculated through Eq. (3.39) as simplified in Eq. (3.40).

$$U_{T_w} = \sqrt{\left[\frac{q}{T_w h}\right]^2 U_q^2 + \left[-\frac{hq}{T_w h^2}\right]^2 U_h^2 + \left[\frac{T_b}{T_w}\right]^2 U_{T_b}^2} \tag{3.39}$$

Simplified as:

$$U_{T_w} = \sqrt{\left[\frac{q}{q+hT_b}\right]^2 (U_q^2 + U_h^2) + \left[\frac{hT_b}{q+hT_b}\right]^2 U_{T_b}^2} \tag{3.40}$$

Hence, Table 3.13 tabulates the wall temperature range covered in the current study with the calculated uncertainty values.

Measured parameters	Wall temperature range	Uncertainty (%)
Heat flux, bulk fluid temperature, tube hydraulic diameter	52 - 95 ^{o}C	± 0.75

Table 3.13: Uncertainty values in the boiler wall temperature calculation.

3.6.3 Saturation ratio

The saturation ratio at the primary heat exchanger wall conditions and bulk fluid conditions is calculated through Eqs. (3.10-3.14) that are a function of the properties of dissolved gases, water, total gas pressure and the fluid temperature.

Assuming that the uncertainty for the vapour pressure data for water P_v, and the gas solubility Bunsen Coefficients, X_g^T, is due to the uncertainty of the thermocouples measuring the temperatures used to extrapolate the values for P_v and X_g^T, the relative uncertainty for the partial gas pressure and the actual gas concentration was calculated through the application of Eqs. (3.10 & 3.11) as in Eqs. (3.41 & 3.42). The latter is simplified through Eq. (3.43).

$$U_{P_g} = \sqrt{\left[\frac{P_{TGM}}{P_g}\right]^2 U_{P_{TGM}}^2 + \left[-\frac{P_v}{P_g}\right]^2 U_{P_v}^2} \tag{3.41}$$

$$U_{C_g} = \sqrt{\left[\frac{P_g X_g^T}{C_g}\right]^2 U_{P_g}^2 + \left[\frac{X_g^T P_g}{C_g}\right]^2 U_{X_g^T}^2} \tag{3.42}$$

Simplified as:

$$U_{C_g} = \sqrt{U_{P_g}^2 + U_{X_g^T}^2} \tag{3.43}$$

Likewise, the relative uncertainty of the gas concentration at saturation conditions is calculated through the application of Eqs. (3.12 & 3.13) as in Eqs. (3.44 & 3.45). The latter is simplified through Eq. (3.46).

$$U_{P_{sat}} = \sqrt{\left[\frac{P_{sys}}{P_{sat}}\right]^2 U_{P_{sys}}^2 + \left[-\frac{P_v}{P_{sat}}\right]^2 U_{P_v}^2} \tag{3.44}$$

$$U_{C_s} = \sqrt{\left[\frac{P_{sat} X_{sat}^T}{C_s}\right]^2 U_{P_{sat}}^2 + \left[\frac{X_{sat}^T P_{sat}}{C_s}\right]^2 U_{C_g}^2} \tag{3.45}$$

Simplified as:

$$U_{C_s} = \sqrt{U_{P_{sat}}^2 + U_{X_{sat}^T}^2} \tag{3.46}$$

Hence, the relative uncertainty of the saturation ratio is calculated through the application of Eq. (3.14) through the incorporation of the uncertainty calculated for the actual gas concentration and the gas concentration at saturation conditions as in Eq. (3.47), simplified through Eq. (3.48).

$$U_\alpha = \sqrt{\left[\frac{C_g}{\alpha C_s}\right]^2 U_{C_g}^2 + \left[-\frac{C_s C_g}{\alpha C_s^2}\right]^2 U_{C_s}^2}$$ (3.47)

Simplified as:

$$U_\alpha = \sqrt{U_{C_g}^2 + U_{C_s}^2}$$ (3.48)

Hence, Table 3.14 tabulates the saturation ratio range covered in the current study with the calculated uncertainty values.

Measured parameters	Saturation ratio range	Uncertainty (%)
Fluid temperature at *TGM*, primary heat exchanger wall or bulk fluid and total gas pressure	0.80 – 1.20	± 2.05

Table 3.14: Uncertainty values in the calculation of the saturation ratio.

3.6.4 System bubble production rate

Assuming no slip conditions, the experimental bubble production rate was calculated through the use of Eq. (3.19). This is a function of the measured bubble concentration, as an output from the image processing software; the sample volume and width and the fluid velocity in the sight glass section. Hence the latter uncertainties were initially calculated, followed by the uncertainty for the bubble production rate.

The experimental sample volume was calculated through the use of Eq. (3.15) that is a function of the length and breadth of the sample image and the resultant focal depth. Hence, the percentage uncertainty was calculated through Eq. (3.49) as simplified in Eq. (3.50). Table 3.15 tabulates the calculated uncertainty.

$$U_V = \sqrt{\left[\frac{L_{si} W_{si} F_d}{V_{sv}}\right]^2 U_{L_{si}}^2 + \left[\frac{W_{si} L_{si} F_d}{V_{sv}}\right]^2 U_{W_{si}}^2 + \left[\frac{F_d L_{si} W_{si}}{V_{sv}}\right]^2 U_{F_d}^2}$$ (3.49)

$$U_V = \sqrt{U_{L_{si}}^2 + U_{W_{si}}^2 + U_{F_d}^2}$$ (3.50)

Measured parameters	Volume	Uncertainty (%)
Length and width of sample image and focal depth	47.38 mm^3	± 7.93

Table 3.15: Uncertainty values in sample volume.

The average bulk fluid velocity was calculated through the use of Eq. (3.18), which is a function of the pipe cross sectional area and the measured volume flow rate. Hence, Eq. (3.51), simplified through Eq. (3.52) was used to calculate the uncertainties in the fluid velocity. Table 3.16 represents the velocity range covered in the current study with the calculated uncertainty values.

$$U_v = \sqrt{\left[\frac{V}{v_{sg}L_{sg}W_{sg}}\right]^2 U_V^2 + \left[-\frac{L_{sg}V}{v_{sg}L_{sg}^2W_{sg}}\right]^2 U_{L_{sg}}^2 + \left[-\frac{W_{sg}V}{v_{sg}L_{sg}W_{sg}^2}\right]^2 U_{W_{sg}}^2} \qquad (3.51)$$

$$U_v = \sqrt{U_V^2 + U_{L_{sg}}^2 + U_{W_{sg}}^2} \qquad (3.52)$$

Measured parameters	Velocity range	Uncertainty (%)
Length and width of sight glass and volumetric flow rate	0.19 – 0.52 m/s	± 0.71

Table 3.16 Uncertainty values in bulk fluid velocity in sight glass.

The relative uncertainty of the system bubble production rate was calculated through the application of Eq. (3.20), as in Eq. (3.53) simplified through Eq. (3.54).

$$U_{PR} =$$

$$\sqrt{\begin{array}{c}\left[\frac{B_cW_{sg}L_{sg}v_{sg}}{PRV_{sv}}\right]^2 U_{B_c}^2 + \left[\frac{W_{sg}B_cL_{sg}v_{sg}}{PRV_{sv}}\right]^2 U_{W_{sg}}^2 + \left[\frac{L_{sg}B_cW_{sg}v_{sg}}{PRV_{sv}}\right]^2 U_{L_{sg}}^2 + \\ \\ \left[\frac{v_{sg}B_cW_{sg}L_{sg}}{PRV_{sv}}\right]^2 U_{v_{sg}}^2 + \left[-\frac{V_{sv}B_cW_{sg}L_{sg}v_{sg}}{PRV_{sv}^2}\right]^2 U_{V_{sv}}^2\end{array}} \qquad (3.53)$$

Simplified as:

$$U_{PR} = \sqrt{U_{B_c}^2 + U_{W_{sg}}^2 + U_{L_{sg}}^2 + U_{v_{sg}}^2 + U_{V_{sv}}^2} \qquad (3.54)$$

Table 3.17 represents the bubble production rate covered in the current study with the uncertainty values.

Measured parameters	Bubble production rate range	Uncertainty (%)
Length and width of sight glass, volumetric flow rate and automated bubble counts	784 – 6920 Bubbles/ s	± 12

Table 3.17: Uncertainty values in the bubble production rate calculation.

3.6.5 Gas volume production rate

The bubble gas volume production rate was calculated through Eq. (3.22) which is a function of the average bubble volume per image and the calculated bubble production rate. Hence, the uncertainty for the average bubble volume per image was calculated through the application of Eq. (3.55), this being a function of the measured mean bubble count per sample image and the mean bubble diameter. The resultant uncertainty in the bubble volume per sample image was calculated through Eq. (3.56), simplified through Eq. (3.57).

$$V_{ba} = \left[\frac{B_c \pi D_b^3}{6}\right] \tag{3.55}$$

$$U_{V_{ba}} = \sqrt{\left[\frac{B_c \pi D_b^3}{6V_{ba}}\right]^2 U_{B_c}^2 + \left[\frac{3D_b B_c \pi D_b^2}{6V_{ba}}\right]^2 U_{D_b}^2} \tag{3.56}$$

Simplified as:

$$U_{V_{ba}} = \sqrt{U_{B_c}^2 + 9U_{D_b}^2} \tag{3.57}$$

Hence, through the use of the uncertainties calculated for the mean bubble volume per sample image and for the bubble production rate as calculated in Section 3.6.4, the uncertainty in the gas volume production rate was calculated through the application of Eq. (3.22), as in Eq. (3.58), simplified through Eq. (3.59). Therefore, Table 3.18 tabulates the calculated uncertainty for the gas volume production rates.

$$U_{V_T} = \sqrt{\left[\frac{PRV_{ba}}{V_T}\right]^2 U_{PR}^2 + \left[\frac{V_{ba}PR}{V_T}\right]^2 U_{V_{ba}}^2}$$ (3.58)

Simplified as:

$$U_{V_T} = \sqrt{U_{PR}^2 + U_{V_{ba}}^2}$$ (3.59)

Measured parameters	Gas volume production range	Uncertainty (%)
Length and width of sample image, focal depth, bubble count and diameter, fluid flow rate.	0.03 – 0.47 L/hour	± 21.6

Table 3.18: Uncertainty values in the calculation of the gas volume production rate.

3.6.6 Volumetric void fraction

The volumetric void fraction was calculated through Eq. (3.23) that is a function of the mean bubble volume per sample volume analysed. Hence, Eq. (3.56), simplified in Eq. (3.57), was used to calculate the uncertainty in the volumetric void fraction, thus incorporating the uncertainties calculated for the mean bubble volume per sample image and the sample volume. The results are tabulated in Table 3.19.

$$U_{\epsilon_v} = \sqrt{\left[\frac{V_{ba}}{\epsilon_v V_{sv}}\right]^2 U_{V_{ba}}^2 + \left[-\frac{V_{sv}V_{ba}}{\epsilon_v V_{sv}^2}\right]^2 U_{V_{sv}}^2}$$ (3.56)

Simplified as:

$$U_{\varepsilon_v} = \sqrt{U_{V_{ba}}^2 + U_{V_{sv}}^2}$$ (3.57)

Measured parameters	Volumetric void fraction range	Uncertainty (%)
Length and width of sample image, focal depth, bubble count and diameter	1E-6 – 2E-3	± 19.67

Table 3.19: Uncertainty values in the calculation of the volumetric void fraction.

3.6.7 Bubble nucleation rate

The bubble nucleation rate was calculated as a function of the bubble production rate as calculated in Eq. (3.20) and the primary heat exchanger surface area under super saturation conditions. Therefore, the propagated uncertainty in the nucleation rate is due to the uncertainties in the bubble production rate and the tube surface area under super saturation conditions. The relative uncertainty in the tube area under super saturation conditions was calculated through the application of Eq. (3.24 & 3.25). Therefore, through the application of Eq. (3.24), Eq. (3.58) was used to calculate the uncertainty in the ratio of the heat exchanger tube surface under super saturation conditions to the total tube relative length.

$$U_{AR_{ss}} = \sqrt{\begin{array}{c} \left[\frac{T_{wo}[T_{wsat} - T_{wr}]}{AR_{ss}[T_{wo} - T_{wr}]^2}\right]^2 U_{T_{wo}}^2 + \left[-\frac{T_{wsat}}{AR_{ss}[T_{wo} - T_{wr}]}\right]^2 U_{T_{wsat}}^2 \\ + \left[-\frac{T_{wr}[T_{wo} + T_{wsat}]}{AR_{ss}[T_{wo} - T_{wr}]^2}\right]^2 U_{T_{wr}}^2 \end{array}} \tag{3.58}$$

Hence, through the application of Eq. (3.25), Eq. (3.59) as simplified in Eq. (3.60) was used to calculate the uncertainty in the actual tube area under super saturation conditions.

$$U_{A_{ss}} = \sqrt{\left[\frac{AR_{ss}A_t}{A_{ss}}\right]^2 U_{AR_{ss}}^2 + \left[\frac{A_t AR_{ss}}{A_{ss}}\right]^2 U_{A_t}^2} \tag{3.59}$$

Simplified as:

$$U_{A_{ss}} = \sqrt{U_{AR_{ss}}^2 + U_{A_t}^2} \tag{3.60}$$

The propagated relative uncertainty of the bubble nucleation rate was calculated through the use of Eq. (3.61) this being a simplification for Eq. (3.26) for the bubble nucleation rate calculation. Therefore, Eq. (3.61) was applied as in Eqs. (3.62), and simplified through Eq. (3.63), to calculate the uncertainty in the nucleation rate.

$$N = \frac{PR}{A_{ss}} \tag{3.61}$$

$$U_N = \sqrt{\left[\frac{PR}{NA_{ss}}\right]^2 U_{PR}^2 + \left[-\frac{A_{ss}PR}{NA_{ss}^2}\right]^2 U_{A_{ss}}^2} \tag{3.62}$$

Simplified as:

$$U_N = \sqrt{U_{PR}^2 + U_{A_{ss}}^2}$$

(3.63)

Table 3.20 tabulates the bubble nucleation range covered in the current study with the uncertainty values.

Measured parameters	Bubble nucleation range	Uncertainty (%)
Length and width of sight glass, volumetric flow rate and automated bubble counts, saturation ratio at the primary heat exchanger wall conditions, tube area under super saturation conditions.	$0.3 - 4$ Bubbles / s cm^2	± 13.1

Table 3.20: Uncertainty values in the calculation of the bubble nucleation rate.

3.7 Summary

This chapter has provided an overview to the design of the test rig, built to investigate typical two-phase flow characteristics in domestic central heating systems. The present study necessitated the design and assembly of a full scale test rig for experimental investigations. A number of experiments were done as part of the investigation in the two-phase flows in domestic central heating systems, with the principal system parameters being, the system flow rate, pressure, heat flux and dissolved gas concentration. A two-phase imaging technique was developed through the use of a high speed camera, high intensity fibre optic light sources and custom made sight glass components. Measuring instruments were installed throughout the system for data collection through the use of an automated data collector. An automated image analysis macro, based on the digitization of images and using the Image-Pro Plus program, was developed as part of this study. All the system instruments and imaging techniques were calibrated using standard methods. A propagated error analysis was completed using standard models, yielding reasonable experimental error values.

CHAPTER 4

Results and Discussion

4.1 Introduction

This chapter presents and discusses the experimental data obtained from the current investigation on the fundamentals of two-phase flow in domestic central heating systems. The results are based on experiments conducted as described in Sections 3.4.1-7 where the principal aim is to analyse the typical bubble characteristics, nucleation and dissolution rates in domestic central heating systems. Results on the dissolved gas composition are also presented and discussed as are the typical flow patterns and measured bubble geometry. Experiments were done in relation to the main five system controlling parameters these being the pressure, heat flux, boiler exit and return temperature, dissolved gas concentration and the system volume flow rate.

It should be mentioned that it was not this study's intention to investigate the long term usage effects on the resultant saturation ratio in a domestic central heating system. Such tests were undertaken at Spirotech bv as part of their industrial research. The expected ratios could be dependent on the type of tap water available at the point of filling. Therefore, it is not the aim of this study to investigate the expected saturation ratios in such systems. Hence, the saturation ratios used in the present study are based on the investigations done by Spirotech and cover the wide range of expected saturation ratios in typical domestic central heating systems.

This chapter is organized as follows; Section 4.2 presents and discusses the dissolved gas composition, Section 4.3 presents and discusses the bubble characteristics at the exit of the boiler, Section 4.4 presents and discusses the bubble production and nucleation rates results, Section 4.5 presents and discusses the bubble dissolution rates and characteristics in horizontal pipes, Section 4.6 presents and discusses the repeatability of our data and Section 4.7 provides a summary for the chapter.

4.2 Dissolved gas composition

The concentrations of dissolved gases were analysed in this study as described in Section 3.4.1. The three gases that are known to predominate in such systems were considered, these being oxygen, hydrogen and nitrogen.

4.2.1 Oxygen gas

Fig. 4.1 illustrates the decay in the dissolved oxygen concentration as a function of time after the system filling with tap water. Upon filling, the average system dissolved oxygen concentration was measured as 7280 PPB equal to 7.2 mg/L water. This concentration suggests that at atmospheric pressure, the tap water used was quasi saturated with oxygen as the oxygen solubility coefficient for water at the measured temperature is 7.9 mg/L water (Gerrard, 1976). Relatively high dissolved oxygen concentrations are expected in water as a result of the fact that circa 21 % of atmospheric air is made up of oxygen gas. It is worth noting that tap water could result in a reduction in the dissolved oxygen concentration when compared to still water exposed to atmospheric air. This is due to the possibility of deaeration in storage tanks and oxidation reactions in the pipework. Therefore, the actual concentration of dissolved oxygen in tap water could depend on the actual supply.

A substantial drop in the oxygen concentration was observed during the first 48 hours after filling, when an average dissolved oxygen concentration of 102 PPB was recorded. After circa 4 days, with a daily system operating time of 8 hours and a flow temperature of 75°C, the dissolved oxygen concentration reduced to 11 PPB. A consistent average concentration of 11 PPB was measured during the subsequent days, thus implying that all oxidation reactions stopped. The system was in operation for circa 8 hours daily. Hence, the water cycled throughout the system in a consistent manner and therefore, the system water volume was in constant contact with the untreated steel surface in the radiator and buffer vessel. Central heating systems are known to incorporate untreated steel surfaces that result in an oxidation or rusting reaction (Heat, 1998).

As indicated in Eq. (2.35) apart from the presence of an exposed steel surface, oxidation requires the presence of both oxygen and water. The latter react to

form ferrous hydroxide that in turn reacts to form ferrous ferrite, water and hydrogen. The formation of black ferrous ferrite as a substitute to the red/brown iron oxide occurs due to the presence of a limited concentration of dissolved oxygen in the water. The presence of heat is also known to increase the rate of oxidation (Davis, 1987). Therefore as reported by Heat (1998) and Lamers (2005), upon filling with fresh tap water, a certain degree of oxidation is expected. This reaction is expected to last until the bulk oxygen content is used up, thus eliminating one of the reactants necessary for the oxidation reaction to take place and consequently terminating the reaction.
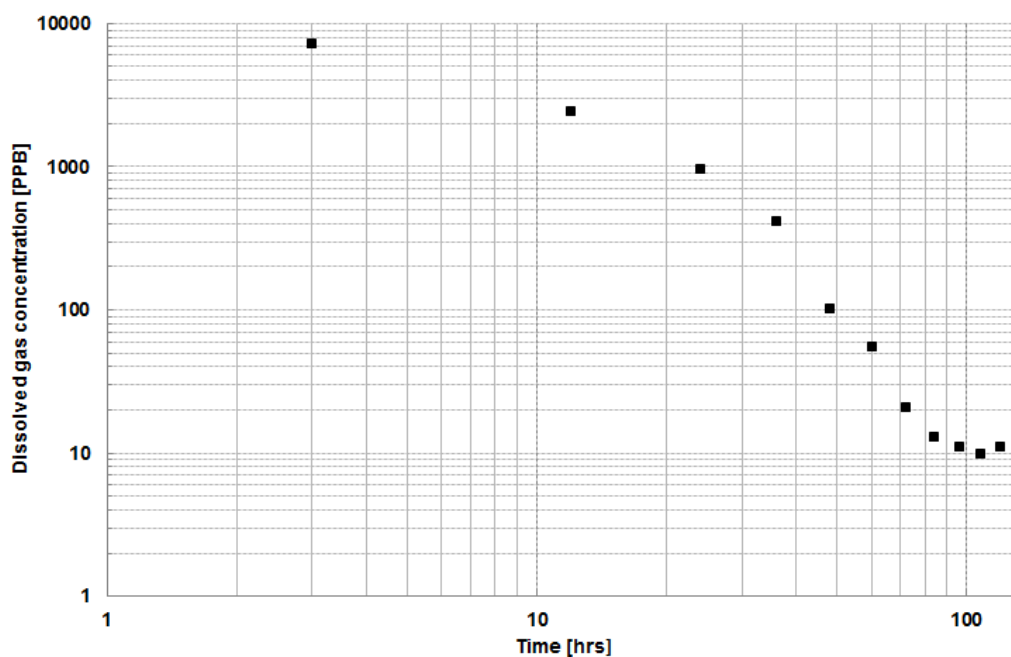
Figure 4.1: Dissolved oxygen concentrations over time after system filling (No error bars shown on graph due to the limited error of 1% in the dissolved gas concentration sensor reading).

Davis (1987), reports similar trends in the depletion of dissolved oxygen as a function of time. Davis also reports that some additional oxidation could occur due to the leakage of air into the system during long term usage as a result of thermal cycling. Such leakages could originate at pipe joints and connections and at the flanges on the negative side of the circulator. Leakages could also occur due to the presence of an undersized or faulty system expansion vessel. A visual inspection of the system water upon filling is also proof to the fact that after circa 100 hours from the system filling, any form of oxidation stops. In fact, the presence of black rust particles in the water resulted in a limited degree of

103

cloudiness in the system water generated during the first 3 days from filling. No increase in the level of water cloudiness was observed after this time period, thus further proofing that the oxidation process was terminated upon the depletion of dissolved oxygen.

4.2.2 Hydrogen gas

Fig. 4.2 illustrates the dissolved hydrogen gas concentration in water as a function of the time lag after the system filling with tap water. As expected, the concentration of dissolved hydrogen in tap water is low and does not result in saturation conditions. Hence, considering the solubility coefficient for hydrogen gas dissolved in water at the dissolved gas testing temperature of $40^{o}C$ and at atmospheric pressure, the maximum concentration of hydrogen gas is 1,490 PPB or 1.49 mg/L water (Baranenko and Kirov, 1989). Low concentrations of hydrogen gas in water, are inherent to the fact that hydrogen is found in very limited concentrations in atmospheric air.
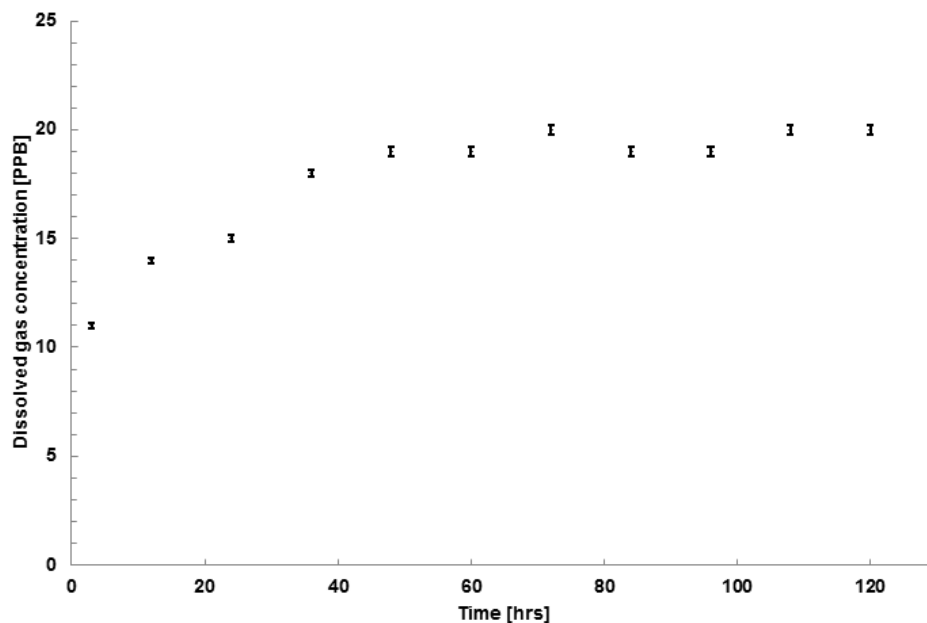
Figure 4.2: Dissolved hydrogen concentrations over time after system filling.

Upon filling, a dissolved hydrogen concentration of 11 PPB was recorded. This increased to an average of 20 PPB after circa 3.5 days from filling. The near doubling in the hydrogen concentration is attributed the oxidation reaction in Eq. (2.33) where hydrogen is one of the by products from the final reaction that leads to the formation of ferrous ferrite. Davis (1987), Heat (1998) and Lamers (2005)

also report similar trends in the increase in dissolved hydrogen. The ferrous ferrite forms a layer on the internal steel surface of the radiator and buffer vessel. This layer is very thin and consequently could break down into fine particles which float in the system water (Davis, 2000). The latter could be attributed to the limited cloudiness observed in the water. This process exposes the steel surface to water and dissolved oxygen thus ensuring that further oxidation reactions take place until the bulk oxygen gas concentration is consumed thus leading to a termination of this reaction.

4.2.3 Nitrogen gas

Fig. 4.3 illustrates the dissolved nitrogen gas concentration as a function of time. The experimental error due to the *TGM* system amounting to ±1.1% is illustrated in the form of error bars on the data points. An average dissolved gas concentration of 18,800 PPB or 18.8 mg/L water was measured. As expected, and considering the solubility coefficient for nitrogen at the testing temperature, the tap water was saturated with nitrogen gas at atmospheric pressure. Throughout the measuring period the dissolved gas concentration was relatively constant. However, some cycling in the nitrogen dissolved gas concentration was evident.

This phenomenon can be attributed to the system cycling where gas is deaerated due to high temperatures, hence during the heating phase. When the system is idle, the gas pockets generated in the radiator and buffer vessel as a result of deaeration, dissolve back to the water due to a higher solubility of nitrogen in water at lower temperatures. Hence this results in a higher dissolved gas concentration.

Other dissolved gases in water such as argon and carbon dioxide are known to amount to less than 1% of the dissolved gas content in water exposed to atmospheric air. This suggests that these gases are present in very low concentrations in their dissolved form in water. Therefore, in agreement with the findings of Davis (1987) and Lamers (2005), the present study suggests that nitrogen is the dominant dissolved gas in a central heating system.
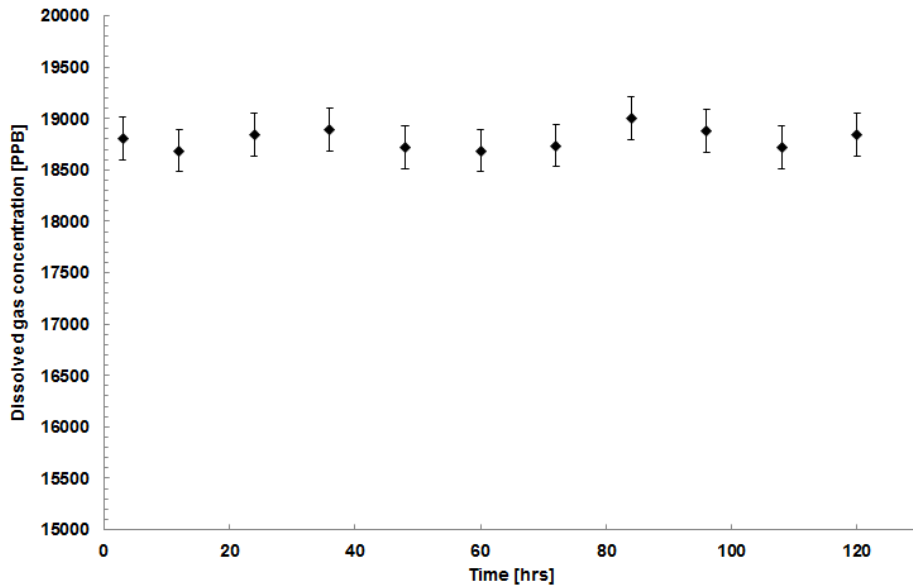
Figure 4.3: Dissolved nitrogen gas concentrations over time after system filling.

4.3 Bubble characteristics in vertical downward flow at boiler exit

This section will present the results for the tests done at the sight glass located on the vertical flow line at the boiler exit. Hence, the volumetric void fraction distribution across the sight glass, the bubble size and shape will be discussed.

4.3.1 Bubble distribution

This section presents the results for the bubble distribution at the boiler exit in a vertical downward bubbly two-phase flow. As illustrated in Figs.4.4-4.6, the results are presented through the measured volumetric void fractions across the pipe section, using sight glass *VSG1* for the experiments as tabulated in Table 3.3 in Section 3.4.2. This data is presented in relation to the position across the pipe section, represented through a dimensionless number r_p/R_p, where a zero value signifies the pipe centre line. Hence, Fig. 4.4 summarizes the results whereas Figs. 4.5&4.6 provide the actual results for the tests conducted in the present study. After considering the errors due to the experimental uncertainty that amount to ±19.6% of the readings values, the results, suggest that a quasi-flat volumetric void fraction profile is expected across the vertical pipe section for a downward two-phase bubbly flow. In all four experiments, marginally lower volumetric void fractions and mean bubble diameters were measured at a

106

distance of 1 mm (0.9 r_p/R_p) from the pipe wall. As illustrated in Fig. 4.7, such a trend is more distinct at higher volumetric void fractions, where the lower system velocities were applied. Fig. 4.4 suggests a trend where higher mean volumetric void fractions across the pipe section are present at lower bulk fluid velocities. As discussed in Section 4.3.2.1, this could be attributed to the large mean bubble diameters measured at low bulk fluid velocities. However, at higher bulk fluid velocities, this trend is not evident and in fact, through the consideration of the experimental errors, there is no distinct difference in the volumetric void fraction measured at the two highest bulk fluid velocities resulting in a Reynolds number of 21.2E+3 and 26.6E+3. This observation could be attributed to the higher bubble production rates with an increase in the bulk fluid velocity as discussed in Section 4.4. Therefore higher bubble counts compensate for any reduction in the bubble diameter with an increase in the bulk fluid velocity.
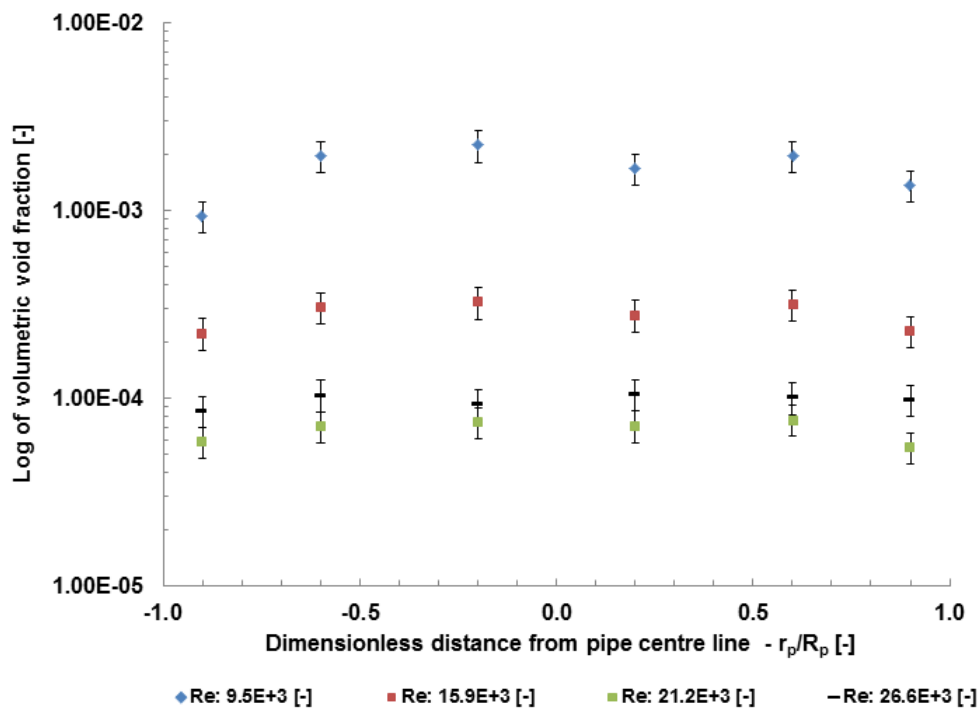
Figure 4.4: Volumetric void fractions with dimensionless distance across vertical pipe at boiler exit with the bulk fluid Reynolds number *(Experiment: BDT in Table 3.3).*

Kashinsky and Randin (1999), reported that most studies in vertical two-phase bubbly flow have been done for cocurrent upward flow. Hence, little consideration has been given to the downward flow scenario. However, the known studies done in bubbly vertical downward flow by Drew and Lahey (1982), Wang et al. (1987), Antal et al. (1991) and Kashinsky and Randin (1999)

reported similar void fraction distributions as measured in the current study with a quasi-constant void fraction in the core region which drops abruptly to zero as the wall is approached. Iskandrani and Kojasoy (2001) also reported that, in two-phase vertical bubbly flows, the presence of voids tends to flatten the liquid velocity profile, thus leading to a homogenous phase distribution across the vertical pipe section. More recently, Lu and Tryggvason (2007) reported similar trends using direct numerical simulations where the full Navier-Stokes equations were solved by a parallelized front-tracking/finite-volume method.

Figure 4.5: Actual volumetric void fractions with dimensionless distance across vertical pipe at boiler exit at 4.5 L/min (top) and 7.5 L/min (bottom) *(Experiment: BDT in Table 3.3).*

Wang et al. (1987) and Kashinsky and Randin (1999) reported a drop in the void fraction at a mean distance of circa 0.9 of the pipe radius from the pipe centre line. The results presented in the current study should be considered in view of the relatively low void fractions present in the system. In fact, as illustrated in Fig. 4.5, maximum mean bubble diameters resulting in a mean volumetric void fraction of circa 2E-3 were measured at the lowest bulk fluid Reynolds number of 9.5E+3. Revankar and Ishii (1992) and Liu (1993) reported that in vertical two-phase pipe bubbly flow characterized with small bubble diameters and void fractions, uniform distributions are more likely across the pipe section in vertical fluid flow.
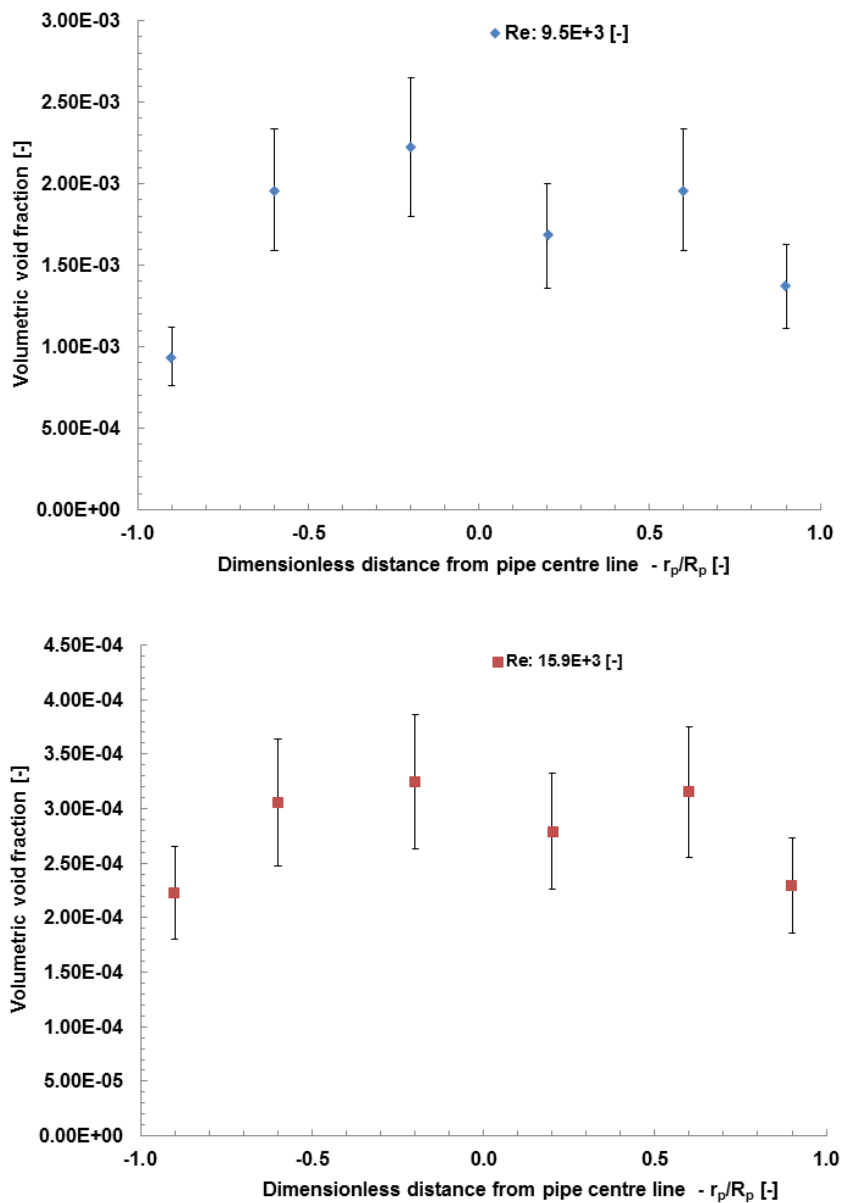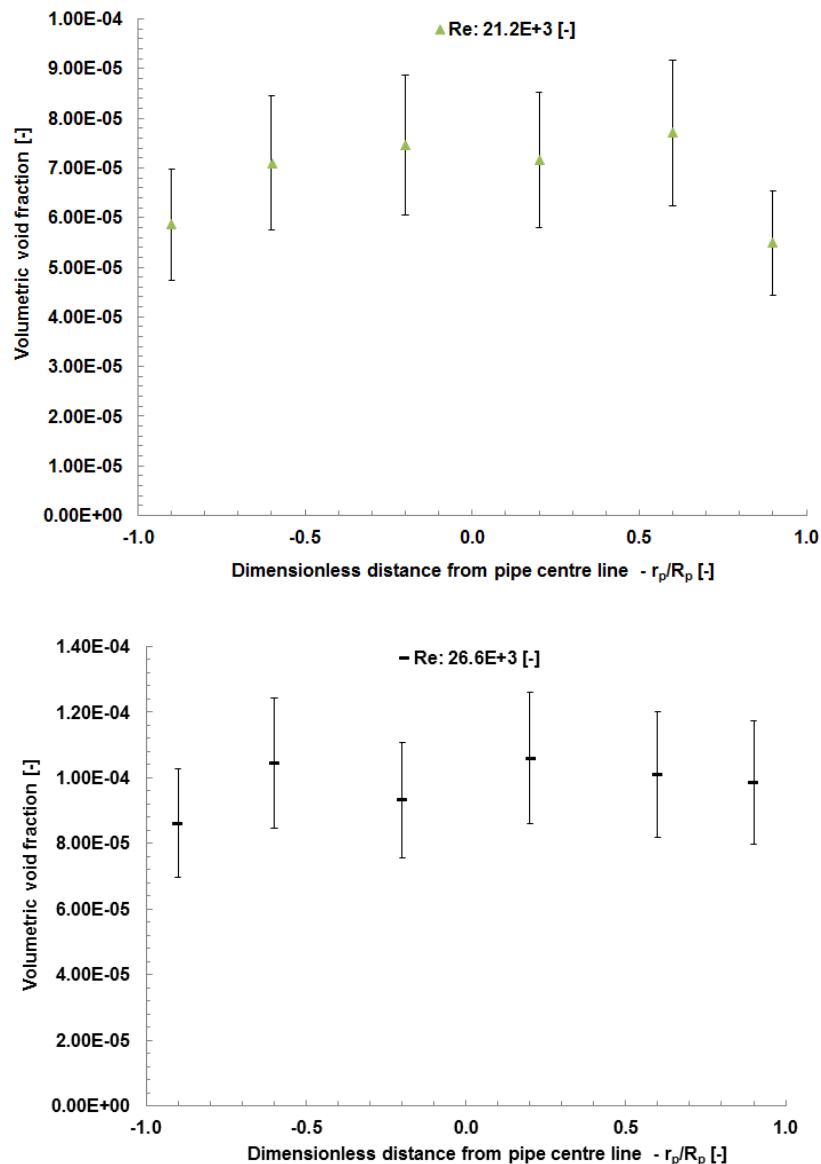

Figure 4.6: Actual volumetric void fractions with dimensionless distance across vertical pipe at boiler exit at 10 L/min (top) and 12.5 L/min (bottom) *(Experiment: BDT in Table 3.3).*

Kashinsky and Randin (1999), reported that low bulk fluid velocities of 0.5 m/s in a pipe with an internal diameter of 42.3mm resulted in more bubbles closer to the wall consequently improving the flatness of the void fraction distribution, with a drop in the void fraction starting at a distance of circa 0.95 from the pipe centre line. They reported that such an effect is more pronounced with the liquid velocity when compared to the bubble size or void fraction. This can be attributed to the reduced effect of liquid turbulence at lower bulk fluid velocities. Hence, such findings contrast to the results of the present study whereby larger void fractions at lower system velocities resulted in a reduction in the flatness of the void fraction distribution. Therefore, the present study suggests that with system fluid velocities less than 0.52 m/s, equivalent to a Reynolds number of 26.5E+3, the turbulence effects created by larger bubbles tend to have a greater effect on the void fraction distribution. Due to the increase in the bubble detachment diameter from the primary heat exchanger wall at lower fluid velocities, (Fsadni et al., 2011), the present study could not investigate void fraction distribution trends with velocity and bubble size independently.

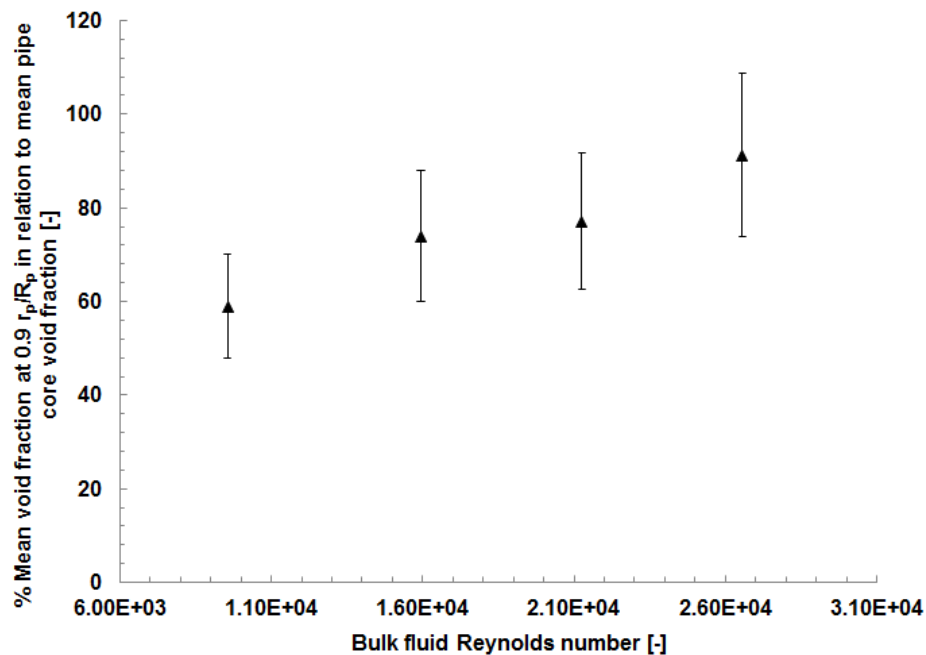**Figure 4.7: Percentage mean volumetric void fraction at 0.9 r_p/R_p in relation to the mean void fraction measured in pipe core with the bulk fluid Reynolds number**.

Kashinsky and Randin (1999) reported that in contrast to an upward flow, in downward bubbly flow, a velocity boundary layer close to the wall is expected as in the case of a single-phase flow. Hence, they referred to the conservation of the

'law-of-the-wall' in gas liquid bubbly flow as contributor to the drop in the void fraction in this area. They also reported that the resultant wall shear stress, or friction velocity, is an appropriate parameter for describing the near wall region in downward bubbly flows. Kashinsky and Randin (1999) reported that the size of the gas bubbles produces a significant effect on the wall shear stress, thus increasing with bubble size, hence, in agreement with the results of the present study, the resultant change in the void fraction distribution with bubble size. They attributed this effect to the higher tubulisation of the flow by big bubbles for which both the size and the relative velocity are higher.

Žun (1980) and Kashinsky and Randin (1999) suggested that the main reason for the bubble migration in the flow away from the pipe wall is a transverse lift force acting on a bubble dependent on the phase relative velocity and the liquid velocity gradient. Furthermore, Antal et al. (1991) related the void fraction distribution across the vertical pipe section with a wall repulsion force dependent on the bubble radius, distance from the wall and the phase relative velocity. Such a repulsion force is assumed to be equal for both down and upward flows. Hence, in a downward flow, both forces act in the same direction therefore pushing the bubbles away from the pipe wall at the region with the strongest velocity gradient, hence, the void fraction distributions as measured in the current study.

The bubble distribution trends for a vertical bubbly downward flow contrast with the expected void fraction distribution in upward vertical pipe flow. Serizawa et al. (1975), Michiyoshi and Serizawa (1986), Revankar and Ishii (1992), Liu and Bankoff (1993) and Hibiki et al. (2003) reported that in contrast to the downward flow void fraction distribution, two-phase upward flow is expected to result in a peak void fraction close to the wall. Kashinsky and Randin (1999) attributed this to the transverse lift force, as originally defined by Žun (1980), acting on the bubble in an upward flow (with an opposite sign to that for a downward flow), thus leading to wall peaked void fraction distribution profiles across the pipe section. Hence, this contrasts to the 'coring' effect as defined by Drew and Lahey (1982), whereby higher void fractions are expected at the pipe core in relation to the region close to the wall in two-phase bubbly downward flow characterized by high void fractions.

111

4.3.2 Bubble size at boiler exit

This section presents the effect of the system flow rate, pressure, heat flux and saturation ratio at the primary heat exchanger wall conditions on the bubble characteristics at the exit side of the boiler. As tabulated in Table 3.4 in Section 3.4.3, the four parameters affecting a central heating system were investigated for effects on the resultant bubble characteristics, principally the resultant bubble diameter. Therefore an initial assumption was made in the form:

$$D_b = f \{ \dot{m}, P_{sys}, Q, \alpha)$$

Where $\dot{m}$ is the mass flow rate, P_{sys} is the system pressure, Q the heating load and α is the saturation ratio as defined by Jones et al. (1999a). All measurements for bubble characteristics were done through a photo imaging technique as discussed in Section 3.3. The measured average bubble diameter and the bubble size distribution are presented. All measurements were recorded after the system reached steady state conditions i.e. *TGM* transducer yielding consistent readings.

4.3.2.1 Bulk fluid velocity

Fig. 4.8 presents the average measured bubble diameter for the range of volume flow rates considered in the present study represented through the dimensionless Reynolds number while Fig. 4.9 presents the resultant bubble size distributions.
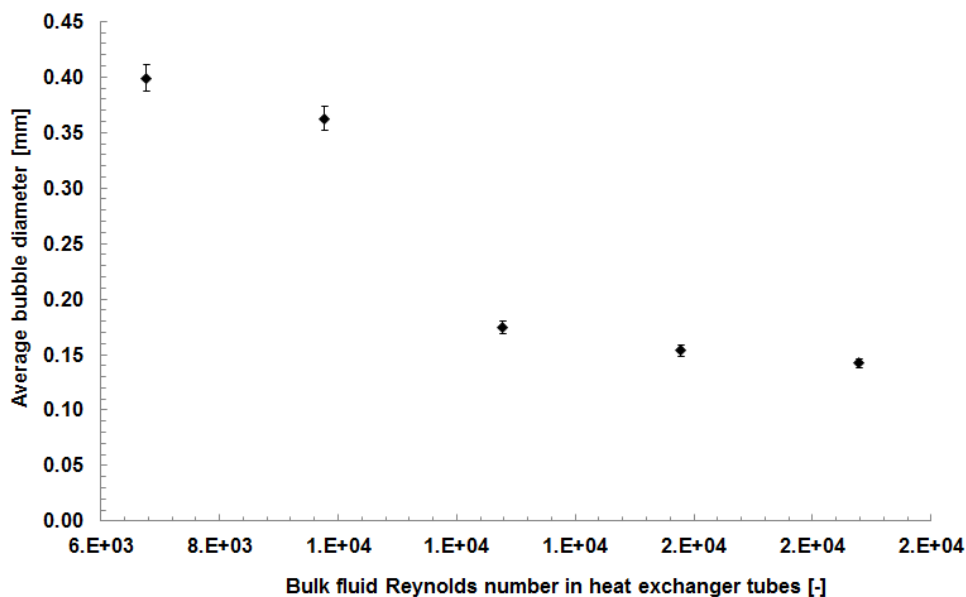

Figure 4.8: Measured bubble diameter with the dimensionless bulk fluid Reynolds number in the heat exchanger tubes at boiler exit *(Experiment: BCT I in Table 3.4).*

112

Fig. 4.8, illustrates the resultant trend between the measured average bubble diameter and the fluid velocity in the heat exchanger tubes. The trend shows a substantial decrease in the bubble diameter with an increase in the bulk fluid velocity. This trend is also reproduced in the cumulative bubble size distribution illustrated in Fig. 4.9. Hence 68% of the bubbles measured at the highest bulk fluid velocity in the heat exchanger tubes, equivalent to a Reynolds number of 18.7E+3, had a diameter below 0.15 mm whereas only 40% of the measured bubbles had a diameter below 0.15 mm at the lowest bulk fluid velocity of 0.3 m/s, equivalent to a Reynolds number of 6.7E+3. An average bubble diameter of 0.39 mm was measured at a Reynolds number of 6.7E+3 in the primary heat exchanger tubes whereas the average bubble diameter at the maximum fluid velocity equivalent to a Reynolds number of 18.7E+3 was measured at 0.14 mm. No data is known to be available in the open literature for bubble characteristics in domestic central heating systems. A number of studies have been done for similar scenarios involving the detachment of bubbles from surfaces exposed to supersaturated fluids under stagnant conditions while very few studies have been done for bubble growth and detachment in supersaturated fluids with fluid flow. The latter studies were done by Winterton (1972a), Al-Hayes and Winterton (1981 a,b) and Hepworth et al. (2003). Similar trends in the measured bubble diameters with fluid velocity in supersaturated solutions were reported in all the latter studies. For bubbles grown on the inside of a Perspex tube in water supersaturated with air, Winterton (1972a) reported bubble diameters in the range of 0.4 to 2 mm with an increase in velocity. Al-Hayes and Winterton (1981b) reported bubble detachment diameters in water supersaturated with air in the range of 1.9 to 1.3 mm with a tube diameter of 19 mm and a fluid velocity in the range of 0.1 to 0.3 m/s. The latter results were reported for a contact angle of 40°, which is similar to that expected on stainless steel surfaces. A study by Hepworth et al. (2003) in bubble detachment diameters in beer supersaturated with carbon dioxide, reported bubble diameters in the range of 0.2 to 0.1 mm for volume flow rates of 0.5 and 2.2 L/min respectively. For stagnant water conditions, supersaturated with carbon dioxide gas, Jones et al. (1999b) reported average bubble detachment diameters in the range of 0.32 to 0.63 mm while Cyr (2001), reported detachment diameters in the range of 0.05 to 0.2 mm in depressurized soda water. As none of the reported experimental conditions from

literature is reasonably similar to the present study, a direct comparison of results cannot be made. Hence, the experimental conditions that are most similar to those used in the present study are those reported by Al-Hayes and Winterton (1981b) at a fluid velocity of 0.3 m/s. Therefore, the detachment diameters reported in the present study are considerably smaller than those reported by Al-Hayes and Winterton. This could be attributed to the larger tube diameter used in the latter study.

In their analysis, Winterton (1972a) and Hepworth et al. (2003) attributed the resultant detachment diameter for a liquid in motion to the balance of the forces acting on the bubble at its nucleating point. The principal forces acting on a bubble with liquid motion are the drag, surface tension and buoyancy forces. Bubble detachment is expected as the drag force equals the surface tension force, thus requiring a balance of forces parallel to the wall surface. Hence, the lift force at right angles to the surface is considered to be too weak to overcome the perpendicular component of the surface tension force (Winterton 1972a). Therefore, as the bulk fluid velocity increases, the drag force on the bubble increases and hence equals the surface tension force at smaller bubble radii, thus resulting in a reduced bubble detachment radius. The validity of this model is enhanced through the consideration of similar trends for the reported
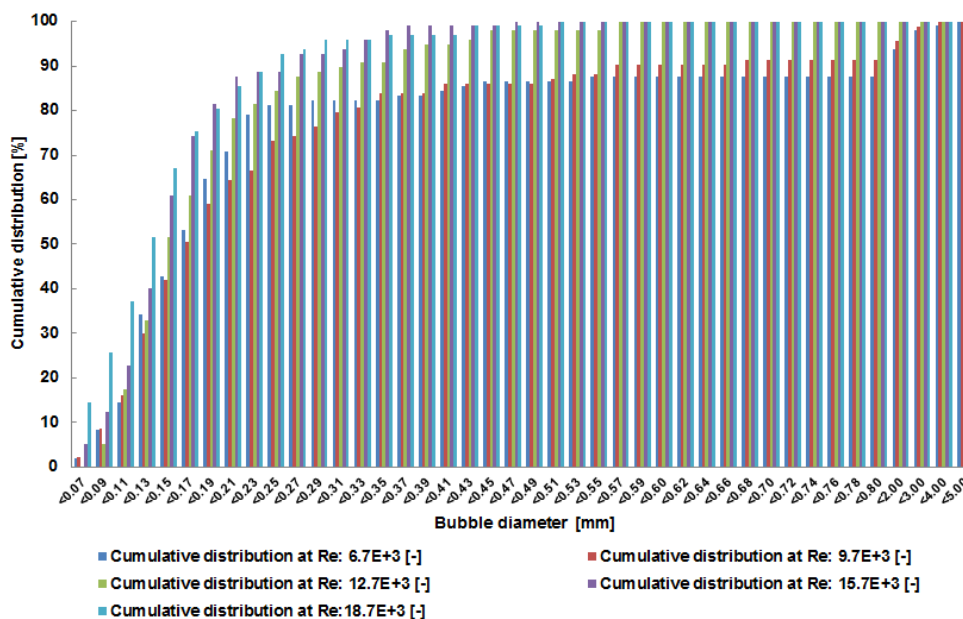

Figure 4.9: Bubble size distributions with the Reynolds number in the primary heat exchanger tubes as measured at the boiler exit *(Experiment: BCT I in Table 3.4).*

114

experimental bubble detachment diameters with velocity in sub cooled flow boiling as reported by Prodanovic et al. (2002).

Hepworth et al. (2003) reported that the direction of liquid motion relative to the nucleation surface had an effect on the bubble detachment diameter. In fact, they reported that tangential liquid motion produced smaller detachment diameters. As illustrated in Fig. 3.17, the primary heat exchanger used in the present study consists of a shell tube type heat exchanger with 12 tubes wound in a helical coil structure around the boiler burner. Consequently, both tangential and normal liquid motions relative to the nucleation surface were present. Therefore, the presence of both types of liquid motion with the nucleation surface is considered to balance out any differences in the bubble detachment diameters. This was done as the limitations of the present study with respect to the boiler heat exchanger did not allow an experimental analysis of the detachment diameters at the boiler wall. A parallel could also be made with studies in sub-cooled flow boiling where similar trends were observed (Prodanovic et al., 2002).

4.3.2.2 System pressure

A change in the system pressure resulted in measured average bubble diameters of 0.18 mm and 0.13 mm at system pressures of 2 and 3.75 bars (abs) respectively. Therefore, as illustrated in Fig. 4.10, larger bubble diameters are expected at lower absolute system pressures. This trend is also reflected in the bubble size cumulative distribution as illustrated in Fig. 4.11. Hence, at 3.75 bars, 82% of the bubbles have a measured diameter of less than 0.15 mm whereas at 2 bars this accounts for 58% of the bubbles.

Most of the research in bubble detachment from smooth surfaces in supersaturated solutions was done through the use of a constant system pressure. This was necessary as super saturation conditions were established through a release in the system pressure. Therefore, none of the studies referred to in Section 2.2.2.2, Winterton (1972a), Al-Hayes and Winterton (1981a,b) and Hepworth et al. (2003), have reported bubble detachment characteristics in supersaturated solutions with a change in the system pressure. Hence, Winterton's (1972a) prediction for bubble detachment diameters in supersaturated solutions through the force balance method, does not predict any

significant changes in the expected bubble detachment diameter with a change in the system pressure.
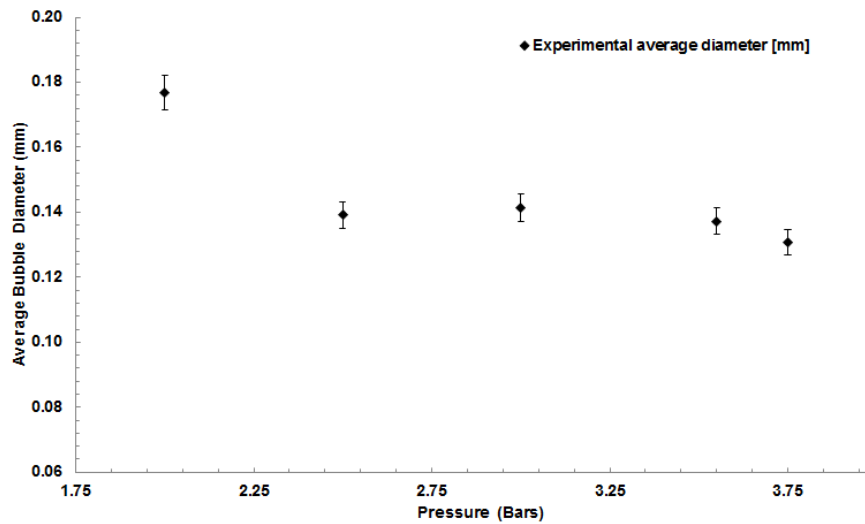
Figure 4.10: Measured bubble diameter with system pressure (abs) at boiler exit
(Experiment: BCT II in Table 3.4).

A similar trend with an increase in the system pressure was observed in sub-cooled flow boiling conditions. Amongst such studies are those done by Tolubinsky and Kostanchuk (1970) and Prodanovic et al. (2002), who conclude that bubble detachment diameters are strongly dependent on the system pressure. Hence, both studies reported a decrease in the bubble detachment diameters with an increase in the system pressure in the range of 2 to 3.75 bars (abs).
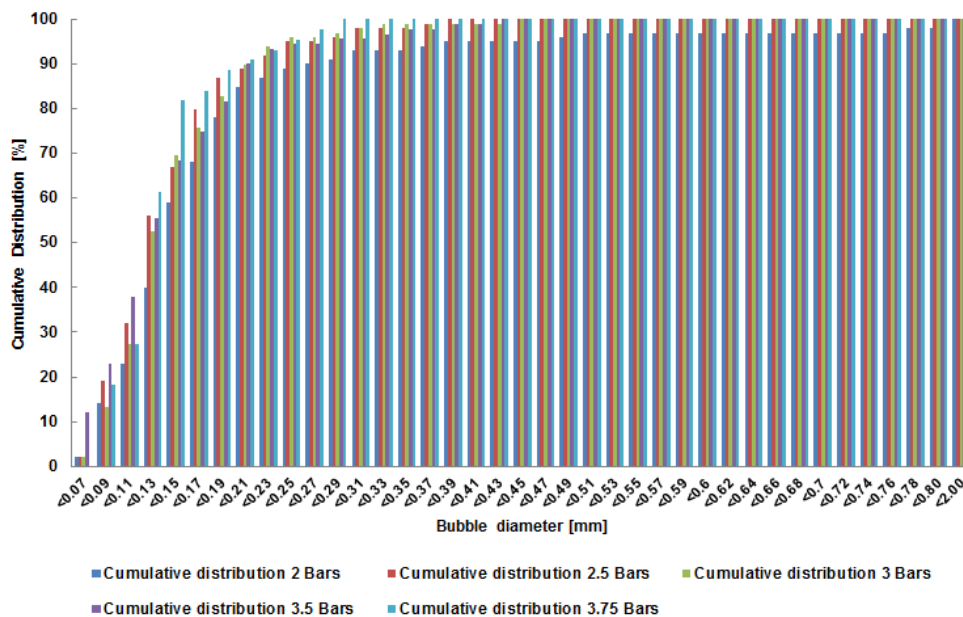

Figure 4.11: Cumulative bubble size distributions with system pressure (abs) at boiler exit
(Experiment: BCT II in Table 3.4).

116

Furthermore, Prodanovic et al. (2002), reported that an increase in the pressure resulted in shorter bubble ejection times from their nucleating point. This theory could be extended to the gas diffusion approach in supersaturated solutions, thus enabling the longer ejection times at lower system pressures to allow more gas to diffuse into the nucleating bubbles hence allowing larger bubble detachment diameters.

4.3.2.3 Heat flux

For a change in heat flux in the range of 17 to 50 kW/m^2 and a corresponding exit temperature of 59°C to 77°C, the average measured bubble diameters, as illustrated in Fig. 4.12, are in the range of 0.142 mm to 0.175 mm respectively. Hence, the increase in boiler wall heat flux, equal to a heating load of 7.5 and 21.5 kW resulted in a 19% increase in the observed experimental average bubble diameters. This trend is also reproduced in the cumulative bubble size distribution chart in Fig. 4.13. Hence, at the lowest heat flux, 78 % of the bubbles were measured with a diameter of 0.15 mm or less while at the highest heat flux, this amounts to 53% of the measured bubbles.
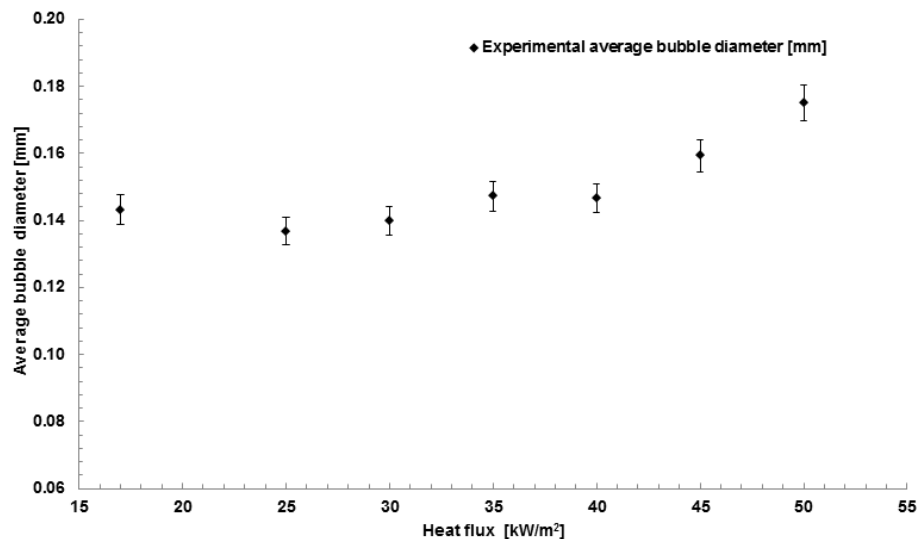

Figure 4.12: Measured bubble diameter with system heat flux and exit temperature at boiler exit *(Experiment: BCT III in Table 3.4).*

As the heating load is increased, higher heat exchanger wall temperatures are observed due to the increase in the difference between the return and flow temperatures. Higher temperatures are known to increase the diffusivity of the

dissolved nitrogen gasses. In view of this, Al-Hayes and Winterton (1981a) and Jones et al. (1999b) predicted shorter bubble growth times as a result of higher diffusion rates with an increase in temperature. However, they do not comment on the expected changes to the bubble detachment diameter with a change in temperature. Hence, using the results of the present study, higher diffusivities are assumed to result in shorter bubble growth times thus allowing the nucleating bubbles to absorb more gas prior to detachment due to the action of the surface tension and drag forces on the nucleating bubble. Hence, the increase in gas diffusivity is assumed to have an overriding effect on the reduction in the surface tension force that is in turn expected to result in reduced bubble detachment diameters.
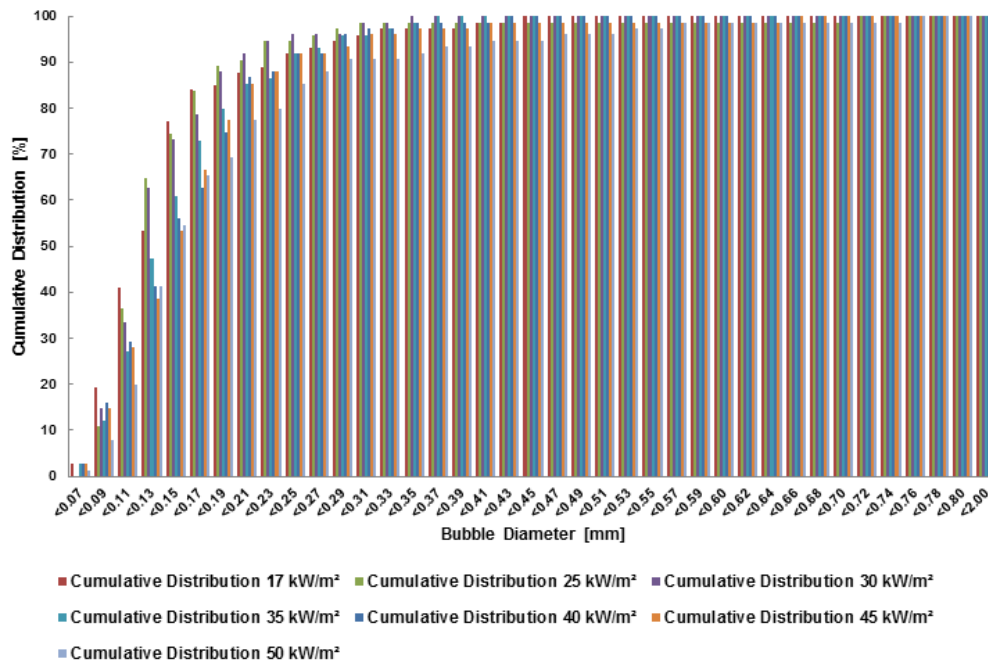
Figure 4.13: Cumulative bubble size distributions with system heat flux and exit temperature at boiler exit *(Experiment: BCT III in Table 3.4).*

Winterton (1972a) and Hepworth et al. (2003) did not report experimental results in the expected bubble detachment diameter with heat flux and surface temperature. Hence, Winterton's force balance prediction does not directly predict a change in the bubble detachment diameter with a change in the tube surface heat flux and temperature. However, a negligible change in the expected bubble diameter is predicted due to a change in the fluid properties with temperature, resulting in a reduction in water density, kinematic viscosity and

surface tension force, all assumed to be equal to the tube wall temperature. Once more, a parallel can be drawn with similar studies in sub-cooled flow boiling as done by Prodanovic et al. (2002). However, contrary to this study, bubble detachment diameters were observed to decrease with increasing heat flux while similar studies in flow boiling by Abdelmessih et al. (1972) observed similar trends to the present study with an increase in bubble diameters with heat flux.

4.3.2.4 Maximum saturation ratio at primary heat exchanger wall conditions

As illustrated in Fig. 4.14, the change in the maximum saturation ratio in the range of 0.9 to 1.2 at the primary heat exchanger wall conditions did not result in any distinct trend in the measured bubble detachment diameters. Hence, all changes observed with the saturation ratio are within the experimental errors of the present study. This trend is also reproduced in the cumulative bubble size distribution chart in Fig. 4.15, where a quasi-uniform distribution is evident. As defined by Jones et al. (1999a), the low super saturation ratios achieved in the present study can be classified as a Type IV non-classical nucleation at the boiler wall conditions. This type of nucleation occurs at pre-existing gas cavities on the surface of the boiler tube wall.
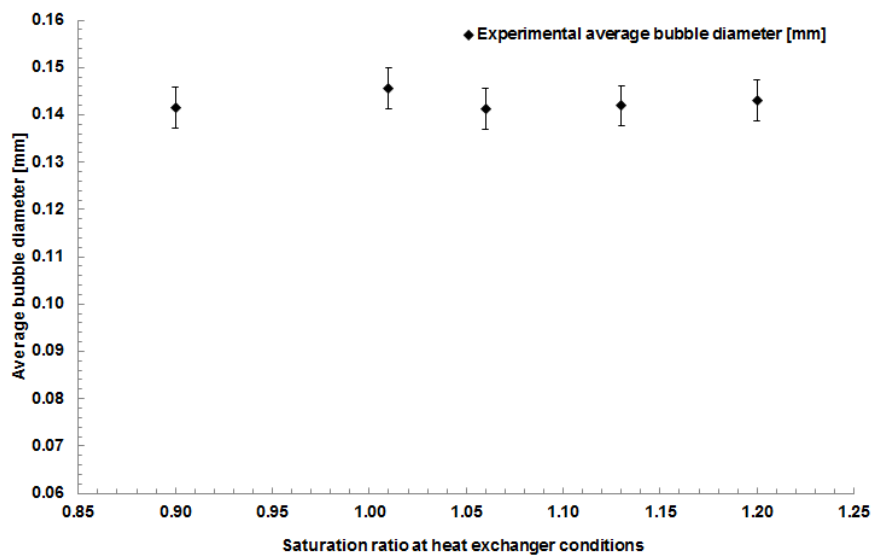

Figure 4.14: Measured bubble diameter with the maximum saturation ratio at the heat exchanger wall conditions *(Experiment: BCT IV in Table 3.4).*

Few literature sources have reported experimental results for measured detachment diameters with saturation ratios. The present results may contrast with recent studies by Hepworth et al. (2003) who reported an increase in the bubble detachment diameter with an increase in dissolved gas content. This fact could be attributed to the relatively high saturation ratios of 3.4 used in their experimental study. Al-Hayes and Winterton (1981a,b) and Jones et al. (1999b) reported that through the application of the diffusion theory, the gas concentration effects the bubble growth rate but does not result in a direct effect on the bubble detachment diameter. This is in agreement with the Winterton (1972a) detachment radius model that is based on the physical aspects of the nucleating bubble, thus governed by the balance of the drag and surface tension forces acting on the nucleating bubble at its nucleating point.
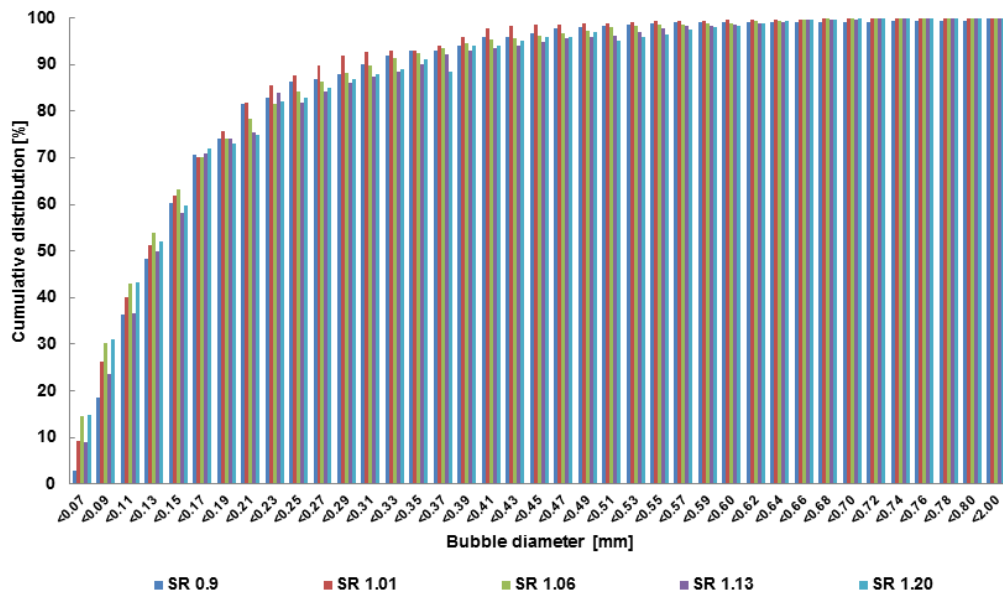
Figure 4.15: Cumulative bubble size distributions with maximum saturation ratio at the heat exchanger wall conditions *(Experiment: BCT IV in Table 3.4).*

The under saturation experimental runs resulted in substantially reduced bubble counts when compared to the experimental runs with supersaturated conditions at the primary heat exchanger wall. However, a small number of bubbles were present. The classical theory for bubble nucleation as defined by Dean (1944) suggests that under saturation conditions should not result in bubble nucleation due to the bulk fluid pressure being higher than the gas pressure in a bubble, thus inhibiting growth of existing gas cavities. The release of micro bubbles from the

primary heat exchanger tubes at under saturation conditions in the present study could be attributed to the experimental errors in the calculation of the saturation ratio at the heat exchanger wall and to localized high temperatures on the tube walls which result in localized super saturation areas at the boiler wall conditions.

The present study demonstrates that the fluid velocity has the largest effect on the measured bubble diameters at the heat exchanger exit. This is in agreement with the findings reported by Winterton (1972a), Al-Hayes and Winterton (1981 a,b) and Hepworth et al. (2003). These findings suggested that the forces acting on the nucleating bubbles have the greatest influence on the detachment diameter at the heat exchanger wall. The presence of antibacterial and corrosion inhibitors in tap water is not expected to affect the bubble detachment diameter. Such additives could marginally affect the total dissolved gas saturation levels. However, as demonstrated in the present study, changes in the saturation ratio are not expected to affect the bubble detachment diameter.

The wall temperature in the condenser does not result in gas super saturation levels, and therefore no bubbles are released from the condenser wall. As a result, similar bubble characteristics are expected in older type non-condensing boilers equipped with a similar primary heat exchanger design.

4.3.3 Bubble shape and breakage events in vertical pipe at the boiler flow line

An analysis of the two measurements recorded manually for each bubble at the boiler exit for the investigation, as described in Section 3.4.3, suggests that most bubbles are spherical in shape, with mean aspect ratios in the range of 0.9 to 1. The latter was calculated through the ratio of D_p/D_n, as illustrated in Fig. 4.16. As discussed by Prodanovic et al. (2002), this ratio provides a numerical quantification for the elongation of the free bubbles in bubbly flows. Figs 4.17-4.20 illustrate the calculated aspect ratios with the bulk fluid velocity, pressure, heat flux and saturation ratios.

The quasi constant mean aspect ratios illustrated in Figs. 4.17-4.20 suggest that the pressure, heat flux and saturation ratio do not result in a measurable effect on

the resultant bubble shape, while a mean aspect ratio of less than 1 for all experiments suggests a minimal bubble elongation along the fluid flow.
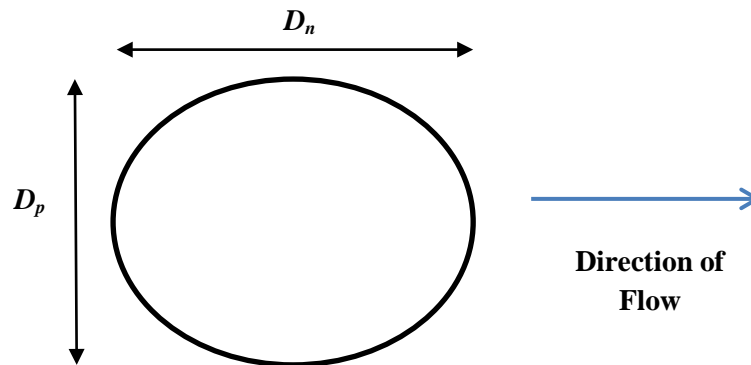
Figure 4.16: The measured bubble geometrical parameters.

A shift in the bubble elongation was evident with a shift in the bulk fluid velocity represented through the dimensionless Reynolds number as in Fig. 4.20. Therefore, higher elongation ratios were observed with lower fluid velocities. This could be attributed to the significantly larger bubble diameters measured with reduced bulk fluid velocities, as discussed in Section 4.4.1. These results are in agreement with the findings done by Liu (1993) who reported that bubble elongation along the flow was observed with the presence of larger bubbles, with minimal elongation observed with smaller sized bubbles
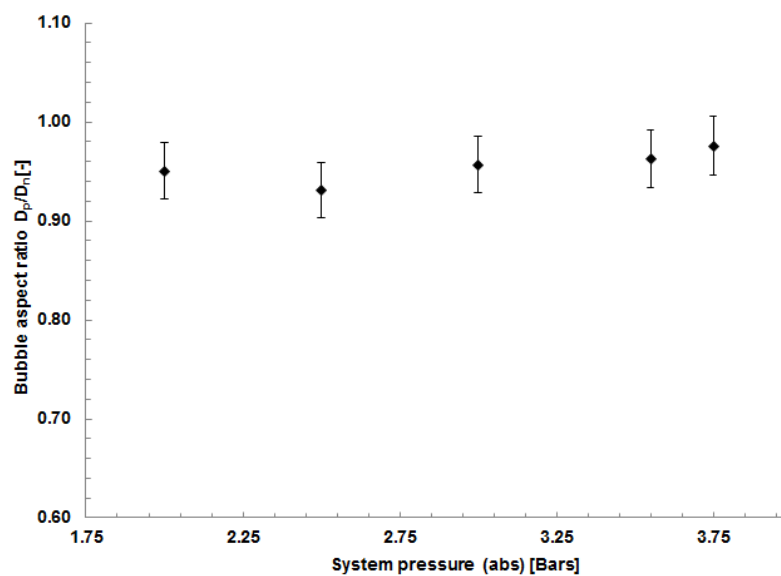
Figure 4.17: Bubble aspect ratio in vertical pipe flow at boiler exit with system pressure (abs) *(Experiment: BCT II in Table 3.4).*

122
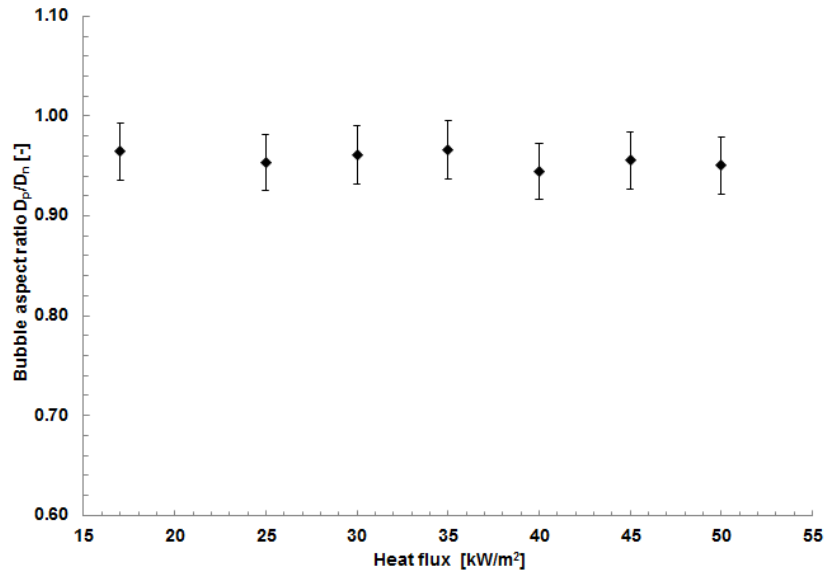
Figure 4.18: Bubble aspect ratio in vertical pipe flow at boiler exit with heat flux.
(Experiment: BCT III in Table 3.4).
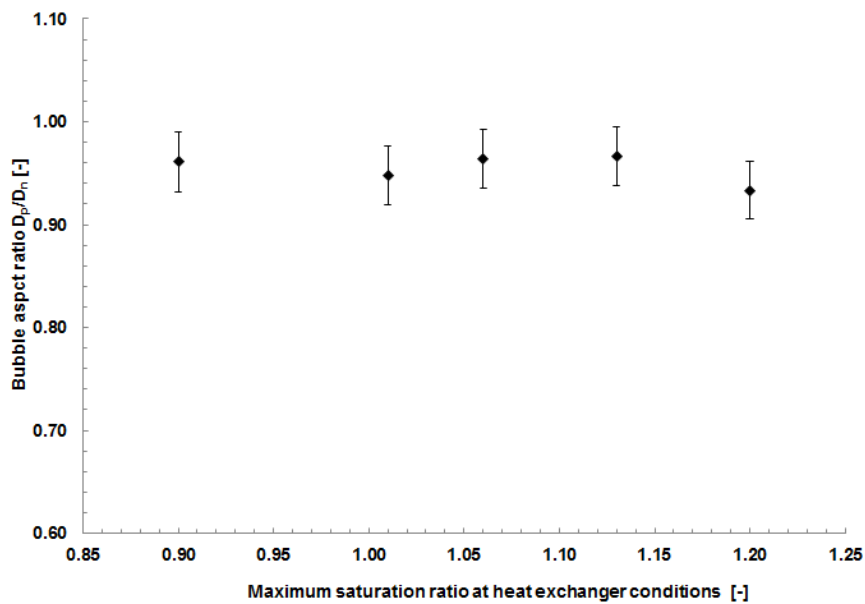
Figure 4.19: Bubble aspect ratio in vertical pipe flow at boiler exit with maximum saturation ratio at the primary heat exchanger conditions *(Experiment: BCT IV in Table 3.4).*

In view of the small bubble sizes measured in the current study, together with the negligible expected relative velocity between the two phases, the effects on the bubble shape of the average pressure fluctuations generated by the turbulent liquid fluctuations, as defined by Kocamustafaogullari et al. (1994), are expected to be negligible.

123

The findings of the present study are also in agreement with studies done by Thang and Davis (1979), Van der Welle (1985), Michiyoshi and Serizawa (1986), Winterton and Orby (1994) and Winterton and Munaweera (2001) who assumed a spherical shape for bubbles flowing in vertical pipe bubbly flow. Similarly, numerical studies done by Lu and Tryggvason (2007) reported quasi spherical bubbles with diameters of 1.53 mm and slightly ellipsoidal bubbles with diameters of 1.84 mm through the application of direct numerical simulations for bubbly air water two-phase downward flow. In view of the relation between the bubble shape and bubble breakage events as discussed by Hesketh et al. (1991), whereby breakage events are expected to occur as a result of substantial bubble elongation with the flow, the quasi-spherical shapes observed in the current study, suggests that bubble breakage can be assumed to be minimal. Bubble coalescence events are also considered to be negligible in the current study due to the relatively low volumetric void fractions measured. In fact, Iskandrani and Kojasoy (2001) reported that bubble coalescence is expected at a void fraction above 65% in bubbly flows.

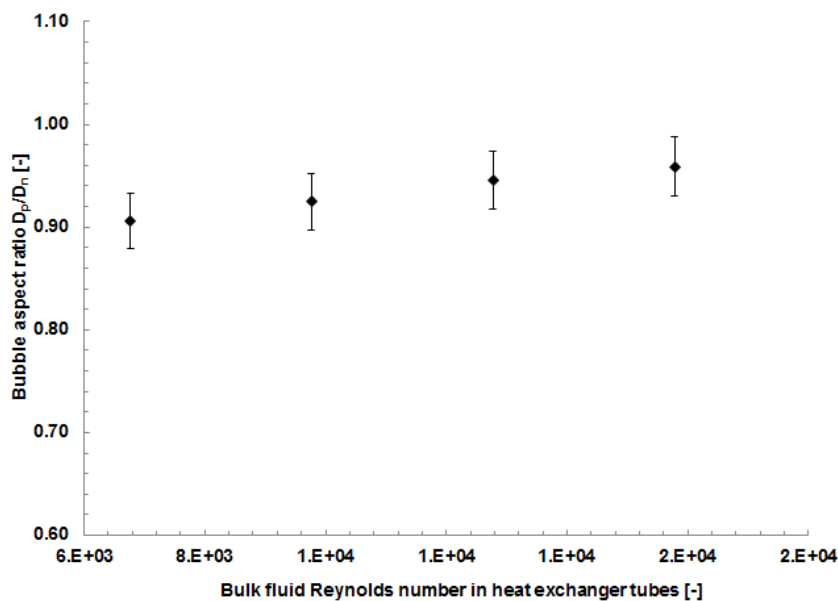**Figure 4.20: Bubble aspect ratio in vertical pipe flow at boiler exit with bulk fluid Reynolds number in the heat exchanger tubes *(Experiment: BCT I in Table 3.4).***

Through the use of the dimensionless Eotvos number and the bubble Reynolds number as defined in Eqs. (2.32) and (2.33), the position of the typical bubbles measured in the current study on the bubble shape regime chart as illustrated in

Fig. 2.8 was established. The calculated dimensionless Eotvos and Reynolds numbers with the measured mean bubble diameters are tabulated in Table 4.1. An assumed relative velocity between the two phases of 1E-3 m/s was assumed (Adrian, 1991).

Mean bubble diameter (m)	Eotvos number (-)	Bubble Reynolds number (-)
3.9E-4	2.36E-2	1.1
1.3E-4	1.00E-2	0.4

Table 4.1: Calculated dimensionless Eotvos and bubble Reynolds numbers with mean bubble diameter.

The calculations tabulated in Table 4.1 resulted in distinctly low values for the dimensionless Eotvos and bubble Reynolds numbers, hence implying that the bubbles measured in the current study fall on the lower left corner of the bubble shape regime chart illustrated in Fig. 2.8. Therefore, this is in agreement with the findings of the present study which confirms that due to the relatively small bubble diameters measured, a quasi-spherical bubble shape can be assumed.

The present study did not allow a photographic visualization of the nucleating bubbles at the primary heat exchanger wall. Hence, the actual bubble aspect ratio at detachment was not measured. However, after consideration of the typical aspect ratios reported by the open literature at the bubble detachment point, and the mean aspect ratios at the exit of the boiler unit as measured in the present study, it can be assumed that following detachment, the smaller bubbles tend to gain a quasi-spherical shape.

4.4 System bubble production and nucleation rates on the boiler wall

As discussed in Section 3.4.4, these tests were done to analyse the bubble production rate at the boiler exit with a range of system parameters. Furthermore, as outlined in Section 3.5.7, the bubble nucleation rate was subsequently calculated through the knowledge of the heat exchanger surface area under super

saturation conditions. Hence, the flow line sight glass *VSG1* was used for these tests. A good representation of the total bubble production rate and the calculated mean nucleation rate at the heat exchanger surface with the relevant experimental uncertainties as calculated in Section 3.6, is given in Figs. 4.21-4.24. As discussed in Section 4.3.1, bubble distribution tests across the sight glass section have shown quasi-uniform bubble dimensions and volumetric void fractions. Hence, the results presented in this section are based on images captured at a representative plane across the sight glass as detailed in Section 3.4.4. As discussed in Section 3.4.5, the tests outlined in Section 3.4.4 were repeated with the camera positioned at sight glass *VSG2*. This was necessary to analyse the possibility of the presence of air bubbles on the system return end to the boiler. The latter tests proved that under no operating conditions were bubbles present in the return line and hence all the bubbles present at *VSG1* can be considered as bubbles that find their origin in nucleation at the primary heat exchanger wall. Furthermore, these results suggest that the bubbles are dissolved or bubble up to high points, such radiators, during their flow in the closed loop central heating system.

As part of this analysis, a consideration was given to the possible existence of a slip ratio between the two phases. Chisholm (1983) defined the slip ratio or phase relative velocity, as the difference between the phase velocities calculated through the subtraction of the fluid velocity from the gas velocity. Kocamustafaogullari et al. (1994) reported that in vertical flow, there exists a positive relative velocity between bubbles and the continuous phase whereas small but negative average relative velocities were observed in the horizontal flow. In their modelling calculations for the void fraction predictions in horizontal pipe bubbly flow, they assumed that the relative velocity is negligible and hence ignored its effects.

Serizawa et al. (1975) reported quasi uniform slip ratio distributions across the pipe section in vertical upward flow. They also reported an increase in the slip ratio with an increase in the void fraction. Similar findings were obtained by Lu and Tryggvason (2007), who reported an increase in the slip ratio with larger bubbles in two-phase bubbly downward flow in the pipe core following direct numerical simulations. Winterton and Munaweera (2001) assumed a

homogenous non slip flow for their study in vertical upward two-phase flow characterized by bubble diameters in the range of 0.1 to 0.9 mm. Furthermore, Thang and Davis (1979) assumed that all bubbles travel in the same direction with the same average velocity. Hence, considering the small bubble diameters measured in the current study and the limited volumetric void fractions, a non-slip flow across the pipe section was assumed.

Coalescence and breakup were assumed to be negligible due to the small bubble size (Hepworth et al, 2003) and due to the low volumetric void fraction which renders the possibility of bubble collision at the exit of the heat exchanger as unlikely (Lubetkin and Blackwell, 1988). Furthermore, the bubble dissolution rates were also assumed to be negligible due to adiabatic conditions at the exit of the heat exchanger and due to the relatively small temperature difference between the bulk fluid and the heat exchanger wall. In fact, an average temperature difference of circa 10 $^{\circ}$C was calculated.
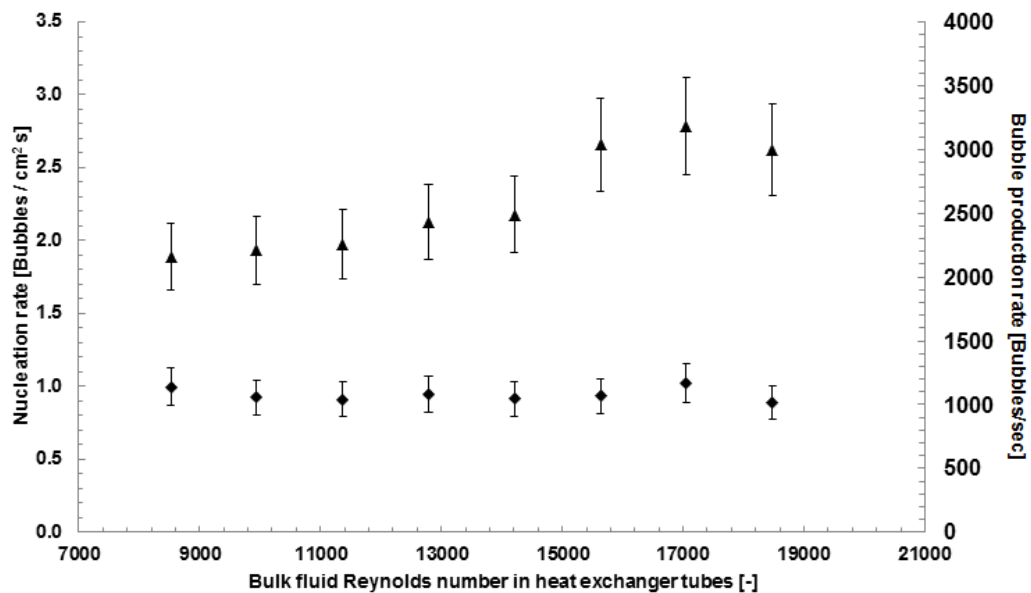
Figure 4.21: Bubble production and nucleation rates measured at boiler exit with bulk fluid Reynolds number in heat exchanger tubes *(Experiment: BNT I in Table 3.5).*

The experimental results have shown that the system bubble production rate is in the range of 784 to 6,920 bubbles per second. Furthermore, the bubble production rate, increased with;

- Increasing bulk fluid velocity

127

- Increasing heat flux

- Increasing super saturation levels

- Decreasing system pressure (abs)

Figure 4.22: Bubble production and nucleation measured at the boiler exit with heat flux at the primary heat exchanger wall *(Experiment: BNT II in Table 3.5).*

Figure 4.23: Bubble production and nucleation rates measured at the boiler exit with the saturation ratio at the primary heat exchanger wall conditions *(Experiment: BNT III in Table 3.5).*
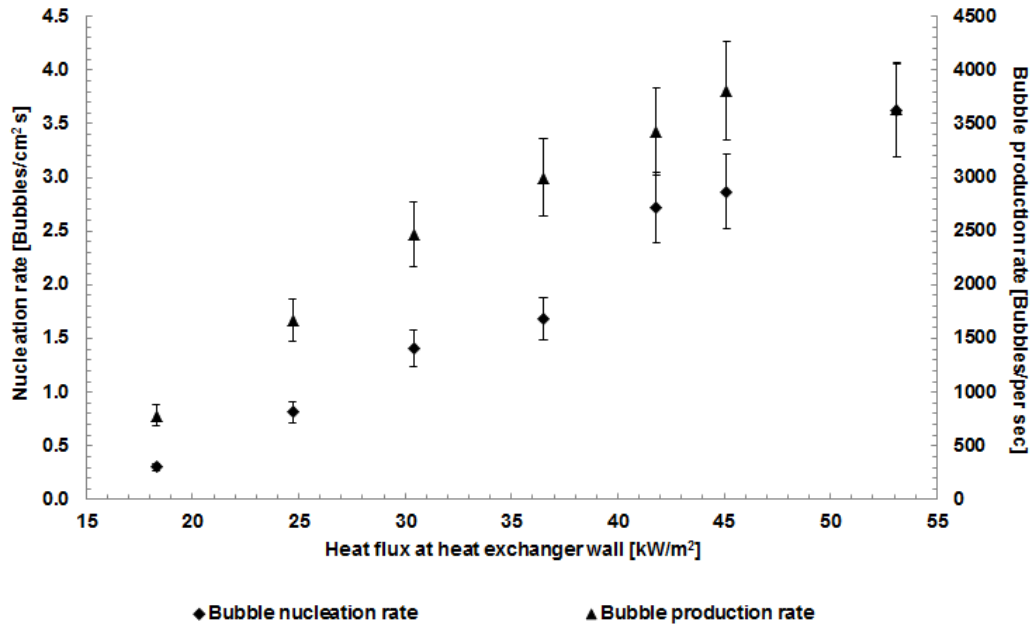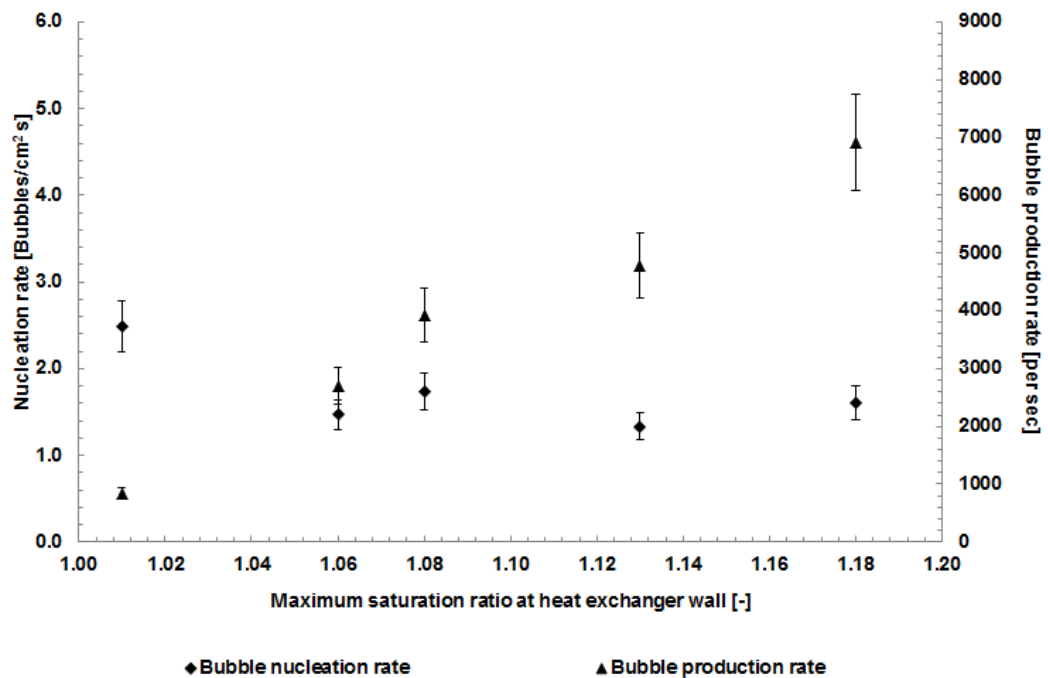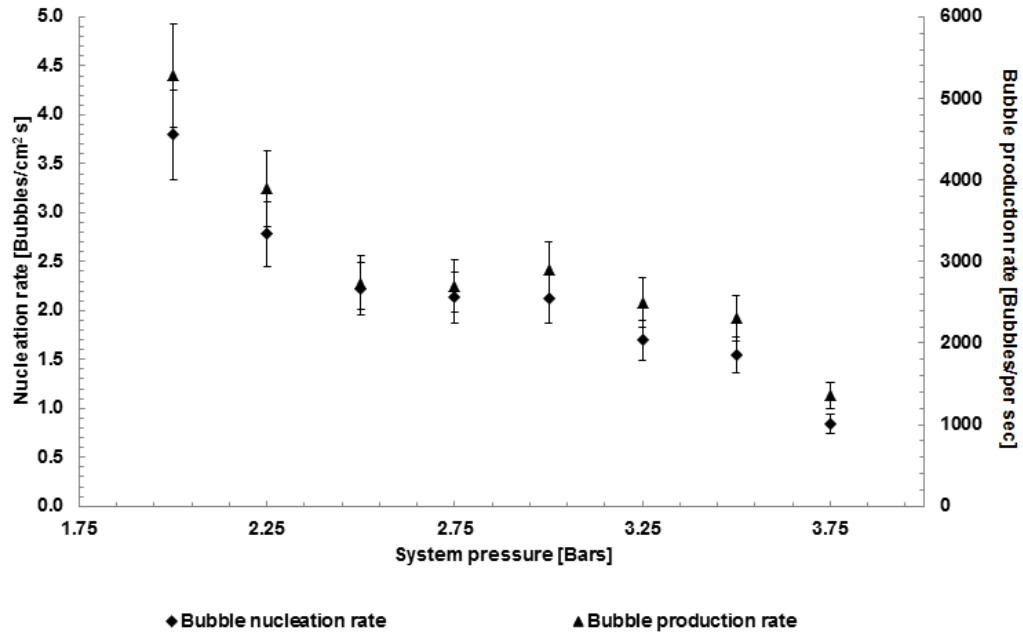
Figure 4.24: Bubble production and nucleation rates measured at the boiler exit with the system pressure (abs) *(Experiment: BNT IV in Table 3.5).*

The calculated bubble nucleation rate per unit surface area, dependent on the calculated heat exchanger surface area under super saturation conditions, ranged between 0.3 to 4 bubbles/cm^2 s. As illustrated in Figures 4.21&4.23, the calculated nucleation rates with the system parameters were not directly proportional to the trends for the bubble production rate as outlined above. Hence, the nucleation rate;

- Increased marginally with bulk fluid velocity
- Increased with heat flux
- Quasi-constant with super saturation levels
- Decreased with system pressure

It is evident that the nucleation rate per unit heat exchanger area is not directly proportional to the resultant system bubble production rate. This phenomenon is attributed to the change in the heat exchanger surface area under super saturation conditions with the system parameters. The latter area is quasi-constant in the experiments done with changing heat flux and system pressure. However, the area under super saturation conditions increases considerably with the bulk fluid gas concentration and fluid velocity. Therefore, as the dissolved gas concentration is increased, a larger heat exchanger surface area is under super saturation conditions as a result of the lower temperature at the primary heat

129

exchanger wall required for saturation conditions. Therefore, the system bubble production rate increases with the dissolved gas concentration whereas the nucleation rate per unit area of heat exchanger is quasi-constant. Hence, the increased heat exchanger area under super saturation conditions results in degassing over a larger surface area and consequently does not result in an increase in the nucleation rate per unit area.

The cavity bubble production model as presented by Hepworth et al. (2003) and outlined in Eq. (2.12), predicted similar trends for bubble production with respect to a change in all of the system parameters. Therefore, our experimental results suggest that the approach by Hepworth et al (2003) in using the penetration theory as simplified by Al-Hayes and Winterton (1981a,b) to include the effects of liquid motion on the bubble growth rate is in agreement with our experimental results. This is true, as an increase in the production rate was observed with an increase in the bulk fluid velocity which is in turn is not represented through the classical models for heterogeneous nucleation. The latter models, also predict an increase in the nucleation rate with an increase in the system pressure. This contrasts to the findings of the present study and to the non-classical model which predicts a reduction in the resultant nucleation rate with system pressure.

Higher liquid velocities increase the mass transfer coefficient for gas entering the bubble from the bulk liquid thus increasing the nucleation rate (Hepworth et al, 2003). An increase in the bulk fluid velocity also results in a decrease in the resultant bubble detachment radius (Winterton, 1972a, Fsadni et al., 2011) and therefore, a higher concentration gradient of gas is assumed to be present at the primary heat exchanger surface, thus enabling more bubbles to be released from the heat exchanger surface at a given time instant. Therefore, the inclusion of the predicted bubble detachment radius in Hepworth et al.'s bubble production model, resulted in nucleation rates being inversely proportional to the predicted bubble detachment radius, thus resulting in good trend predictions with respect to the changing system parameters.

Higher heat flux levels or system heating loads, resulted in higher heat exchanger wall temperatures, consequently increasing the dissolved gas diffusivity at the heat exchanger wall conditions. Therefore, as predicted by Hepworth et al., this

leads to an increase in the resultant bubble nucleation rate. Furthermore, an increase in the bulk fluid saturation ratio, results in an increase in the dissolved gas concentration gradient, thus enabling a higher bubble production rate, with the nucleation rate being quasi-constant due to the experimental conditions. Hence the latter result in an increase in the heat exchanger surface area under super saturation conditions with increased bulk fluid dissolved gas concentrations. The effect of pressure on the nucleation rate can be attributed to the classical theory for bubble formation and growth (Dean, 1944) as given in the Laplace Equation as in Eq. (2.7) and illustrated in Fig. 2.4. Therefore, higher system pressures require higher gas pressures in the bubble for nucleation and growth at the heat exchanger wall, consequently leading to an increase in the nucleation time and a reduction in the nucleation rate (Jones et al., 1999b).

4.4.1 Volumetric void fraction at boiler exit

The resultant cumulative volumetric void fraction and gas flow rates with system conditions are presented through Figs. 4.25-4.32. A maximum volumetric void fraction of 6.6E-4 was measured at the boiler exit through sight glass *VSG1* while the corresponding gas volume flow rate was calculated as 470 cm^3 of Nitrogen gas per hour at the maximum saturation ratio at the primary heat exchanger wall.
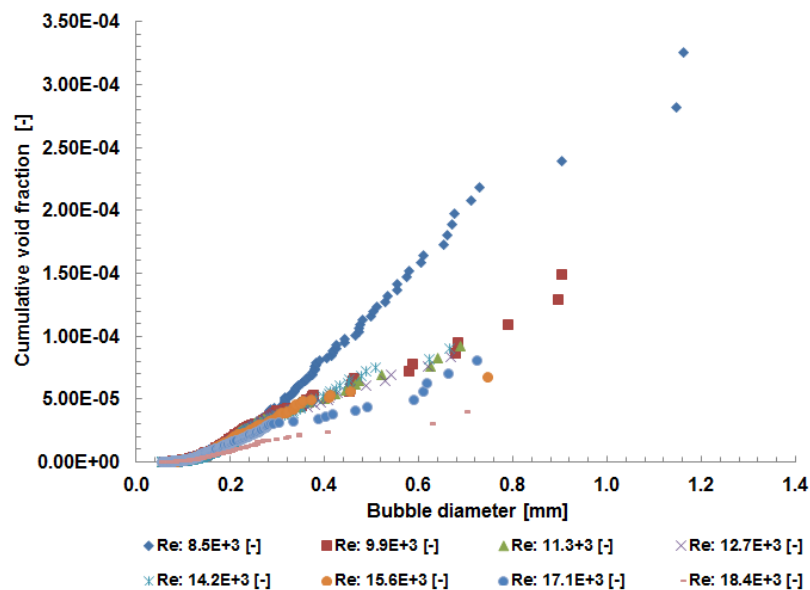

Figure 4.25: Cumulative volumetric void fraction at boiler exit (*VSG1*) with bubble size for bulk fluid velocity tests *(Experiment: BNT I in Table 3.5)*.

The experimental error of ±19.67% in the volumetric void fraction calculation is not illustrated in Figs. 4.25, 4.27, 4.29 and 4.31 due to the large number of data points shown on these charts.
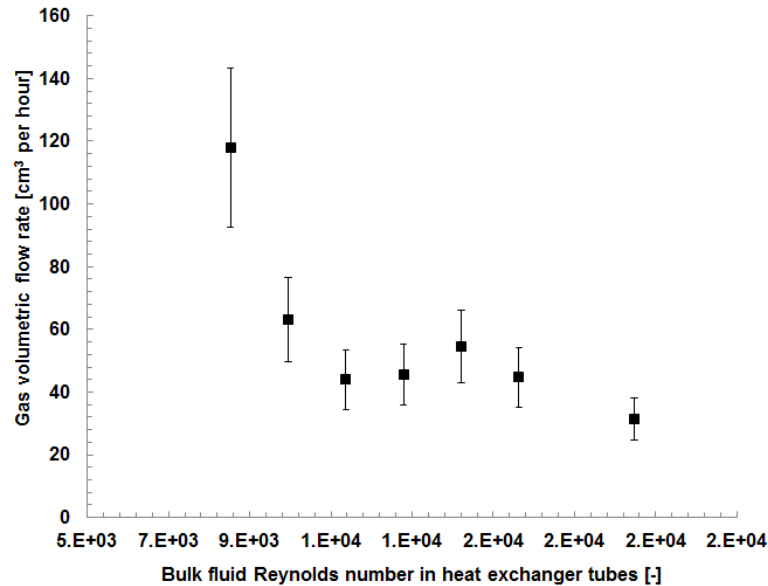
Figure 4.26: Gas volume flow rate at boiler exit (*VSG1*) with bulk fluid Reynolds number in the heat exchanger tubes *(Experiment: BNT I in Table 3.5)*.

Figs. 4.25 & 4.26 illustrate the fact that in spite of the higher bubble production rates at elevated bulk fluid velocities, quantified through the bulk fluid Reynolds number, larger volumetric void fractions and gas volume flow rates were calculated for the lower bulk fluid velocities. This is inherent to the fact that larger bubble diameters were measured at lower bulk fluid Reynolds numbers. Therefore, as the volume of the second phase is a function of the cube of the bubble radius, higher volumetric void fractions and gas volume flow rates were measured at the lower bulk fluid velocities.

The cumulative volumetric void fraction and gas volume flow rates with heat flux are illustrated in Figs. 4.27 & 4.28. As predicted, these results are directly proportional to the bubble size measurements and bubble production rates measurements discussed in Sections 4.3.2.3 & 4.4 respectively. Hence, an increase in the volumetric void fraction and the gas volume flow rate was measured with heat flux. The presence of a single bubble measured with a diameter of circa 1.5 mm at a heat flux of 53.1 kW/m^2, could be attributed to a

possible coalescence event between the primary heat exchanger wall and the vertical sight glass.
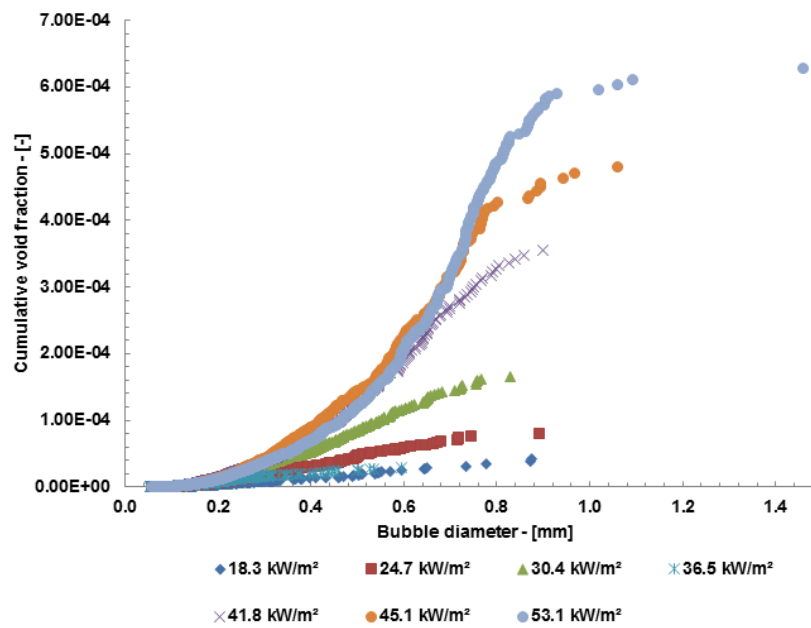
Figure 4.27: Cumulative volumetric void fraction at boiler exit (*VSG1*) with bubble size for heat flux at the primary heat exchanger *(Experiment: BNT II in Table 3.5).*

Figure 4.28: Gas volume flow rate at boiler exit (*VSG1*) with heat flux at the primary heat exchanger surface *(Experiment: BNT II in Table 3.5).*

Similar predictions are illustrated in Figs. 4.29 & 4.30, where the cumulative volumetric void fraction and gas volume flow rate with the maximum saturation ratio at the primary heat exchanger wall are illustrated.
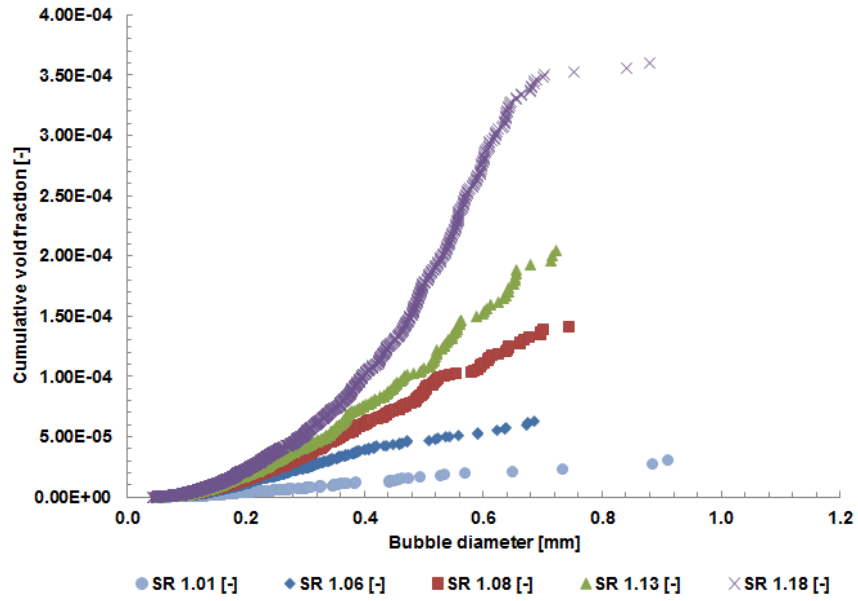
Figure 4.29: Cumulative volumetric void fraction at boiler exit (*VSG1*) with the maximum saturation ratio at the primary heat exchanger surface *(Experiment: BNT III in Table 3.5).*
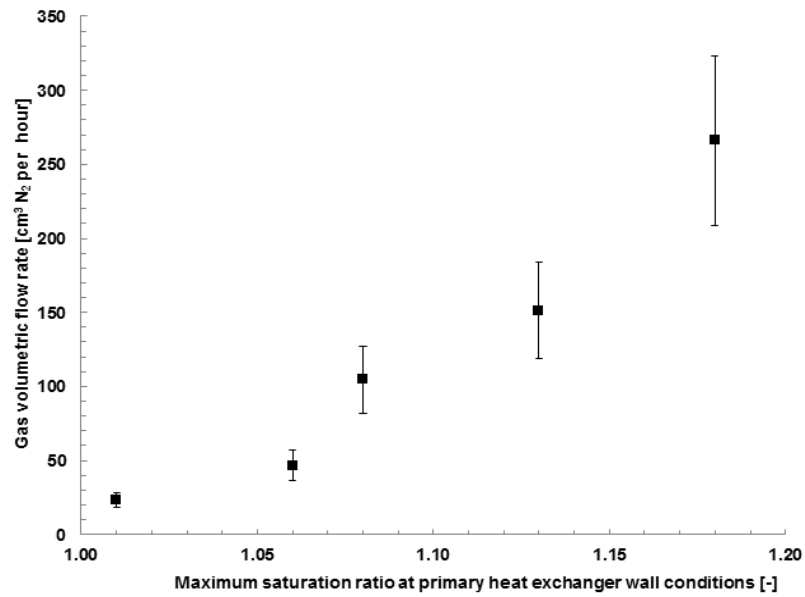
Figure 4.30: Gas volume flow rate at boiler exit (*VSG1*) with maximum saturation ratio at the primary heat exchanger surface *(Experiment: BNT III in Table 3.5).*

The increase in the volumetric void fraction with saturation ratio is solely attributed to the higher bubble production rates as quasi-constant bubble diameters are expected with a change in the maximum saturation ratio at the primary heat exchanger wall.
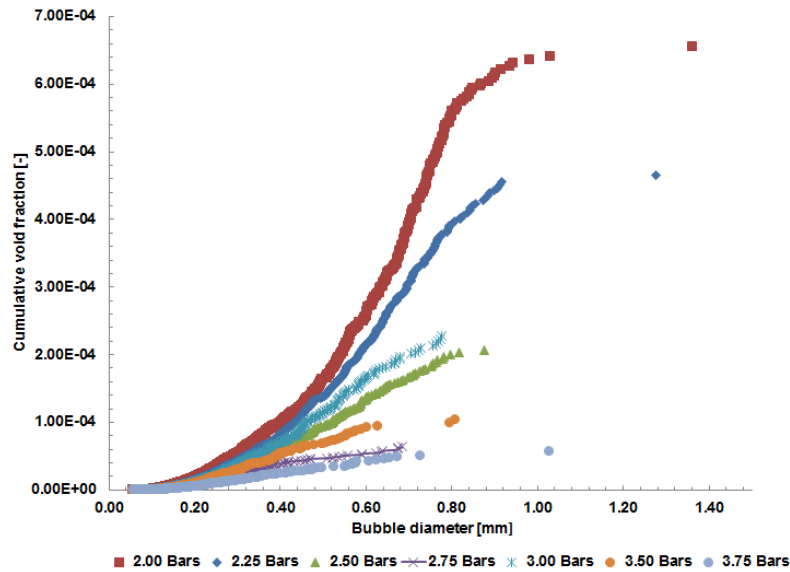
Figure 4.31: Cumulative volumetric void fraction at boiler exit (*VSG1*) with bubble size for system pressure (abs) tests *(Experiment: BNT IV in Table 3.5)*.

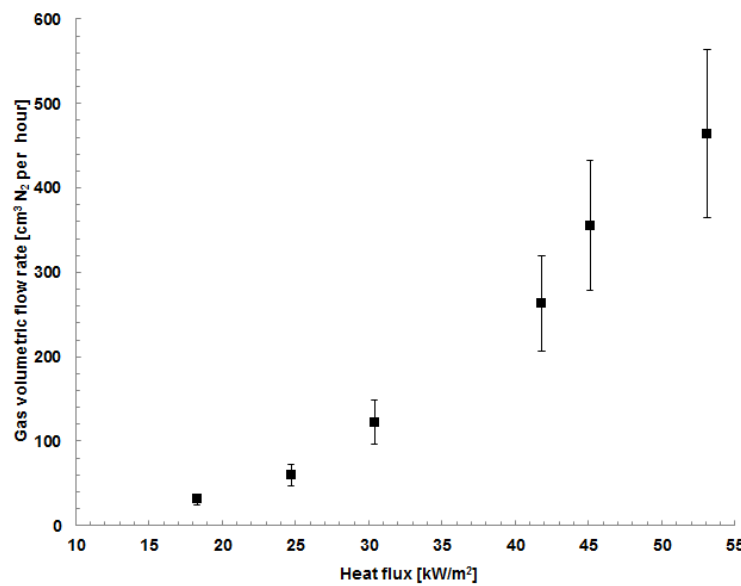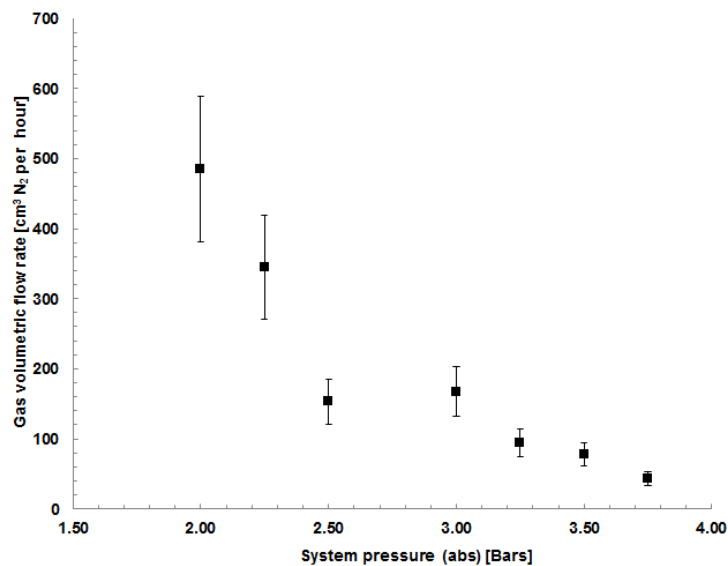**Figure 4.32: Gas volume flow rate at boiler exit (*VSG1*) with heat flux at the primary heat exchanger surface *(Experiment: BNT IV in Table 3.5)*.**

Figs. 4.31 & 4.32 illustrate the cumulative volumetric void fraction and gas volume flow rates with the system pressure. This data is proportional to the bubble production results, hence resulting in a higher void fraction at lower system pressures. Furthermore, the larger bubble diameters measured at lower system pressures, as discussed in Section 4.3.2.2, also contribute to the higher volumetric void fractions at lower pressures. The results illustrated in Fig. 4.31, also suggest that a coalescence event could have resulted in a single bubble diameter of circa 1.4 mm measured at the lowest system pressures.

4.5 Bubble behaviour in straight horizontal pipes

This section will present the results for the tests done at the horizontal sight glasses *HSG1&2*, as outlined in Section 3.4.6 with the relevant experimental parameters tabulated in Table 3.6. Hence the volumetric void fraction distribution, bubble size distribution, dissolution and behaviour in supersaturated solutions with bulk fluid velocity, saturation ratios, and flow line temperature will be presented. The analysis done in the present study has shown that bubbles are mostly spherical in shape and hence minimal distortion is present due to the surrounding bulk fluid flow. This is in agreement with recent studies done on bubbly flows (Winterton and Munaweera, 2001), where slip ratios of 1 were observed with similar bulk fluid velocities. The Reynolds number in the pipe work under consideration in the present study, was in the range of 13,800 to 26,500. Hence, the velocity profile for fully developed turbulent flow can be assumed for the present study. The range of bubble diameters measured at both sight glasses is in the range of 0.05 mm to 1.5 mm.

4.5.1 Void fraction and bubble distribution in horizontal pipes in system flow line

The horizontal pipe results illustrated in Figs. 4.33 - 4.39 illustrate the volumetric void fraction distribution with the saturation ratio and fluid velocity, quantified through the dimensionless bulk fluid Reynolds number, for the horizontal pipe tests *HPT_US* and *HPT_FR I-VI* as Tabulated in Table 3.6 across sight glasses *HSG1&2*. The relevant experimental uncertainty of ±19.67%, as calculated in Section 3.6.6, is illustrated in Figs. 4.33 – 4.39 in the form of error bars on the individual data points. The tests suggest that the volumetric void fraction distribution along straight horizontal pipes is strongly dependent on the gravity effect and the bulk fluid velocity. The results presented in this section contrast with the results obtained for vertical downward flow volumetric void fraction distributions whereby quasi homogenous distributions were measured across the sight glass test section. Hence, it is clear that the void fraction distribution in horizontal pipes is effected by the buoyancy effect of bubbles thus resulting in a higher void fraction at the upper section of the pipe.
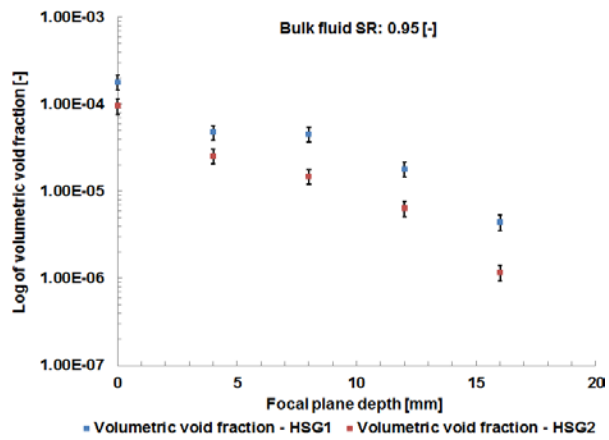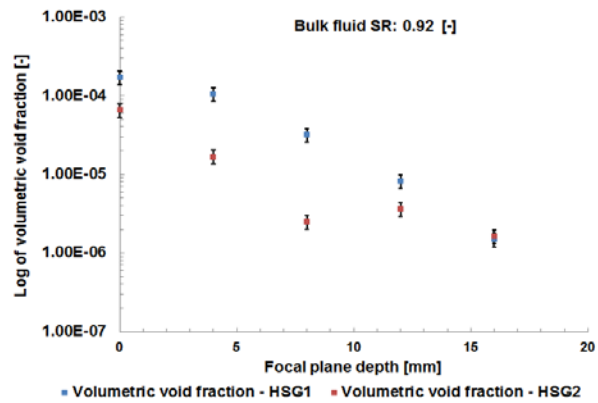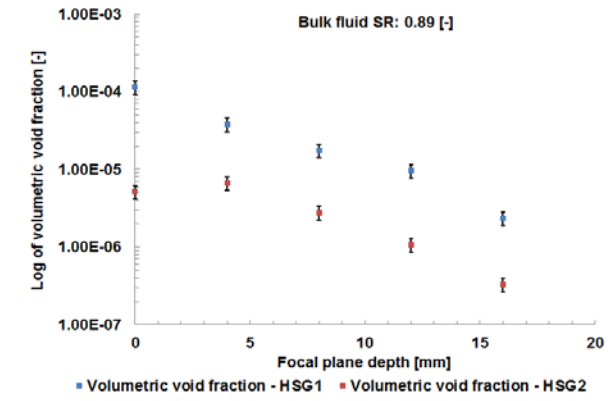
Figure 4.33: Volumetric void fraction for horizontal under saturation pipe tests *(Experiment: HPT_US in Table 3.6).*
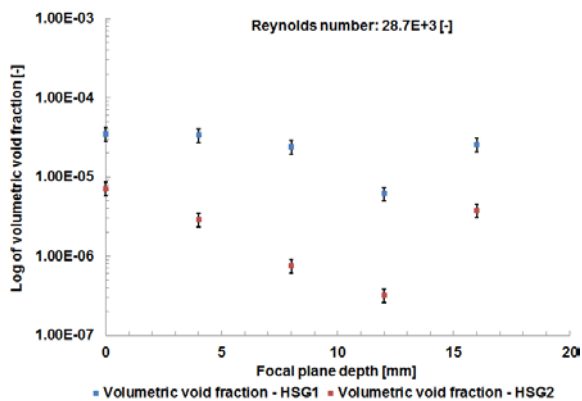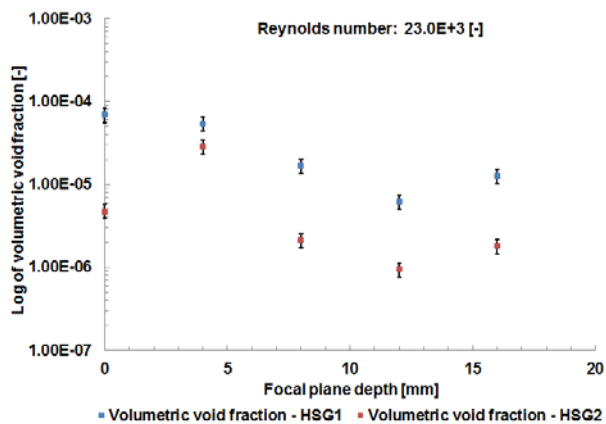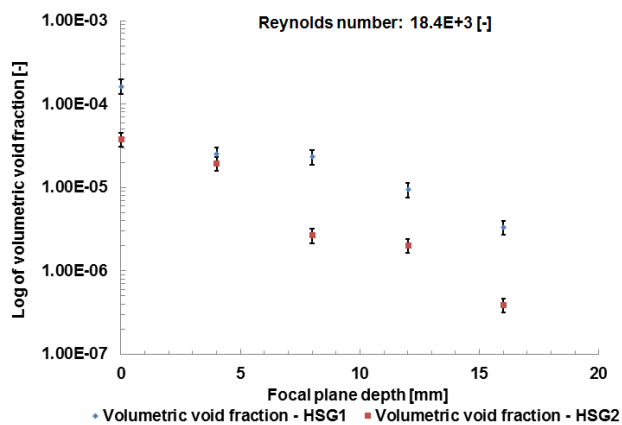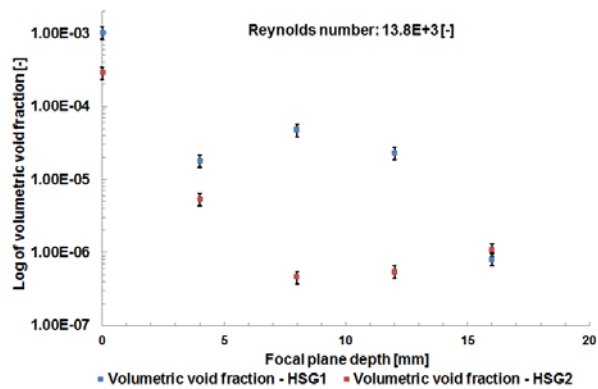
Figure 4.34: Volumetric void fraction for horizontal under saturation pipe tests with bulk fluid Reynolds number and high flow temperature *(Experiment: HPT_FR I in Table 3.6)*.
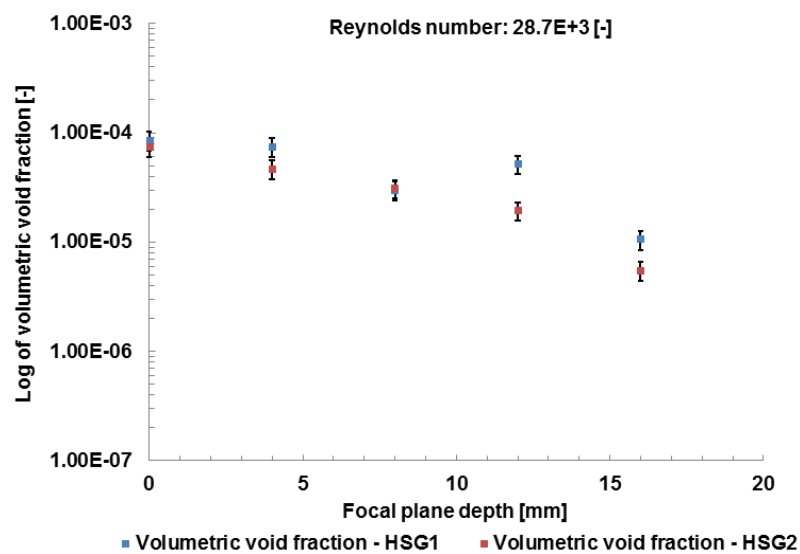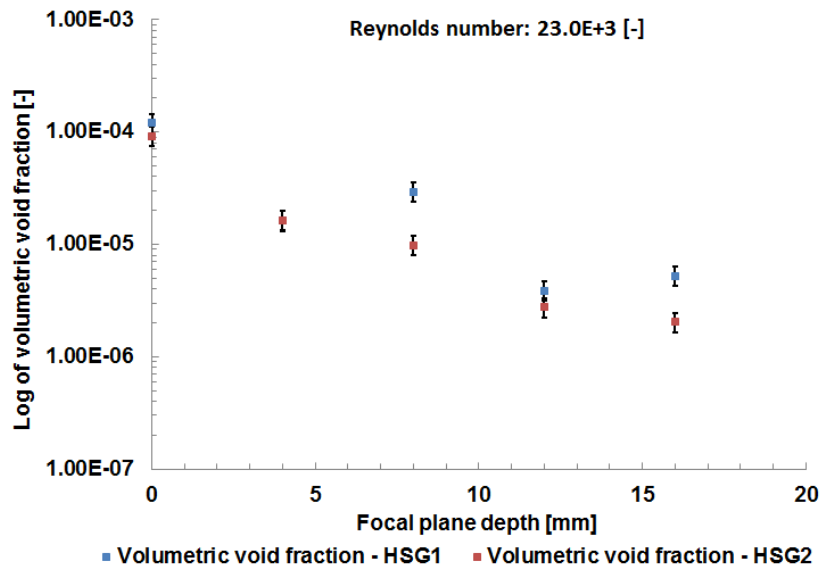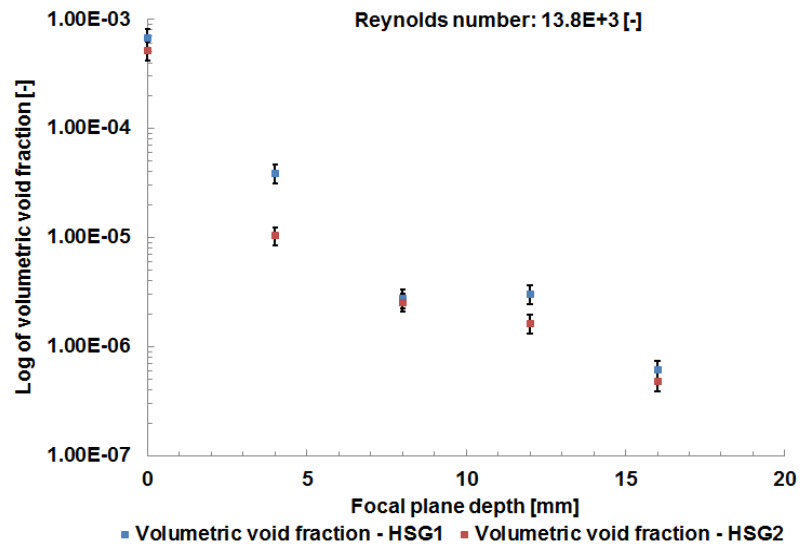
Figure 4.35: Volumetric void fraction for horizontal saturation pipe tests with bulk fluid Reynolds number and high flow temperature: *(Experiment: HPT_FR II in Table 3.6).*
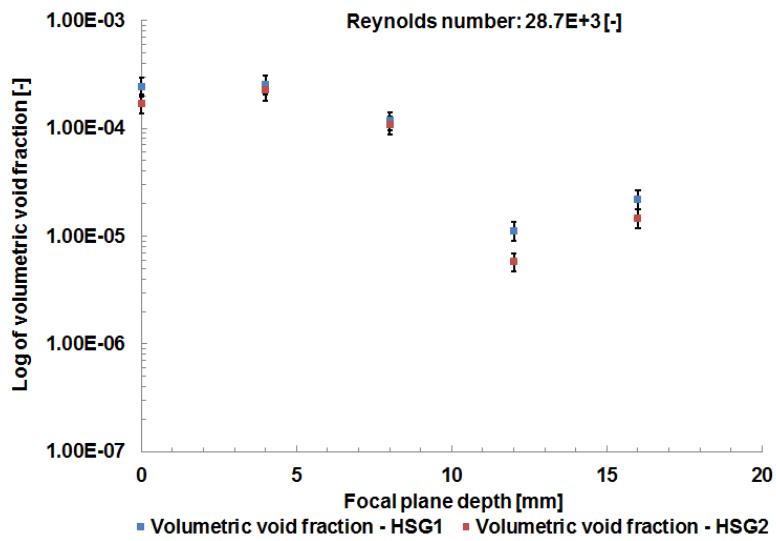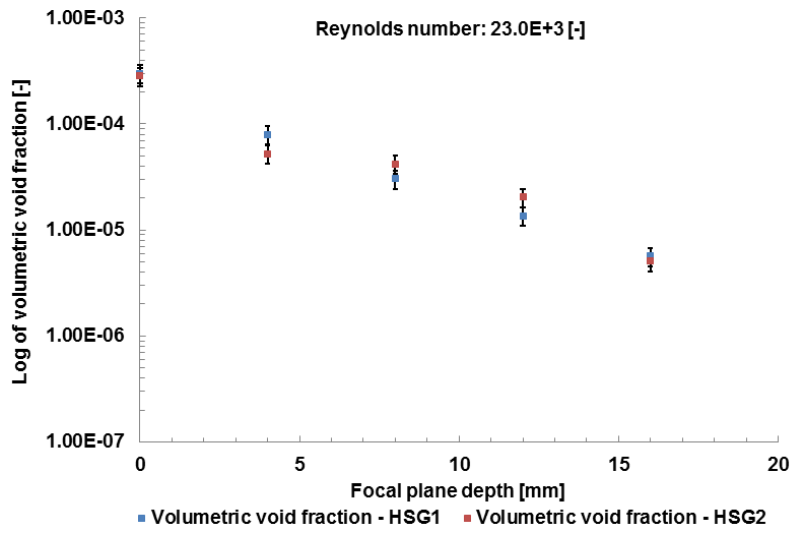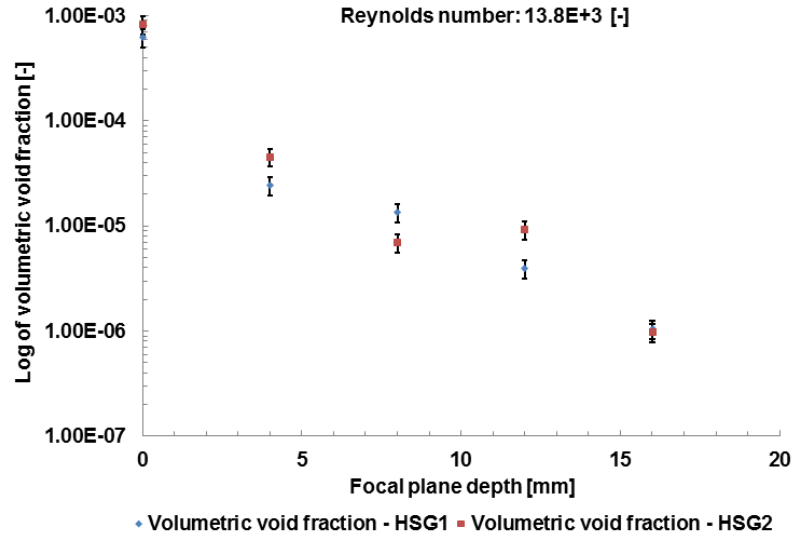
Figure 4.36: Volumetric void fraction for horizontal super saturation pipe tests with bulk fluid Reynolds number and high flow temperature *(Experiment: HPT_FR III in Table 3.6).*
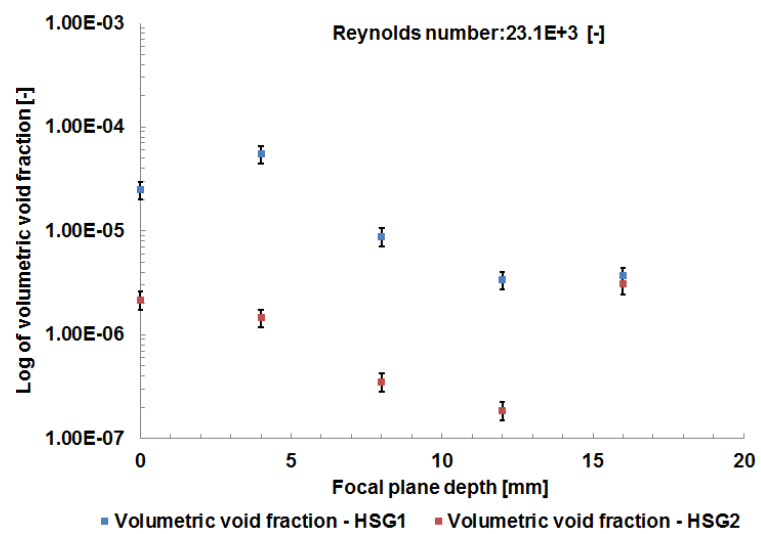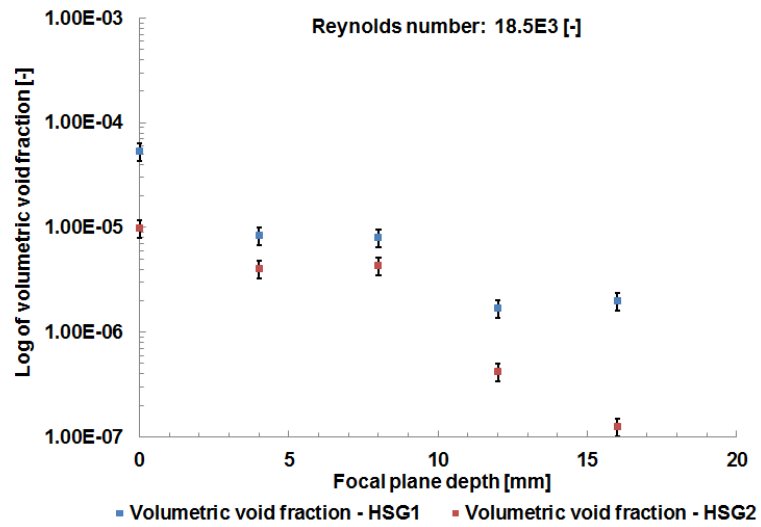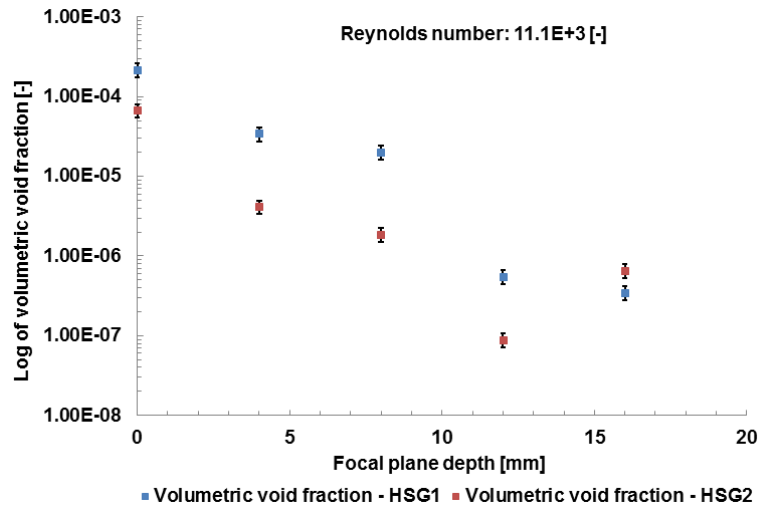
Figure 4.37: Volumetric void fraction for horizontal under saturation pipe tests with bulk fluid Reynolds number and low flow temperature *(Experiment: HPT_FR IV in Table 3.6).*
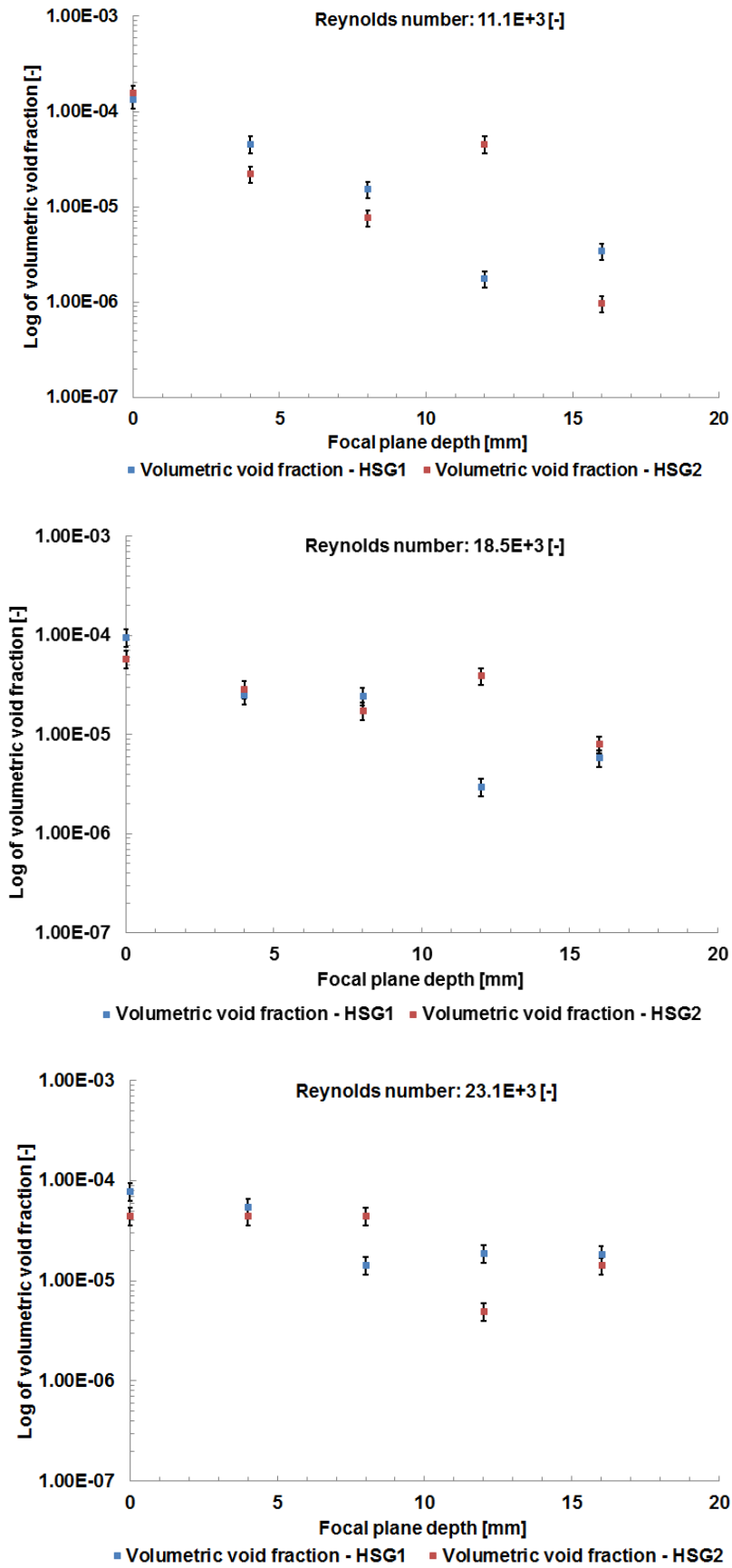
Figure 4.38: Volumetric void fraction for horizontal saturation pipe tests with bulk fluid Reynolds number and low flow temperature *(Experiment: HPT_FR V in Table 3.6).*
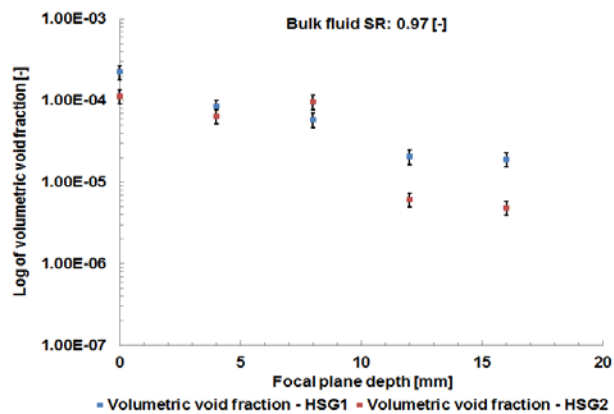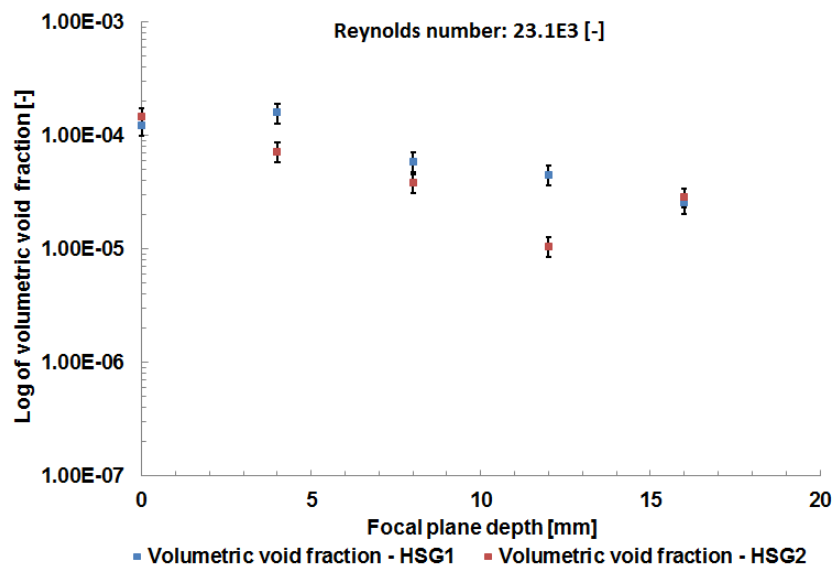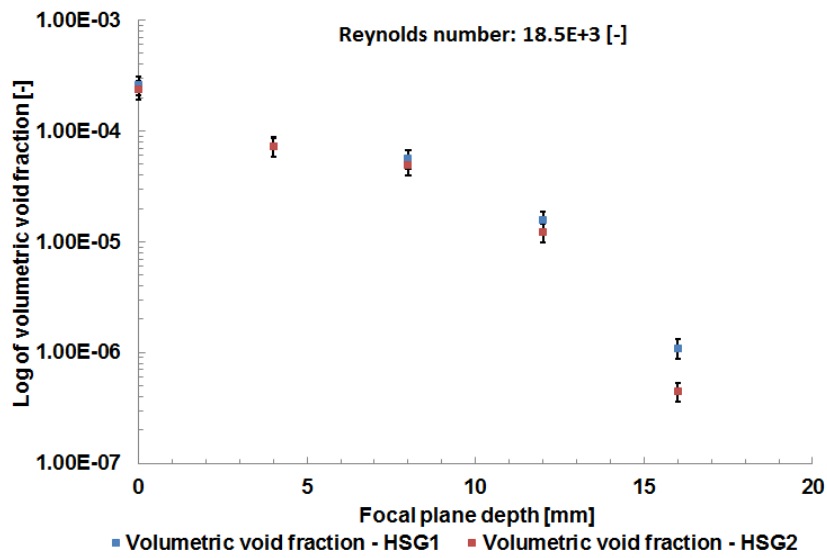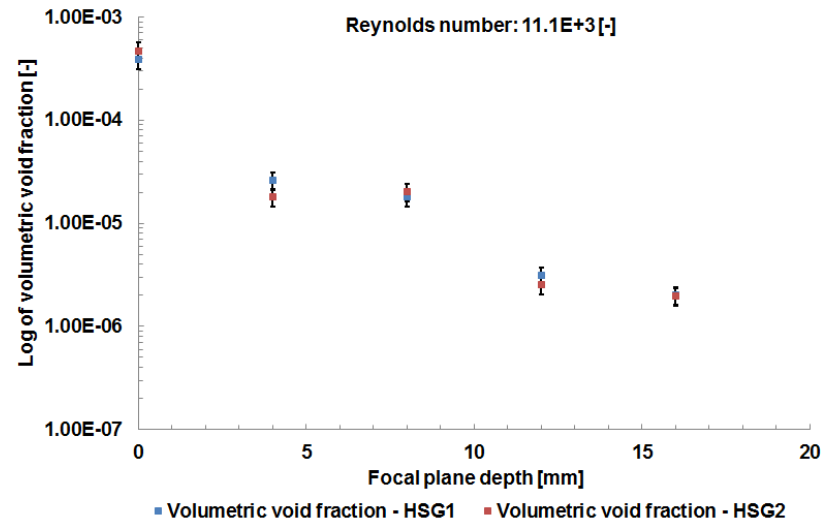
Figure 4.39: Volumetric void fraction for horizontal super saturation pipe tests with bulk fluid Reynolds number and low flow temperature *(Experiment: HPT_FR VI in Table 3.6).*

143

Fig. 4.40 summarizes the results by presenting the mean percentage volumetric void fraction measured at the focal depth of 16 mm in relation to the relevant void fraction measured at the topmost focal plane (0mm) with bulk fluid velocity. Hence, for all testing conditions, a significantly higher void fraction was measured at the topmost focal plane. As illustrated in Fig. 4.40 such trends are also evident after considering the experimental uncertainty represent through error bars on the individual data points.
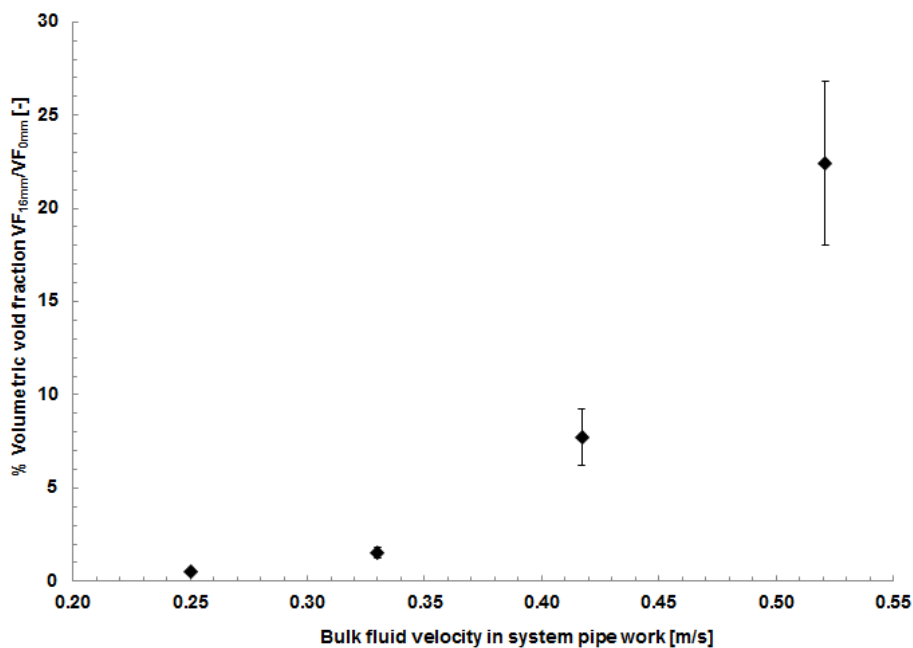
Figure 4.40: Mean % volumetric void fraction measured at a pipe depth of 16 mm in relation to that measured at the 0 mm plane for horizontal pipe tests with bulk fluid velocity.

Furthermore, as illustrated in Figs 4.34 - 4.39, a higher percentage void fraction at the top section of the pipe was consistently measured at lower bulk fluid velocities. Therefore, a more evenly distributed volumetric void fraction profile is expected with higher bulk fluid velocities. Such a phenomenon could be attributed to the higher degree of turbulence, thus resulting in an improved dispersion of the second phase and to the presence of larger bubbles at lower bulk fluid velocities. Hence, larger bubbles result in stronger buoyancy forces consequently resulting in higher volumetric void fractions at the upper most section of the pipe.

The flattening of the void fraction distribution across the pipe line with bulk fluid velocity has also been reported by Iskandrani and Kojasoy (2001). The overall

system mean volumetric void fraction and bulk fluid temperature, does not appear to have on effect on the resultant horizontal pipe void fraction distribution. This is also consistent with the similar void fraction distribution patterns measured at the two sight glasses *HSG1&2*, irrespective of whether under or super saturated bulk fluid conditions were present.

The trends in the void fraction distribution reported in the present study are in agreement with the findings reported by Kocamustafaogullari and Wang (1991), Beattie (1996) and Iskandrani and Kojasoy (2001). In fact, Iskandrani and Kojasoy defined horizontal bubbly pipe flow as a bubbly flow whereby due to the dominating influence of the buoyancy force, bubbles flow mainly in the upper portion of the pipe, while the lower portion of the channel carries more liquid with the void fraction nearing zero at the bottom. However, a direct comparison with experimental data available in the open literature sources is not possible due to the minimal consideration given by literature to horizontal bubbly pipe flow. This gap in literature is emphasized by Iskandrani and Kojasoy (2001), whereby they stated that most related experimental studies were done for vertical pipe flow. They reported that further experimental work is necessary to attain a thorough physical understanding of the internal flow structure and flow field of a bubbly two-phase flow-pattern.

Kocamustafaogullari and Wang (1991), Beattie (1996) and Iskandrani and Kojasoy (2001) reported a distinct void fraction peak near the top of the wall at a radial position of about 80 – 90% from the pipe centre line. This finding could be attributed to the higher bulk fluid velocities used. However, such a phenomenon could not be identified and measured in the present study due to the limitations of the focal depth at which measurements were taken. In fact, Kocamustafaogullari and Wang (1991) and Iskandrani and Kojasoy (2001) made use of the double-sensor resistivity probe method and the hot-film anemometry method in their experimental work, hence enabling more measurement intervals along the pipe section.

Iskandrani and Kojasoy (2001) reported that the increased bubble population towards the top of the pipe creates an additional resistance to the liquid flow resulting in a retardation of the liquid mean velocity towards the top of the tube.

They also reported that a reduction in the mean liquid velocity in the latter region would result in a considerable increase of velocity in the rest of the pipe required to maintain the overall continuity. In their studies in horizontal bubbly pipe flow, Kocamustafaogullari and Wang (1991), Kocamustafaogullari et al. (1994) and Iskandrani and Kojasoy (2001) reported that in all their experiments, the peak void fraction never exceeded 65%. Hence, they concluded that the latter percentage indicates a maximum packing void fraction in the channel above which coalescence of bubbles occurs thus resulting in larger slug bubbles. Hence, the void fractions measured in the present study are much lower than the maximum at which slug flow is predicted, and hence bubble coalescence can be assumed to be insignificant. The measured void fractions with fluid velocity are in agreement with the findings done by Kocamustafaogullari and Wang (1991) who reported similar trends with the measured void fraction and bulk fluid velocity. Hence, in agreement with the findings of the present study, they reported a decrease in the average void fraction with an increase in bulk fluid velocity and a significant decrease in the value of the maximum void fraction, this being at the top of the horizontal pipe.

4.5.2 Bubble dissolution in horizontal pipes in system flow line at under saturation bulk fluid conditions

A good representation for the reduction in the mean bubble diameter and the relevant experimental uncertainties with the experimental parameters as illustrated in Table 3.6 and represented through the ratio R_x/R_0, is given in Fig. 4.41. Fig 4.42 illustrates the measured bubble ratios and the relevant experimental uncertainties at the five focal planes across the pipe depth. The experimental results are in reasonable agreement with the expected trends whereby a higher bubble dissolution rate was measured with increasing under saturation conditions. However, a direct comparison with experimental data and dissolution mathematical models available in literature sources is not possible as very limited consideration has been given by previously reported studies to similar physical conditions. As discussed in Section 2.2.4.1 of the present study, most bubble dissolution experimental studies and mathematical models were done for isolated bubbles under stagnant fluid conditions or for stationary bubbles on a wall under a bulk fluid flow. Hence, the gap in the available

literature on dissolution data and models for free moving bubbles in bubbly flows.
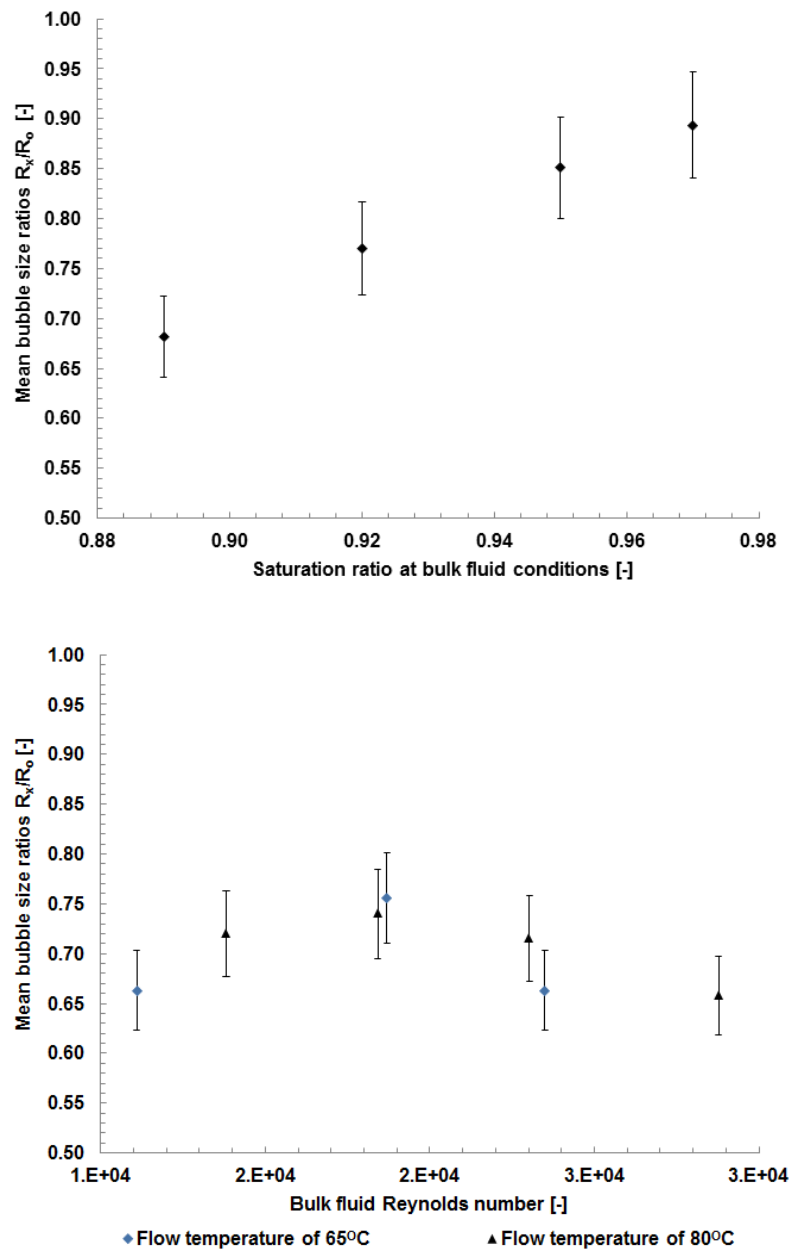
Fig. 4.41: Mean bubble size rations R_x/R_o with under saturation conditions for Experiments HPT_US (Top) and HPT_FR I and HPT_FR IV (Bottom) as in Table 3.6.

The measured mean bubble size ratios for the under saturation tests with a constant bulk fluid velocity *HPT_US* as in Fig. 4.41, yield a quasi linear relationship between the mean measured bubble radii ratios and the increase in the bulk fluid saturation ratio whereas the results for tests *HPT_FR I&IV* as in Fig. 4.41, suggest a minimal decrease in the resultant bubble dissolution rate with a reduced velocity. The reduction in the bulk fluid velocity from a maximum of

0.52 m/s to 0.25 m/s doubled the time for the bubble to flow through the pipe section under consideration. Hence, assuming that the bulk fluid turbulence effects are ignored, an opposite result is expected due to the increased time lag for bubbles to move between the two sight glasses, thus allowing more gas to diffuse out of the bubbles. Therefore, the results of the present study suggest that the increase in the degree of turbulence enhances the dissolution rate, thus overriding the effects expected by the increase in the time lag. The relative velocity in the direction of fluid flow between the bubbles and the bulk liquid phase was calculated to be in the range of 1E-3 to 9E-5 m/s through Eq. (4.1) (Adrian, 1991) and assuming an acceleration of 3g or less, as done in a related study by Shedd (2005). Therefore, the velocity gradient experienced by the bubbles can be assumed to be negligible for the purposes of the present study.

$$u_{rel} = \frac{\rho_g D_b^2 a}{36\mu} \tag{4.1}$$

As discussed by Liebermann (1957), Cable (1967) and Kentish et al. (2006), the presence of a relative motion between a bubble and the fluid, results in a velocity gradient and therefore the interaction between the flow of the liquid around the bubble and the concentration field in the liquid near the bubble would enhance the diffusion process whereby gas diffuses out of a gas bubble to a liquid in an under saturated state. Hence, in view of the negligible relative velocity between the two phases, it can be assumed that the degree of turbulence, enhances the concentration gradient around the bubble which is free flowing in the liquid, thus leading to the phenomenon of turbulent diffusion as classified by Kress and Keyes (1973) and Lezhnin et al. (2003) and quantified through the Sherwood number. Hence, the turbulence in the fluid is assumed to constantly introduce fresh under saturated bulk fluid around the dissolving bubble, thus increasing the gradient of the gas concentration boundary layer with the surrounding fluid. These results contrast to the findings by Shedd (2005), who reported that for free bubbles dissolving in a bubbly flow, it would be reasonable to use the pure diffusion model, thus assuming stagnant conditions with no relative velocity or degree of turbulence considerations.

A direct comparison with the bubble sizes and void fractions measured at the boiler flow line at sight glass *VSG1* is not possible due to the different testing

conditions used and due to the presence of a 90 degree bend between the vertical pipe and the straight horizontal pipe housing sight glasses *HSG1&2*.A comparison of the data obtained in the present study for bubble dissolution with experimental results reported in literature sources suggests that the dissolution rate observed for free bubbles flowing in a bubbly flow are significantly greater than the rates reported for the dissolution of an isolated sphere in stagnant water conditions and for static bubbles exposed to a velocity gradient. A number of recent studies (Kentish et al., 2006 and Shedd, 2005) have reported a good agreement between experimental results and correlations for the diffusion based models developed by Epstein and Plesset (1950) and Bankoff (1964) for isolated bubble experiments.

Hence, a comparison of our experimental results with results reported by Epstein and Plesset (1950) for the dissolution of isolated bubbles in under saturated solutions, suggests that a considerably longer dissolution time is necessary for similar bubble size ratios and original bubble diameters as investigated in the present study. Hence, through their experimental analysis, they reported a time lag of circa 92 seconds required for the dissolution of a bubble with an original diameter of 0.2 mm in water at an under saturation ratio of 0.75. Therefore, considering the time lag range of 3.3 to 6.9 seconds required for bubbles to flow between the two sight glasses, a major factor controlling the dissolution in turbulent flow is the turbulent diffusion process. Therefore, the present study reports that even though the relative velocity between the two phases is negligible, the degree of turbulence around the gas bubbles does result in an enhanced diffusion rate, consequently, considerably increasing the bubble dissolution rate. Hence, a good model for turbulent diffusion should incorporate the Sherwood number to incorporate the effects of the degree of turbulence on the diffusion process. Cable and Frade (1988), reported that as a gas diffuses out of a static isolated bubble, the inward flow of the solution always tends to make the solute accumulate around a dissolving bubble and consequently, this retards the dissolution rate for the isolated bubble. Therefore, this effect can be considered to be negligible for free bubbles flowing in a turbulent bubbly flow, hence, the reason for the higher dissolution rates measured in the present study.
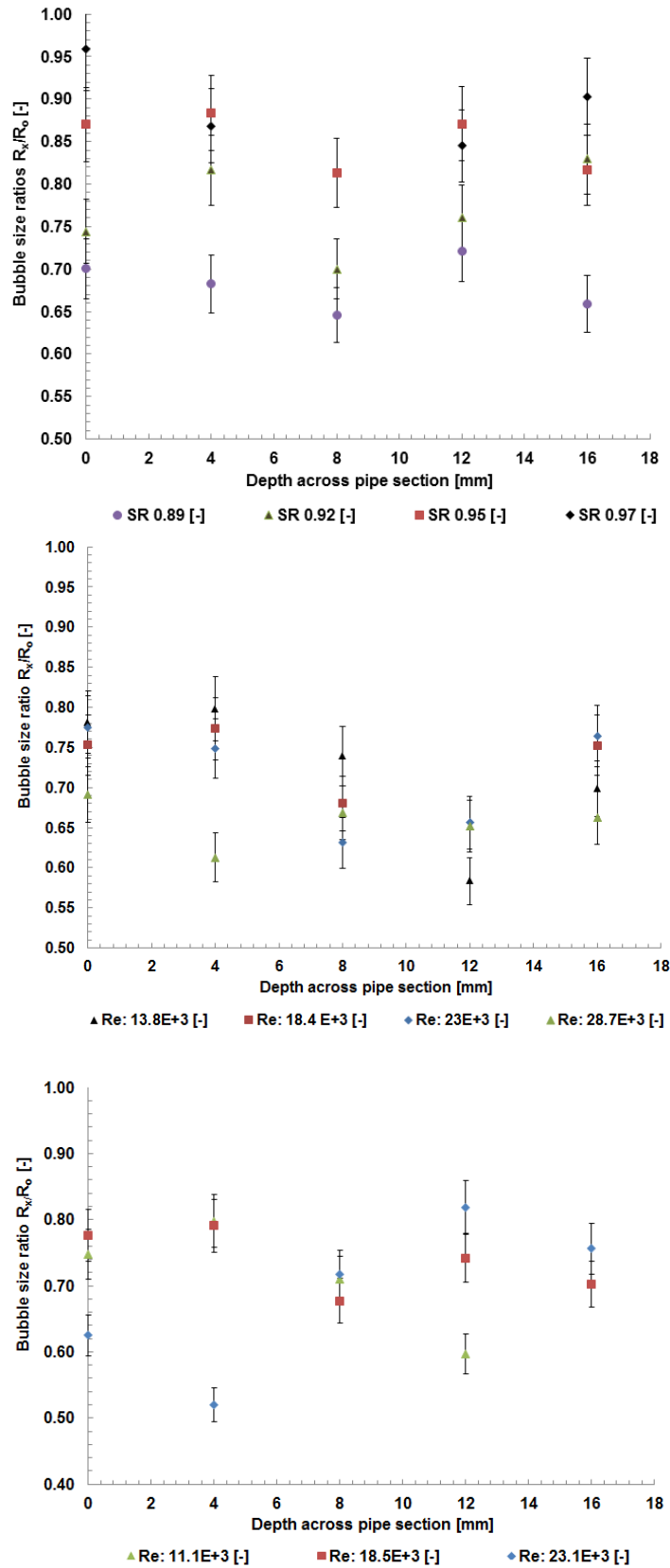
Fig. 4.42: Bubble size ratios R_x/R_o measured at intervals along the pipe depth for under saturation tests *(Experiments: HPT_US (Top), HPT_FR I (Middle) & IV (Bottom) in Table 3.6).*

Fig. 4.42, illustrates the results for the mean bubble size ratios and their relevant experimental uncertainties along the depth across the horizontal sight glass section for the under saturated tests *HPT_US* and *HPT_FR I&IV*. After considering the effects of the experimental uncertainties on the measured data, these results suggest that, the dissolution rate is more intense in the core section of the pipe whereas the dissolution measured at the top of the pipe tends to be slightly less than that measured at the core section. This phenomenon could be attributed to the presence of a larger density of bubbles in the upper section of the pipe as a result of stratification effects due to gravity, hence leading to a localized higher density of dissolved gas in the bulk fluid and consequently delaying the bubble dissolution process. However, the similar effect present at a pipe depth of 16 mm cannot be attributed to high localized gas densities as the bubble density was the lowest at this level. Walter and Blanch (1986) as cited in Hesketh et al. (1991), observed higher bubble breakage events at the centre of a pipe in turbulent flow. Hence, such a phenomenon could have contributed to the lower bubble size ratios measured at the centre of the pipe as illustrated in Fig. 4.43 through the assumed breakage of the larger sized bubbles present in the pipe core. The effects of the velocity boundary layer could have also contributed to this effect. Due to the limited consideration given by the open literature to the dissolution of free bubbles in bubbly flows, a direct comparison with similar results in literature is not possible.

The reduction in the volumetric void fraction with the system under saturation ratios and the bulk fluid velocity are illustrated in Figs. 4.44. As expected, the void fractions follow the trends shown by the changes in the bubble size. However, the measured changes in the void fractions were marginally different from the expected volumetric changes due to the measured bubble size. This could be attributed to the larger error in calculating the void fraction and to a low degree of bubble breakage events between the two sight glasses. The minimal effects that such events have on the present study can be attributed to the small bubble diameters (<1.5 mm) and the quasi spherical bubble shape observed in all experiments. In fact, Hesketh et al. (1991) reported that bubble elongation along the pipe up to four times the original diameter, is expected prior to a bubble breakage event.
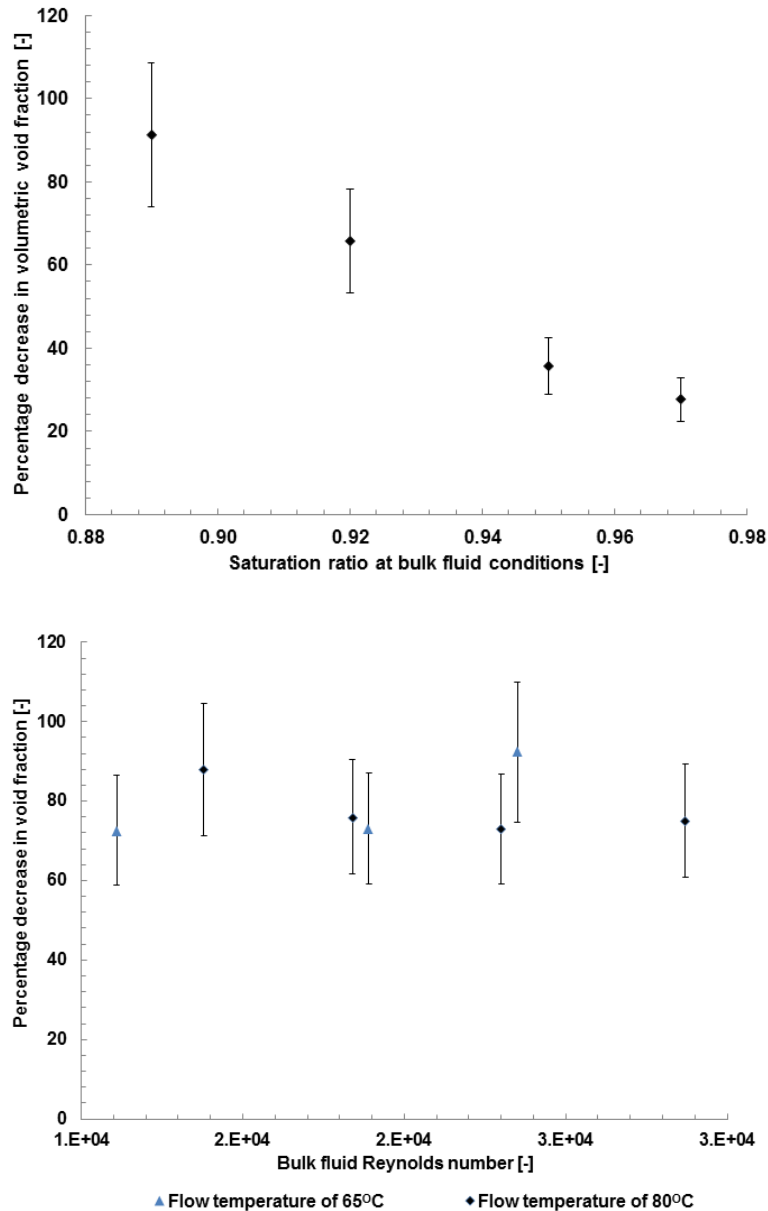
Fig.4.43: Reduction in void fraction with under saturation conditions *(Experiment: HPT_US (Top) and HPT_FR I & IV (Bottom) in Table 3.6).*

Through the consideration of the experimental uncertainties, a comparison of the results presented for the tests at high flow temperatures *HPT_FR I* with the corresponding results for low flow temperatures *HPT_FR_IV*, as in Figs. 4.42 and 4.43 does not yield any distinct trends in the bubble dissolution rate with a change in the bulk fluid temperature. Hence, quasi similar results were achieved for bubble dissolution with bulk fluid velocity at a high and low flow temperature. Such results could be attributed to the limited temperature range of 15 K, investigated in the present study as is expected in the flow line of a typical system. Gas and fluid properties, such as the gas diffusivity and fluid surface

tension, are expected to change with temperature. The former is expected to increase, while surface tension decreases with the bulk fluid temperature. Hence, some effects on the dissolution rates could be expected with temperature. However, in agreement with the findings of the present study, recent studies done by Shedd (2005), have reported that, provided similar gas concentration levels are maintained, the system temperature results in a minor impact on the dissolution rates of bubbles. This is in agreement with the results reported by Kentish et al. (2006), who reported that the surface tension affects for bubble dissolution with diameters larger than 300 μm are considered as minimal. Furthermore, most dissolution models as presented in the open literature (Epstein and Plesset, 1950; Bankoff, 1964; Honda et al., 2004; Ljunggren and Eriksson, 1997) assumed surface tension independence and hence this further supports the assumption for minimal effects on the bubble dissolution rate with temperature.

The present study did not investigate the effects of the system pressure on the bubble dissolution rate. However, the effect of pressure on the resultant bubble dissolution rate is assumed to be negligible. Hence, as discussed by Shedd (2005), changes to the bulk fluid pressure do not result in a change to the dissolution rate, because the increase in the concentration gradient is balanced by an increase in the amount of gas in the bubble. The influence of undetected contaminants in the water on the diffusivity and the overall bubble dissolution rate is also assumed to be negligible. Liebermann (1957), reported that contaminants introduced intentionally in water such as a neutral detergent, soap, mineral oil and vegetable oil did not significantly affect the dissolution rate for freely rising bubbles in water.

4.5.3 Bubble behaviour in saturated and supersaturated solutions in horizontal pipes in system flow line

A good representation for the change in the mean bubble diameter with respect to the experimental parameters as illustrated in Table 3.6 for the high and low temperature saturated and supersaturated tests, *HPT_FR II, III, V & VI,* and their relevant experimental uncertainties, are illustrated in Fig. 4.44 The resultant bubble ratios measured at the five focal planes across the pipe depth are given in Fig. 4.45.
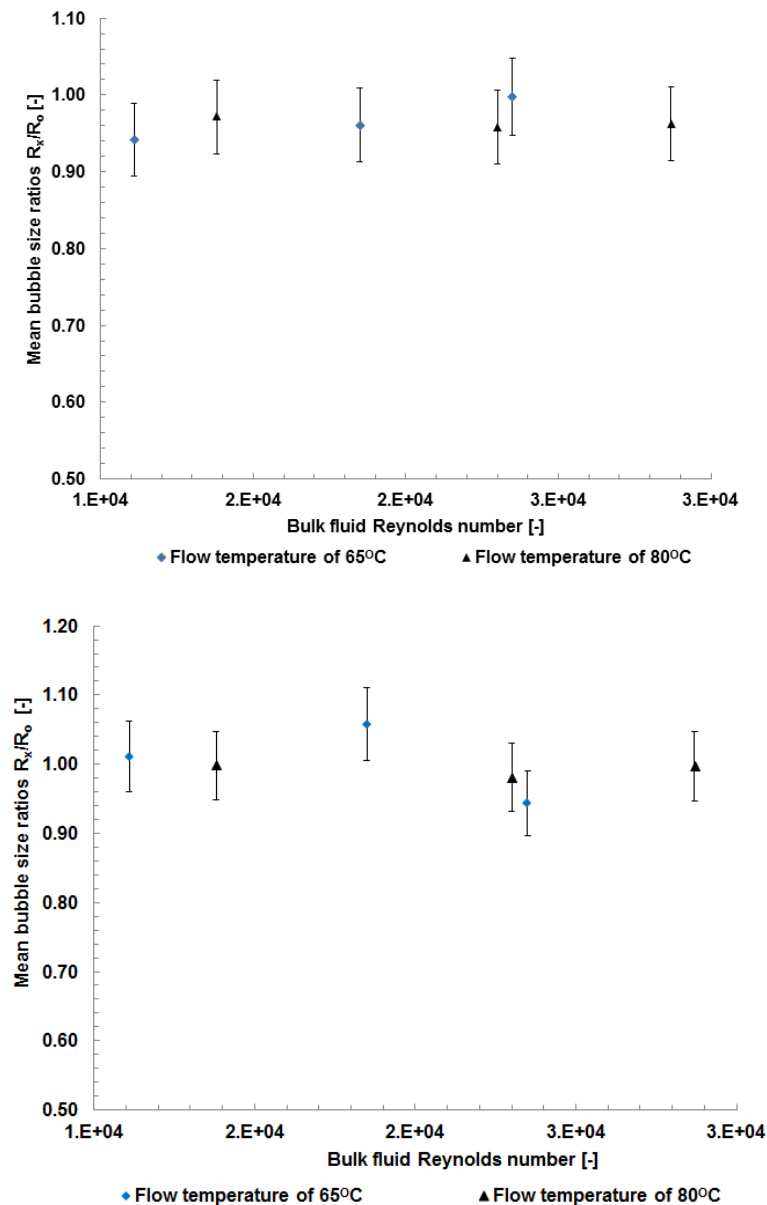
Fig. 4.44: Mean bubble size ratios R_x/R_o for saturated and supersaturated tests (Experiment: HPT_FR II & V (Top) and supersaturated tests, HPT_FR III & VI (Bottom) in Table 3.6).

Through the consideration of the resultant experimental errors, the bubble size ratios illustrated through the charts as in Fig. 4.44, suggest that at bulk fluid saturation and super saturation conditions, bubble size ratios close to unity are expected. Hence, minimal bubble dissolution or growth was measured through the bulk fluid system flow line saturation range of 1 to 1.1. Furthermore, in line with the observations done in the bubble dissolution investigation, no measurable trends are evident with a change in the bulk fluid temperature. The measured bubble size ratios at saturation conditions (ratio of 1) resulted to be consistently marginally less than unity, hence suggesting a minimal degree of bubble

154

dissolution. Such an effect can be attributed to a limited bubble breakage hence resulting in a reduction in the mean diameter between sight glasses *HSG1&2*. Furthermore, this phenomenon could be attributed to the tolerance range of the *TGM* system. A direct comparison of these results cannot be made with existing literature sources due to the minimal consideration given by literature to similar physical scenarios. However, the findings of the present study tend to be in agreement with those reported by Epstein and Plesset (1950), who stated that at saturation conditions, an isolated stationary bubble is expected to be stable against diffusion, but will still result in dissolution over time due to the effects of surface tension.

Bubble growth at bulk fluid super saturation conditions of 1.1, is insignificant, particularly when compared to the bubble dissolution measured in under saturated bulk fluid conditions. Hence, the results of the present study suggest that bubble growth due to gas diffusion from the bulk fluid into free bubbles in turbulent bubbly flow is minimal at low super saturation levels. The observed phenomena could be attributed to the slower bubble growth process particularly when considering the limited time range for bubbles to flow between sight glasses *HSG1&2,* with a maximum of 6.9 seconds. In their numerical modelling for bubble growth, Sun and Beckermann (2010) reported an increase in radius in a square root of time fashion for bulk fluid super saturation ratios of 1.1 and 1.2.

A reference to the theory of bubble nucleation and growth for isolated stationary bubbles in supersaturated conditions as discussed in Section 4.4 suggests that bubble growth is diffusion controlled. Such views were reported by Epstein and Plesset (1950), Liebermann (1957) and Cable and Frade (1988). A number of studies have been reported on the numerical simulation of bubble growth in two-phase bubbly flows. However, the open literature gives little consideration to related experimental studies. In their numerical investigation into bubble growth in liquids and melts with super saturation conditions, Arefmanesh et al. (1992) and Sun and Beckermann (2010) stated that the bubble growth process is in general complicated, involving simultaneous mass, momentum and energy transfer between the expanding bubble and the fluid surrounding it. Arefmanesh et al. (1992) reported that due to these complexities, there is no known analytical solution to predict bubble growth under general conditions. Similar conclusions

were made by Payvar (1987) and Shafi and Flumerfelt (1997). The latter reported that bubble growth numerical solutions are arbitrary as bubble growth dynamics could be dependent on a combination of complex physical conditions, particularly in turbulent flow conditions as is the case with the present study. Hence, our results suggest that even though the bubble nucleation and growth at the heat exchanger wall is significant at similar saturation ratios, the same cannot be said for the free bubbles in bubbly turbulent flow as typical in the system flow line. Therefore, the growth of bubbles at the primary heat exchanger wall can be attributed to the presence of nucleation cavities which are not present in the bulk fluid. This confirms the phenomenon of heterogeneous nucleation at the primary heat exchanger wall as defined by Jones at al. (1999a). Hence, bubble growth due to mass diffusion for free bubbles in a turbulent flow can be considered to be negligible over a horizontal pipe distance of 2.3 m at the system flow line.
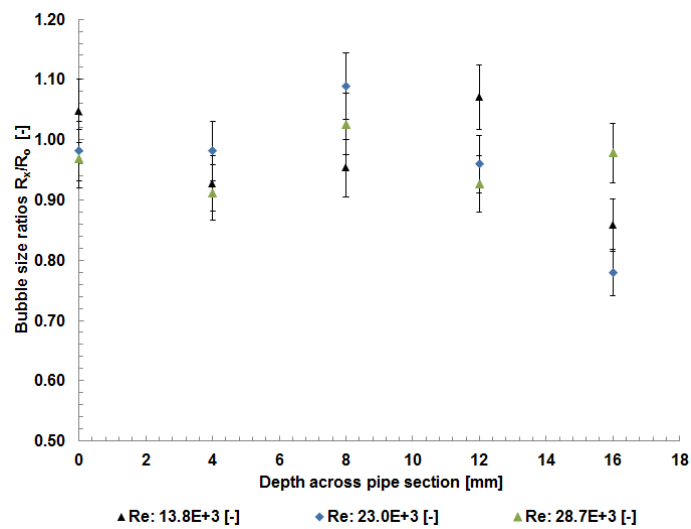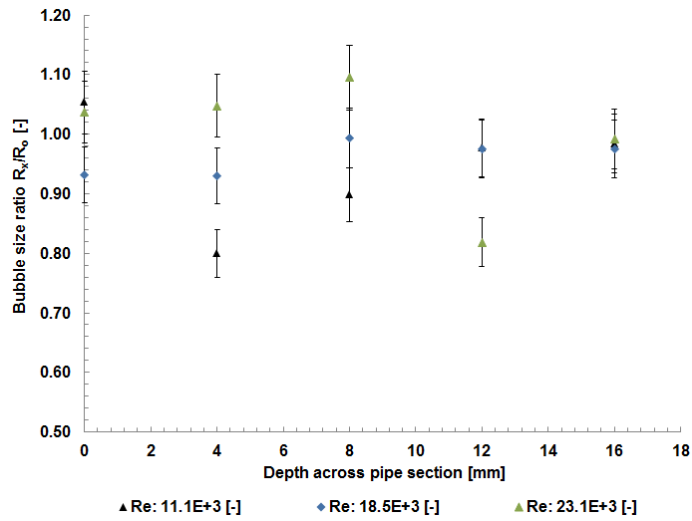
Fig. 4.45: Bubble size ratios R_x/R_o measured at intervals along the pipe depth for saturated tests *(Experiments: HPT_FR II (Top) and HPT_FR V (Bottom) in Table 3.6).*
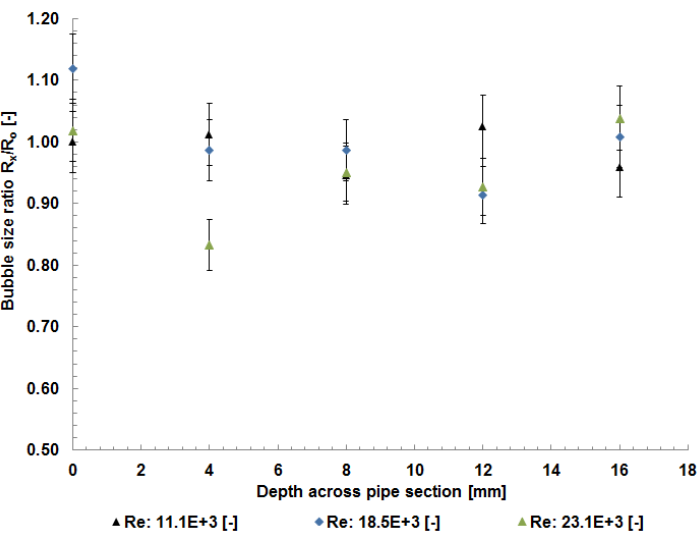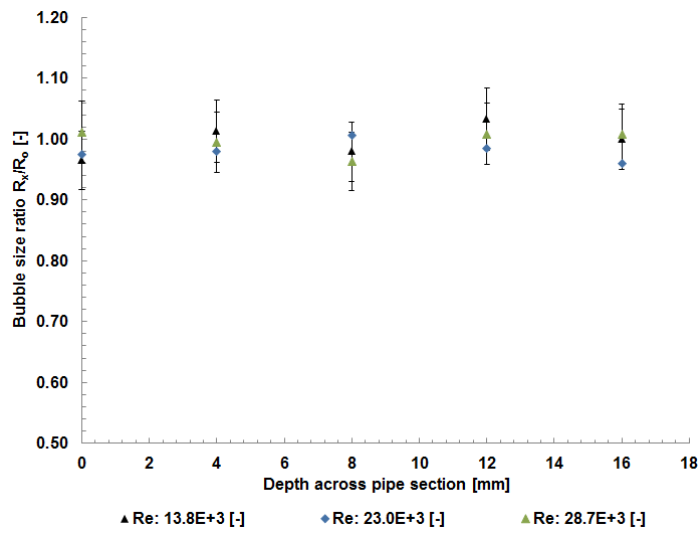
Fig. 4.46: Bubble size ratios R_x/R_o measured at intervals along the pipe depth for super saturated tests *(Experiments: HPT_FR III (Top) and HPT_FR VI (Bottom) in Table 3.6).*

157

Cable (1967) reported that it is far easier to obtain a reasonable agreement between theory and experiments for dissolving bubbles in under saturated solutions when compared to bubbles growing in super saturated solutions. Similarly, through the investigation of air bubble growth by rectified diffusion, Crum (1977) reported that as the surface tension was reduced as is the case at elevated bulk fluid temperatures, the observed and predicted bubble growth rates differ significantly. This further emphasizes the complexity of the physical scenario characterizing the present study and the inherent difficulties in fully understanding the mechanism leading to bubble behaviour. Figs. 4.45 and 4.46 illustrate the measured bubble ratios across the pipe depth together with the relevant experimental uncertainties. Through a consideration of the experimental uncertainties in the measured data, the charts do not suggest particular trends, hence implying a uniform bubble behaviour across the pipe section at saturated and super saturated conditions.

4.6 Repeatability

The repeatability of the experimental results is an issue that could affect the results in two-phase bubbly flow studies. This is particularly true when considering the application of the complex imaging technique used in the present study. Hence, the experimental data obtained through image processing could be affected by variations in the background lighting, particles present in the system water and the possible soiling of the sight glass through the limited passage of time. However, it should be noted that it is not the scope of the present study to investigate the change in the two-phase flow regime with the ageing of the system. Hence, repeatability studies were done through the application of the standard experimental preparations as discussed in Section 3.4.

A measure of the repeatability for the results obtained in the present study, was done through a repeat of the bubble nucleation test *BNT III* as highlighted in Section 3.4.4, done at the vertical sight glass, *VSG1*. The parameter considered is the maximum system saturation ratio at the primary heat exchanger wall conditions. No repeat tests were done for the horizontal pipe tests, hence using sight glasses *HSG1&2*. This is due to the consistent trends measured at the two flow temperatures with otherwise identical system conditions.

The results obtained through the repeat of the nucleation test with the system saturation ratio at the primary heat exchanger wall conditions are illustrated in Figs. 4.47 - 4.53. It is clear that the data which was taken circa two months apart is repeatable within the experimental uncertainty for most saturation ratios within the saturation ratio range considered. However, at the highest saturation ratio, it is evident that the data for the bubble production rate obtained during the repeated experiment is on the extreme end of the error bar for the original data. Furthermore, Figs. 4.52 & 4.53 highlight the fact that the results calculated for the cumulative void fraction and the gas volume flow rates are not repeatable at the highest saturation ratio. This could be attributed to the error in measuring the bubble diameter combined with the general errors in identifying between in focus and out of focus bubbles, compounded with the high bubble count characterizing the results at the maximum saturation ratio.
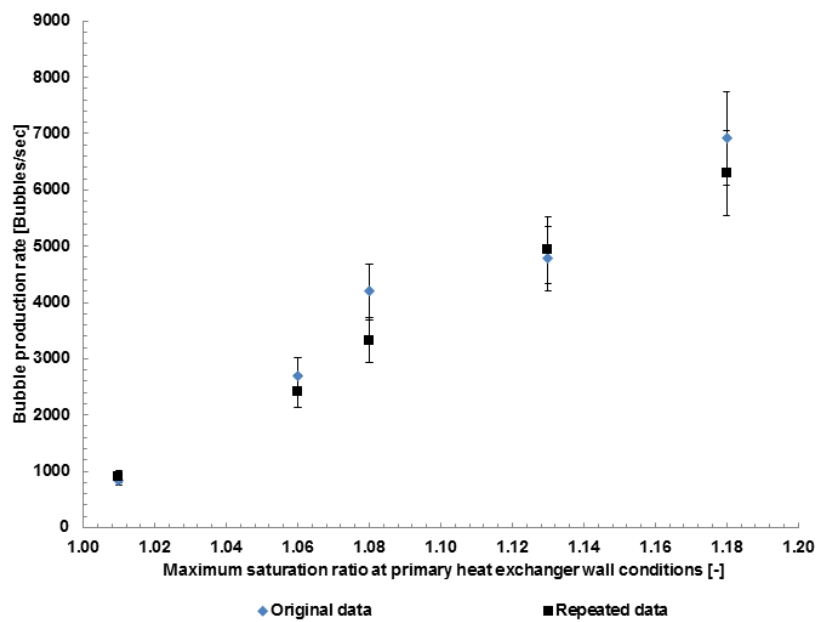
Fig. 4.47: Test for repeatability – Bubble production rate at measure at boiler exit through sight glass *VSG1.*
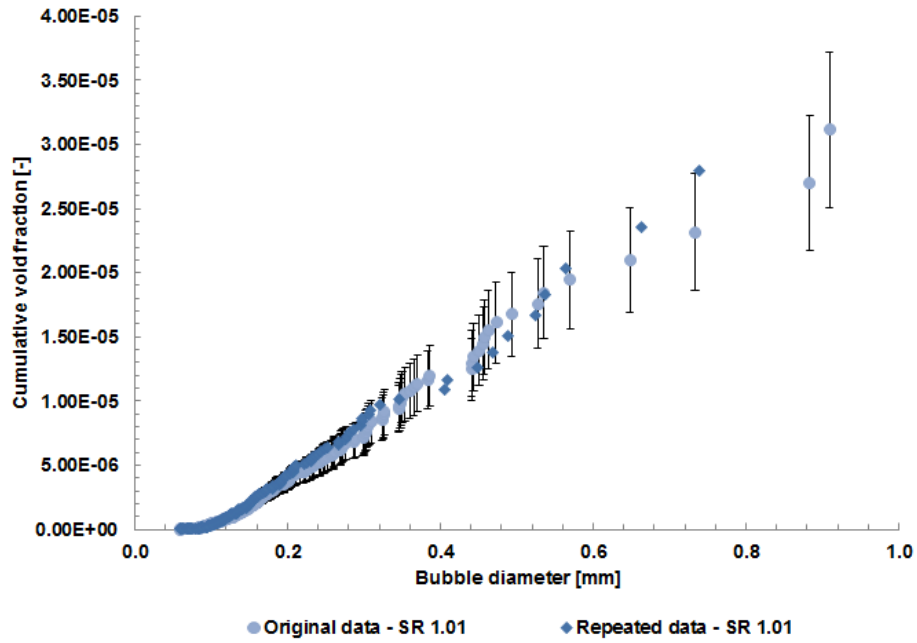
Fig. 4.48: Test for repeatability – Cumulative void fraction SR 1.01.
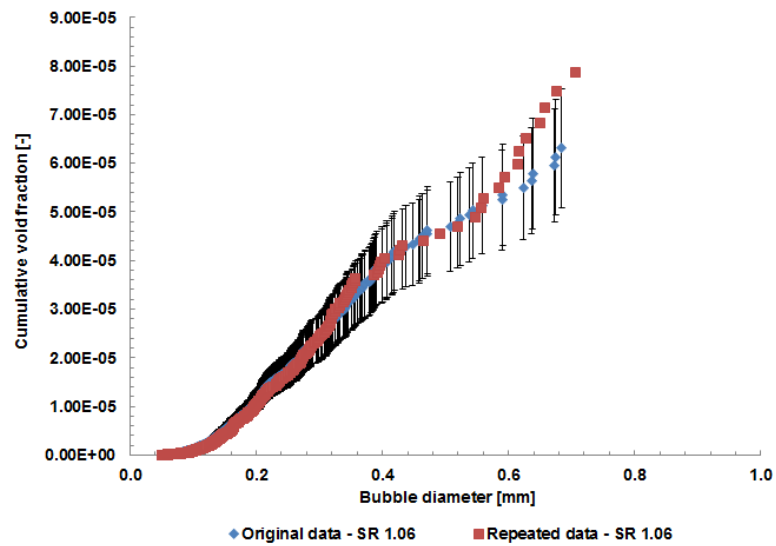
Fig. 4.49: Test for repeatability – Cumulative void fraction SR 1.06.
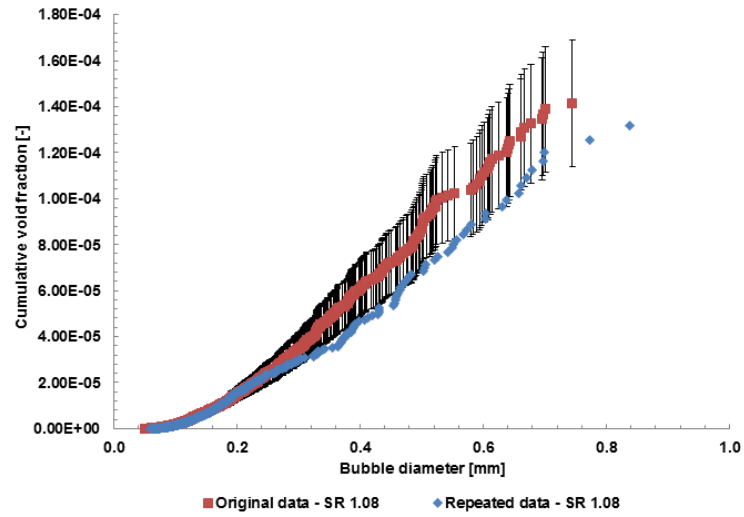
Fig. 4.50: Test for repeatability – Cumulative void fraction SR 1.08.
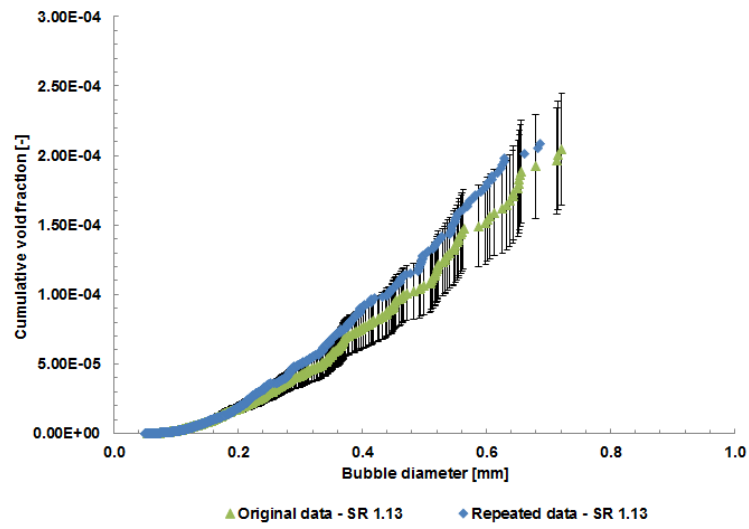
Fig. 4.51: Test for repeatability – Cumulative void fraction SR 1.13.
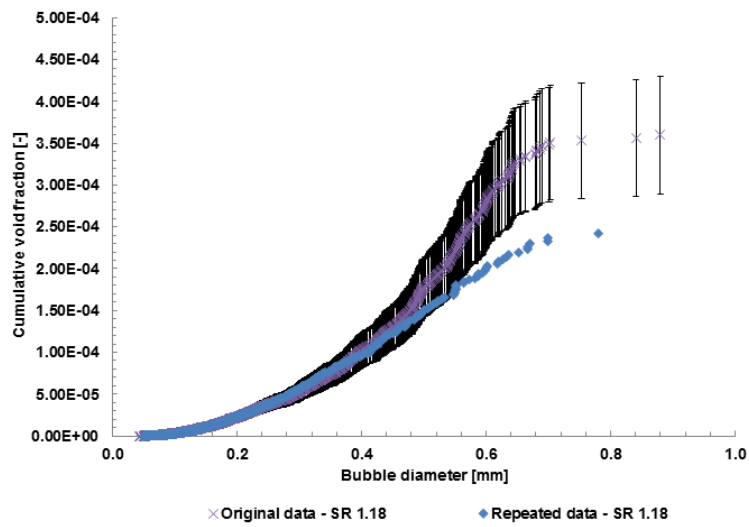
Fig. 4.52: Test for repeatability – Cumulative void fraction SR 1.18.
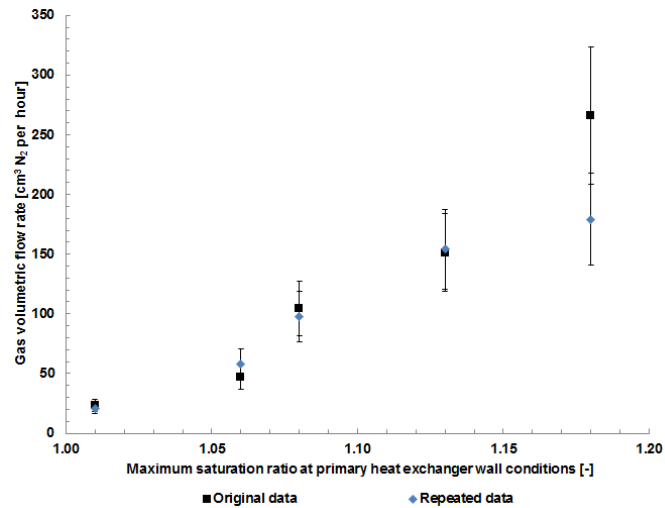
Fig. 4.53: Test for repeatability – Gas volume flow rate at measure at boiler exit through sight glass *VSG1*.

4.7 Summary

This chapter presented and discussed the experimental results for the two-phase flow characteristics in a wet domestic central heating system. Bubbles nucleate at the primary heat exchanger due to super saturation conditions. After detachment, a bubbly two-phase flow results in the system flow line. An analysis of the dissolved gasses present in the system suggests that the dominant dissolved gas is nitrogen. Tests done on the return end to the boiler suggest that all bubbles are dissolved or bubble up to high parts in the system, and hence no bubbles are present on the return end to the boiler.

Bubble distribution experiments done across vertical and horizontal pipes suggest that distribution in vertical pipes for downward flow is quasi-homogeneous across the pipe section while the distribution in horizontal pipes is a function of the bulk fluid flow velocity and the gravitational effects. The mean bubble diameters measured at the boiler exit are in the range of 0.13 mm to 0.39 mm with the system parameters. The bubble size is highly dependent on the bulk fluid velocity. Hence, the largest bubbles were measured at the lower bulk fluid velocities. The bubble size is also marginally dependent on the system pressure and the heat flux on the boiler wall. Bubble shape analysis done for bubbles present in vertical downward flow suggests that the bubbles are mostly spherical in shape with bubble shape ratios in the range of 0.9 to 1. A minimal elongation

162

in the flow direction was measured with larger sized bubbles at the lower bulk fluid velocities.

Bubble production rates were shown to increase with the system velocity, heat flux and saturation ratio and decrease with the system pressure. The trends in the calculated nucleation rates at the boiler wall with the bulk fluid saturation ratio and velocity were not directly proportional to the trends shown by the bubble production rates with the same system parameters due to the inconsistent heat exchanger surface area under super saturation conditions with the changing system parameters.

Experiments done on bubble dissolution in horizontal bubbly two-phase flow have shown that the rate of dissolution is a function of the bulk fluid under saturation ratio and the bulk fluid velocity. Significantly higher dissolution rates were measured when compared to data for isolated bubbles in stagnant fluid conditions as published in the open literature, hence suggesting a significantly enhanced dissolution process with turbulent flow conditions.

The next Chapter presents the relevant theoretical models correlated to the data measured in the present study.

CHAPTER 5

Models and Correlations

5.1 Introduction

This chapter presents and discusses the relevant correlations adopted for the data collected during the present study. As discussed in the previous Chapters, a direct comparison with relevant sources in the open literature could be difficult due to the limited consideration given to bubble formation in supersaturated solutions under turbulent flow conditions. Hence, as a case in point, only one model is

available in the open literature for the prediction of the bubble detachment diameter for bubbles nucleating in super saturation conditions under a fluid flow regime.

Therefore, Section 5.2 will present and correlate data to the models for the bubble size prediction at the nucleation point, Section 5.3 will present and correlate data to the bubble nucleation models, Section 5.4 will present and correlate data to the bubble dissolution models while Section 5.5 will present the results derived through Computational Fluid Dynamics (*CFD*) for the prediction of the second phase distribution in horizontal pipes for two-phase bubbly flows.

5.2 Bubble size prediction models

As discussed in Section 2.2.3, the theoretical approach that exists for predicting the detachment size of nucleating bubbles originating in a supersaturated solution under fluid flow conditions, with no knowledge of the nucleating time, is based on the resolution of the forces acting on the surface of the nucleating bubble on the boiler heat exchanger wall, parallel to the wall surface. Other models were developed to predict the bubble size in developed two-phase bubbly flows. Amongst these models are the Hinze approach as adapted by Winterton and Munaweera (2001) and the Winterton and Orby (1994) model. However, as these models are based on experimental data obtained through the artificial insertion of micro bubbles in the flow, they are not considered adequate for a correlation with the data collected through the present study.

Winterton's (1972a) approach for the prediction of bubble detachment diameters is based on the force balance theory and was developed through data obtained from bubbles nucleating under supersaturated fluid flow conditions. Hence, the models presented by Winterton (1972a) for predicting the mean bubble detachment diameter as presented in Eqs. (2.14) & (2.15) were used to compare our data. A number of recent studies have adapted the use of the Winterton (1972a) model with good results. Amongst these are studies done by Al-Hayes and Winterton (1981a,b) and Hepworth et al. (2003).

The experimental conditions of the present study did not allow a direct measurement of the bubble diameters at detachment from the boiler wall.

However, the positioning of the sight glass at the exit end of the boiler with sufficient insulation to ensure isothermal conditions, allowed the authors of the present study to assume that the observed bubble diameters are reasonably equal to the detachment diameters, thus enabling a comparison to the relevant predictions by the Winterton (1972a) models for bubble detachment diameters at zero and finite contact angles. Hence, the effects of bubble coalescence and dissolution were assumed to be negligible due to the limited distance travelled by the bubbles and due to the isothermal conditions.

The velocity profile in the channel was identified through the application of Eq. (2.21). This yielded a value for the dimensionless η between 5 and 30, hence suggesting a bubble detachment into the transition flow regime, for all experimental conditions. As discussed in Section 2.2.3, the open literature gives little consideration to the expected contact angles with surface and fluid flow conditions. Hence, as no data is available to predict the dynamic contact angles on the heat exchanger stainless steel tube surface, the extreme cases were considered for the finite contact angle model, these being $\theta_o = 30^o$, $\theta_r = 20^o$ and $\theta_a = 40^o$ (Winterton, 1972b).

The equivalent hydraulic diameter for the rectangular boiler tubes, calculated through Eq. (3.7) was used to calculate the tube radius R in Eqs. (2.14) & (2.15). As reported by Hesselgreaves (2001), the hydraulic diameter is calculated through the consideration of the cross sectional area and the wetted perimeter of the rectangular heat exchanger tubes. Hence, the application of the hydraulic diameter enables the rectangular section to be modelled as a circular tube section. A good representation of the average measured bubble diameters with respect to the experimental parameters, as originally presented in Section 4.3.2, and the best model prediction, is given in Figs. 5.1 – 5.4. The best prediction is provided by the Winterton (1972a) model for bubble detachment diameters at finite contact angles. Its predictions are illustrated in Figs. 5.1 – 5.4. The zero contact angle model under predicted bubble diameters with an error in excess of 100% in comparison to the experimental diameters. Therefore, the model's predictions are only presented in Fig. 5.1, where a similar trend to the experimental and finite contact angle model predictions was observed.
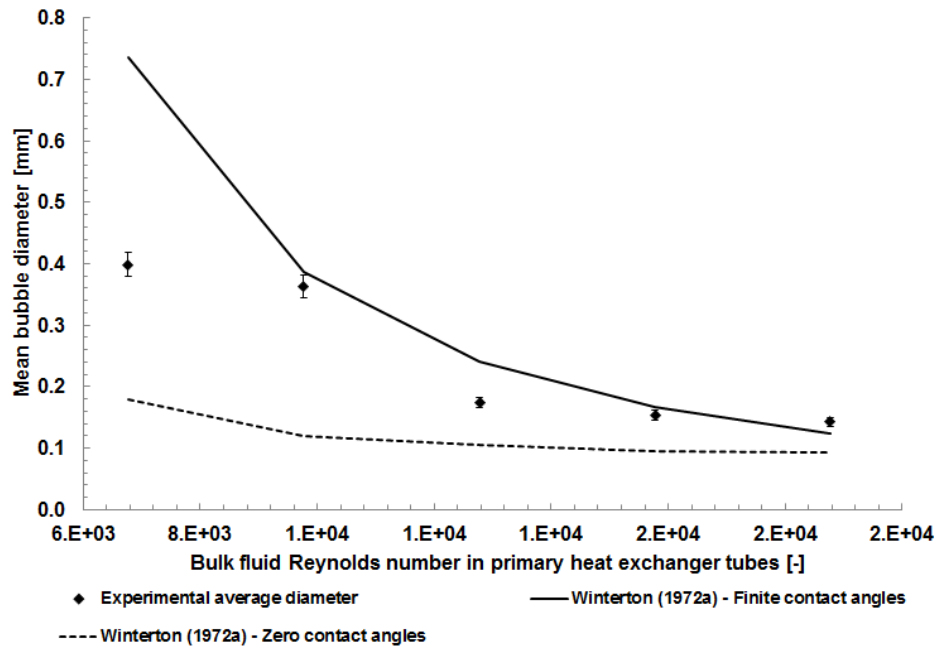
Figure 5.1: Experimental and predicted bubble diameters with bulk fluid Reynolds number in the primary heat exchanger tubes.

The experimental results are in reasonable agreement with the theoretical predictions of Eq. (2.15). Winterton's finite contact angle model predicts the bubble diameters with changing system parameters with a mean absolute error of 20%. When considering the limitations of the present study and the general limitations inherent to two-phase flow studies (Winterton and Munaweera, 2001), the discrepancies between theory and experimental results are considered to be reasonable. In one case, where the system velocity is at its lowest, the predicted detachment diameter is circa 45% larger than the experimental value. This could be attributed to the size limitations of the camera image. Large bubbles could have been ignored due to the fact they were not fully captured in the picture frame and as a result the experimental average could be understated.

The effect of the flow velocity on the bubble detachment diameter as seen in this study is in agreement with the Winterton (1972a) models. The Winterton model captured the effect of velocity on the predicted bubble detachment diameter through the inclusion of the Weber and Reynolds dimensionless numbers. Similar trends were also evident in studies done by Al-Hayes and Winterton (1981b). This suggests that the Winterton approach of balancing the drag and surface tension forces at the bubble detachment point as illustrated in Fig. 2.3, is representative of the actual physical regime.

166
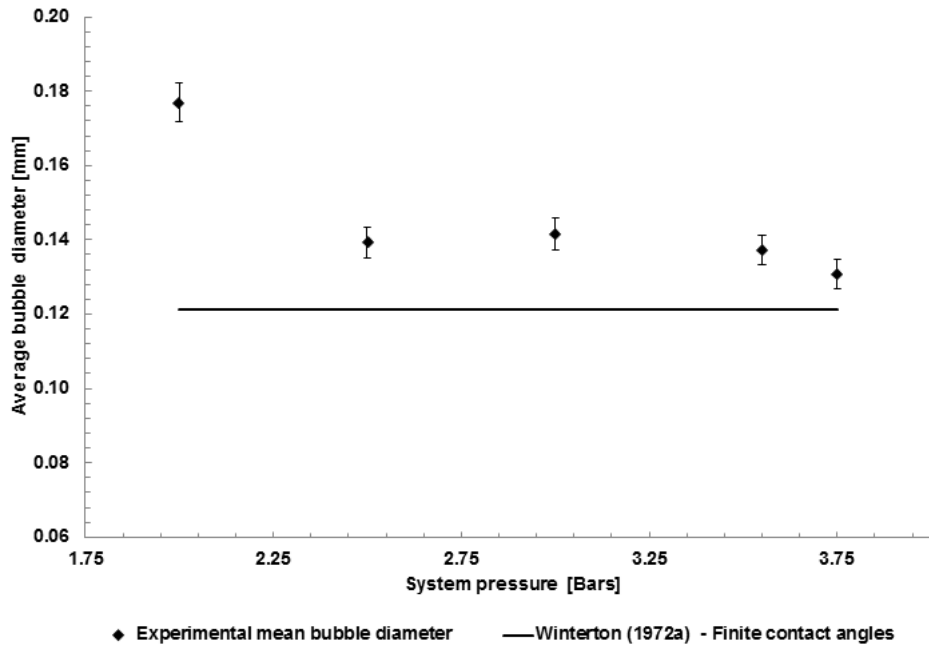
Figure 5.2: Experimental and predicted bubble diameters with the system pressure.

The Winterton (1972a) finite contact angle model predicted a bubble diameter, circa 15% less than the experimental results in the system pressure tests as illustrated in Fig. 5.2. Larger bubble diameters, with an average of 0.177mm were observed at the lowest system pressure, this being of 2 Bars (abs). This trend was not predicted by the Winterton (1972a) bubble detachment model for finite contact angles due to the limited change in water properties with the pressure range used in the present study.
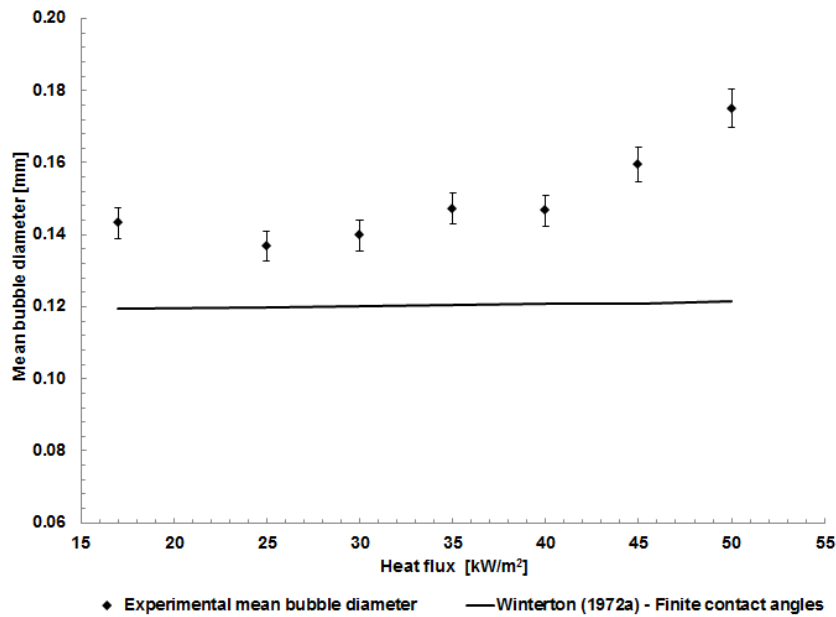
Figure 5.3: Experimental and predicted bubble diameters with heat flux at the primary heat exchanger wall.

167

For a change in heat flux, as illustrated in Fig. 5.3, the Winterton (1972a) finite contact angle model resulted in a predicted bubble diameter of circa 20% less than the experimental results. The increase in boiler wall heat flux from 17 to 50 kW/m^2, equal to a heating load of 7.5 and 21.5 kW respectively, resulted in a 19% increase in the observed experimental bubble diameters. A negligible increase in diameter was also predicted by the Winterton detachment model for finite contact angles due to a change in the fluid properties, resulting in a reduction in water density, kinematic viscosity and surface tension with temperature. In fact, as the heating load was increased, higher boiler wall temperatures were observed due to the increase in the difference between the return and flow temperatures. Higher temperatures increase the diffusivity of the dissolved nitrogen in gasses, hence possibly resulting to enhanced bubble growth thus resulting in larger bubble detachment diameters.

An increase in the saturation ratios did not result in a change in the bubble detachment radius. An experimental average bubble size of circa 0.14 mm was observed. As illustrated in Fig. 5.4, this trend is in agreement with the Winterton's (1972a) approach for finite contact angles. It is worth noting that at super saturation ratios, the Winterton model for zero contact angles predicted a decrease in bubble detachment diameters with increasing super saturation ratios. This is a result of the decrease in the nucleation site radius with increasing pressure difference between the bubble and the bulk fluid as defined by Dean (1944).
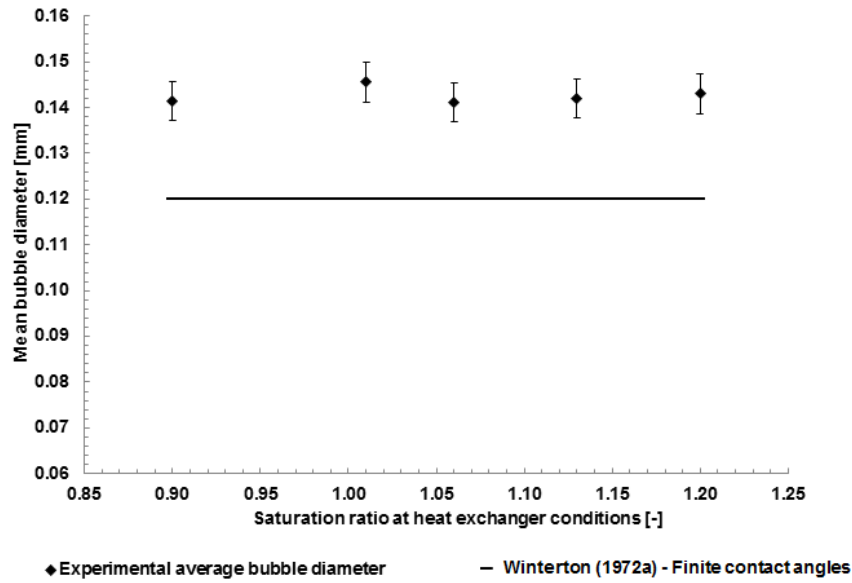
Figure 5.4: Experimental and predicted bubble diameters with the maximum saturation ratio at the primary heat exchanger wall conditions.

The Al-Hayes and Winterton (1981a,b) and the Jones et al. (1999a) approach for the bubble growth time are based on the diffusion theory and suggest that the gas concentration effects the bubble growth rate but does not result in a direct effect on the bubble detachment radius. This is in agreement with Winterton's detachment radius model which is based on the physical aspects of the bubble, thus governed by the balance of the drag and surface tension forces acting on the nucleating bubble.

Lower contact angles are expected to reduce the surface tension force holding the bubble to the nucleating surface. Therefore, a reduced bubble detachment diameter is predicted as lower drag forces are required to equalise the surface tension force. Hence, the zero contact angle model (Winterton, 1972a) under predicted our results considerably. It is worth noting that as the theory of bubble nucleation states that bubbles nucleate in a cavity, some form of contact angle with the surface is always assumed to be present. Hence, in his zero contact angle model, Winterton (1972a) assumed advancing and receding contact angles of 90° and 0° respectively.

Contact angles are predicted to increase with surface roughness (Hong et al. 1994). As most modern domestic central heating boilers make use of stainless steel heat exchangers, similar surface conditions and thus contact angles are

169

expected with most contemporary boiler brands. However, it is worth noting that surface scaling as a result of multiple system refilling and prolonged usage could increase the heat exchanger surface roughness and consequently increase the bubble detachment diameters.

The present study does not examine the bubble behaviour following detachment from the nucleation point. Winterton (1972a) and Hepworth et al. (2003), reported that as the drag and surface tension forces equalize, the bubble vibrates in a fixed position until finally sliding on the surface before being carried into the main stream flow. They reported that the phenomenon of sliding is not considered to have an effect on the bubble detachment diameter as it is the velocity required to detach the bubble from its nucleation point that is expected to determine the detachment diameter. Bubble sliding following detachment and prior to lift off to the bulk fluid flow, was also reported in experiments in sub cooled flow boiling. (Prodanovic et al., 2001)

The reasonable prediction given by Winterton's finite contact angle model through the use of the equivalent hydraulic diameter for the rectangular tubes used in the present study, suggests that wider rectangular heat exchanger tubes should result in larger bubble diameters. Furthermore, the coil sectional and assembly design should have a minimal effect on the bubble detachment diameters as Winterton's model was originally developed for straight round tubes.

5.2.1 New correlation for bubble size prediction

To correlate the predicted average bubble diameter with respect to the parameters controlling a wet central heating system, the Winterton model (1972a) for the prediction of bubble detachment diameters in supersaturated solutions with finite contact angles as in Eq. (2.15), was adopted. As no data is available with respect to the dynamic contact angles on the boiler wall, this term was eliminated and replaced by a constant as in Eq. (5.1). The effect of the system pressure and heat flux on the predicted bubble size was included through a dimensionless form. This was necessary as the Winterton model (1972a) for finite contact angles did not capture the effect of heat flux and system pressure on the predicted bubble diameter. As in the original Winterton model (1972a), the Reynolds number was

included to represent the effect of the bulk fluid velocity on the bubble diameter. The numerical constant and exponents for the three dimensionless numbers, were optimized through the iteration method.

$$\frac{r}{R} = \frac{0.002716}{We} \left(\frac{P_{sys}}{P_{atm}} \right)^{-0.461} \left(\frac{q}{q_{max}} \right)^{0.113} \text{Re}^{0.705} \tag{5.1}$$

The validity range of the correlation as in Eq. (5.1), which could be used to predict the expected mean bubble diameter at the boiler flow line, is based on the experimental parameter range used in the present study as illustrated in Table 5.1.

Bulk fluid velocity in heat exchanger tubes (m/s)	System pressure (abs) (Bars)	Heat flux (kW/m^2)	System heating load (kW)	Duct hydraulic diameter (mm)
0.29 - 0.85	2 - 3.75	17 - 50	7 – 21.5	7.9

Table 5.1: Bubble size correlation validity range.

The correlation data is compared to the experimental data for all system parameters as illustrated in Fig. (5.5). Our new correlation predicted the bubble diameter at the exit of the boiler tube with a mean absolute error of 8%. Furthermore, after excluding the experimental data at low velocities, all experimental data points are between ± 12% of the new correlation prediction. The experimental error for the velocity tests could be more significant due to the size limitations of the sight glass section, thus resulting in the elimination of the larger bubbles at lower velocities. The present study considered the limitations of the statistical error analysis as a result of the limited number of data points available. However, a larger set of test runs was not possible due to the narrow parameter range present in such systems. The manual technique used in bubble measurement also limited the number of experimental runs possible. Therefore, further investigation into the validity of our new correlation could be necessary.
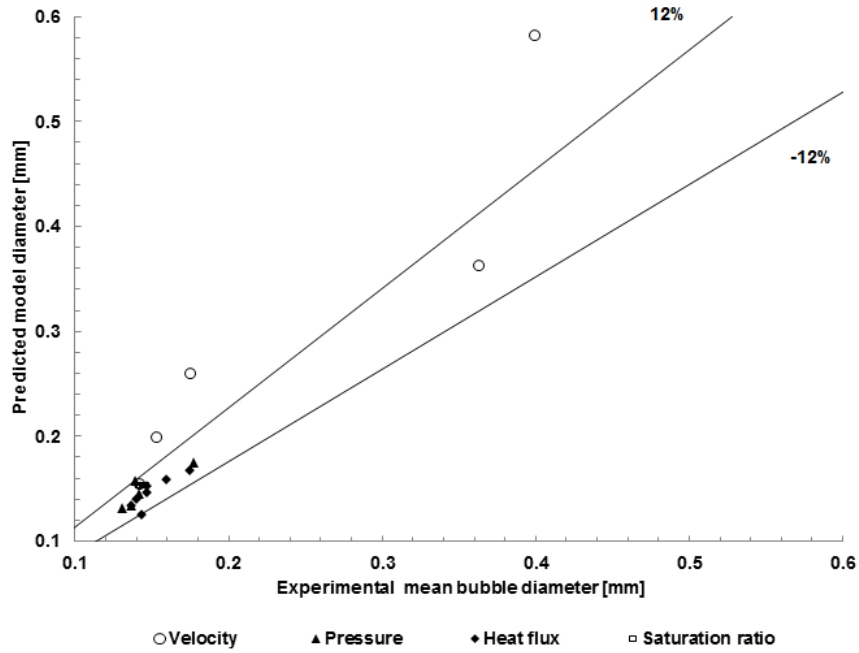
Figure 5.5: Error plot for mean experimental and the present study bubble size correlation results.

5.3 Bubble nucleation on the surface of the primary heat exchanger

The experimental results for the bubble production and nucleation rates as discussed in Section 4.4 are compared to the theoretical predictions through the application of the classical and non-classical nucleation models as discussed in Section 2.2.2.

As discussed in Section 2.2.2.2.1, the simplified classical nucleation equation by Lubetkin and Blackwell (1988) suggests that the exponent part is identical to Wilt's (1986) model for homogeneous nucleation. Eq. (2.11) due to Lubetkin and Blackwell (1988), requires large saturation ratios, in excess of 1000, for observable nucleation rates. Therefore, the low saturation ratios used in their study and in the present study do not result in predicted nucleation rates. Therefore, Lubetkin and Blackwell's (1988) elimination of the geometric factor in the exponent renders their equation for heterogeneous nucleation as originally developed by Blander and Katz (1975) ineffective at predicting nucleation at low saturation ratios. Furthermore, the classical nucleation model for heterogeneous nucleation (Wilt, 1986) on conical cavities does not result in reasonable

172

predictions with the application of moderate static contact angles as expected on a stainless steel surface.

Hence, to correlate our results, the non-classical nucleation model as presented by Hepworth et al. (2003), (Eq. (2.12)), was modified as in Eq. (5.2). Hence, as the precise surface conditions are not known, the nucleation cavity density term was replaced with an empirical proportionality constant, *F*, used to correlate our data. Furthermore, the fluctuating heat exchanger surface area under super saturation conditions with system parameters, necessitated the inclusion of the relevant defining parameters in the correlation. Hence, the first term in Eq. (5.2) defines the area of the heat exchanger coil under super saturation conditions. The saturation point L_{css} was calculated through the assumption of a linear rise in the wall temperature (Prabhanjan et al., 2002). Hence, the first term on the right hand side of Eq. (5.2) represents the nucleation site density. The values calculated for this term, compare well to the nucleation site densities measured in studies with flat plate heat exchangers under similar experimental conditions (Verschaeren, 2010).

The gas concentration is expressed through the use of the saturation ratio, as this is the principle parameter used in most systems containing dissolved gases. The bubble radius at detachment was calculated through the force balance equations as predicted by Winterton (1972a), and as correlated to our experimental data for bubble detachment radii (Eq. 5.1). A static contact angle of 52° for water saturated with air on stainless steel was adopted (Ponter and Yekta-Fard, 1985). The gas diffusivity was calculated through the application of the Wilke-Chang estimation method (Appendix IV), as presented by Reid et al. (1987). Our data was correlated to the Hepworth et al. (2003) non-classical model through the application of an iterative optimization method.

$$J_1 = \left[\frac{F}{[L_c - L_{css}]P_{ts}} \right] \left[\frac{K_g \, C_{sg} \, (\alpha - 1)}{r^{3/2}} \right] \tag{5.2}$$

where $F = 6.91E{+}4$

Bulk fluid velocity in heat exchanger tubes (m/s)	System pressure (abs) (Bars)	Heat flux (kW/m^2)	System heating load (kW)
0.39 - 0.85	2 - 3.75	17 – 50	7.5 - 21.5

Table 5.2: Bubble nucleation correlation validity range.

The resultant predictions through Eq. (5.2) are illustrated in Figs. 5.6 - 5.9 while Fig. 5.10, illustrates a comparison between the correlated prediction and our experimental results. The correlation has an overall mean absolute error of 24%. 71% of the data points are located between ± 25% of the model's prediction while 89 % of the data points are located between ± 45 % of the model's prediction. Such results should be considered in view of the lack of practical models available to predict nucleation rates in supersaturated solutions at non-classical conditions (Hepworth et al., 2003, Lubetkin and Blackwell, 1988, Jones et al., 1999a) as well as the general difficulties in analysing two-phase flows (Winterton and Munaweera, 2001). Literature on nucleation in solutions supersaturated with nitrogen in engineering applications is also limited as most studies are based on nucleation in H_2O and CO_2 solutions (Lubetkin and Blackwell, 1988, Carr et al., 1995, Jones et al., 1999a,b). Furthermore, most studies in bubble formation at fractional super saturation levels are constrained to environmental studies in gases dissolved in natural bodies of water with a free surface. As discussed in Section 4.4, the limitations of the present study did not allow a measurement of the bubble nucleation through the application of a constant heat exchanger area under super saturation conditions. This limits the potential interpretation of the results in identifying the parameters that are expected to have the most significant effect on the resultant nucleation rate.

However, through the assumption of a constant surface area under super saturation conditions, higher liquid velocities can be assumed to increase the bubble nucleation rate. Such a phenomenon can be attributed to an increase in the mass transfer coefficient for gas entering the bubble from the bulk liquid thus increasing the nucleation rate (Hepworth et al., 2003). Hence, due to a decrease in the resultant bubble detachment radius with an increase in the bulk fluid velocity, a higher concentration gradient of gas is assumed to be present at the

primary heat exchanger surface, thus enabling more bubbles to be released from the heat exchanger surface at a given time instant. Therefore, the inclusion of the predicted bubble detachment radius in the Hepworth et al. (2003) model is considered to be representative of the nucleation regime as this yields nucleation rates that are inversely proportional to the predicted bubble detachment radius. Similar assumptions can be made for the resultant percentage of super saturation that is considered to be proportional to the nucleation rate in the Hepworth et al. (2003) model. Furthermore, the reasonable agreement between the experimental results and the nucleation model prediction for the heat flux and pressure can be attributed to the fact that the temperature is proportional to the nucleation rate while the pressure is inversely proportional to the nucleation rate.

The effect of the fluid velocity is not captured in the classical models for heterogeneous nucleation (Wilt, 1986). The latter models also predict an increase in the nucleation rate with an increase in pressure. This contrasts to the findings of the present study and to the non-classical model which predicts a reduction in the resultant nucleation rate with system pressure.
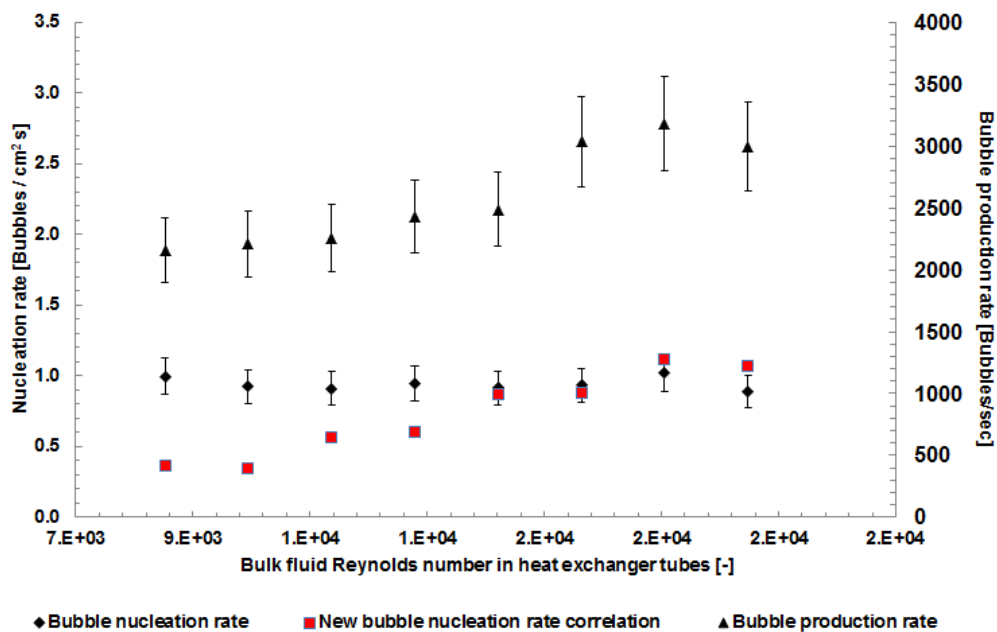
Figure 5.6: Experimental nucleation rate and system bubble production rate with the bulk fluid Reynolds number in the primary heat exchanger tubes.
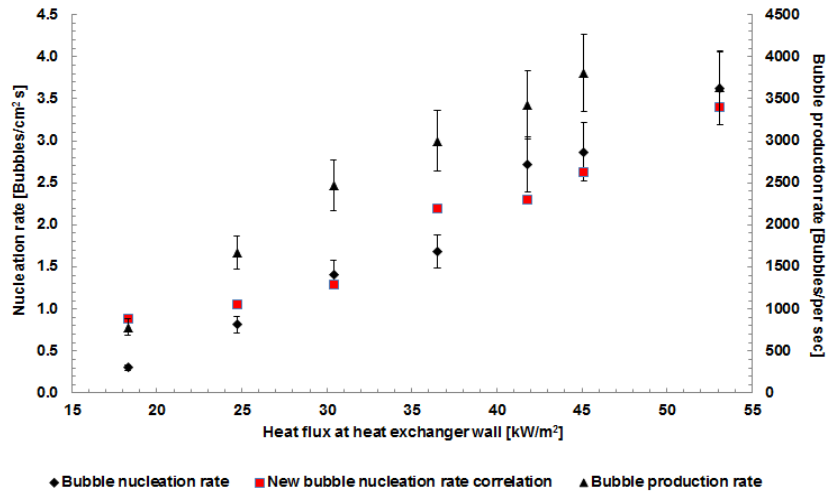
Figure 5.7: Experimental nucleation rate and system bubble production rate with heat flux.
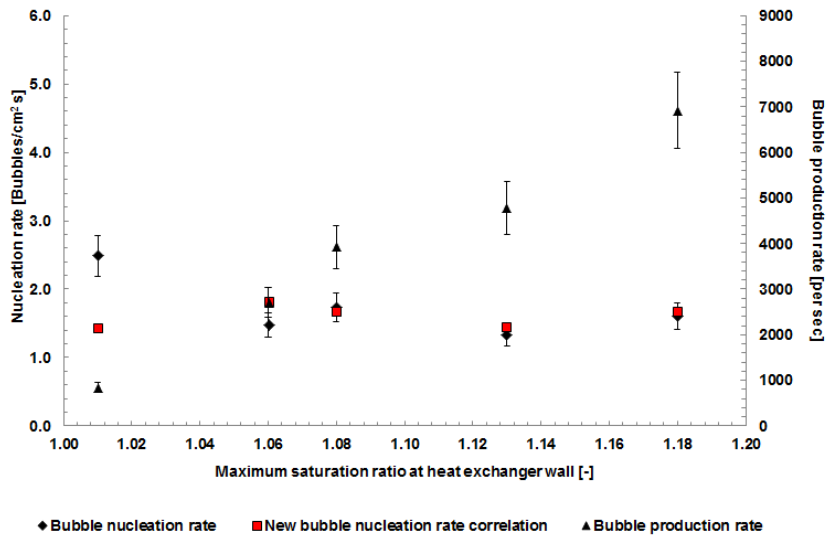
Figure 5.8: Experimental nucleation rate and system bubble production rate with the maximum saturation ratio at the primary heat exchanger wall conditions.
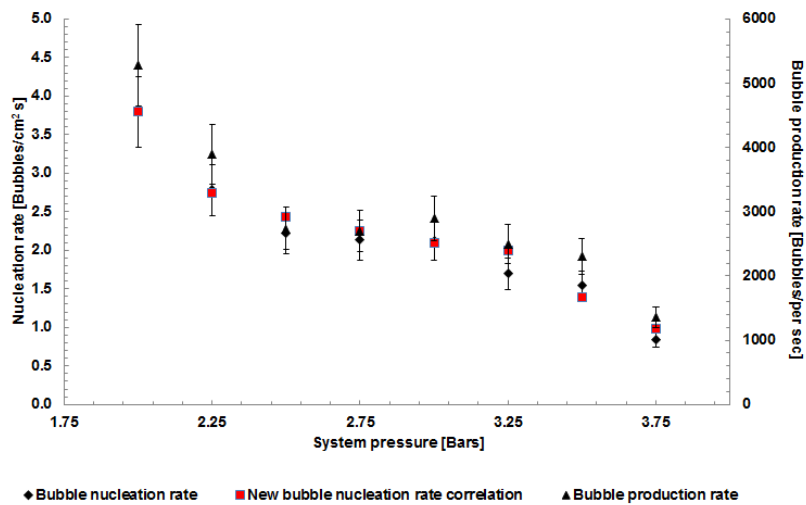
Figure 5.9: Experimental nucleation rate and system bubble production rate with system pressure (abs).

176
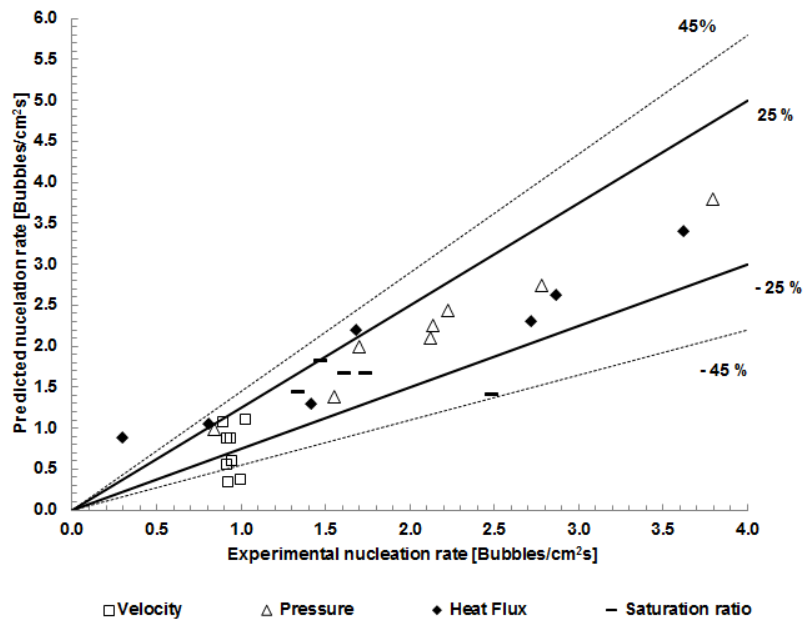
Figure 5.10: Error plot for mean experimental and the present study bubble nucleation correlation results.

Studies done by Wilt (1986) for classical nucleation, and Hepworth et al. (2003) for non-classical nucleation suggest that the nucleation rate also depends on the resultant contact angle and therefore, scaling on the primary heat exchanger wall through a prolonged use of a central heating system with untreated water, could result in a change in the surface characteristics and therefore effect the overall nucleation rate. Hence, as discussed in Section 6.3, the effect of the surface contact angle on the resultant nucleation rate, with prolonged system usage should be further investigated.

5.4 Bubble dissolution in under saturated turbulent bubbly flow in horizontal pipe work

The experimental results for the bubble dissolution in under saturated turbulent bubbly flow in horizontal pipes as discussed in Sections 4.5.2 (*HPT_US* (Constant velocity), *HPT_FR I* (Constant under saturation conditions at high flow temperature) and *HPT_FR IV* (Constant under saturation conditions at low flow temperature)) are compared to the theoretical predictions as discussed in Section 2.2.4.1.

To correlate the predicted bubble radius in horizontal pipe flow in a domestic central heating system, the Epstein and Plesset (1950) model for bubble

177

dissolution, Eq. (2.24), was adapted for the present study as in Eq. (5.3), thus assuming surface tension independence. This model was developed for isolated bubbles in a stagnant pool of water. Hence, the dimensionless Sherwood number was included to capture the enhanced turbulent diffusion process due to the convective mass transfer from the bubble to the liquid. This was necessary as significantly higher dissolution rates were measured in the present study in relation to dissolution rates presented in the open literature for diffusion controlled isolated bubble dissolution (Epstein and Plesset, 1950).

As discussed in Section 2.2.4.1, the Sherwood number was used by Kress and Keyes (1973) and Lezhnin et al. (2003) to quantify the enhanced bubble dissolution in turbulent flow. The empirical correlation identified by Lezhnin et al. (2003) for the calculation of the Sherwood number was used as given in Eq. (2.29). The nitrogen gas diffusivity was calculated through the application of the Wilke-Chang estimation method (Reid et al., 1987) as presented in Appendix IV. This model has a general accuracy of circa 20% (Perry and Green, 1998). The Sherwood number correlation proportionality constant was optimized through the iteration method. The validity range of this correlation is based on the experimental parameter range used in the present study as illustrated in Table 5.3.

$$\epsilon_b^2 = 1 - Sh[x^2] \qquad (5.3)$$

where; $\epsilon_b = \frac{R_x}{R_o}$; $x^2 = \left[\frac{2B}{R_o^2}\right] t$; $B = \frac{D(C_E - C_0)}{\rho_g}$; and the proportionality constant for the Sherwood number as in Eq. (2.29) is; $F = 0.20$.

Bulk fluid velocity in pipe work (m/s)	System heating load (kW)	Saturation ratio at bulk fluid conditions (-)	Horizontal pipe work internal diameter (mm)	Bulk fluid temperature (°C)
0.25 - 0.52	10 – 21.2	0.89 - 0.97	20	65 – 80

Table 5.3: Dissolution bubble size correlation validity range.

The correlation data is compared to the experimental data for the tests done with varying under saturation ratios and bulk fluid velocities as illustrated in Fig. 5.11. The correlation predicted the expected bubble radius after a measured time *t* with

178

a mean absolute error of 10.4%. Furthermore, 87% of the data points are between ± 25% of the new correlation predictions. A similar correlation, done through the combination of the Sherwood number with the Bankoff (1964) isolated bubble dissolution model as in Eq. (2.27), yielded quasi-identical results to those illustrated in Fig. 5.11.

In view of the general limitations characterizing two-phase flow experimental studies, the bubble dissolution correlation presented in the present study is considered to predict the expected bubble radius as a result of dissolution in horizontal straight line pipe work with reasonable accuracy. Therefore, the combination of the isolated bubble diffusion controlled model (Epstein and Plesset, 1950) with the Sherwood number, incorporated to capture the ratio of the convective to the diffusive mass transport through the inclusion of the dimensionless Reynolds and Schmidt numbers, yields reasonable predictions. Hence, the Sherwood number captures the enhanced bubble dissolution due to the turbulent diffusion characteristics present in turbulent bubbly pipe flow with reasonable accuracy due to the Sherwood number being proportional to the bulk fluid Reynold's number, hence capturing the effects of the magnitude of turbulence in the bulk fluid.
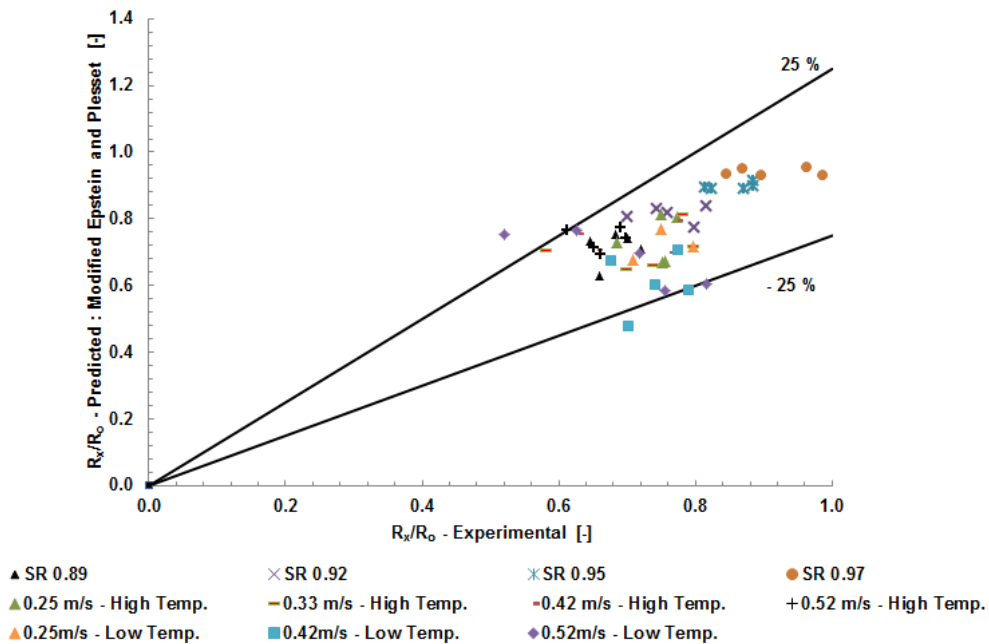
Figure 5.11: Error plot for mean experimental and the present study bubble nucleation correlation results.

The correlation results suggest that the effect of the bulk fluid temperature on the dissolution rate is negligible, provided that similar levels of gas concentration are maintained. This is in agreement with the measurements made in the present study and with recent findings done by Shedd (2005). In fact, Shedd reported that provided similar gas concentration levels are maintained, the system temperature results in a minor impact on the dissolution rates of bubbles. Furthermore, most dissolution models (Epstein and Plesset, 1950; Bankoff, 1964; Ljunggren and Eriksson, 1997; Honda et al., 2004), assumed surface tension independence and hence, this further supports the assumption for minimal effects on the bubble dissolution rate with temperature. Hence, for the purposes of the current study, the effect on the predicted diffusion rate through the inclusion of the surface tension effects is considered as negligible.

5.5 Phase distribution in bubbly two-phase flow

The experimental results for the second phase distribution in vertical and horizontal pipes as discussed in Sections 4.3.1 & 4.5.1, are compared to the theoretical predictions through the application of a CFD simulation using the two-phase Mixture method. The subsequent sub-sections will present and discuss the theory and methodology used for this simulation.

5.5.1 Software

This project made use of the FLUENT Version 5/6 CFD software package together with the use of the Gambit package for meshing purposes. Three dimensional CAD models of the system pipework were developed through the use of Pro Engineer Wildfire V2 software and subsequently imported into Gambit for meshing purposes. FLUENT is based on the Finite Volume Method that is one of the three numerical discretization techniques used in CFD. Talukdar et al. (2004) reported that this method was developed specifically to solve the equations of heat transfer and fluid flow, where the governing partial differential equations are converted into numerical form by a physically based transformation of the equations. Hence, as a first step, the Finite Volume Method divides the domain in consideration into a number of control volumes or cells where the variable of interest is located at the centroid of the control volume. The

differential form of the fluid governing equations is then integrated over each control volume.

The interpolation profiles are then assumed in order to describe the variation of the concerned variable between cell centroids. In this manner, the discretization equation expresses the conservation principle for the variable inside the control volume. A unique fact about the Finite Volume Method is that the resulting solution satisfies the conservation of quantities such as mass, momentum and energy. Hence, considering the centroid as illustrated in Fig. 5.12;

- The rate of increase of mass in the fluid element = Net rate of flow of mass into fluid element.
- Rate of increase of momentum of fluid particle = Sum of forces on fluid particle (Newton's Second Law of Motion).
- Rate of increase of energy of fluid particle = Net rate of heat added to fluid particle + Net rate of work done on fluid particle (First law of thermodynamics).

Considering the fluid element as illustrated in Fig. 5.12, the centre of this element is located at the position *x, y, z*. Therefore, the fluid flow governing equations are derived through the analysis of the changes in mass, momentum and energy of the fluid flow across its boundaries. Furthermore, where necessary, the action of sources inside the element is also taken into consideration.
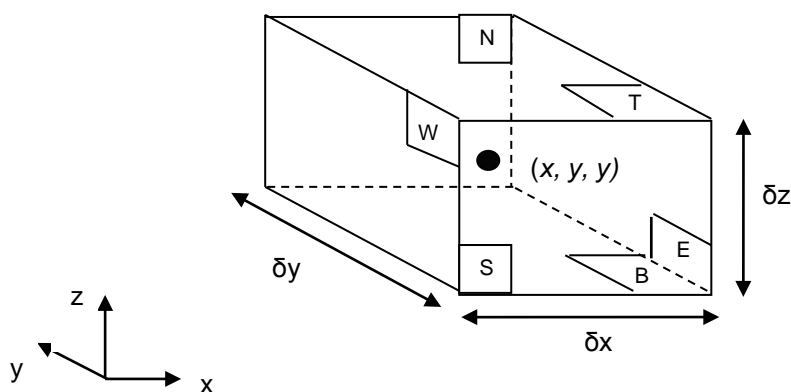
Figure 5.12: Fluid element for conservation laws, (Verteeg and Malalasekera, 2007).

The Finite Volume Method, considers the fluid properties to be a function of space and time and thus the density, pressure, temperature and velocity vector are functions of *x, y, z* and T_b (bulk fluid temperature) (Verteeg and Malalasekera, 2007). By considering the mass flow rate across face *W* as illustrated in Fig. 5.12, the mass conservation equation for unsteady, three dimensional flow in a compressible fluid is given by Eq. (5.4).

$$\frac{\partial \rho}{\partial T_b} + \frac{\partial (\rho u)}{\partial x} + \frac{\partial (\rho v)}{\partial y} + \frac{\partial (\rho w)}{\partial z} = 0 \qquad (5.4)$$

Therefore, considering an incompressible flow, the change in density is equal to zero and thus Eq. (5.4) is reduced to Eq. (5.5).

$$\frac{\partial u}{\partial x} + \frac{\partial v}{\partial y} + \frac{\partial w}{\partial z} = 0 \qquad (5.5)$$

The momentum equation in three dimensions is derived through the consideration of the forces acting on the element, these being the surface and the body forces. The latter could result due to the centrifugal coriolis and electromagnetic forces whereas the former could result due to pressure, viscous and gravity forces. Therefore, the rate of increase of the *x* momentum per unit volume of fluid particle is given by Eq. (5.6).

$$\rho \frac{du}{dt} = \frac{\partial (-P_l + \tau_{xx})}{\partial x} + \frac{\partial \tau_{yx}}{\partial y} + \frac{\partial \tau_{zx}}{\partial z} + S_{Mx} \qquad (5.6)$$

where, P_l is the pressure, this being a normal stress, τ is the viscous stress and S_{Mx} are the source terms referring to the contribution due to the body forces acting on the element. Similarly, the *y* and *z* components of the momentum equations are given in Eqs. (5.7) & (5.8).

$$\rho \frac{dv}{dt} = \frac{\partial \tau_{xy}}{\partial x} + \frac{\partial (-P_l + \tau_{yy})}{\partial y} + \frac{\partial \tau_{zy}}{\partial z} + S_{My} \qquad (5.7)$$

$$\rho \frac{dw}{dt} = \frac{\partial \tau_{xz}}{\partial x} + \frac{\partial \tau_{yz}}{\partial y} + \frac{\partial (-P_l + \tau_{zz})}{\partial z} S_{Mz} \qquad (5.8)$$

The third governing equation for fluid flow is the energy equation that is derived from the first law of thermodynamics. Therefore, this yields the rate of increase of energy of a fluid particle per unit volume. This equation will not be applied in the present study as all simulations were done assuming isothermal conditions.

5.5.2 Model setup – Mesh

The three dimensional CAD model was designed as a round pipe with an internal radius of 0.02 m and a total length of 0.6 m, with the initial 0.1 m as a vertical run. A radius of 0.01 m was used at the bend. The latter representative model, with a total horizontal pipe length of 0.5m was used following the results of a full scale simulation which suggested that the horizontal flow stabilizes after circa 0.3 m from the horizontal bend. Hence the flows analysed through the experiments done at *HSG1&2* are assumed to be at steady state. In fact, *HSG1* is at a distance of 0.8 m from the bend while *HSG2* is at a total distance of 3.1 m from the bend. The model was imported into Gambit and subsequently meshed through the use of a Hex Core (Native) mesh with a resultant cell count of circa 586,070 cells. Hanging nodes were permitted. The resultant mesh was checked for its cell skewness levels. The FLUENT User Guide (2006), states that the number of cells resulting in a skewness value greater than 0.9 should be as low as possible. Upon inspection, the generated mesh resulted in a total of 8 cells having a skewness greater than 0.9. This is considered as a reasonably low number, particularly when considering the total cell count of the model.

After saving the generated mesh as a mesh file, this was operated upon using a command prompt, namely the *utility tpoly* command. This function was necessary due to the fact that the Hex Core mesh could contain features that interfere with the partitioning. The latter could be hanging nodes and overlapping parent-child faces that are located between the core of the hexahedral cells and the surrounding body-fitted mesh. Hence, the *utility tpoly* command, converted the transitional hexahedral cells into polyhedral cells. The resultant mesh file was then read in the FLUENT solver program. As suggested by the FLUENT User Guide (2006), particular attention was paid to the minimum cell volume thus ensuring that this did not result in a negative value.

5.5.3 Model setup – FLUENT

The two-phase flow was simulated through the use of one of the three multiphase methods available in FLUENT, this being the Mixture method. Basu et al. (2003) reported that the Mixture method is most suitable for bubbly flows, hence the use of this method in the present study. Furthermore, Emmanouil et al. (2007) reported that the Mixture method is less intensive on memory, hence making it more relevant to the hardware resources available in the present study. Emmanouil et al. (2007) also reported that the Mixture method is a time saving compromise due to the fact that it solves the continuity and momentum equations as given in Eqs. (5.5) and (5.6), through the assumption that both phases behave as a mixture. Basu et al. (2003) also reported that the Mixture method is suitable for a low to moderate density of the second phase, hence making this method relevant for the relatively low second phase densities measured in the present study.

After importing the meshed model in the FLUENT solver, a pressure based solver model, enabling a pressure-based Navier Stokes solution algorithm was selected. The fluid flow was assumed to be in a steady state, hence implying that the solution is time independent. The relevant gravitational force was specified due to the effect expected on the buoyancy of the bubbles. The closure of the partial differential equations is the Standard $K\text{-}\varepsilon$ Turbulence model where one equation is solved for the turbulence kinetic energy K as in Eq. (5.9) and another equation is solved for the turbulent dissipation ε as in Eq. (5.10). This model assumes isotropic turbulence (Launder and Spalding, 1974).

$$\frac{\partial(\rho K)}{\partial t} + \frac{\partial}{\partial x_j}\left(\rho K u_j\right) = \frac{\partial}{\partial x_j}\left[\left(\mu + \frac{\mu_t}{\sigma_K}\right)\frac{\partial K}{\partial x_j}\right] + G_K + G_b - \rho\varepsilon \qquad \textbf{(5.9)}$$

$$\frac{\partial(\rho\varepsilon)}{\partial t} + \frac{\partial}{\partial x_j}\left(\rho\varepsilon u_j\right) = \frac{\partial}{\partial x_j}\left[\left(\mu + \frac{\mu_t}{\sigma_\varepsilon}\right)\frac{\partial\varepsilon}{\partial x_j}\right] - \rho C_2\left[\frac{\varepsilon^2}{K+\sqrt{\upsilon\epsilon}}\right] + C_{1\varepsilon}\frac{\epsilon}{K}(G_K + C_{3\epsilon}G_b) -$$

$$C_{2\varepsilon}\rho\frac{\epsilon^2}{K} \qquad \textbf{(5.10)}$$

where, G_b is the generation of turbulent kinetic energy due to the buoyancy of the second phase, $C_{1\varepsilon}$, $C_{2\varepsilon}$, $C_{3\varepsilon}$ are constants σ_K and σ_ε are the turbulent Prandtl

numbers for K and ε respectively. G_K is the generation of the turbulent kinetic energy due to the mean velocity tensor calculated through Eq. (5.11).

$$G_K = \mu_t S^2 \tag{5.11}$$

S is the deformation tensor given by Eq. (5.12);

$$S = \sqrt{2 S_{ij} S_{ij}} \tag{5.12}$$

μ_t is the eddy viscosity given by Eq. (5.13);

$$\mu_t = \rho C_\mu \frac{K^2}{\varepsilon} \tag{5.13}$$

where; C_μ is a function of the mean strain and rotation rates, the angular velocity of the system rotation and the turbulence fields. The model constants have the following values;

$C_{1\varepsilon}$ = 1.44; $C_{2\varepsilon}$ = 1.92; C_μ = 0.99; σ_k = 1.0; σ_ε = 1.3. The Schiller-Neumann drag law was selected to define the drag forces between the two phases. This was necessary as bubbles were assumed to have an approximate spherical shape (FLUENT User Guide, 2006). The boundary conditions applied are; a velocity inlet for the inlet side (vertical pipe) and a pressure outlet for the outflow side (horizontal pipe). The latter was selected as the FLUENT User Guide (2006) reported that this type of outlet is more suitable for the multiphase models.

A system pressure of 2.7 Bars (abs) was specified for all the simulations done. The two phases were also assumed to be travelling at the same velocity, with no mass transfer. No bubble nucleation was included in the model. Therefore a uniform second phase distribution was assumed at the pipe vertical inlet. As tabulated in Table 5.4, simulations were run using two volumetric void fractions based on the experimental results discussed in Section 4.5.1. The higher average volumetric void fraction of 1.05E-4was measured during the experimental test *HPT_FR VI* at a bulk fluid velocity of 0.25 m/s at the sight glass *HSG2*, while the lower volumetric void fraction of 1.49E-6 was measured during the experimental test *HPT_FR IV* at sight glass *HSG2*, at a velocity of 0.52 m/s.

To solve the defined model, the mass and momentum conservation equations, Eqs. (5.4) – (5.8) and the multiphase model should be discretized and solved on the predefined mesh. Hence, a first order discretization scheme was used on all equations while the SIMPLE (Semi-Implicit Method for Pressure Linked Equations) scheme was used for the pressure-velocity coupling. The solutions converged after circa 1750 iterations with the criteria for the residual convergence set at 1×10^{-5}.

Parameter	Low bulk fluid velocity (ms^{-1})	Medium bulk fluid velocity (ms^{-1})	High bulk fluid velocity (ms^{-1})
V (both phases-no slip) (ms^{-1})	0.25	0.42	0.52
K $(m^2 s^{-2})$	5E-2	4.5E-2	4.5E-2
ρ (kgm^{-3})	1000	1000	1000
Re (-)	11,100	23,000	26,500
Volumetric void fraction (-)	1.49E-6 1.05E-4	1.49E-6 1.05E-4	1.49E-6 1.05E-4
T_b (^oC)	65	65	65
P (Pa) (abs)	2.7E5	2.7E5	2.7E5
D_b (m)	0.20E-3	0.15E-3	0.15E-3
R (m)	0.1	0.1	0.1
Multi-phase model	Mixture	Mixture	Mixture
Convergence residual value (-)	1E-5	1E-5	1E-5
Phase distribution across inlet (vertical tube)	Uniform across pipe section	Uniform across pipe section	Uniform across pipe section

Table 5.4: Inlet dimensions, velocities and turbulent characteristics for all cases.

5.5.4 Mesh independence test

A mesh independence test was performed so as to establish whether the increase in the number of cells contained in the mesh as described in Section 5.4.2 would result in a change in the resultant output. Hence, a mesh file was generated with a total cell count of 876,000 cells. The latter cell count was generated through the

decrease of the maximum size value and growth rates specified in the size function in the Gambit pre-processing software. The mesh independence test was run using a volumetric void fraction of 1.05×10^{-4}. Identical results to those achieved with the smaller cell count were achieved. Hence, this test proved that the smaller cell count model was sufficient for the purposes of the present study and therefore this model was adopted for all simulations, as shorter and more practical computational times were achieved.

5.5.5 Comparison of results and discussion

The results of the simulations as outlined through Table 5.4 are illustrated through the phase distribution plots for the second phase (Nitrogen gas) as in Figures 5.13, 5.15, 5.17, 5.19, 5.20, 5.21, while Figures 5.14, 5.16, 5.18 illustrate the resultant mixture velocity contour plots that are identical for both sets of simulations done. As discussed in Section 4.3.1, the experimental results have shown a void fraction distribution across the vertical pipe for a two-phase downward flow to be quasi-homogenous. This result is also reproduced in all the CFD simulations carried out in the present study. Hence, these contours suggest that the CFD two-phase mixture method can accurately reproduce the expected volumetric void fraction distribution in vertical pipes. However, the minimal reduction in the volumetric void fraction close to the tube walls is not reproduced. This could be attributed to the narrow boundary layer hence the CFD simulation did not reproduce the resultant drop in the void fraction at a distance of 1 mm (0.9 r_p/R_p) from the pipe wall. As discussed in Section 4.3.1, the *coring* effect as defined by Drew and Lahey (1982), whereby higher void fractions could occur at the pipe core in relation to the region close to the wall in two-phase bubbly downward flow is also not represented in the CFD plots, even at the highest bulk fluid velocity and volumetric void fraction.

An analysis of the phase distribution at the bend suggests that the second phase stabilizes as a stratified bubbly flow after circa 0.3 m of horizontal pipe run, with lower bulk fluid velocities resulting in a marginal reduction of this *stabilization length*. The distribution of the second phase after the bend could be attributed to the resultant velocity profiles, hence suggesting that the fluid turbulence has a dominating effect on the phase distribution. This is in agreement with findings

reported by Crowe et al. (1996), who reported that the dispersion of bubbles is controlled by the local velocity fluctuations due to turbulence. However, after circa 0.3 m of a straight horizontal flow, the buoyancy forces are assumed to dominate. In fact, through their numerical simulations for bubbly flows with low Reynolds numbers, Esmaeeli and Tryggvason (1998) reported that for bubbles with relatively small diameters, the dynamics are independent of the surface tension and mostly dependent on the buoyancy force.
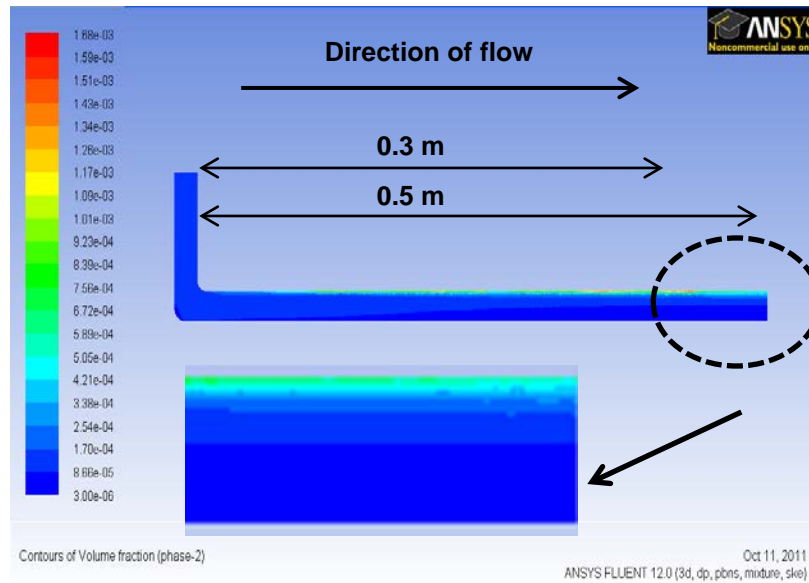
Figure 5.13: CFD volume fraction contour plot of second phase (nitrogen) at 0.25 m/s with a volume fraction of 1.05E-4 (Inlet at vertical end).
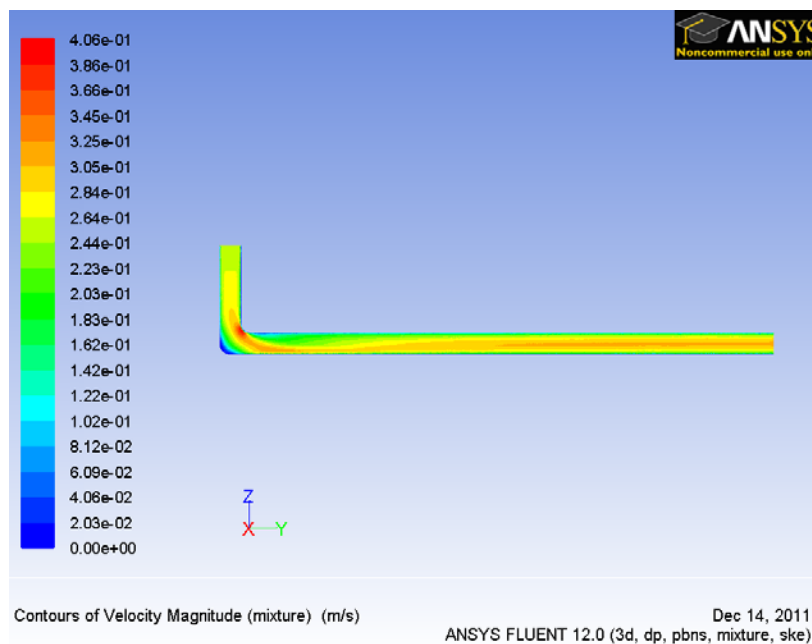
Figure 5.14: CFD volume mixture velocity contour plot at a velocity of 0.25 m/s.

188
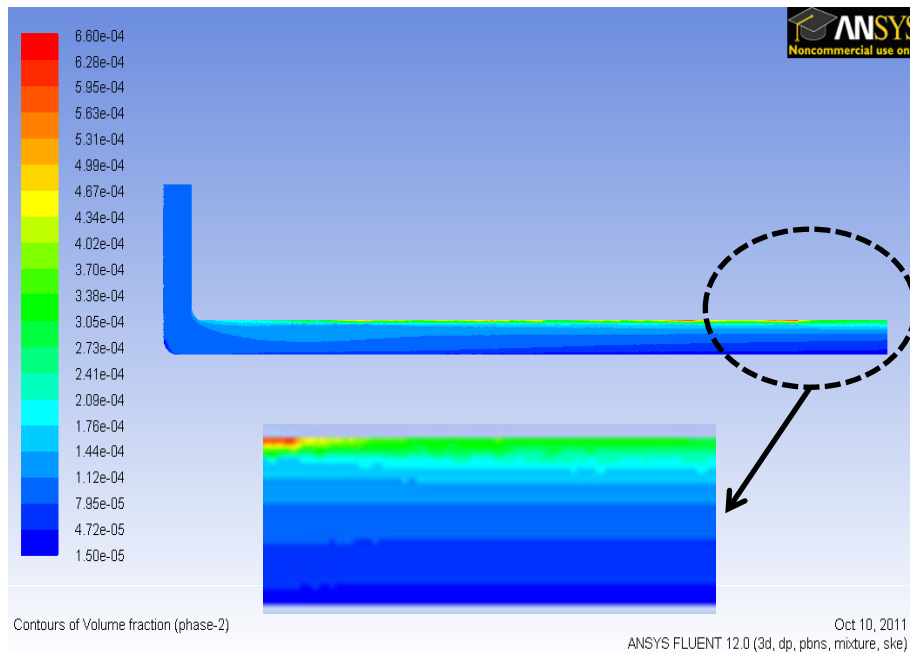
Figure 5.15: CFD volume fraction contour plot of the second phase (nitrogen) at 0.42 m/s with a volume fraction of 1.05E-4.
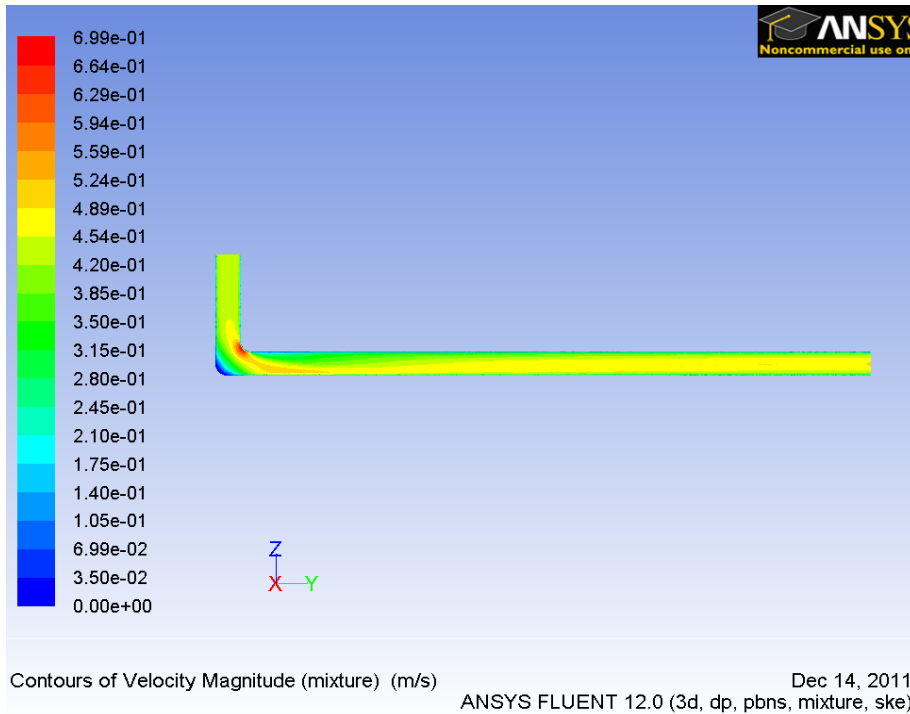
Figure 5.16: CFD volume mixture velocity contour plot at a velocity of 0.42 m/s.
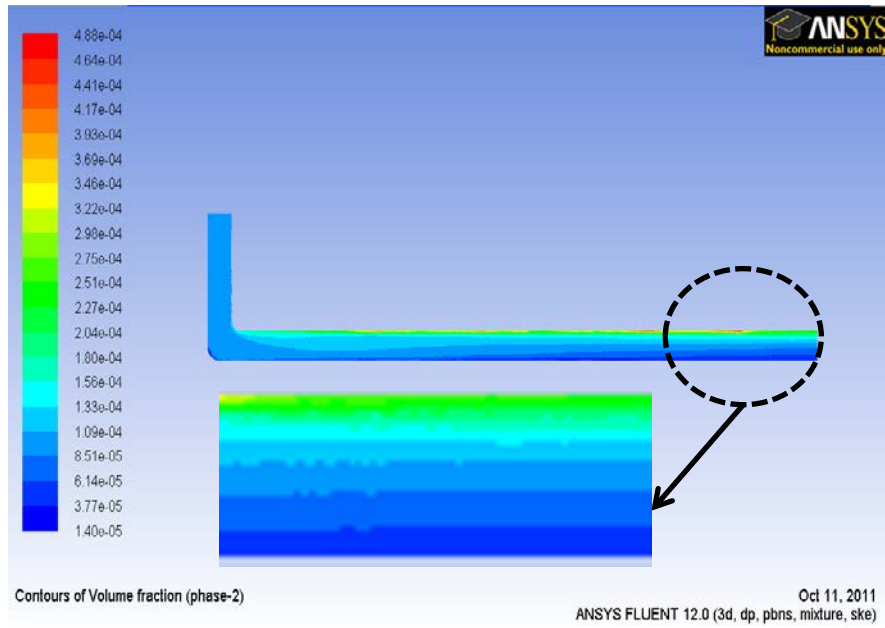
Figure 5.17: CFD volume fraction contour plot of second phase at 0.52 m/s with a volume fraction of 1.05E-4.
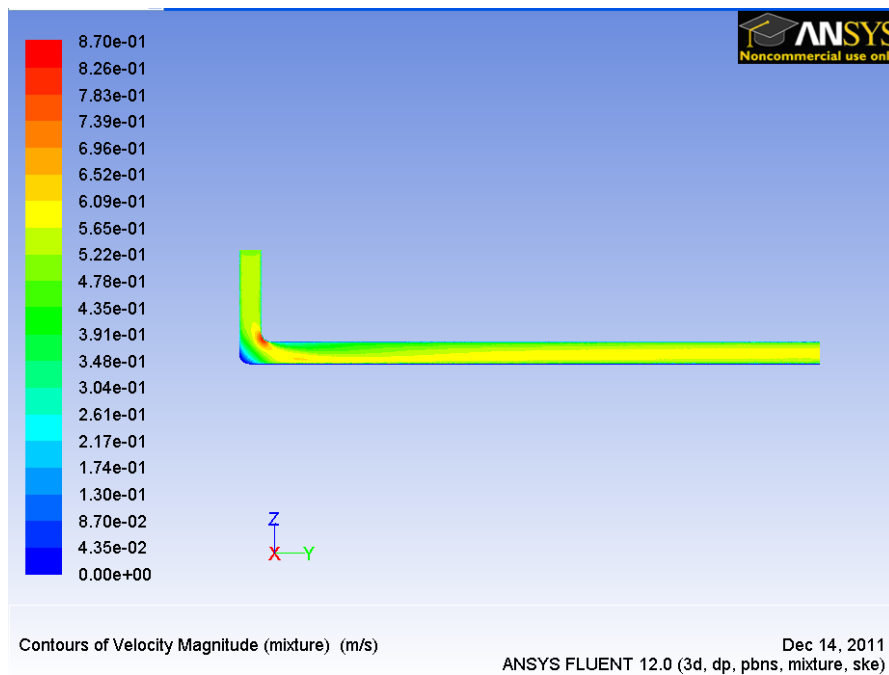
Figure 5.18: CFD volume mixture velocity contour plot at a velocity of 0.52 m/s.
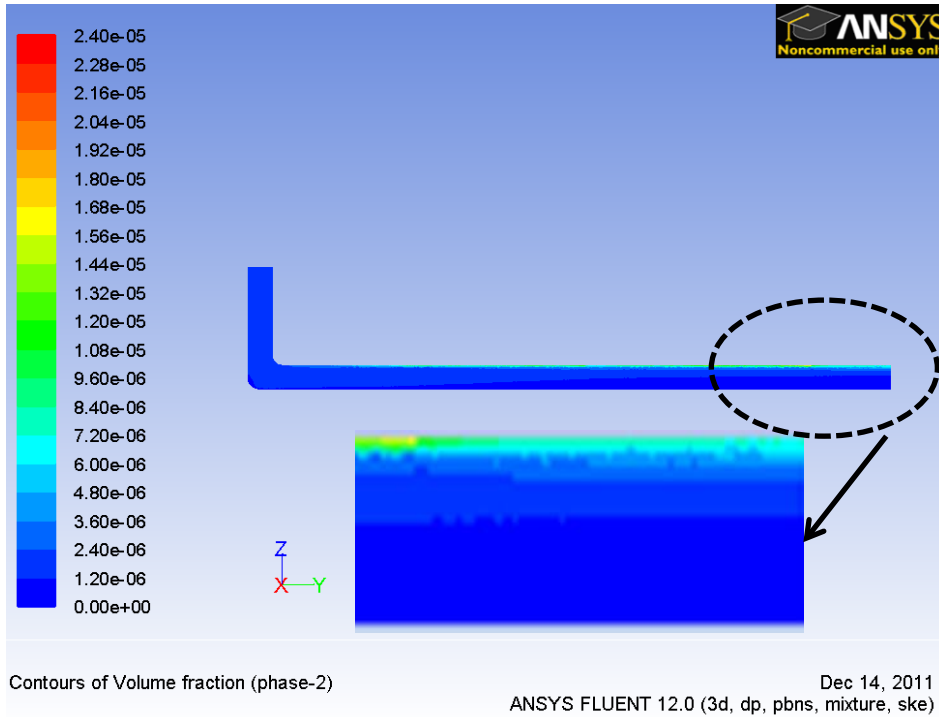
Figure 5.19: CFD volume fraction contour plot of second phase at 0.25 m/s with a volume fraction of 1.49E-6.
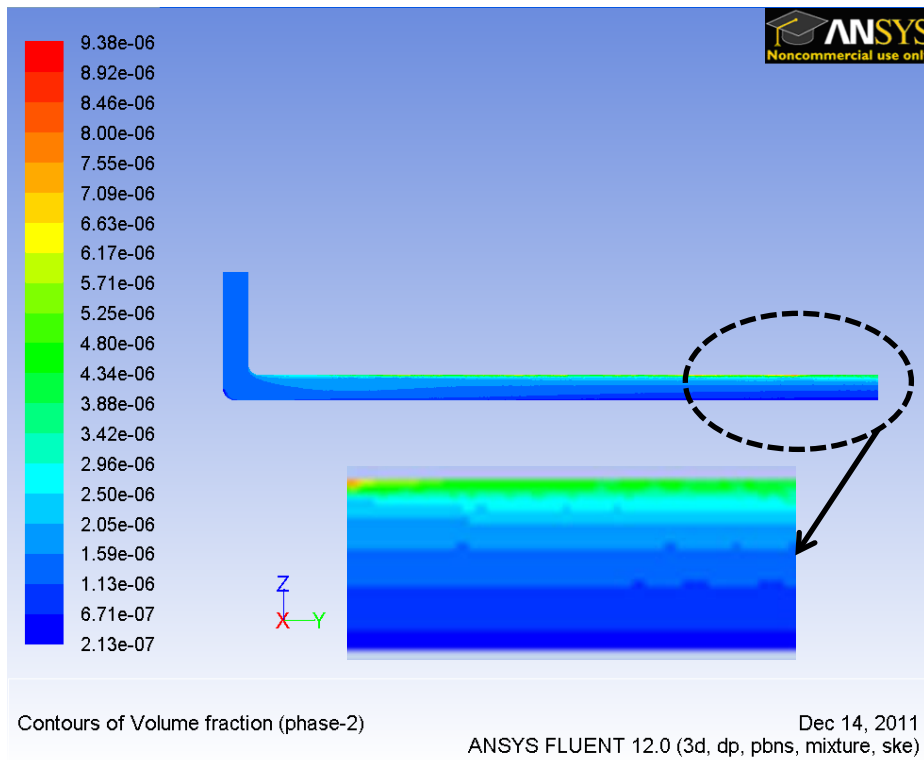
Figure 5.20: CFD volume fraction contour plot of second phase at 0.42 m/s with a volume fraction of 1.49E-6.
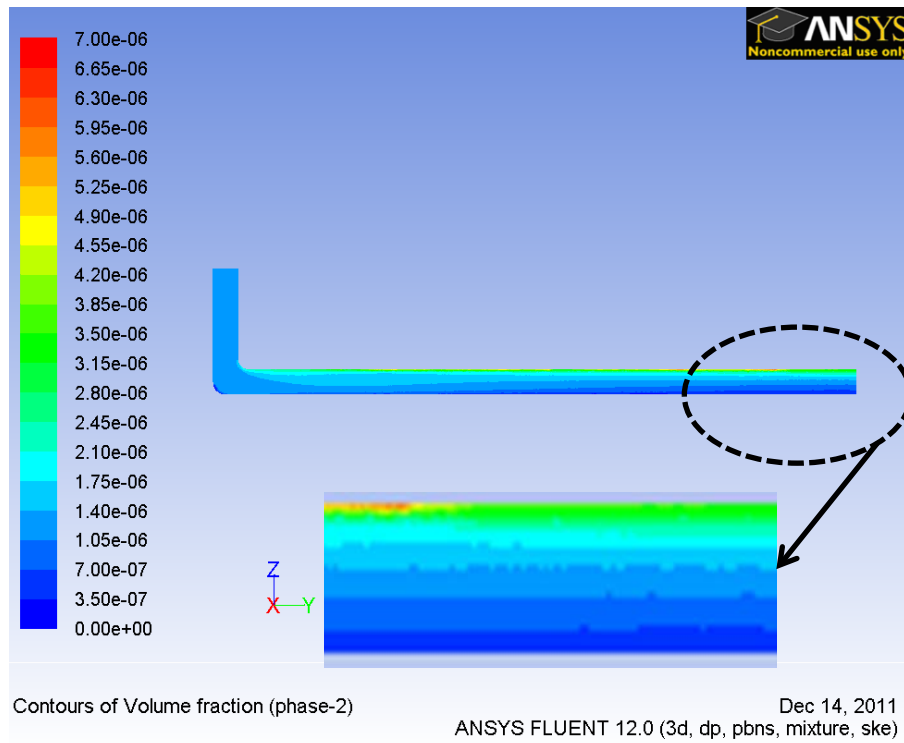
Figure 5.21: CFD volume fraction contour plot of second phase at 0.52 m/s with a volume fraction of 1.49E-6.

Hence, in agreement with the results of the present study, as discussed in Section 4.5.1, and with results reported in the open literature by Kocamustafaogullari and Wang (1991) and Iskandrani and Kojasoy (2001), the CFD second phase distribution profiles suggest a phase distribution that is dominated by the buoyancy forces, particularly at the lower bulk fluid velocities. Therefore, as the bulk fluid velocity is increased, a flattening of the void fraction distribution across the pipe depth is also predicted through the CFD plots due to the increase in the magnitude of turbulence as reported by Crowe et al. (1996).

The experimental results and the CFD predictions did not suggest any distinct relation between the actual resultant volumetric void fraction and the resultant phase distribution across the pipe section. Hence, the averaged experimental phase distribution results, as illustrated in Fig. 4.24, will be used for the purpose of this comparison. A comparison with the experimental results measured at *HSG1&2* is made through the consideration of the steady state void fraction distribution; hence the enlarged section for the CFD plots at a distance of circa 0.3 m from the bend. The graph in Fig. 5.22, illustrates the volumetric void fraction at a depth of 16 mm as a percentage of the void fraction measured at the

192

top of the pipe for experimental and CFD results. This relation is particularly relevant for the current study as higher void fraction percentages at the top of the pipe are desirable for an enhanced deaeration process. The CFD results were derived through the use of the resultant contour plot colour scale. The actual volumetric void fractions measured at the pipe depth for experiments *HPT_FR IV* and *HPT_FR VI* are compared to the CFD predictions through Figs. 5.23 & 5.24.

After considering the general limitations inherent to a two-phase flow study (Winterton and Munaweera, 2001), the CFD predictions through the application of the two-phase Mixture method, are considered to be in satisfactory agreement with the experimental results. However, the latter prediction tends to predict higher volumetric void fractions at the lower end of the pipe for all the experimental velocities considered. As illustrated in Fig. 5.22, this trend is most evident at a bulk fluid velocity of 0.42 m/s. This could be attributed to the assumption of a constant bubble diameter in the CFD simulation. Therefore, the model under predicted the buoyancy forces for the larger bubbles present in a distributed bubble size range. The relevant experimental errors also contributed to the variation between the predicted and the experimental values. This is evident at a bulk fluid velocity of 0.52 m/s where the predicted value is within the experimental error of the measured volumetric void fractions.

Figure 5.22: Experimental and CFD output mean % volumetric void fraction measured at a pipe depth of 16 mm in relation to that measured at the 0 mm plane for horizontal pipe tests with bulk fluid velocity.

193
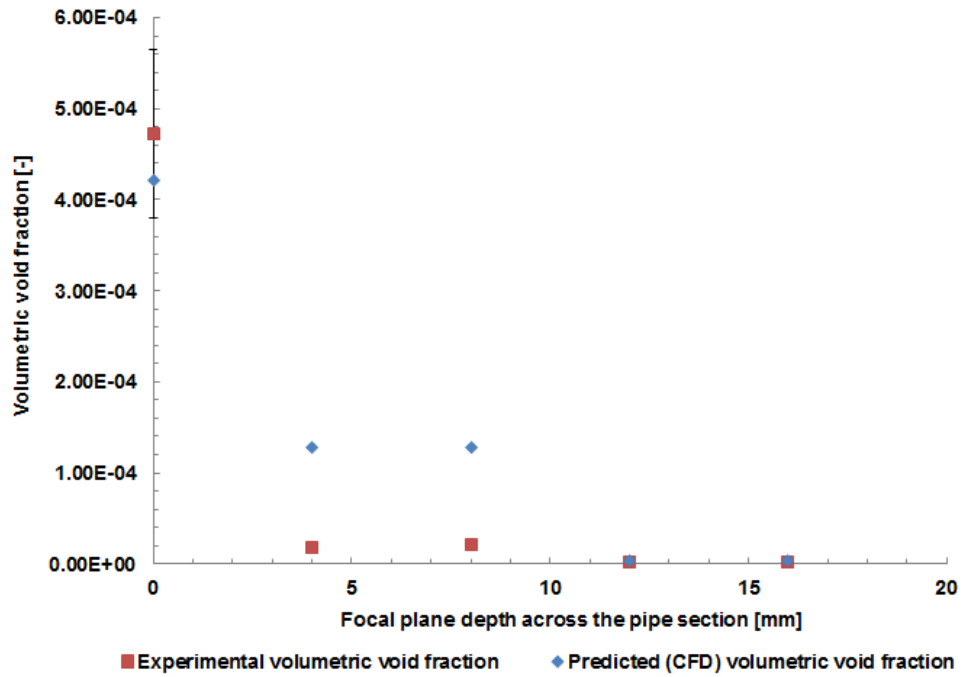
Figure 5.23: Experimental and CFD output for the volumetric void fraction across the pipe depth for Experiment *HPT_FR VI* (0.25m/s) at sight glass *HSG2*.
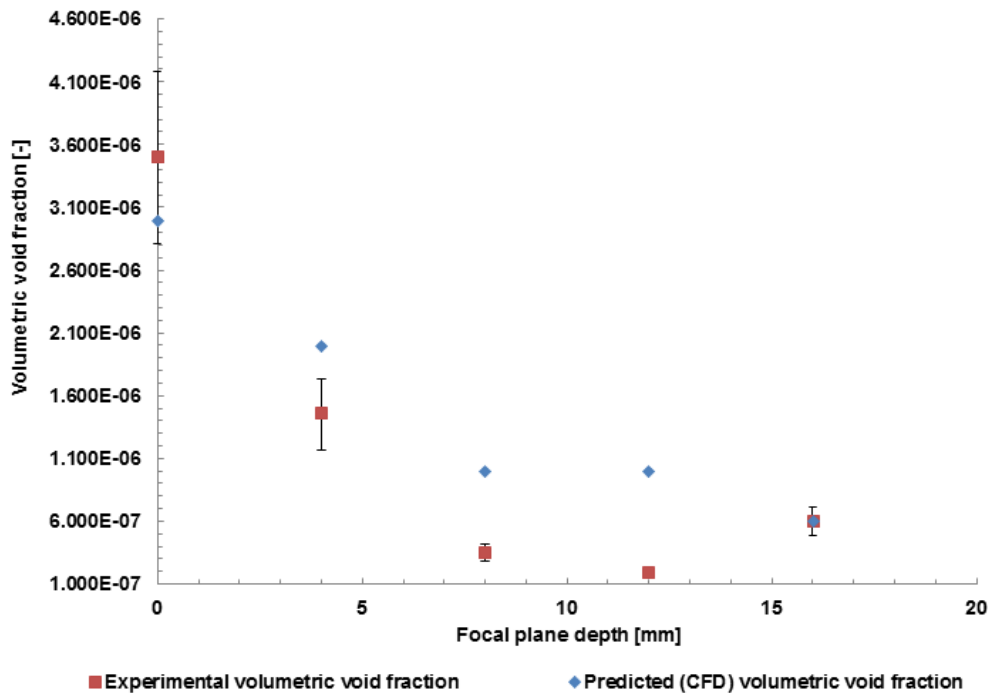
Figure 5.24: Experimental and CFD output for the volumetric void fraction across the pipe depth for Experiment *HPT_FR IV* (0.52m/s) at sight glass *HSG2*.

5.5.6 System improvement

After validating the use of the Mixture method for the two-phase flow regime considered in the present study, two sets of simulations were done through the application of larger pipe diameters. This was done following the consideration that larger void fractions are expected at the upper section of the pipe at lower bulk fluid velocities. This is a desirable property for deaertion, as it enhances the system performance. This is inherent to the design of passive deaerators, which consist of a vertical column designed to capture bubbles. Hence, as tabulated in Table 5.5, a 26 mm pipe internal diameter was used. A volumetric void fraction of 1.05×10^{-4} was used for all the CFD simulations in this section. The equivalent velocities calculated to ensure equal volume flow rates, are tabulated in Table 5.5.

Parameter	Low bulk fluid velocity (ms^{-1})	Medium bulk fluid velocity (ms^{-1})	High bulk fluid velocity (ms^{-1})
V (both phases-no slip) (ms^{-1})	0.15	0.25	0.31
K (m^{2}s^{-2})	5.1E-2	4.8E-2	4.7E-2
ρ (kgm^{-3})	1000	1000	1000
Re (-)	8,500	14,200	18,000
Volumetric void fraction (-)	1.05E-4	1.05E-4	1.05E-4
T (^{o}C)	65	65	65
P (Pa) (abs)	2.7E5	2.7E5	2.7E5
D_b (m)	0.20E-3	0.20E-3	0.20E-3
R (m)	0.13	0.13	0.13
Multi-phase model	Mixture	Mixture	Mixture
Convergence residual value (-)	1E-5	1E-5	1E-5
Phase distribution across inlet (vertical tube)	Uniform across pipe section	Uniform across pipe section	Uniform across pipe section

Table 5.5: Parameters used for the CFD two-phase simulations for model validation.

The results are illustrated through Figs. 5.25 – 5.27. Figure 5.28 highlights the percentage volumetric void fraction at a depth of 16 mm in relation to the void fraction at the top of the tube.

The volume contour plots confirm the trends highlighted through the experimental results and CFD simulations as discussed in the previous section whereby lower bulk fluid velocities, result in a higher volumetric void fraction at the upper section of the horizontal tube. Hence, the use of wider pipes would benefit deaeration through passive deaerators. Passive deaerators are installed to reduce the bubble count at the boiler exit thus reducing the overall saturation ratio present in the system's water. Consequently, the overall bubble nucleation rate at the primary heat exchanger wall is also reduced. Such devices consist of a vertical column and a float valve at the upper end of the column. Passive deaerators are normally connected to straight horizontal pipes. This is done to maximize the effect of buoyancy. Hence, air bubbles float up the column and accumulate at the top end.
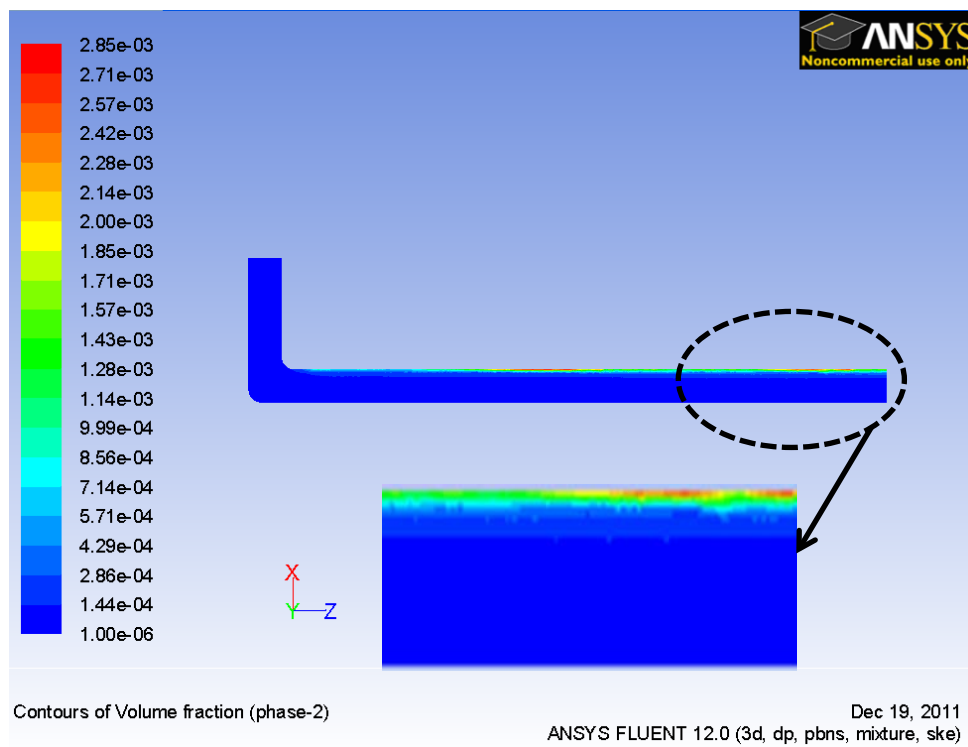
Figure 5.25: CFD volume fraction contour plot of second phase at 0.15 m/s with a volume fraction of 1.05E-4 for a 26 mm internal diameter pipe.
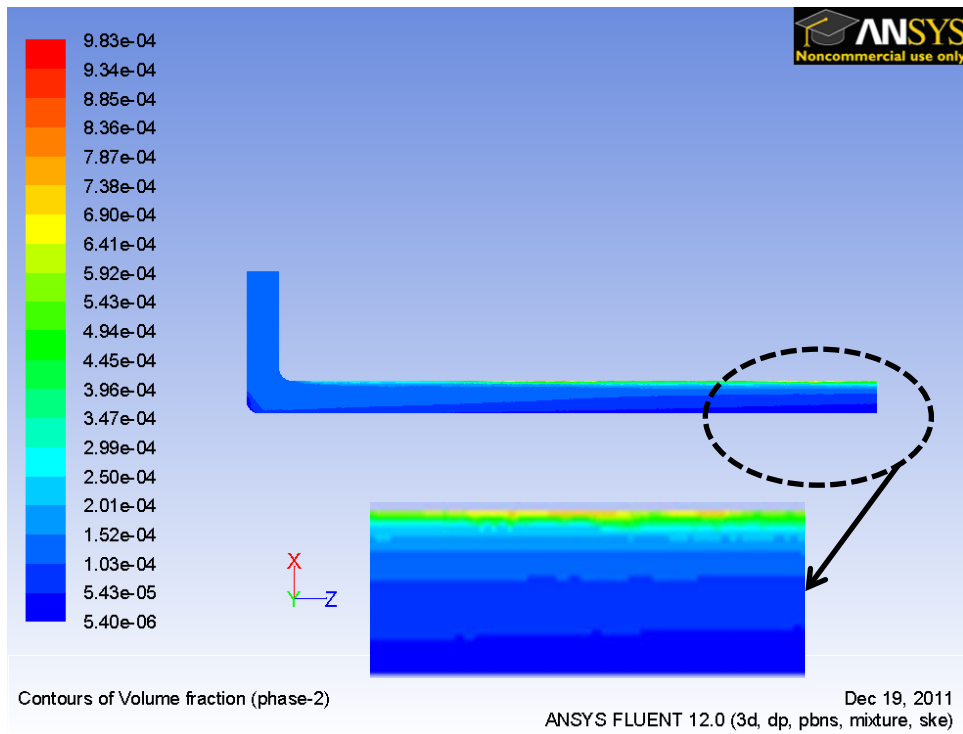
Figure 5.26: CFD volume fraction contour plot of second phase at 0.25 m/s with a volume fraction of 1.05E-4 for a 26 mm internal diameter pipe.
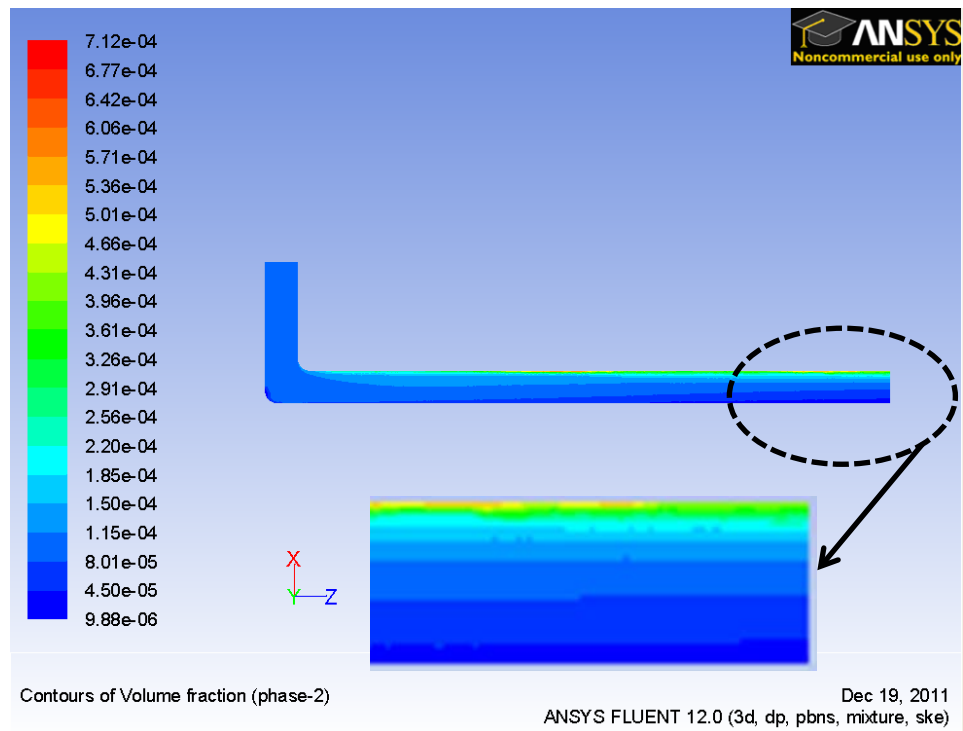
Figure 5.27: CFD volume fraction contour plot of second phase at 0.31 m/s with a volume fraction of 1.05E-4 for a 26 mm internal diameter pipe.
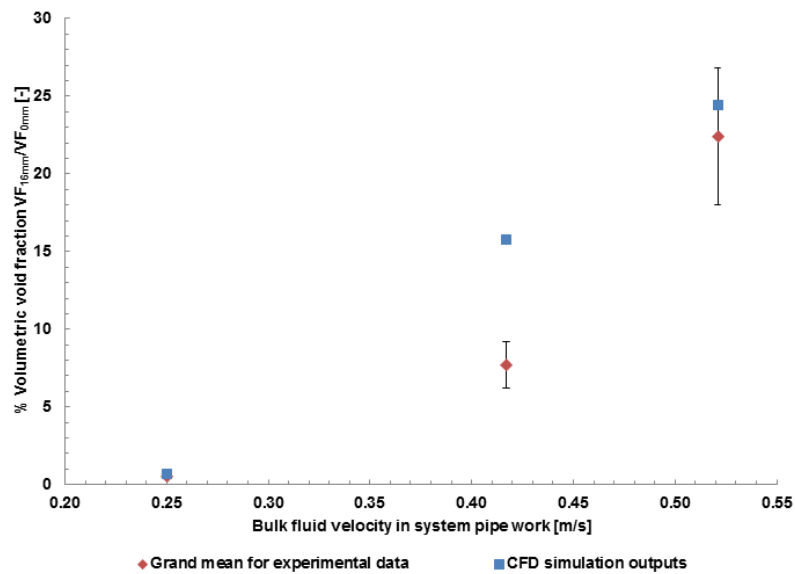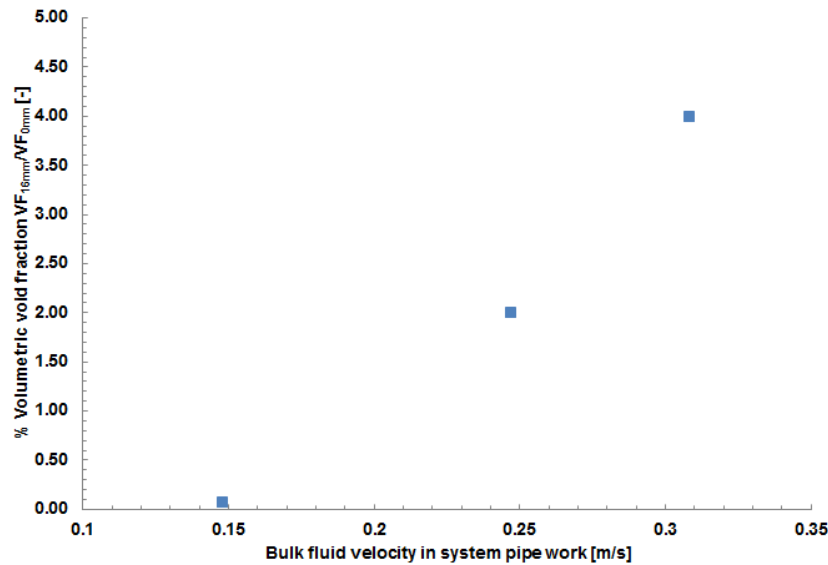
Figure 5.28: CFD output mean predicted percentage volumetric void fraction measured at a pipe depth of 16 mm in relation to that measured at the 0 mm plane for horizontal pipe tests with bulk fluid velocity for a 26 mm internal diameter pipe.

The excess air is then exhausted through the action of a float valve. Higher volumetric void fractions at the upper section of the horizontal pipe, combined with lower bulk fluid velocities are expected to facilitate the passive deaeration process used in domestic central heating systems. Hence, bubbles flowing at the top of the pipe tend to bubble up the deaerator column at a higher efficiency when compared to the bubbles flowing in the centre of the horizontal pipe. Furthermore, the lower bulk fluid velocities reduce the possibility of bubbles flowing through the deaerator device with the bulk fluid. Therefore, lower system velocities should lead to improved deaeration rates, thus reducing the system susceptibility to problems related to two-phase flow, namely cold spots in radiators, excessive noise, pipework blockages and cavitation corrosion.

5.6 Summary

This chapter presented and discussed the relevant correlations adopted for the data collected in the present study. Hence, Chapter 5 presented an extension to the use of the mostly theoretical bubble size prediction, nucleation and dissolution models to more practical grounds. The understanding of the fundamentals and the development of theoretical models for the prediction of bubble size at detachment, nucleation, dissolution and phase distribution in a wet

central heating system is considered to be essential in the optimization of such systems. This is due to the adverse effects which such bubbles could have on the system performance.

The principal conclusions derived through this research project will be discussed in the next Chapter.

CHAPTER 6

Conclusions

6.1 Conclusions

The two-phase characteristics in domestic central heating systems were investigated experimentally in the current study. This necessitated the design and construction of an experimental test rig at Brunel University, in the United Kingdom. Furthermore, photographic and image analysis techniques were developed as part of the current study. A number of experiments followed with the aim of investigating; the bubble characteristics at the boiler flow line, the bubble nucleation on the primary heat exchanger wall, bubble dissolution in horizontal pipe flow and the second phase distribution in horizontal pipes. Additionally a detailed evaluation for the existing bubble size prediction, nucleation and dissolution models and correlations was also conducted as part of the current study. The important conclusions that can be drawn from the present study are summarized in the following subsections.

6.1.1 Bubble size and shape characteristics at boiler flow line exit

Mean bubble diameters in the range of 0.13 mm to 0.39 mm have been measured with the system parameters. It has been shown that, the bulk fluid velocity has the largest effect on the resultant bubble detachment diameter from the primary heat exchanger wall. In fact, a considerable reduction in the bubble diameter was measured with an increase in the bulk fluid velocity. Other system parameters such as the heat flux and pressure have shown a marginal effect on the bubble sizes whereas the limited saturation ratio range reached in the present study did not result in any effect at all.

The data gathered in the present study, is reasonably consistent with the relevant theory for the prediction of bubble detachment diameters in supersaturated solutions. The Winterton (1972a) approach, predicts the bubble radius on

detachment for bubbles that extend into the transition region of the flow before breaking free from their nucleating point in round pipes. This theory, is based on the resolution of the forces acting on the bubble at its nucleation point and parallel to the boiler wall surface. Therefore, the present study extends the use of this theoretical model to non-circular, rectangular ducts and provides data with respect to the characteristics of bubbles present in a domestic central heating system. Particular attention has been drawn to the variation in bubble size with the system flow rate, whereby a clear trend is evident between the identified model and the measured data.

The present study has suggested a new correlation for wet central heating systems based on the Winterton (1972a) approach. The new correlation, incorporates the effect of pressure, bulk fluid velocity and heat flux on the predicted bubble diameter at the exit of the boiler and has predicted the bubble diameters at the exit of a central heating boiler with reasonable accuracy, yielding a mean absolute error of 8%.

Bubble shape analysis, has resulted in a mean aspect ratio in the range of 0.9 to 1 with all the system parameters. This suggests that bubbles flowing out of the boiler unit into a vertical pipe with a downward flow, can be reasonably assumed to be quasi-spherical in shape.

6.1.2 Bubble nucleation and system bubble production rates

The present study investigated the fundamentals of bubble nucleation in a domestic wet central heating system at the super saturation levels present at the primary heat exchanger wall conditions. Bubble nucleation due to dissolved nitrogen gas occurs at significant levels at super saturation levels in the range of 1 to 20%. Mean bubble nucleation rates, ranging from 0.3 to 4 bubbles / cm^2 s resulting in a system bubble production rate of 784 to 6,920 bubbles per second were measured. A maximum volumetric void fraction of 6.6E-4, resulting in a gas volume flow rate of 0.47 L of Nitrogen gas per hour, was measured at the boiler exit with typical system conditions.

Experimental measurements have shown an increase in the bubble production rate from the system primary heat exchanger, with an increase in heat flux,

saturation ratio and bulk fluid velocity, whereas a decrease in the bubble production rate was evident with an increase in pressure. The calculated nucleation rate at the system heat exchanger wall is not proportional to the bubble production rate due to a change in the heat exchanger surface area under super saturation conditions with system parameters.

A comparison of the experimental data for bubble nucleation was done through the application of the classical and non-classical heterogeneous nucleation models. The classical nucleation theories are considered to be inadequate at predicting nucleation in more practical solutions characterized with low super saturation levels, as in the current study. The simplified classical model by Lubetkin and Blackwell (1988) for heterogeneous nucleation is also considered as inadequate at predicting nucleation in solutions with a low degree of super saturation. Furthermore, a direct comparison of the nucleation results to the non-classical nucleation model as presented by Hepworth et al. (2003) was not possible due to insufficient knowledge with respect to the surface nucleation site density.

Therefore, a correlation using the non-classical model as presented by Hepworth et al. (2003), and incorporating the primary heat exchanger surface area under super saturation conditions was developed to fit our bubble nucleation data, resulting in a mean absolute error of 24%. Further improvement to this model is considered important for design purposes. Therefore, as discussed in Section 6.3, investigations into the effect the surface conditions such as the density and size of nucleation sites as well as the resultant contact angles at the primary heat exchanger wall, are considered to be important for an improved understanding of the nucleation phenomenon, thus leading to an improved model fit.

6.1.3 Bubble behaviour in horizontal under saturated, saturated and supersaturated bubbly two-phase flow

The bubble dissolution rates measured for the bubble size ratios are in the range of 0.4 to 12 % per second or 0.65 to 18 % per meter of horizontal pipe work with system conditions, hence increasing with lower bulk fluid under saturation ratios and higher velocities. The dissolution mechanism is mainly dependent on the gas concentration in the bulk fluid and the degree of turbulence, while the effects of

the phase relative velocity, surface tension and bulk fluid temperature and pressure are considered to be negligible. The decrease in the bubble size as it flows through the system pipework, is a result of the gas mass transfer from the bubble to the ambient liquid. The importance of this study is emphasized by the minimal consideration given by the open literature to the dissolution of free bubbles in under saturated bubbly water flow at constant pressure conditions. Hence, the present study extends the knowledge concerning bubble dissolution to a practical case, thus leading to a better understanding of the bubble behaviour in the flow lines of a typical contemporary domestic central heating boiler.

The dissolution rate across the pipe depth has also been analysed, with results suggesting a slightly higher dissolution rate expected in the centre of the horizontal pipework. The present study has suggested a new correlation for wet central heating systems based on the Epstein and Plesset (1950) isolated bubble dissolution models, with the inclusion of the Sherwood number as defined by Lezhnin et al. (2003) to incorporate the effects of turbulent diffusion on the mass transfer process. Hence, the proposed model presents a practical adaptation to the mostly theoretical bubble dissolution models for isolated bubble conditions, as reported in the open literature. The proposed model, has predicted the expected dissolution rate with a reasonable accuracy, with a mean absolute error of 10.4%.

At saturated bulk fluid conditions, the present study results suggest that a minimal degree of bubble dissolution takes place in horizontal two-phase bubbly flow. Furthermore, at super saturated bulk fluid conditions, no significant bubble growth was measured at a bulk fluid saturation ratio of 1.1. Such results can be attributed to the fact that the bubbles under investigation are free bubbles in a turbulent bubbly flow and hence, as reported by Arefmanesh et al. (1992), and Shafi and Flumerfelt (1997) and Sun and Beckermann (2010), the resultant bubble growth dynamics could be dependent on a combination of complex physical conditions, that are difficult to quantify.

6.1.4 Volumetric void fraction distribution in the system horizontal pipework

The present study has suggested a strong dependence of the second phase distribution across the horizontal pipe depth, on the gravitational effects and on

the bulk fluid velocity. The effect of the mean volumetric void fraction across the pipe depth on the second phase distribution profile is considered to be negligible. A comparison of the experimental results with a CFD simulation through the application of the multiphase fluid mixture model has yielded reasonably good comparisons between the theoretical predictions and the experimental measurements. Therefore the present study has validated a CFD model for the phase distribution, and extends this study to propose wider pipes to be used in the flow line of a domestic central heating system for enhanced system deaeration through passive techniques.

6.2 Recommendations for deaeration efficiency improvement

The present study demonstrates that, the largest bubbles are observed at the lower system velocities. Large bubbles are known to facilitate the passive deaeration process used in wet domestic central heating systems. This is inherent to the design of such systems, normally consisting of a vertical column and a float valve to trap and deaerate air bubbles along the horizontal system pipe work at the exit side of the boiler.

The latter is the principal design concept applied to the passive deaerator range manufactured and supplied by Spirotech bv. Such devices are considered to be a good representative of passive deaertaors used in such systems, due to their widespread use in households across Europe. In fact, such systems are used as standard devices in most installations done by British Gas in the United Kingdom. Furthermore, passive deaerators supplied by other known companies such as Pneumatex AG, also make use of the same concept through the application of similar designs.

Due to higher buoyancy forces, larger bubbles are known to collect in such columns at higher rates than their smaller counterparts. Therefore, lower system velocities should lead to improved deaeration rates, thus reducing the system susceptibility to problems related to two-phase flow. Furthermore, as demonstrated in Section 5.5.6, wider pipe work would ensure a higher percentage void fraction at the upper section of the horizontal pipe work, thus further

facilitating the capture of bubbles through the passive deaerator. The positioning of the deaerator close to the boiler outlet should also ensure that the effect of dissolution on the mean bubble diameter is minimized.

Finally, lower boiler flow temperatures and higher system pressures result in lower saturation levels at the primary heat exchanger wall conditions, consequently reducing the bubble count in the system.

6.3 Recommendations for future work

Based on the experiments conducted as part of the present study, the issues that require further investigations include the following;

- The effect of scale deposits on the surface of the heat exchanger, through a prolonged usage of the system, should be investigated. Such deposits could affect the bubble nucleation process due to the change in the stainless steel surface finish, thus affecting the resultant bubble contact angles on the surface of the heat exchanger. Hence, it is recommended to conduct similar experiments as done in the present study, using heat exchangers with varying levels of scale deposits.

- The use of different primary heat exchanger geometries and surface finish quality was considered during the present study. However, this has proved to be very difficult as a result of the domestic boiler architecture and setup. Hence, further investigations into the effect the heat exchanger architecture and surface conditions such as the density and size of nucleation sites, as well as the resultant contact angles at the primary heat exchanger wall, are considered to be important for an improved understanding of the bubble nucleation phenomenon. It is also recommended, to extend the latter studies to further develop the bubble nucleation model correlation presented in the present study.

- The bubble nucleation calculations presented in the present study, have considered the linear rise in the primary heat exchanger water side wall temperature between the return and flow sides. This has been done

through calculation, as a reliable method of measurement was not technically feasible. Hence, a recommendation is made for further experimental investigation into the resultant heat exchanger wall temperatures with system heating load conditions.

- Further investigation into the effects of water additives, such as chemicals added for rust preventive measures, is recommended. Such additives could affect the surface tension of water, hence affecting the two-phase characteristics.

- Further experimental studies are recommended for bubble dissolution in horizontal pipes at varying system pressures. The present study and a number of studies in the open literature have assumed that the effect of the bulk fluid pressure on bubble dissolution is negligible. However, further experimental work is recommended for an investigation into the effect of this parameter on the rate of bubble dissolution in domestic central heating systems.

References

Adrian R.J., 1991. Particle-imaging techniques for experimental fluid mechanics, *Annual Review of Fluid Mechanics*, 23, pp. 261 - 304.

Abdelmessih A.H., Hooper F.C., Nangia S., 1972, Flow effects on bubble growth and collapse in surface boiling, *International Journal for Heat Mass Transfer*, 15, pp. 115-125.

Akiyama M., Tachibana F., 1974, Motion of vapor bubbles in subcooled heated channel, *The Japan Society of Mechanical Engineers*, 17 (104), pp. 241-247.

Al-Hayes R.A.M., Winterton R.H.S., 1981a, Bubble growth in flowing liquids, *International Journal of Heat and Mass Transfer*, 24, pp. 213-221.

Al-Hayes R.A.M., Winterton R.H.S., 1981b, Bubble diameter on detachment in flowing liquids, *International Journal of Heat and Mass Transfer*, 24, pp. 223-229.

Antal S.P., Lahey Jr. R.T., Flaherty J.E., 1991, Analysis of phase distribution in fully developed laminar bubbly two-phase flow, *Int. J. Multiphase Flow*, 17 (5), pp. 635-652.

Arefmanesh A., Advani S.G., Michaelides E.E., 1992, An accurate numerical solution for mass diffusion-induced bubble growth in viscous liquids containing limited dissolved gas, *International Journal of Heat and Mass Transfer*, 37 (7), pp. 1711-1722.

Bakos G.C., Spirou A., Tsagas N.F., 1999, Energy management method for fuel saving in central heating installations, *Journal of Energy and Buildings*, 29, pp. 135-139.

Balaban-Irmenin Yu.V., Fokina N.G., 2007, Internal-corrosion inhibitors for pipelines carrying deaerated heating water, *Journal of Power and Technology*, 41, (5), pp. 37-43.

Baranenko V.I., Kirov V.S., 1989, Solubility of hydrogen in water in a broad temperature and pressure range, *Translated from Atomnaya Énergiya*, 66 (1), pp. 24-28.

Basu N., Troshko A., Nurnberg G., 2003, *Modelling of Two-phase Flow and Boiling with FLUENT*, Fluent Inc., Available at: http://www.scribd.com/doc/3754733/Basu [Accessed Date: 2nd December 2011]

Battaglia J., 1985, *Deaeration system*, Pittsburgh, U.S. Pat. 5,383,958.

Battino R., ed., 1982, *Nitrogen and Air, Solubility Data Series,* – Volume 10, Oxford Pergamon Press.

Beattie D.R.H., 1996, Flow characteristics of horizontal bubbly pipe flow, *Nuclear Engineering and Design*, 163, pp. 207-212.

Bejan A., 1993, *Heat Transfer*, New York, John Wiley & Sons, Inc.

Bisperink C.G.J., V., Prins A., 1994, Bubble growth in carbonated liquids, *Colloids Surfaces A: Physiochemical and Engineering Aspects*, 30, pp. 237-253.

Blander M., Katz J.L., 1975, Bubble nucleation in liquids, *AIChE Journal*, 21 (5), pp. 51 - 84.

Bulloch J.H., 2003, Deaerator feedwater vessel weld cracking monitored over a service time of around 80,000 hours, *International Journal of Pressure Vessels and Piping*, 80, pp. 607-615.

Cable M., 1967, The dissolving of stationary gas bubbles in a liquid, *Chemical Engineering Science*, 22, pp. 1393-1398.

Cable M., Frade J.R., 1988, The influence of surface tension on the diffusion-controlled growth or dissolution of spherical gas bubbles, *Proceedings of the Royal Society of London. Series A, Mathematical and Physical Sciences*, 420, pp. 247-265.

Carr M.W., Hillman A.R., Lubetkin S.D., 1995, Nucleation rate dispersion in bubble evolution kinetics, *Journal of Colloid and Interface Science*, 169, pp.135 - 142.

Che D., Yanhua L.,Chunyang G., 2004, Evaluation of retrofitting a conventional natural gas fired boiler into a condensing boiler, *Journal of Energy Conservation & Management*, 45, pp. 3251-3266.

Chisholm D., 1983, *Two-phase flow in pipelines and heat exchangers*, United Kingdom, Longman.

Coleman, H.W., Steele, W.G., 1999, *Experimentation and uncertainty analysis for engineers*, 2nd ed., New York, John Wiley& Sons Inc.

Committee On Climate Change (CCC), 2008, *Building a low-carbon economy – The UK's contribution to tackling climate change*, London.

Crowe C.T., Troutt T.R., Chung J.N., 1996, Numerical models for two-phase turbulent flows, *Annu. Rev. Fluid. Mech.*, 28, pp. 11-43.

Crum L.A., 1977, *Measurements of the growth of air bubbles by rectified diffusion*, United States Naval Academy, Office of Naval Research, Technical Report No. 377.

Cry D.R., 2001, *Bubble growth behaviour in supersaturated liquid solutions*, PhD Thesis, The University of Maine.

Davis J.R., ed., 2000, *Corrosion; Understanding the basics*, Ohio, ASM International.

Davis R.D., 1987, Corrosion problems in central heating systems, *Anti-corrosion methods and materials*, 34 (4), pp. 6-11.

Dean R. B., 1944, The formation of bubbles, *Journal of Applied Physics*, 15, pp. 446-451.

Delale C.F., Hruby J., Marsik F., 2003, Homogenous bubble nucleation in liquids: The classical theory revisited, *Journal of Chemical Physics*, 18 (2), pp. 792-806.

Desloge E. A., 1968, *Thermal Physics*, New York, Holt, Rinehart and Winston, Inc.

Dhir V.K., 1998, Boiling heat transfer, *Annual Rev. Fluid Mech.,* 30, pp. 365-401.

Drew D.A., Lahey R.T., 1982, Phase-distribution mechanisms in turbulent low-quality two-phase flow in a circular pipe, *J. Fluid Mech.*, 117, pp. 91-106.

Duda J.L., Vrentas J.S., 1971, Heat or mass transfer-controlled dissolution of an isolated sphere, *International Journal of Heat and Mass Transfer*, 14, pp. 395 - 408.

Dwyer T., 2008, *Development of Domestic Condensing Boilers to Save Energy*, London South Bank University.

Eastoe J., Ellis C., 2007, De-Gassed water and surfactant-free emulsions: History, controversy, and possible applications, *Advances in Colloid and Interface Science*, 134, pp. 89 – 95.

Edzwald J.K., 1995, Principles and applications of dissolved air flotation, *Wat. Sci. Tech.*, 31, (3-4), pp. 1-23.

Elperin T., Forminyk A., 2003, Four stages of the simultaneous mass and heat transfer during bubble formation and rise in a bubbly absorber, *Chemical Engineering Science*, 58 (15), pp. 3555 - 3564.

Emmanouil V., Skaperdas E.P., Karapantsios T.D., Matis K.A., 2007, Two-phase simulations of an off-nominally operating dissolved-air flotation tank, *International Journal for the Environment and Pollution*, 30, pp. 213-230.

Epstein P.S., Plesset M.S., 1950, On the stability of gas bubbles in liquid-gas solutions, *The Journal of Chemical Physics*, 18 (11), pp. 1505-1509.

Esmaeeli A., Tryggvason G., 1998, Direct numerical simulations of bubbly flows: Part 1. Low Reynolds number arrays, *J. Fluid Mech.*, 377, pp. 313-345.

European Commission, DG for Energy and Transport, 2002, *Labelling and other measures for heating system in dwellings*, Final Technical Report, Save II Action, Available at: http://www.eci.ox.ac.uk/research/energy/downloads/eusaveheating/full report.pdf [Accessed Date: 18th September, 2011].

European Commission, Climate Action, 2011, Roadmap for moving to a low-carbon economy in 2050**,** Available at: http://ec.europa.eu/clima/policies/roadmap/index_en.htm [Accessed Date: 21th December, 2011].

Ferrell R.T., Himmelblau D.M., 1967, Diffusion coefficient of nitrogen and oxygen in water, *Journal of Chemical Engineering Data*, 12, pp. 111-115.

FLUENT User's Guide, 2006, Version 6.3, Fluent Inc, on CDROM.

Fogg P.T.G., 2003, Some Aspects of the Solubility of Gases in Liquids, *Monatshefte für Chemie*, 134, pp. 619 – 631.

Francis M.J., Pashley R.M., 2006, The effect of de-gassing on the dispersion of fine oil droplets in water, *Journal of Colloid and Surfaces A: Physicochem Eng. Aspects*, 287, pp. 36-43.

Frolich P.K., Tauch E.J., Hogan J.J., Peer A.A., 1931, Solubilities of gases in liquids at high pressure, *Journal of Industrial and Engineering Chemistry*, 23 (5), pp. 548-550.

Fsadni, A.M., Ge Y.T., Lamers A.G., 2011, Measurement of bubble detachment diameters from the surface of the boiler heat exchanger in a domestic central heating system, *Applied Thermal Engineering*, 31 (14-15), pp. 2808-2818.

Gerrard W., 1976, *Solubility of Gases and Liquids*, New York, Plenum Press.

Guo L., Feng Z., Chen X., 2001, An experimental investigation of the frictional pressure drop of steam–water two-phase flow in helical coils, *International Journal of Heat and Mass Transfer*, 44 (14), pp. 2601-2610.

Hailemariam L., Okos M., Campanella O., 2007, A mathematical model for the isothermal growth of bubbles in wheat dough, *Journal of Food Engineering*, 82, pp. 466-477.

Heat O., 1998, *Koordinierte schlußbericht: Gase in kleinen und mittleren wasserheiznetzen*, TU Dresden, Institut für Energietechnik..

Heide K., Hartmann E., Stelzner Th., Muller R., 1996, Degassing of a cordierite glass melt during nucleation and crystallization, *Thermochimica Acta*, 280-281, pp. 243-250.

Hepworth N.J., Boyd J.W.R., Hammod J.R.M., Varley J., 2003, Modelling the effect of liquid notion on bubble nucleation during beer dispense, *Chemical Engineering Science*, 58, pp. 4071-4084.

Hesketh R.P., Etchells A.W., Fraser Russel T.W., 1991, Experimental observations of bubble breakage in turbulent flow, *Ind. Eng. Chem. Res.*, 30, pp. 835-841.

Hesselgreaves, J.E., 2001, *Compact heat exchangers – Selection, design and operation*, New York, Pergamon.

Hibiki T., Situ R., Mi Y., Ishii M., 2003, Local flow measurements of vertical upward bubbly flow in an annuls, *International Journal of Heat and Mass Transfer*, 46, pp. 1479-1496.

Hill G., Holman J., 1995, *Chemistry in context*, London, Nelson.

Honda T., Kishikawa Y., Tokita T., Ohsawa H., Kawashima M., Ohkubo A., Yoshii M., Uda K., Suzuki A., B. Smith, ed., General model for estimating bubble dissolution and droplet evaporation times, *Optical Microlithography XVII*, 2004, Proc. SPIE 5377, pp. 319-328.

Hong K.T., Imadojemu H., Webb R. L., 1994, Effects of oxidation and surface roughness on contact angle, *Experimental Thermal and Fluid Science*, 8, pp. 279-285.

Image-Pro, 2010, *Image-Pro Plus Start-Up Guide*, MediaCybernetics,

Iskandrani A., Kojasoy G., 2001, Local void fraction and velocity field description in horizontal bubbly flow, *Nuclear Engineering and Design*, 204, pp.117-128.

Jones S.F., Evans G.M., Galvin K.P., 1999a, Bubble nucleation from gas cavities – A review, *Advances in Colloid and Interface Science*, 80, pp. 27-50.

Jones S.F., Evans G.M., Galvin K.P., 1999b, The cycle of bubble production from a gas cavity in a supersaturated solution, *Advances in Colloid and Interface Science*, 80, pp. 51-84.

Karagianni M., Avranas A., 2009, The effect of deaeration on the surface tension of water and some other liquids, *Journal of Colloid and Surfaces A: Physicochem Eng. Aspects*, 335, pp. 168-173.

Karapantsios T.D., Kostoglou M., Divinis N., Bontozoglou V., 2008, Nucleation, growth and detachment of neighbouring bubbles over miniature heaters, *Journal of Chemical Engineering Science*, 63, pp. 3438-3448.

Kashinsky O.N., Randin V.V., 1999, Downward bubbly gas-liquid flow in a vertical pipe, *Int. J. Multiphase Flow*, 25, pp. 109-138.

Kentish S., Lee J., Davidson M., Ashokkumar M., 2006, The dissolution of a stationary spherical bubble beneath a flat plate, *Chemical Engineering Science*, 61, pp. 7697 - 7705.

Kirkaldy J.S., 1956, The time-dependent diffusion theory for condensation on spherical and plane surfaces, *Canadian Journal of Physics*, 36, pp. 446 - 455.

Knapp R., Daily J.W., Hammitt F.G., 1970, *Cavitation*, London, Mc Graw Hill Book Company.

Kocamustafaogullari G. and Wang Z., 1991, An experimental study on local interfacial parameters in a horizontal bubbly two-phase flow, *Int. J. Multiphase Flow*, 17 (5), pp. 553-572.

Kocamustafaogullari G., Huang W.D., Razi J., 1994, Measurement and modelling of average void fraction, bubble size and interfacial area, *Nuclear Engineering and Design*, 148, pp. 437-453.

Kostoglou M., Karapantsios T. D., 2007, Bubble dynamics during the non-isothermal degassing of liquids; exploiting microgravity conditions, *Advances in Colloid and Interface Science*, 134-135, pp. 125-253.

Kress T.S., Keyes J.J., 11973, Liquid phase controlled mass transfer to bubbles in co-current turbulent pipeline flow, *Chemical Engineering Science*, 28, pp.1809-1823.

Kwak H.Y., Oh S.D., 2004, Gas-vapour Bubble Nucleation – A Unified Approach, *Journal of Colloid and Interface Science*, 278, pp. 436-446.

Lamers A., 2005, *Langdurige experimenten ketelproefstand*, Unpublished research, Eindhoven, Spirotech R&D.

Launder B.E., Spalding D.B., 1974, The numerical computation of turbulent flow, *Computer Methods in Applied Mechanics and Engineering*, 3 (2), pp. 269-289.

Lezhnin S., Eskin D., Leonenko Y., Vinogradov O., 2003, Dissolution of air bubbles in a turbulent water pipeline flow, *Heat and Mass Transfer*, 39, pp. 483-487.

Liebermann L., 1957, Air bubbles in water, *Journal of Applied Physics*, 4 (3), pp. 205 - 211.

LITREMETER, 2010, *500 Series Data Sheet*, LITREMETER Ltd., England.

Liu T.J., 1993, Bubble size and entrance length effects on void development in a vertical channel, *International Journal of Heat and Mass Transfer*, 19, pp. 99-113.

Liu T.J., Bankoff S.G., 1993, Structure of air-water bubbly flow in a vertical pipe-II. Void fraction, bubble velocity and bubble size distribution, *International Journal of Heat and Mass Transfer*, 36 (4), pp. 1061-1072.

Ljunggren S., Eriksson J.C., 1997, The lifetime of a colloid-sized gas bubble in water and the cause of the hydrophobic attraction, *Colloids and Surfaces A: Physical and Engineering Aspects*, 129-130, pp. 151 - 155.

Lu J., Tryggvason G., 2007, Effect of bubble size in turbulent bubbly downflow in a vertical channel, Chemical Engineering Science, 62, pp. 3008-3018.

Lubetkin. S., Blackwell M., 1988, The nucleation of bubbles in supersaturated solutions, Journal of Colloid and Interface Science, 26, pp. 610-615.

Michiyoshi I., Serizawa A., 1986, Turbulence in two-phase bubbly flow, *Nuclear Engineering and Design*, 95, pp. 253-267.

Mishima K., Hibiki T., Saito Y., Nishihara H., Tobita Y., Konishi K., Matsubayashi M., 1999, Visualisation and measurement of gas-liquid metal two-phase flow with large density difference using thermal neutrons as microscope probes, *Nuclear Instruments and Methods in Physics Research*, 424, pp. 229-234.

Naphon P., Wongwises S., 2006, A review of flow and heat transfer characteristics in curved tubes, *Renewable and Sustainable Energy Reviews*, 10 (5), pp. 463-490.

Naslund M., 1997, *On the Design of residential condensing gas boilers*, PhD Thesis, Department of Heat and Power Engineering, Lund Institute of Technology.

Nicholas J.V., White D.R., 1994, *Traceable temperatures: An introduction to temperature measurement and calibration*, Chichester England, Wiley.

Oldenziel D.M., 1983, *The use of the Spirovent micro bubble deaerator for the suppression of cavitation in a circulation pump*, Delft, Delft Hydraulics Laboratory.

Orbisphere Model 3654 Portable Analyzer, 2009, *User Manual*, Hach Lange.

Owhadi A., Bell K.J., Crain B., 1968, Forced convection boiling inside helically-coiled tubes, *International Journal of Heat and Mass Transfer*, 11 (12), pp. 1779-1793.

Payvar P., 1987, Mass transfer-controlled bubble growth during rapid decompression of a liquid, *International Journal of Heat and Mass Transfer*, 30 (4), pp. 699-706.

Perry R.H., Green, D., 1987, *Perry's Chemical Engineer's Handbook*, 7th Edition, London, McGraw-Hill.

Ponter A.B., Yekta-Fard M., 1985, The influence of environment on the drop size – contact angle relationship, *Colloid and Polymer Science*, 263, pp. 673-681.

Prabhanjan D.G., Raghavan G.S.V., Rennie T.J., 2002, Comparison of heat transfer rates between a straight tube heat exchanger and a helically coiled heat exchanger, *Int. Comm. Heat Mass Transfer*, 29 (2), pp. 185-191.

Pradanovic V., Fraser D., Salcudean M., 2001, Bubble behaviour in sub cooled Flow Boiling of Water at low Pressures and Low Flow Rates, *Int. J. Multiphase Flow*, 28, pp. 1-19.

Singh R., Shyy W., 2007, Three-dimensional adaptive Cartesian grid method with conservative interface restructuring and reconstruction, *Journal of Computational Physics*, 224, pp. 150-167.

Reid, R. C., Prausnitz, J. M., Poling, B. E., eds, 1987, *Properties of gases and liquids,* 4th edition, New York, McGraw Hill.

Rettich T.R., Battino R., Emmerich W., 1984, Solubility of gases in liquids; XVI. Henry's law coefficients for Nitrogen in water at 5 to 50°C, *Journal of Solution Chemistry*, 13 (5), pp. 335-348.

Revankar S.T., Ishii M., 1992, Local interfacial area measurement in bubbly flow, *International Journal of Heat and Mass Transfer*, 35 (4), pp. 913-925.

Roffelsen. F., 1984, *Method of and Apparatus for the Degasification of Circulation Systems for Liquids*, Helmond, U.S. Pat. 4,456,172.

Rohsenow W.M., Hartnett J.P., Cho Y.I., 1988, *Handbook of Heat Transfer*, 3rd Edition, New York, McGraw-Hill Handbooks.

Sander R., ed, 1999, *Compilation of Henry's law constants for inorganic and organic species of potential importance in environmental chemistry*, London, Max Planck Institute of Chemistry.

Sato Y., Sekoguchi K., 1975, Liquid velocity distribution on two-phase bubble flow, Int. J. Multiphase Flow, 2, pp. 79-95.

Sauer J., Schmeink C., Wastell D.G., 2007, Feedback quality and environmentally friendly use of domestic central heating systems, *Journal of Ergonomics*, 50 (6), pp. 795-813.

Scriven L. E., 1959, On the dynamics of phase growth, *Chemical Engineering Sciences*, 10, pp. 1-13.

SEDBUK, 2009, *Boiler efficiency database, Department for Environment, Food and Rural Affairs*, Available at: http://www.sedbuk.com [Accessed Date: 4th December, 2010].

Semmens M.J., Ahmed T., 2003, Gas transfer from small spherical bubbles in natural and industrial systems, *J. Environ. Sys.,* 29 (2), pp. 101 - 123.

Serizawa A., Kataoka I., Michiyoshi I., 1987, Turbulence structure of air-water bubbly flow-II. Local properties, *Int. J. Multiphase Flow*, 2, pp. 235-246.

Shäfer K., Lax E., 1962, *Eingenschaften der Materie in Ihrem Aggregatzuständen, 2. Teil, Bandteil b, Lösungsgleichgewichte I*, Berlin, Springer-Verlag.

Shafi M.A., Flumerfelt R.W., 1997, Initial bubble growth in polymer foam process, *Chemical Engineering Science*, 52 (4), pp. 627-633.

Shah R.K., Sekulić D.P., 2003, *Fundamentals of heat exchanger design*, New Jersey USA, John Wiley & Sons., Inc..

Shedd T.A., 2005, General model for estimating bubble dissolution and droplet evaporation times, *Chemical Engineering Science*, 4 (3), pp. 033004-1-8.

Slezov V.V., Abyzov A.S., Slezova Zh.V., 2003, The nucleation of gas filled bubbles in low-viscosity liquids, *Colloid Journal*, 66 (5), pp. 575-583.

Spirotech, 2007, Deaeration and Dirt Separation to Control System Water Quality, The cpd Collection, Available at: http://www.e3bw.co.nz/files/docs/t_Separation_to_Control_System_Water_Quality.pdf [Accessed September 28, 2011].

Spreitzer K., Rückbrodt D., Straky H., Observer-based Estimation of the water-mass-flow through a central heating boiler, *American Control Conference*, Anchorage AK, 2002, 37, pp. 5054-5059.

Sun Y., Beckermann C., 2010, Phase-field modelling of bubble growth and flow in a Hele-Shaw cell, *International Journal of Heat and Mass Transfer*, 53, pp. 2969-2978.

Talanquer V., Oxtoby D.W., 1995, Nucleation of bubbles in binary fluids, *Journal of Chemistry and Physics*, 22 (5), pp. 2156-2164.

Thang N.T., Davis M.R., 1979, The structure of bubble flow through venturis, *Int. J. Multiphase Flow*, 5, pp. 17-37.

The Building Regulations, Conservation of Fuel and Power – Part L1A, 2010, Office of the Deputy Prime Minister, London.

The Heating and Hot Water Industry Council, 2010, *Written evidence from the heating and hot water industry council*, Available at: http://www.publications.parliament.uk/pa/cm201011/cmselect/cmbis/561/561vw11.htm [Accessed June 26, 2012].

Thorncroft G.E., Klausner J.F., Mei R., 1998, An experimental investigation of bubble growth and detachment in vertical upflow and downflow boiling, *International Journal of Heat and Mass Transfer*, 41, pp. 3857-3871.

Tolubinsky V.I., Kostanchuk D.M., Vapour bubbles growth rate and heat transfer intensity at sub cooled water boiling, *4th International Heat Transfer Conference*, 1970, 5, paper B2.8.

Vaillant, 2010, *Instructions for installation and servicing ecoTEC*, Valliant Ltd., Rochester.

Van der Welle, R., 1985, Void fraction, bubble velocity and bubble size in two-phase flow, *Int. J. Multiphase Flow*, 11 (3), pp.317-345.

Verschaeren R., 2010, *Degassing nucleation sites in water flow under practical heating conditions*, Master in Mechanical Engineering, Technical University Eindhoven.

Versteeg H.K., Malalasekera, W., 2007, *Computational Fluid Dynamics – The Finite Volume Method*, 2 nd Edition, United Kingdom, Pearson – Prentice Hall.

Wang S.K., Lee S.J., Jones Jr O.C., Lahey Jr R.T., 1987, 3-D Turbulence structure and phase distribution measurements in bubbly two-phase flows, *Int. J. Multiphase Flow*, 13 (3), pp. 327-343.

Wang Y., Sefiane K., Barber J., Wilson S., Das K., Experimental and theoretical study of a single vapour bubble constrained between superheated or subcooled parallel plates, *Proceedings of the 2nd Micro and Nano Flows Conference (MNF09)*, Brunel University, 1st – 2nd September 2009, London, UK.

Watten B.J., Smith D.R., Ridge J., 1997, Continuous monitoring of dissolved oxygen and total dissolved gas pressure based on head-space partial pressures, *Journal of the World Aquaculture Society*, 28 (4).

Weiss M., Ditmar L., Junginger M., Patel M.K., Blok K., 2009, Market diffusion, technological learning and cost-benefit dynamics of condensing gas boilers in the Netherlands, *Journal of Energy Policy*, 37, pp. 2962-2976.

Wilt P.M., 1986, Nucleation rates and bubble stability in water – Carbon dioxide solutions, *Journal of Colloid and Interface Science*, 112 (2), pp. 530-538.

Winterton R.H.S., 1972a, Sizes of bubbles produced by dissolved gas coming out of solution on the walls of pipes in flowing Systems, *Chemical Engineering Science*, 27, pp. 1223-1230.

Winterton R.H.S., 1972b, Cover gas bubbles in recirculating sodium primary coolant, *Nuclear Engineering and Design*, 22, pp. 262-271.

Winterton R.H.S., Munaweera J.S., 2001, Bubble size in two-phase gas-liquid bubbly flow in ducts, *Chemical Engineering and Processing*, 40, pp. 437 - 447.

Winterton R.H.S., Orby P., Bubble size in ducts in ducts and bubble columns, *Proceedings of the 10th International Heat Transfer Conference*, Brighton, 1994, 6, pp. 259-299.

Xin R.C., Ebadian M.A., 1997, The effects of Prandtl number on local and average convective heat transfer characteristics in helical pipes, *Journal of Heat Transfer*, 119, pp. 467-473.

Yanagida H., 2008, The effect of dissolve gas concentration in the initial growth stage of multi cavitation bubbles; Difference between vacuum degassing and ultrasound degassing, *Journal of Ultrasonics Sonochemistry*, 15, pp. 492-496.

Yang S.R., Kim R.H., 1988, A mathematical model of the pool boiling nucleation site density in terms of the surface characteristics, International *Journal of Heat Transfer*, 31(6), pp. 1127-1135.

Yang W.J., Echigo R., Wotton D.R., Hwang J.B., 1967, Experimental studies of the dissolution of gas bubbles in whole blood and plasma – II. Moving bubbles or liquids. *Chemical Engineering Science*, 22, pp. 1393 - 1398.

Yildiz A., Güngör A., 2009, Energy and exergy analysis of space heating in buildings, *Journal of Applied Energy*, 86, pp. 1939-1948.

Young C.L., Battino R., Clever H.L., 1982, *The Solubility of gases and Liquids – Introductory Information, Nitrogen and Air, Solubility Data Series – Volume 10*, Pergamon Press, Oxford.

Žun I., 1980, The transverse migration of bubbles influenced by walls in vertical bubbly flow, *Int. J. Multiphase Flow*, 6, pp. 583-588.

Appendix I

Block diagram – LabVIEW
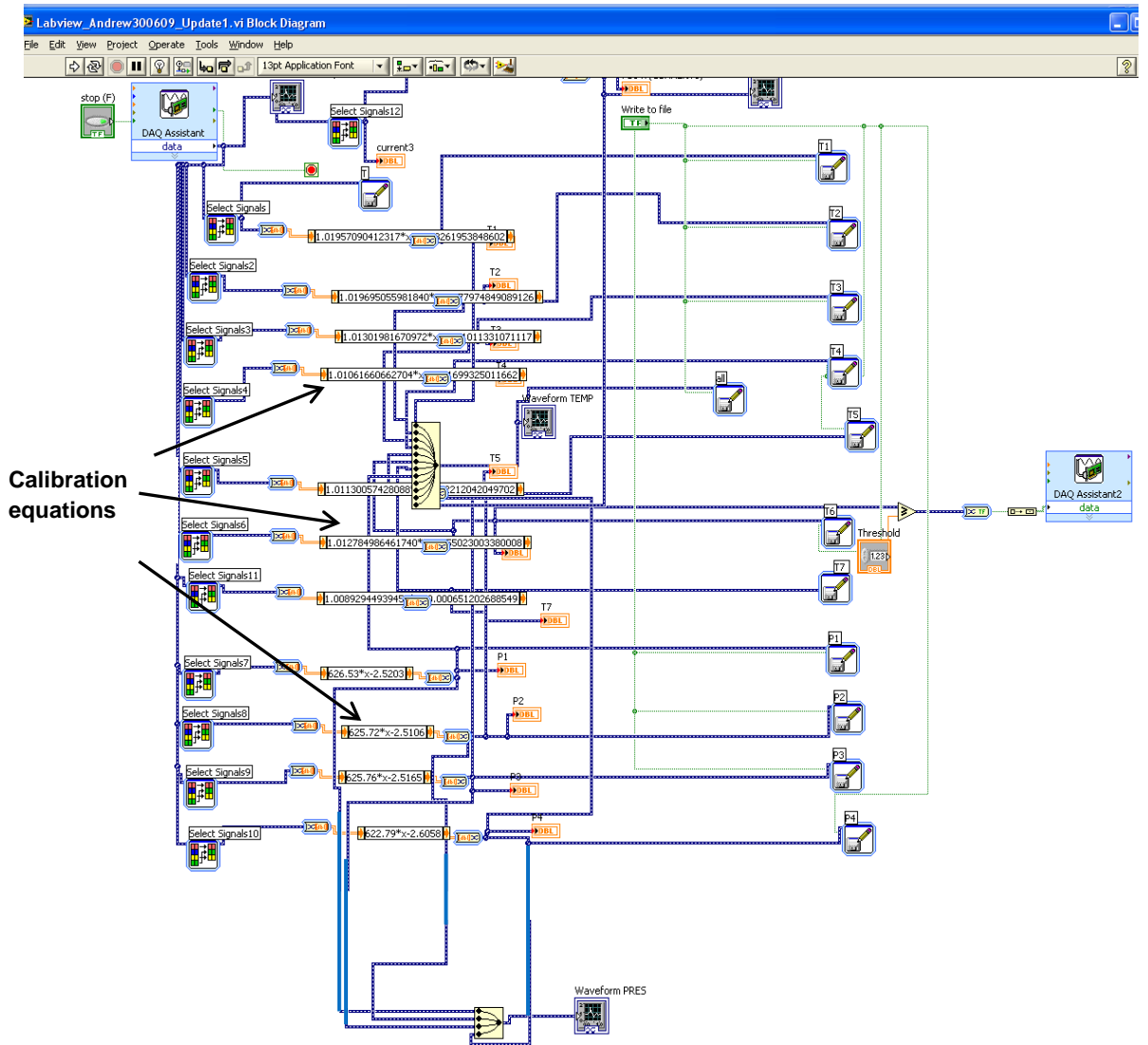
Figure A1: LabVIEW block diagram

Appendix II

Image-Pro Plus macro routine script

```
Option Explicit

Dim gDirStart As String

Sub ProcessDirectory()
Dim IName As String*255
Dim fName As String
Dim workStr As String
Dim docID As Integer, TempID As Integer
Dim i As Integer
Dim FirstImage As Boolean


If gDirStart = "" Then
  gDirStart = "C:\"
 End If

workStr = GetFilePath("", "*", "", "Select a file in the desired directory", 0)


   If workStr = "" Then
    Exit Sub
   End If
ret = IpAppCloseAll()


   gDirStart = Left(workStr, InStrRev(workStr, "\"))


   DebugClear
```

```
ret = IpOutputClear()


i = 0

 ret = IpMacroStop("Please select the correct calibration in the system settings
window.", 0)


  fName = Dir(gDirStart + "*.*", 32)


  While fName <> ""
 Debug.Print GetAttr(gDirStart + fName); " "; fName


              docID = IpWsLoad(gDirStart + fName, "")
              ret = IpSCalSetLong(SCAL_SYSTEM_CAL, SCAL_APPLY, 0)
        If docID >= 0 Then
        If i = 0 Then FirstImage = True


              Call FocusFilter(docID, FirstImage)
              Wait(1)
              ret = IpDcUpdate(DC_FETCH)
              ret = IpDcSaveData("",  S_Y_AXIS + S_X_AXIS + S_DDE)
              TempID = IpSnap()
              ret = IpWsSaveAs(gDirStart + fName + "_processed.tif", "TIF")
              ret = IpDocCloseEx(TempID)


              ret = IpAppSelectDoc(docID)
              ret = IpDocClose()
              i = i + 1
              Else
                    Debug.Print "Error loading "; gDirStart + fName
              End If
```

```
    fName = Dir()

  Wend

  ret = IpMacroStop("All images in directory processed.", MS_MODAL)

End Sub


Private Sub FocusFilter(ImgID As Integer, FirstImg As Boolean)

Dim FilterDoc As Integer

Dim ObjFound As Boolean

Dim numobj As Long

        ret = IpFltFlatten(0, 20)

        FilterDoc = IpWsDuplicate()

        ret = IpFltSobel()

        ret = IpAppSelectDoc(ImgID)

        ret = IpBlbShow(1)

        ret = IpBlbLoadSetting("D:\PhD\Image Pro\Macro by Image
Pro\bubles.env")

        numobj = IpBlbCount()

        If numobj = 0 Then

                ObjFound = False

        Else

                ObjFound = True

        End If


 ret = IpBlbUpdate(0)

 If ObjFound Then

  If FirstImg Then

   Begin Dialog UserDialog 400,105,"Adjust Settings" ' %GRID:10,7,1,1

    Text 20,14,340,42,"Please adjust the count settings to include all wanted
objects. Out of focus objects will be removed in the next step.",.Text1

    PushButton 150,70,90,21,"Continue",.PushButton1
```

```
End Dialog

Dim FstDlg As UserDialog

Dialog FstDlg

ret = IpBlbSaveSetting("D:\PhD\Image Pro\Macro by Image Pro\bubles.env")

Debug.Print ret

End If


ret = IpBlbCount()

ret = IpBlbUpdate(0)

ret = IpBlbSaveOutline("D:\PhD\Image Pro\Macro by Image Pro\bubles.scl")

ret = IpAppSelectDoc(FilterDoc)

ret = IpBlbLoadOutline("D:\PhD\Image Pro\Macro by Image Pro\bubles.scl")

ret = IpBlbLoadSetting("D:\PhD\Image Pro\Macro by Image Pro\OOF
bubles.env")


If FirstImg Then

Begin Dialog UserDialog 400,77,"Adjust Settings" ' %GRID:10,7,1,1

  Text 20,14,340,28,"Please adjust the intensity filter to remove out of focus
objects.",.Text1

  PushButton 150,49,90,21,"Continue",.PushButton1

End Dialog

Dim SndDlg As UserDialog

Dialog SndDlg

ret = IpBlbSaveSetting("D:\PhD\Image Pro\Macro by Image Pro\OOF
bubles.env")

End If

ret = IpBlbMeasure()

ret = IpBlbFilter()

ret = IpBlbSaveOutline("D:\PhD\Image Pro\Macro by Image Pro\Filtered
bubles.scl")

ret = IpDocCloseEx(FilterDoc)
```

```
  ret = IpAppSelectDoc(ImgID)

  ret = IpBlbLoadOutline("D:\PhD\Image Pro\Macro by Image Pro\Filtered
bubles.scl")

  ret = IpBlbLoadSetting("D:\PhD\Image Pro\Macro by Image Pro\bubles.env")

  ret = IpBlbMeasure()

 If FirstImg Then

  ret = IpDcShow(3)

  ret = IpTemplateMode(1)

  ret = IpDcMeasList(DC_LOAD, "D:\PhD\Image Pro\Macro by Image
Pro\BubleDataList.dcl")

  ret = IpTemplateMode(0)

  Begin Dialog UserDialog 400,70,"Measurements Selection" ' %GRID:10,7,1,1

   Text 10,14,380,14,"Please adjust your measurement selection list if
required.",.Text1

   OKButton 150,42,90,21

  End Dialog

  Dim dlg As UserDialog

  Dialog dlg

 End If

End If


 If ObjFound And FirstImg Then

 FirstImg = False

 ElseIf Not ObjFound And FirstImg Then

 FirstImg = True

 Else

 FirstImg = False

 End If


End Sub
```

Appendix III

Calibration charts
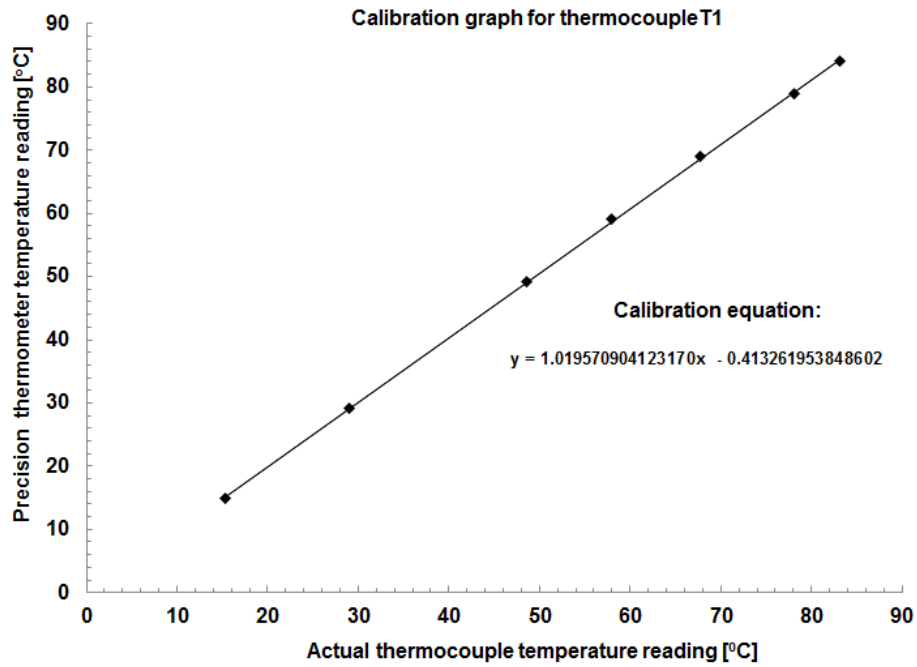
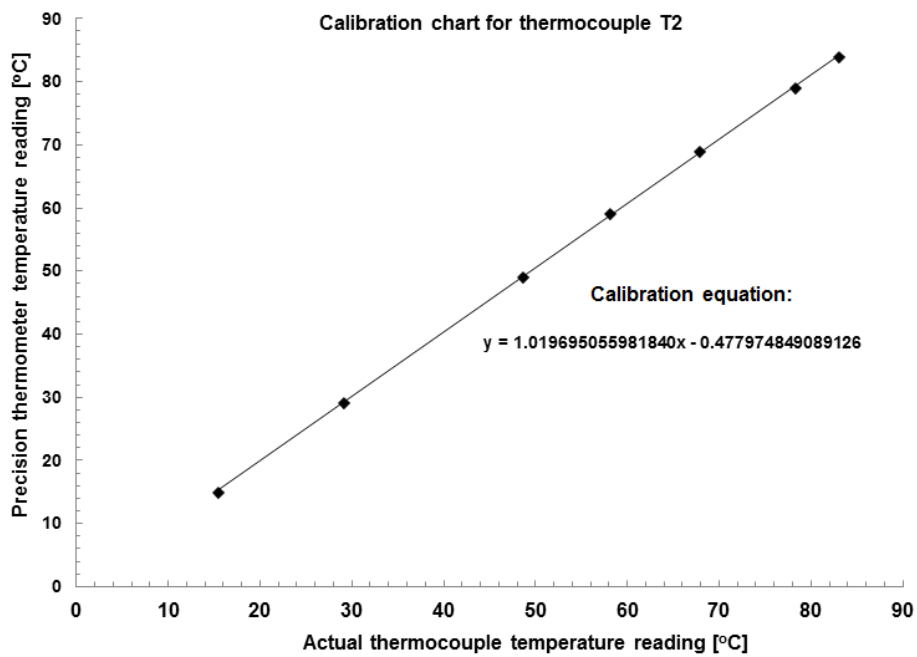**Figure A2: Calibration charts for thermocouple *T1* as in Fig. 3.1.**

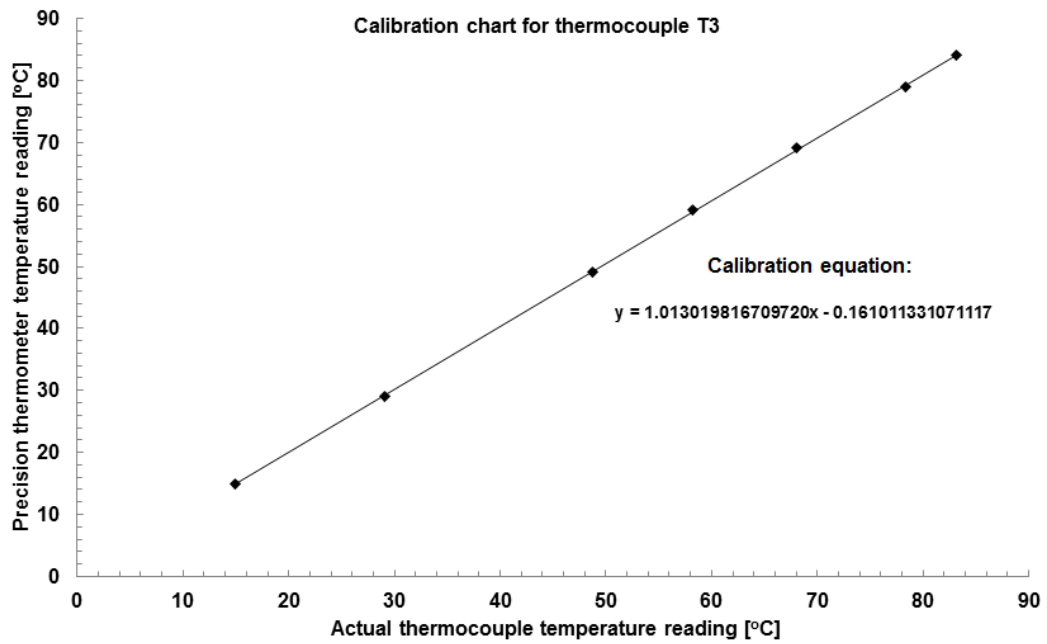**Figure A3: Calibration charts for thermocouple *T2* as in Fig. 3.1.**

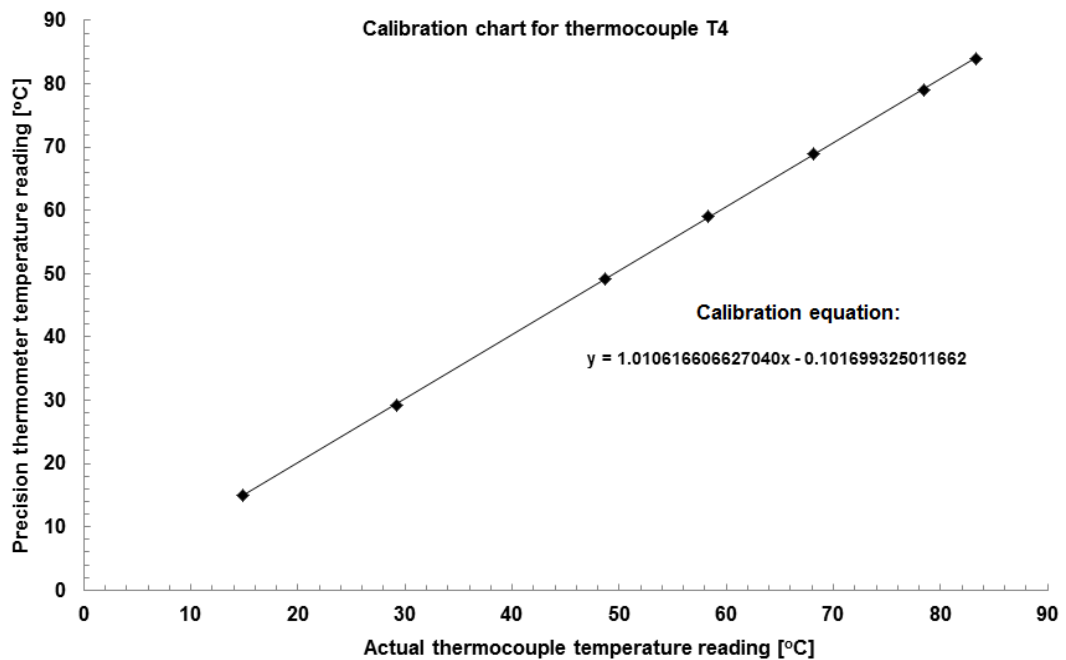**Figure A4: Calibration charts for thermocouple *T3* as in Fig. 3.1.**

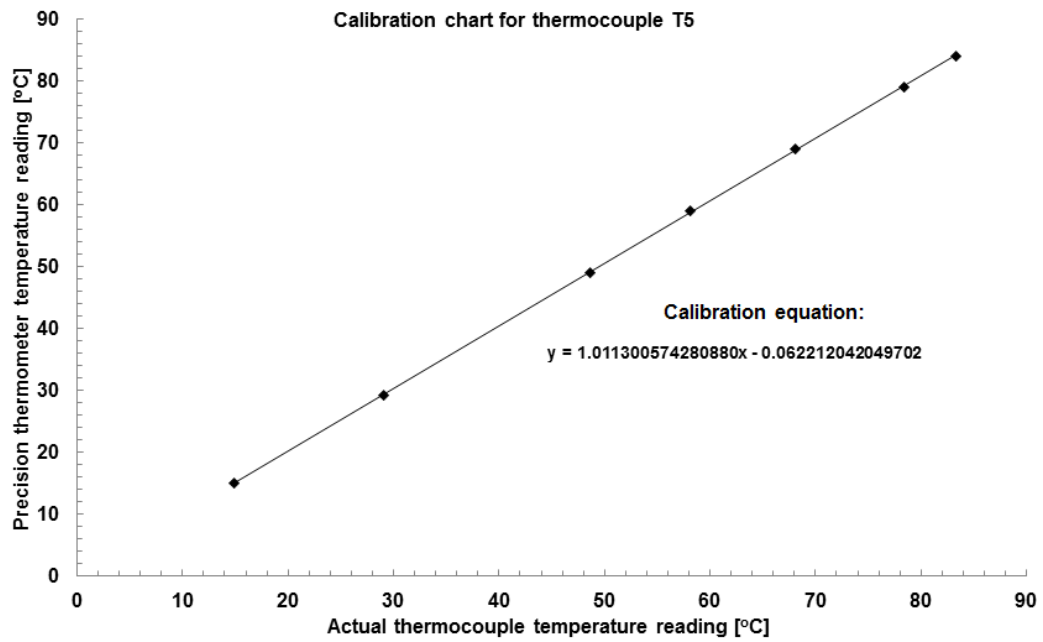**Figure A5: Calibration charts for thermocouple *T4* as in Fig. 3.1.**

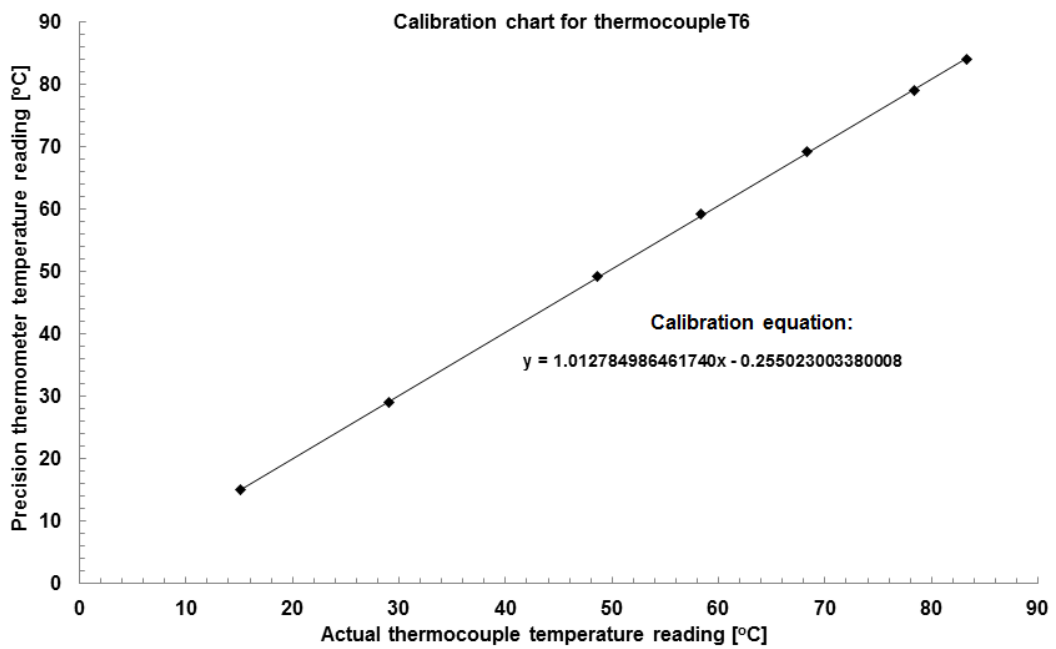**Figure A6: Calibration charts for thermocouple *T5* as in Fig. 3.1.**

Figure A7: Calibration charts for thermocouple *T6* as in Fig. 3.1.
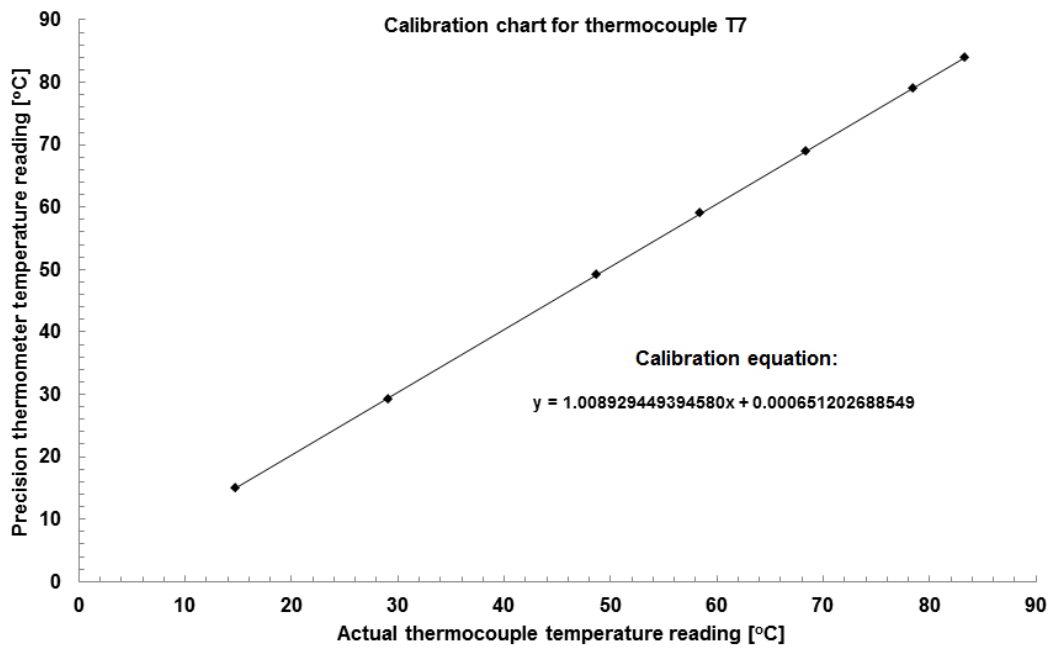
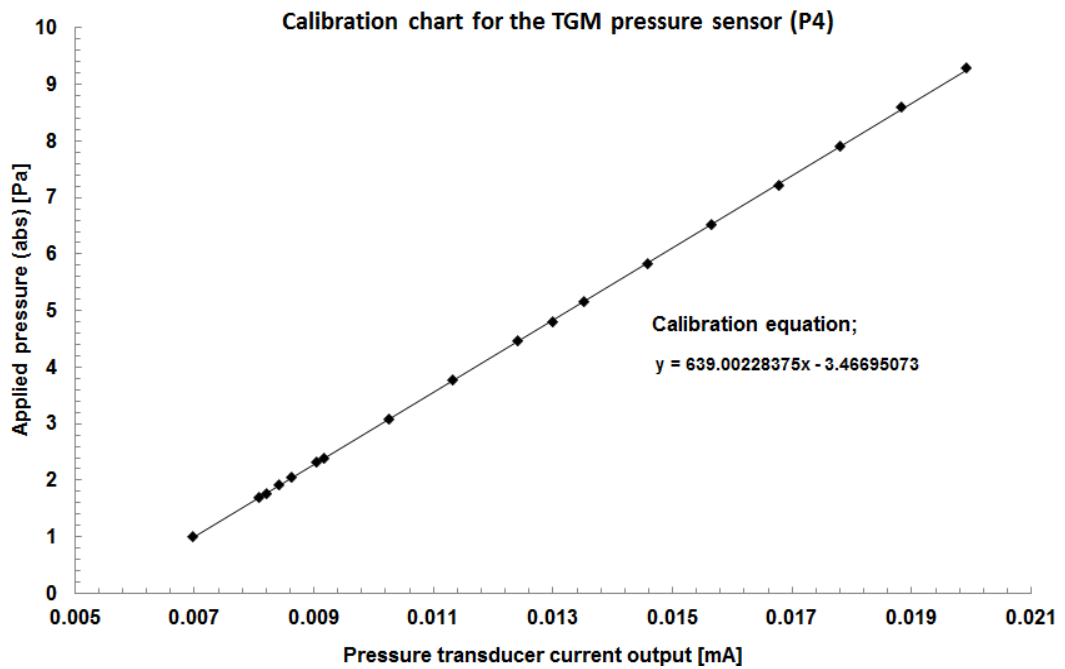**Figure A8: Calibration charts for thermocouple *T7* as in Fig. 3.1.**

Figure A9: Calibration charts for *TGM* pressure transducer *P4* as in Figs. 3.1 and 3.7.

Appendix IV

Wilke-Chang estimation method

This correlation was used so as to calculate the diffusivity of nitrogen in water. This was necessary as experimental data published in literature sources such as Ferrell and Himmelblau (1967) only included diffusivity data till circa 55 $^{\circ}$C.

$$D_{AB} = \frac{7.4E - 8(\emptyset M_B)^{1/2}T}{\eta_B V_A^{0.6}}$$

Where:

D_{AB} Mutual diffusion coefficient of solute A at very low concentrations in solvent B,   (cm^2/s)

M_B Molecular weight of solvent B,   (g/mol)

T Temperature,   (K)

η_B Viscosity of solvent B,   (cP)

V_A Molar volume of solute A at its normal boiling temperature (cm^3/mol)

$\emptyset$ Association factor of solvent B,   (-)

Wilke and Chang recommended a value of 2.6 (Reid et al., 1987) for the association factor of solvent *B* when this consists of water. This model has a general accuracy of circa 20% (Perry and Green, 1998). Reid et al., (1987) reported that a number of modifications to this model have been suggested over time. However, none of these suggestions are widely accepted.